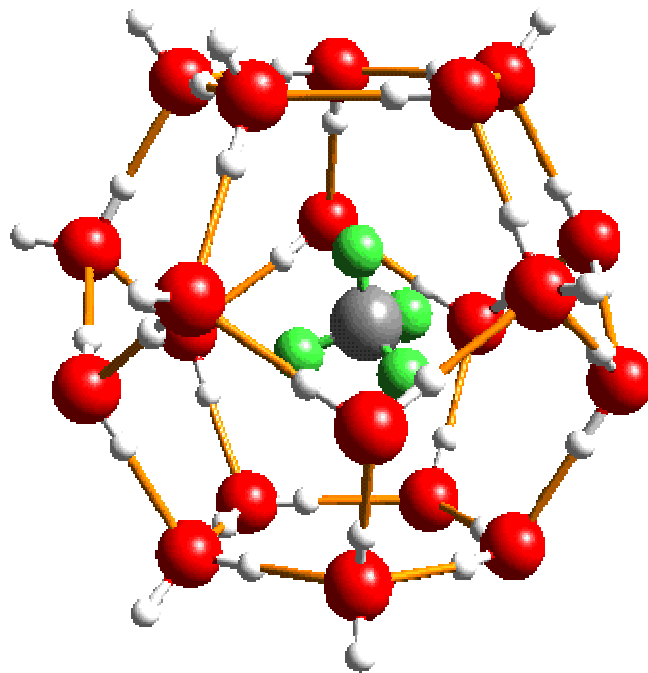# Theoretical Modeling and Analysis for Gas Hydrate Quantification from Prestack Seismic Data in the Northern Deepwater Gulf of Mexico

**A Report to the Gas Hydrates JIP,
Operated by ChevronTexaco**

November 2003

Reservoir Services Group
Data Consulting Services, Schlumberger
3600 Briarpark Drive
Houston, Texas USA

Table of Contents

Table of Figures

A.   Seismic Data Reprocessing

B.   Stratigraphic Evaluation of Gas Hydrates

E. **Quantitative Estimation of Gas Hydrates**

In making interpretations and analysis of field data, our employees will give customers the benefit of their best judgment. However, since all interpretations are opinions based on inferences from electrical or other measurements, we cannot, and do not guarantee the accuracy or correctness of any interpretation. We shall not be liable or responsible for any loss, cost, damage, or expenses whatsoever incurred or sustained by the customer resulting from any interpretation made by any of our employees.

1.0 Summary

Gas hydrates are metastable compounds of gas, such as methane or CO_2, and liquid, such as fresh water or seawater. The properties of gas hydrates depend upon pressure, temperature and the composition of the gas and liquids. Naturally occurring gas hydrates are found in nature under specific conditions of pressure (approximately 200 to 2000 psi), temperature (-10° to $+10^o$ C), and in areas that are gas prone. Gas hydrates contain roughly 170 ft^3 of gas at standard conditions per cubic foot of hydrate.

Gas hydrates forming in wells, pipelines and facilities can be safety hazards. Naturally occurring gas hydrates can also cause problems if wells have to be drilled through the hydrate zones to reach deeper, conventional deposits of oil and gas. Seafloor stability in areas prone to gas hydrate deposits are also a safety issue when it comes to drilling, producing, setting platforms and laying pipelines in deep water. On the positive side, vast deposits of naturally occurring gas hydrates can be a potential source of energy. Thus, detection of gas hydrates and its characterization is important from both a hazard and a resource point of view.

To address both the tools and technology needed to detect and characterize gas hydrates, the Department of Energy of the United States government sponsored a Joint Industry Project (JIP) in 2001. ChevronTexaco was awarded management of the project. WesternGeco carried out the seismic detection and characterization part of the project beginning 4Q2002, finishing at the end of 3Q2003. This report documents the procedure and findings. It also recommends possible sites for drilling verification. The wells are due to be drilled in 2Q2004.

The work proceeded in two basic parts. In Part 1 we address the initial screening for gas hydrates of six deepwater Gulf of Mexico (GOM) blocks using seismic attributes calculated from the poststack data without the benefits of well logs. The issue we raise is the following: Can speculative data from the Gulf of Mexico that is acquired and processed with no gas hydrate focus be used for gas hydrate detection. We obtained an affirmative answer to this question. From the initial screening of the speculative data, two prime candidate areas emerged: Keathley Canyon 195 and Atwater Valley 14. Keathley Canyon was chosen for the presence of a bottom simulating reflector (BSR) mappable over one-half of the project area. Atwater Valley was chosen for the numerous seafloor mound features, some possibly similar to Bush Hill as seen in Green Canyon 185. Green Canyon Blocks 184/185, an area with a known hydrate mound feature (Bush Hill), also provided useful knowledge for modeling and gas hydrate saturation estimation.

We designed a reprocessing flow for the data from the above mentioned blocks. Key steps of the processing that added value are: 2 ms sampling, amplitude preserving 3D Kirchhoff prestack time migration, detailed velocity analysis and demultiple. Amplitude preservation is a key requisite prior to prestack inversion for extracting gas hydrate properties from seismic data.

Part 2 concerns the application of inversion and analysis techniques to extract gas hydrate properties and saturations. For this, we designed a new workflow. We term this a 5-step workflow. This included creating a detailed stratigraphic interpretation framework for subsequent inversion, and to identify structural and depositional morphology associated with gas hydrate features. Numerous horizons were mapped and attributes were generated for each area. These were used to further delineate potential hydrates as well as guide the elastic inversion process.

The obtained inversion results, along with a detailed lithologic description of the shallow GOM sediments and a relationship to the seismic waveforms, were used to derive the physical rock model and hydrate elastic properties. This model was in part created using analog gas hydrate well information from both onshore and offshore wells as well as previously published theories. A key result from the modeling indicated that the seismic-inversion P-wave relationship was of primary importance in predicting hydrate sensitivity. The S-wave response was more difficult to accurately model and of only secondary importance.

The final results from the modeling were separate 3D volumes estimating gas hydrate saturation for the Keathley Canyon Block 195 area and the Atwater Valley Block 14 area. Because of the shale content in the GOM near-water bottom sediments, hydrate saturation estimation results will likely tend toward the maximum possible values. However, by exploiting the large amount of high-resolution 3D seismic coverage in the deepwater GOM, the model provides a useful tool to quantitatively estimate gas hydrate occurrences without the necessity of having a BSR present to provide primary delineation. This model is also updateable for improved accuracy when actual drilling and sampling information becomes available in the JIP Phase 2.

2.0 Introduction

In deep ocean sediments, natural gas hydrates are stable only at a very shallow interval below the seafloor. The gas hydrate stability zone (GHSZ) is determined by water depth, pore pressure, seafloor temperature, thermal gradient, and gas and fluid composition. Gas hydrates, composed predominantly of methane and water and found in arctic and global deepwater basins, have traditionally been viewed as both a curiosity and a drilling hazard. However, as the search for oil and gas extends into ever-deeper waters, particularly within the northern Gulf of Mexico, the focus in hydrates is shifting toward their potential as an untapped energy resource.

Locating likely areas of gas hydrates using remote sensing techniques, such as seismic, is relatively straightforward in many parts of the world where bottom-simulating reflectors (BSR) are readily evident. A BSR is a high-amplitude reflector that approximately parallels the seafloor, and which results from the strong acoustic impedance contrast between the gas hydrate-bearing sediments above the reflector and the underlying sediments containing free gas. Because the BSR follows a thermobaric surface rather than a structural or stratigraphic interface, it is normally observed to crosscut other reflectors. However, locating gas hydrates in the Gulf of Mexico is much more challenging. BSRs are rarely observed on seismic data in the Gulf of Mexico. There are many theories as to why this is the case. One reason is that the GOM sediments are too chaotic and heterogeneous to observe a BSR. Others believe that BSRs do exist in the GOM, but are largely undetectable due to inadequacies of current seismic data. It should be noted that the presence of a BSR, seafloor mounds, amplitude blanking, or other gas hydrate indicators cannot positively confirm the existence of hydrates. To better determine the existence of gas hydrates, and to quantify actual hydrate saturation, one needs first to extract relevant elastic parameters from seismic inversion, and then relate those parameters to the occurrence of gas hydrate using an appropriate rock model. Therefore, the quantification procedure is indirect.

WesternGeco, an affiliate of Schlumberger Technology Corporation and as a member of the ChevronTexaco Gas Hydrates JIP consortium, proposed using 3D seismic data to screen six Gulf of Mexico blocks in five separate areas, choosing two blocks for additional work, in the search for gas hydrates prior to drilling. The absence of well logs and other hard data presented a key challenge in the study.

Gas Hydrate Modeling & Analysis: The 5-step process*

E) Quantitative analysis
- Quantify gas hydrate rock properties

A) Reprocessing
- At highest resolution

Hydrate Characterization

B) Stratigraphic evaluation
- Where are potential hydrate zones

D) Rock property inversion
-Identify Hydrates (1D)
-Map Hydrates (3D)

C) Seismic attribute analysis
- Flag anomalous zones

*Patent pending
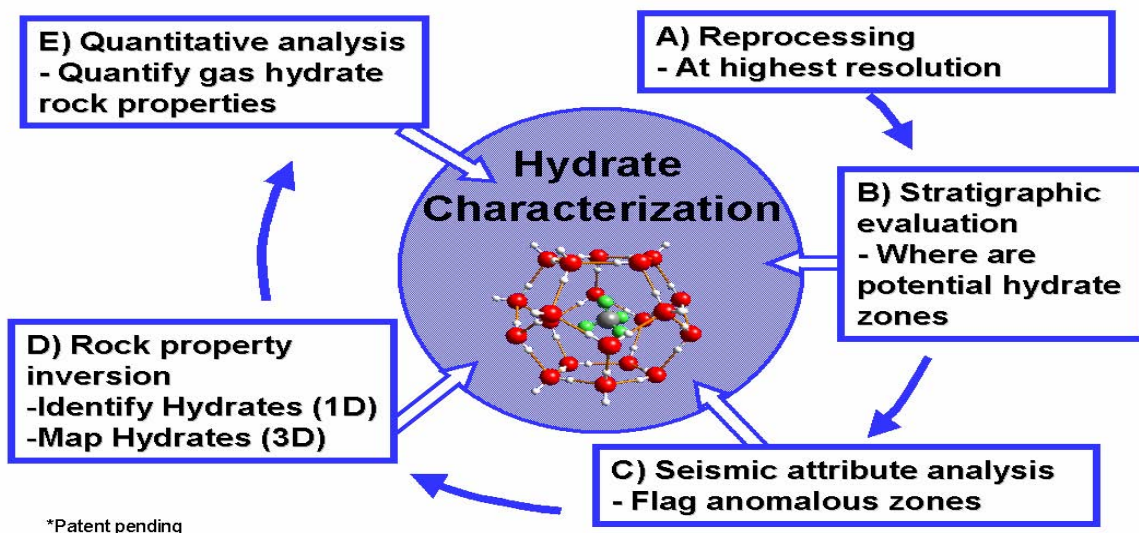
The primary JIP mission, which proceeded in two phases, was to determine whether speculative seismic survey data could be used to find, delineate and quantify natural gas hydrate occurrences. To that end, WesternGeco employed a proprietary five-step integrated multidisciplinary approach that included: 1). Reprocessing conventional 3-D seismic data at the higher resolution using an amplitude-preserving flow with prestack time migration, 2) a detailed stratigraphic evaluation and interpretation to identify potential hydrate zones, 3) seismic attribute analysis to further delineate anomalous zones, 4) full-waveform prestack inversion to characterize acoustic properties of gas hydrates in 1D (Mallick, 1995) and subsequent hybrid inversion in 3D (Mallick et al., 2000), and 5) quantitative estimation of gas hydrate saturation using rock property models.

The 5-step workflow for gas hydrate detection and quantification is independent of whether a BSR is present or absent. It is intended to provide a framework for gas hydrate characterization using an integrated geological and geophysical approach. Full-waveform prestack inversion (FWPI) and a detailed assessment of rock physics models for gas hydrates are centerpieces of the methodology. The remainder of the report will follow this workflow.

Results of recent gas hydrate drillings worldwide, such as the Mallik 2L-38 well in Northern Canada and Ocean Drilling Program's (ODP) Leg 164 wells at Blake Ridge on the Atlantic coast, have demonstrated a consistent relationship between the rock elastic properties and gas hydrate saturations in the sediments. Higher gas hydrate concentrations create an increase in the elastic properties. There are numerous rock physics models in the literature that attempt to quantify this effect. There have also been empirical studies performed on hydrates describing the acoustic properties (e.g., the weighted average equation by Lee, 1996). The advantage of an empirical relationship is that it is based upon real observations, and very simple to implement. However, empirical studies are not necessarily valid in all geological settings and for rock properties different from where they were formulated. In these frontier areas, where little data is available, results from quantitative hydrate modeling can provide a valuable starting point. We have attempted this in the current work by evaluating the predictions of several relevant rock models for gas hydrates, and validating some of our observations using the drilling data from both the Mallik and Blake Ridge wells.

In our study and with no available drilling information, we designed a quantitative estimation procedure that included elastic property inversion, rock physical modeling, and quantitative gas hydrate saturation calculation. Realistic gas hydrate quantitative estimation based on seismic data relies on accurate elastic property estimation from seismic inversion and a practical gas hydrate rock physical model. Full-waveform prestack inversion was applied at numerous locations to estimate high-resolution Vp, Vs, and density. The elastic properties were extrapolated in 3-D using the Hybrid inversion process which integrates pseudo well log curves derived from the full-waveform prestack inversion in a conventional linear prestack inversion for robustness and efficiency. Technical details for these inversion schemes are documented later in the report. The reliability of our initial predictions will be ascertained in the Phase 2 drilling program. There are numerous sources of ambiguities. Gas hydrate saturation estimates must be calibrated to well data. It should be noted that, despite the large number of drilled hydrate wells worldwide, quality hydrate logging and coring data are scarce, especially in the Gulf of Mexico. Such data are urgently needed. This must also be supplemented by controlled laboratory measurements of the various properties of gas hydrates. This is, in part, being addressed by other JIP consortium members.

Note that the seismic technology, as a remote sensing tool, is appropriate for gas hydrate detection. However, the data requirements are numerous: high S/N and wider frequency contents are just two of the main prerequisites. As of late, the seismic industry has progressed to meet these requirements. An example of this can be seen below using the single-sensor data (Q* data) in the East Breaks area of the Gulf of Mexico. A subtle BSR crosscutting the strata in the shallow sediments is clearly revealed along with several dewatering features (mud

volcanoes?). These may be related to shallow hazards as well. The high fidelity of the Q data clearly helped in the identification of such features.
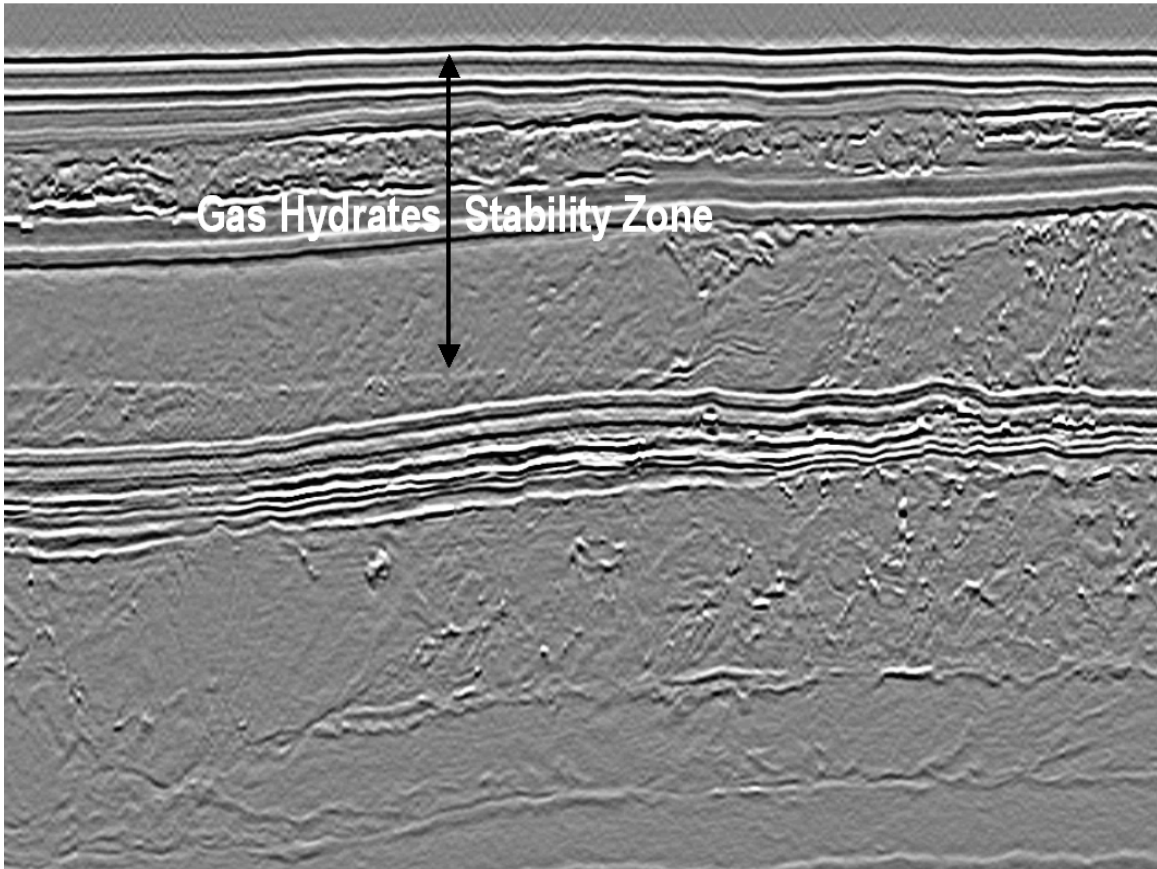
A.   Seismic Data Reprocessing

In keeping with the flow of the 5-step process, we began our work with the reprocessing of the 3-D post-stack seismic data from WesternGeco's multiclient data library. Initially this was done for the Green Canyon Blocks 184-185 and later for the Atwater Valley Block 14 and the Keathley Canyon Block 195 areas.   Each output area covered one 3 by 3 mile OCS block.   The reprocessing consisted of a prestack time migration (PSTM) amplitude preserving AVO sequence, as opposed to the original data, which were processed through a standard stack and migration sequence as listed below. The objectives of the reprocessing were to prepare the data for seismic inversion as well as improve the structural imaging and overall resolution. This also included processing at 2 ms sampling, instead of the original 4 ms, to help enhance the temporal resolution, particularly in the near sea-floor section.

- **Original Processing Flow**
    – SEG_D Conversion - 4ms sample rate
    – Navigation merge with seismic / Trace editing & SWATT
    – Spherical Divergence & Exponential gain
    – Signature Deconvolution / Shot Consistent Deconvolution
    – Parabolic Radon Transform Demultiple
    – DMO 24 offsets   -   Stolt Migration each offset (Green Canyon)
    – Velocity analysis & NMO correction
    – Mute and PSTM Stack   & Demigration
    – Poststack FDCP migration
    – 3D RNA

The reprocessing flow necessary to provide the best solution for the inversion and modeling process was not the optimum flow for structural and stratigraphic interpretation. The needs for interpretation were optimal imaging and resolution of the faults, hydrate features and other near-surface lithology. The inversion requirements were for maintaining true amplitude relationships. Because it was not possible to achieve all the desired data characteristics in a single volume, the final processing flow diverged following signature deconvolution. This resulted in the creation of two separate volumes for each area, one to be used for structural interpretation and one for full-waveform inversion. The complete flow for each is shown below.

- **Reprocessing Flow (Structural interpretation volume)**
    – SEG_D Conversion at 2 ms
    – Navigation
    – Trace editing
    – Swell noise Attenuation (SWATT)
    – Signature Deconvolution
    – Shot Deconvolution
    – Kirchhoff Prestack Time Migration
    – Velocity analysis
    – Radon Demultiple
    – Convert to Zero Phase
    – BP filter
    – RAAC

- **Reprocessing Flow (Full-waveform Inversion volume)**
    - SEG_D Conversion at 2 ms
    - Navigation
    - Trace editing
    - Swell Noise Attenuation (SWATT)
    - Signature Deconvolution
    - Kirchhoff Prestack Time Migration
    - Velocity analysis
    - Convert to Zero Phase
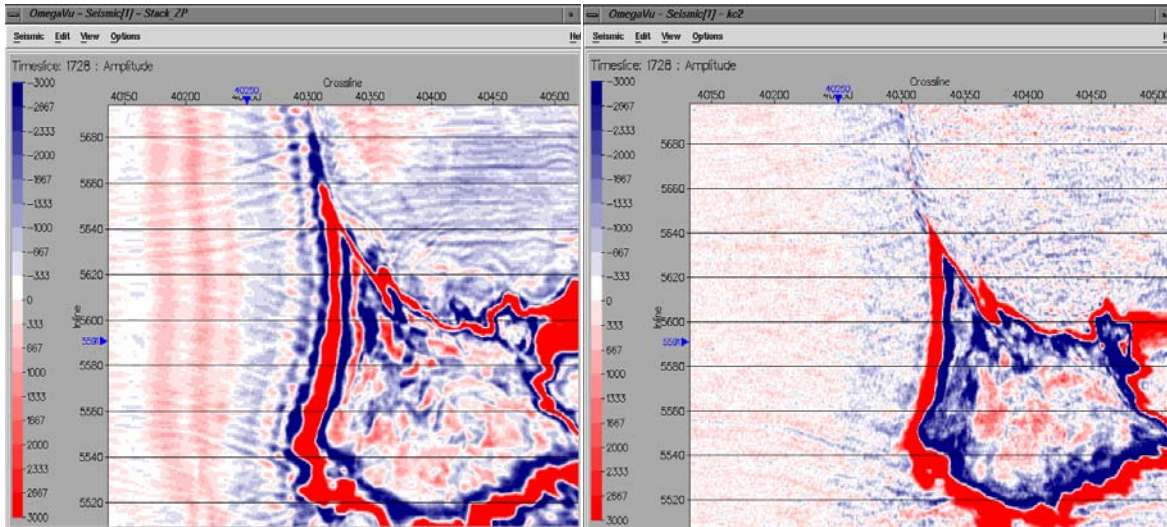
Figure A.1. Keathley Canyon 195 time slice 1728 showing original processing (right) and reprocessing (left). Improvements in resolution and phase control can be seen.
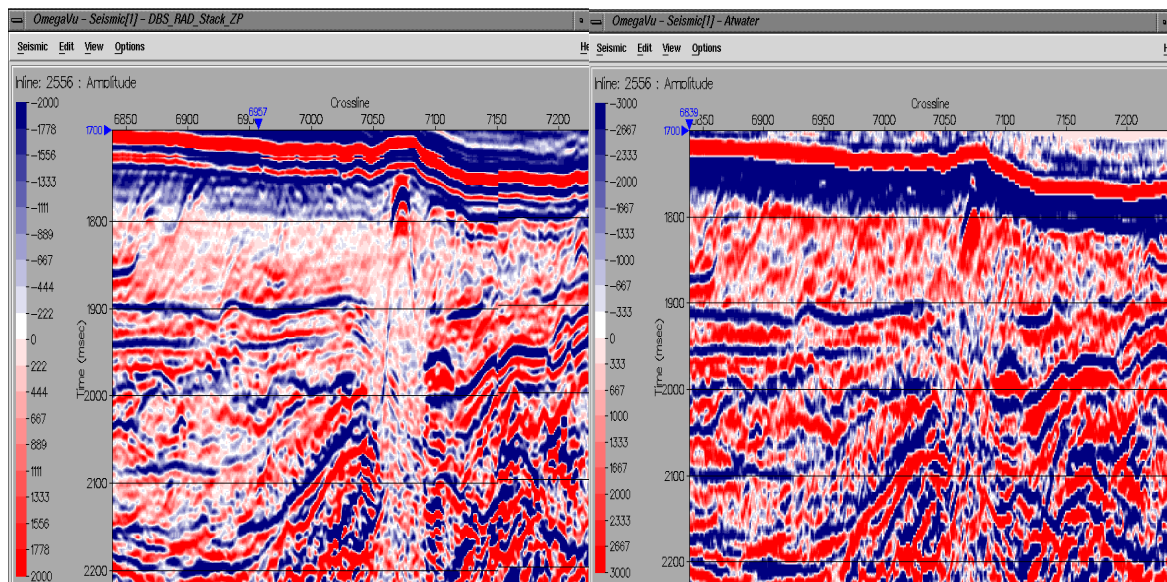
Figure A.2. Atwater Valley 14 inline 2556 showing original processing (right) and reprocessing (left). Gas chimney below mound and shallow reflectors more clearly imaged.

The overall improvements obtained from the reprocessing can be seen in terms of quality, resolution, imaging and phase and amplitude control. All these factors were necessary for detailed interpretation and quality attribute analysis, as well as for maintaining confidence in the inversion results and subsequent modeling and saturation estimations. Two examples are shown above in Figures A.1 and A2 comparing original and reprocessing data over Keathley Canyon and Atwater Valley areas. Figure A3 below shows the original and re-processed data for a line over the Green Canyon test area.
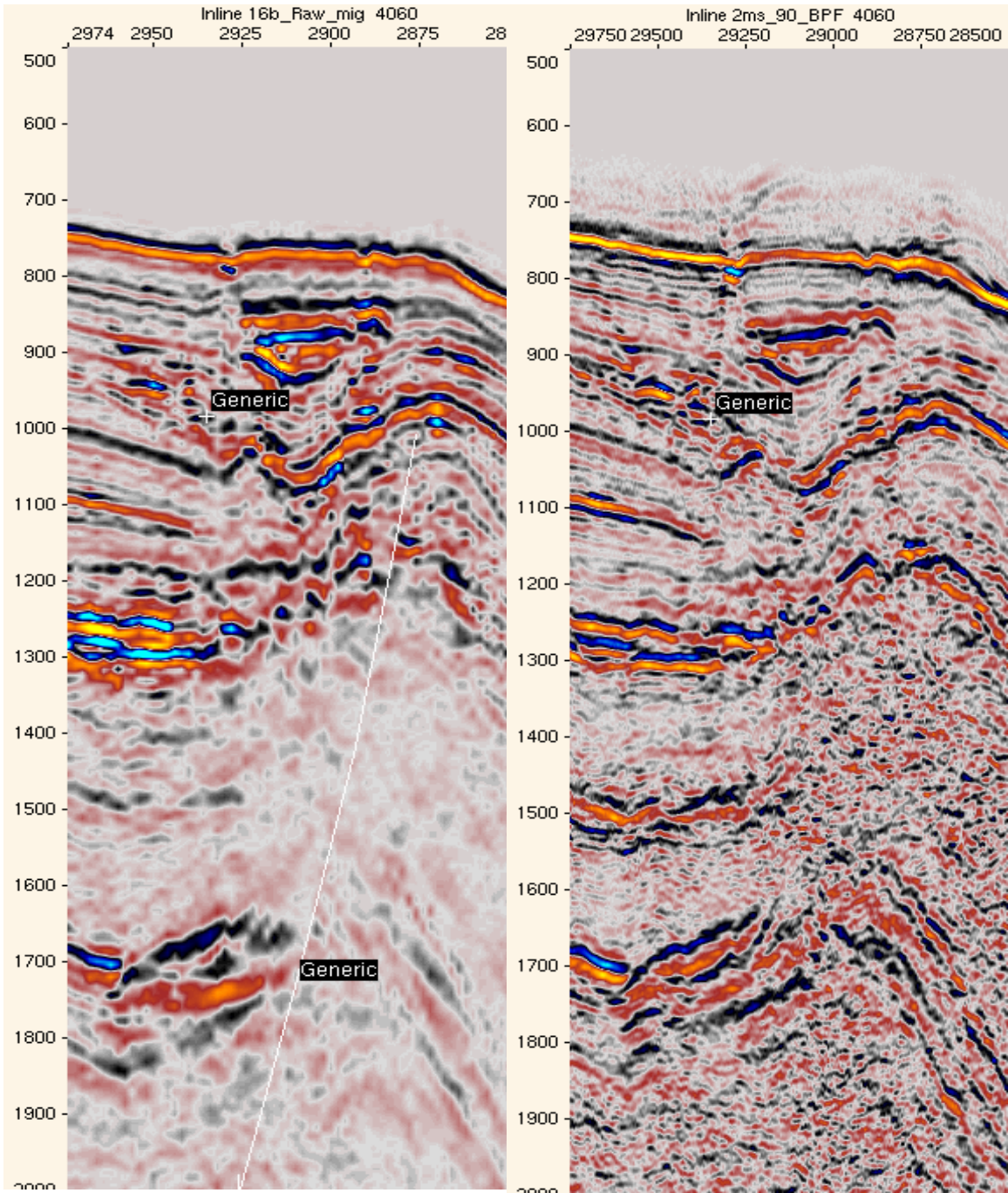
Figure A.3. Green Canyon 184-185 N-S line 4060 (east of Bush Hill) showing original 4 ms data (left) and re-processed PSTM 2 ms data (right).

14

A complete and detailed discussion of the data reprocessing can be found in the reprocessing summaries included at the end of this report following the appendices.

B.   Stratigraphic Evaluation

B.1 Initial Screening - Part 1

Six Gulf of Mexico blocks in five separate areas were in the original list for initial gas hydrate screening. Post-stack migrated multiclient data, which was part of WesternGeco's speculative data library, was made available. All seismic data were sampled at 4 ms and processed through a standard post-stack sequence. Because digital well log information were not available, only published literature information was used to facilitate our work. Some qualitative hydrate information was available for nearby wells in the Green Canyon 184/185 area, however logged intervals excluded the hydrate zone of interest. Seismic characteristics known to be indicative of hydrate occurrences and potential hydrate zones were used in the screening process. Some of these criteria are listed below in Figure B.1 with notations for each area examined:

Seismic Indicators of Shallow Gas Hydrates	Green Canyon 184	Green Canyon 185	Atwater Valley 14	Keathley Canyon 195	Alaminos Canyon 856	Miss. Canyon 802
Large variability in amplitude strength, continuity, lateral consistency within GHSZ	X	X				
Presence of gas and water in near surface sediments (shallow water flow type features)	X	X	X			
Gas chimneys		X	X			X
Mud volcanoes		X	X	X		
"Shingling" of reflectors with increased amplitudes at shallow depths		X	X	X		X
Sea floor failures and slumping		X	X	X		
Presence of a BSR				X		
Widespread strongly attenuated blanking zones		X	X			X
Possible polarity reversals at or near the water bottom interface	X	X	X			

Figure B.1. Table of seismic indicators used for initial screening of the six blocks.

Many of the indicators listed above were found on the five surveys strongly suggesting the presence of gas hydrates. However, the objectives of the early Phase 1 work were not to positively confirm nor deny the existence of hydrates at any of the locations. More definitive and quantitative analysis would result from the subsequent inversion and modeling work. A summary of each area is reviewed in the following sections along with a ranking as to the quality of hydrate characteristics observed.

B.1.1 Atwater Valley 14

The Atwater Valley 14 Block is ranked #1 as to the quality of the hydrate characteristics.

The data appeared to be near zero-phase as evidenced by the water bottom reflector in which the increase in acoustic impedance shows as a peak or positive excursion with low-amplitude negative leading side lobe. There are numerous prominent features present on the seafloor

(Figure B.2). One area of probable gas hydrate mounds was identified on the western and central area of the survey (MC Block 981, AT Blocks 13, 14). Most mounds follow a general northwest-southeast trend corresponding to the fault fabric. One mound ("D") exhibits weak amplitude polarity reversal at water-mound interface (Figure B.3). Another mound ("F") shows a deeper polarity reversal (Figure B.4b). Both reversal anomalies are indicative of a possible BSR. The central region shows a possible hydrate mound and associated slump ("G"). Most mounds appear to be less than 180 m (600 ft.) wide. There is no regional BSR evident in the area. There does exist some weak amplitude blanking below the mounds extending about 0.4 seconds below the mudline (BML). The hydrate stability zone for 90-96% methane is estimated to extend below the mudline (approximately 800-1000 m) based upon thermal heat flow estimates (~1.0 sec TWT).

Possible hydrate locations (centered at):
Line 2802 Crossline 6957 27° 58' 50.5"N   89° 17' 42.4"W (location A)
Line 2767 Crossline 6956 27° 58' 27.6"N   89° 17' 42.5"W (location B in MC Block 981)
Line 2738 Crossline 6931 27° 58' 08.8"N   89° 17' 53.6"W (location C)
Line 2670 Crossline 6926 27° 57' 24.6"N   89° 17' 54.6"W (location D in Block 13)
Line 2602 Crossline 6861 27° 56' 39.9"N   89° 18' 23.6"W (location E)
Line 2556 Crossline 7073 27° 56' 11.8"N   89° 16' 46.0"W (location F in Block 14)
Line 2616 Crossline 7262 27° 56' 51.9"N   89° 15' 20.4"W (location G)
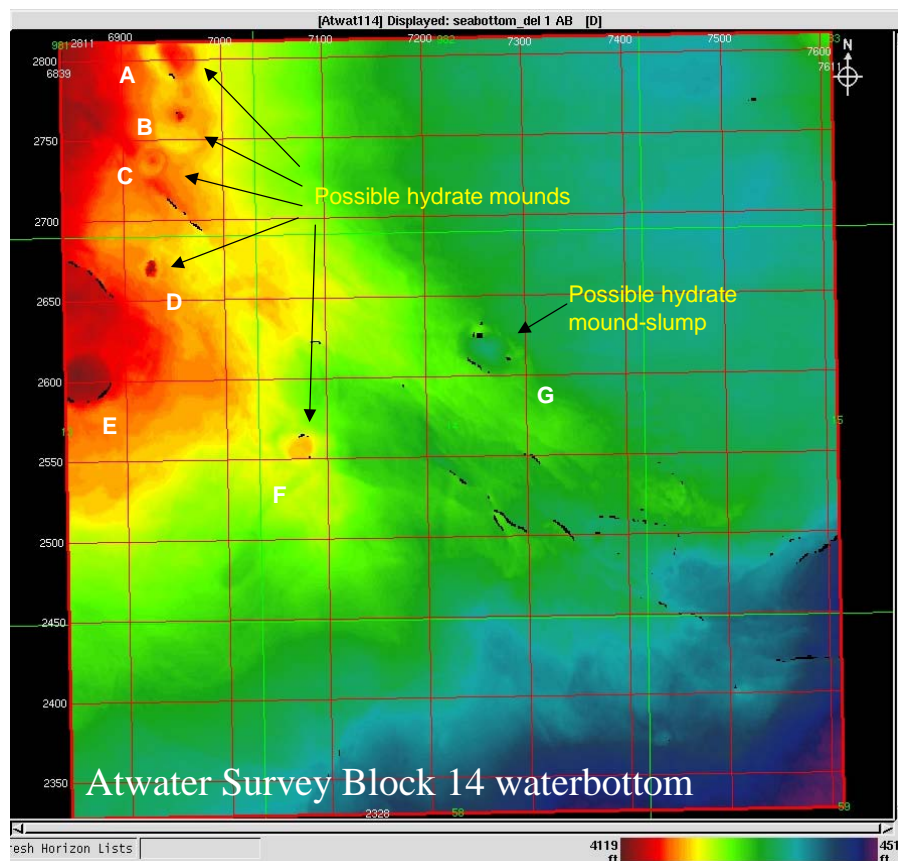
Figure B.2. Atwater Valley 14 water bottom map with seafloor mounds.

Interpretation:
Water bottom
Shallow unconformity
Top Luann salt

Location D (inline 2670/xline 6926 Block 13) with polarity reversal at water-mud interface and amplitude blanking zone below mound.
Location B (inline 2767/xline 6958 MC Block 981) apparent gas chimney.
Location F (inline2556/xline 7073 Block 14) amplitude blanking zone and within Block 14.
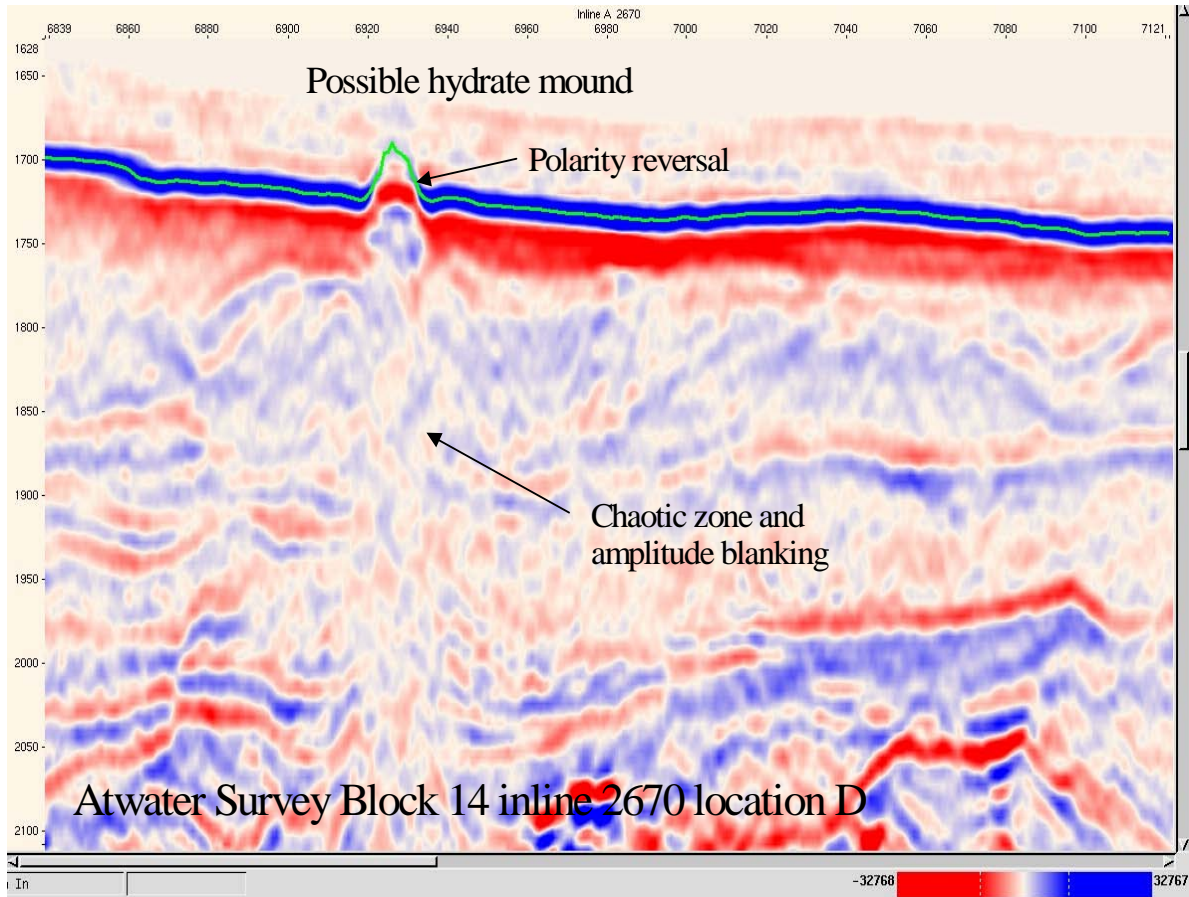
Figure B.3. Atwater Valley 14 seismic section showing possible hydrate mound "D" with associated chaotic zone and amplitude blanking.

Possible hydrate mound

Gas chimney

Atwater Survey Block 14 inline 2767 location B

Possible hydrate mound

BSR?

Amplitude blanking

Atwater Survey Block 14 inline 2556 location F
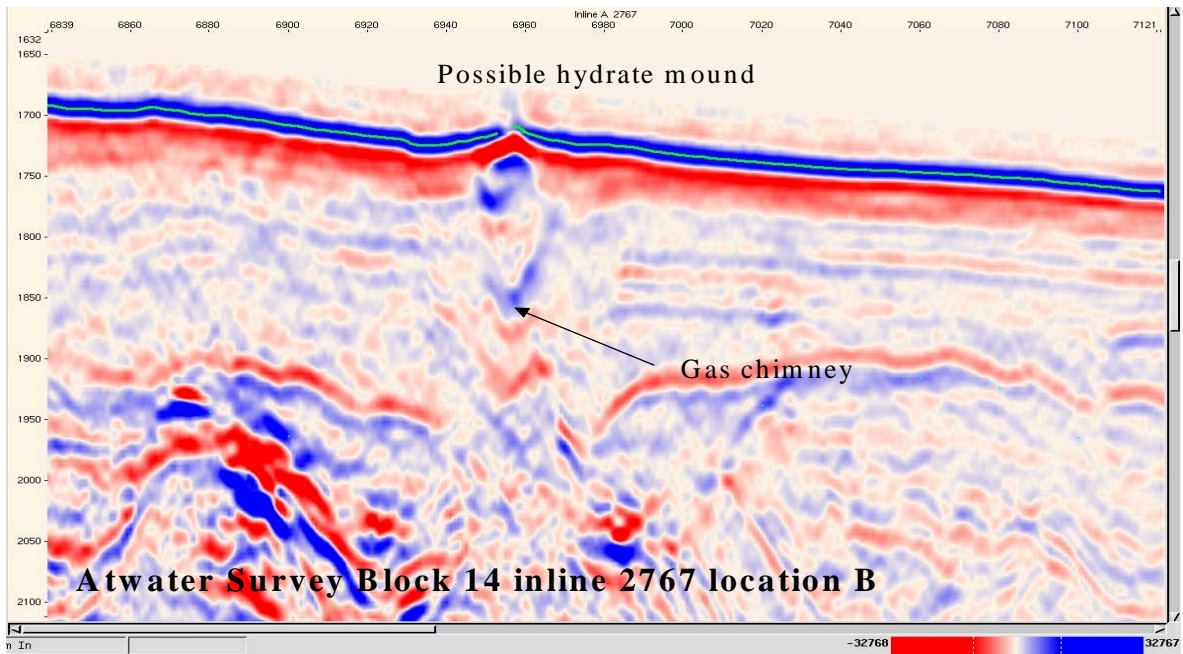
Figure B.4a (top), B.4b (bottom). Atwater Valley 14 Inline seismic lines showing possible hydrate mounds "B" (top) and "F" (bottom) with amplitude blanking and gas chimneys.

B.1.2 Keathley Canyon 195

The Keathley Canyon 195 block is ranked #2 as to the quality of the hydrate characteristics.

As shown in Figure B.6, the data appear to be zero-phase as evidenced by the water bottom reflector in which the increase in acoustic impedance shows as a peak or positive excursion without leading side lobe.

A large graben area (Figure B.5) with associated slumping exists in the eastern part of Block 194 and western part of Block 195. However, no distinct hydrate features are present in this area. There are possible surface hydrates in the region surrounding area "B". This includes an amplitude blanking zone 0.5-0.6 seconds below the mud layer. A possible BSR is evident in the eastern part of Blocks 151 and 195. Several water bottom pockmark features, which could be gas release or hydrate collapse features, are evident ("A1", "A2"). A possible hydrate mound can be seen within location "C" (Figures B.5, B.6). The gas hydrate stability zone of 90-96% methane is estimated to extend below the mudline approximately 800-1000 m (~1.0 sec TWT).

Possible hydrate locations (centered at):
Line 5383 Crossline 40212 26° 45' 56.8"N   92° 59' 41.9"W (location A1)
Line 5384 Crossline 40269 26° 45' 57.2"N   92° 59' 16.2"W (location A2)
Line 5489 Crossline 40283 26° 47' 05.6"N   92° 59' 10.1"W (location B)
Line 5593 Crossline 40470 26° 48' 12.8"N   92° 57' 45.2"W (location C in Block 152)
Line 5457 Crossline 40212 26° 46' 44.9"N   92° 59' 42.3"W (location D)

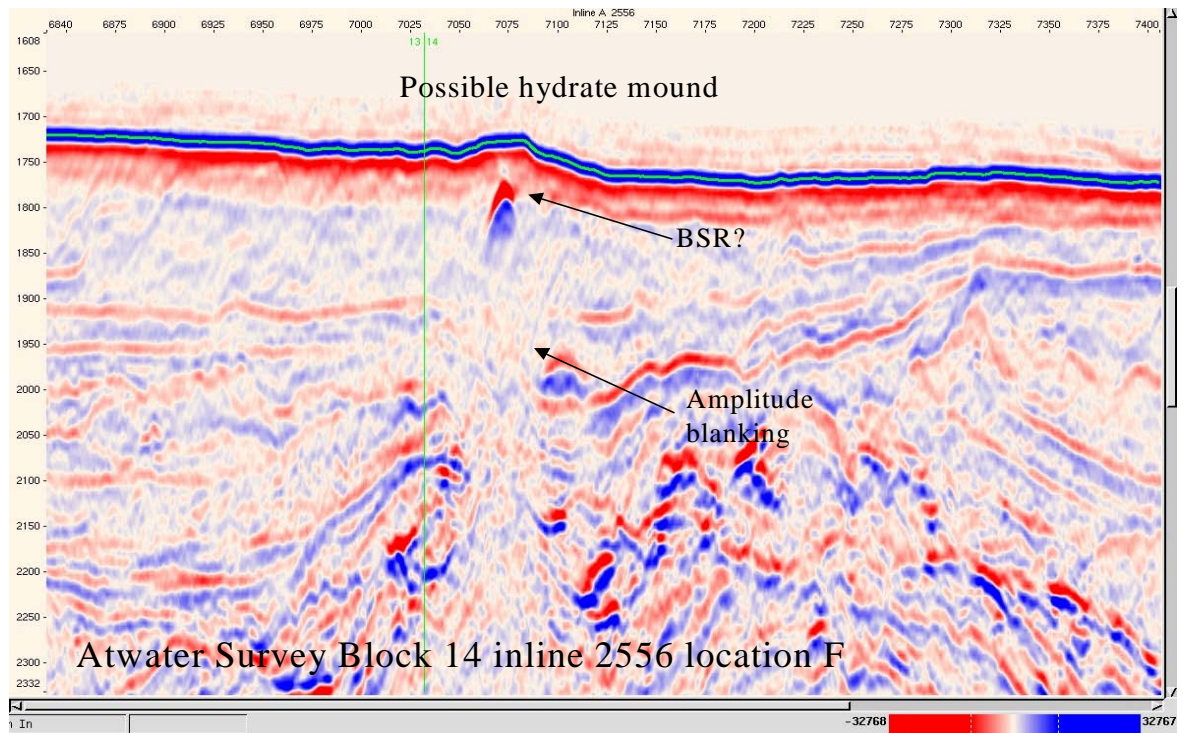**Figure B.5. Keathley Canyon 195 waterbottom map with possible BSR and gas hydrate related structures.**

Interpretation:
Water bottom
Base slope fan
BSR

Possible area for investigation:
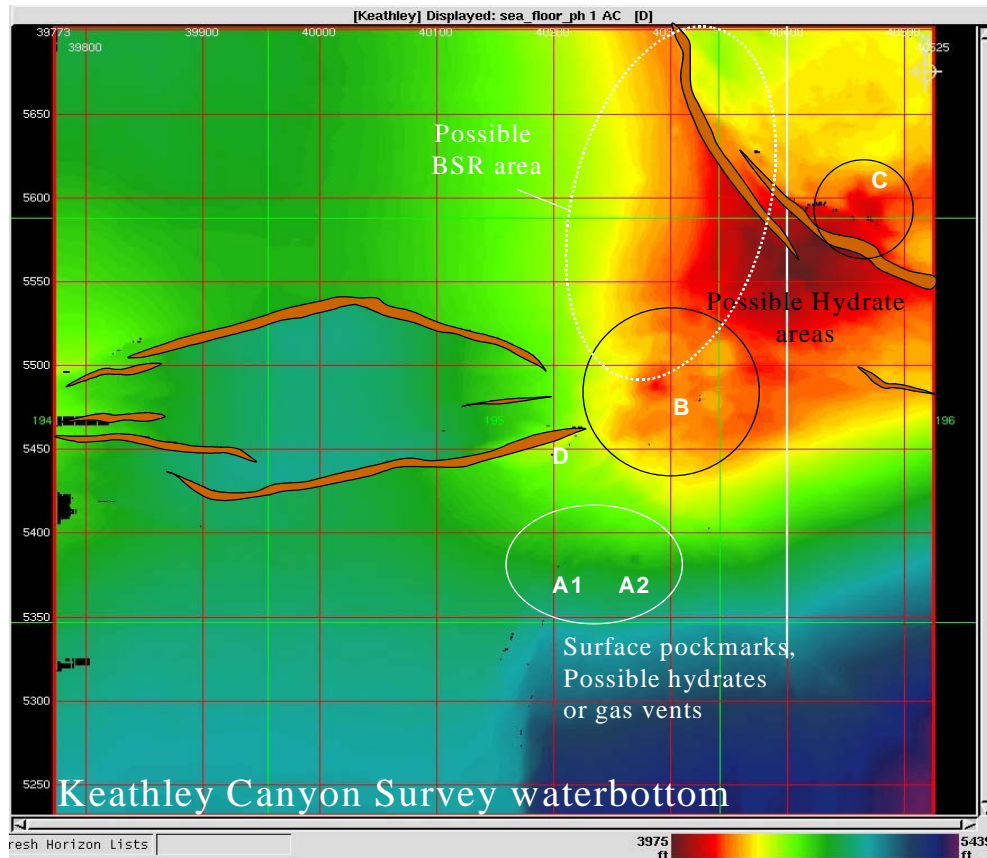Location C (inline 5593/xline 40470 Block 152) mound with some amplitude shingling, lateral variation and adjacent to apparent BSR.
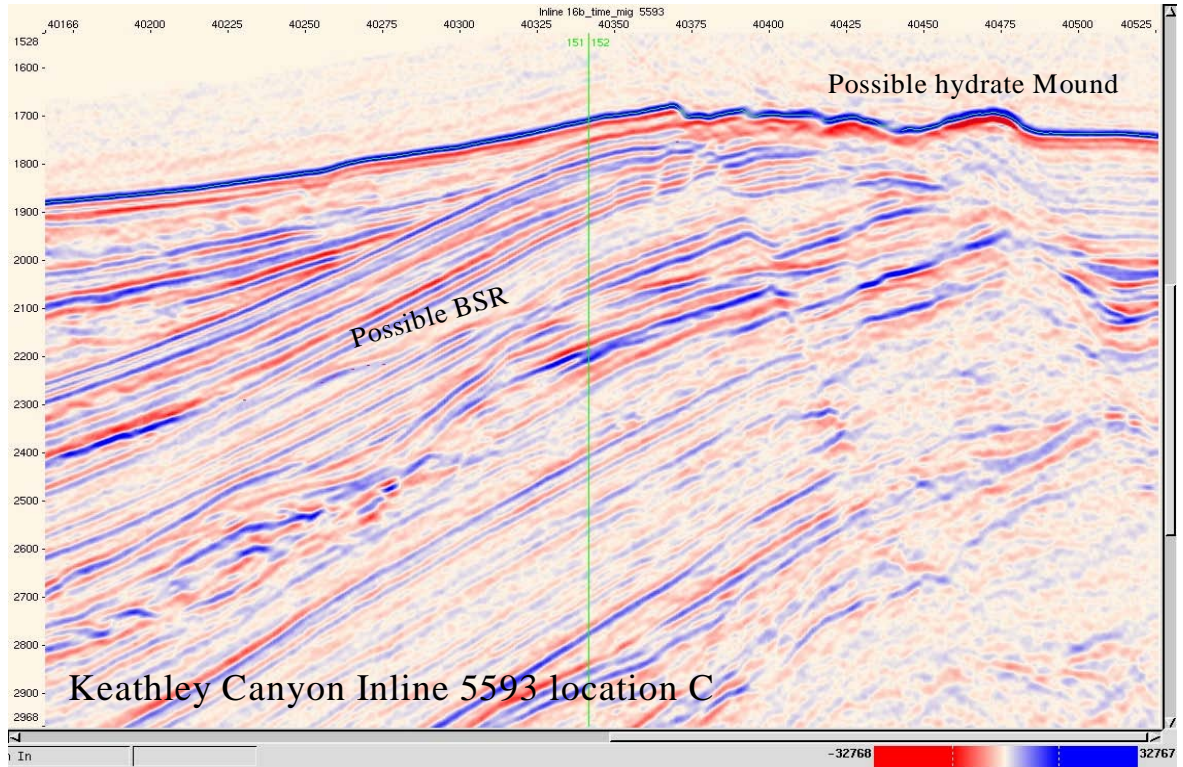
Figure B.6. Keathley Canyon 195 with possible BSR and hydrate mound.

B.1.3 Mississippi Canyon 802

The Mississippi Canyon 802 Block is ranked #3 as to the quality of the hydrate characteristics.

The data appear to be zero-phase as evidenced by the water bottom reflector in which the increase in acoustic impedance shows as a peak or positive excursion without leading side lobe.

An area of possible gas hydrate mounds was identified in the eastern part of Block 801 and western part of Block 802 (Figure B.7). No amplitude polarity reversal is evident at the water-mound interface. However, a possible gas chimney is evident below mound "A" (Figure B.8). Also, some weak amplitude blanking below the mound extends about 0.2 seconds BML. It is likely that some mounds could be mud volcanoes and not hydrates if the gas-fluid flux is too high. Mound "A" appears about 250 m (820 ft) wide, although most are smaller. No BSR is evident or associated with any of the mounds or other areas. The hydrate stability zone of 90-96% methane is estimated to extend below the mudline approximately 600-800 m (~800 ms TWT).

Possible hydrate locations (centered at):
Line 6049 Crossline 946 28° 09' 36.6"N   89° 30' 03.7"W (location B)
Line 6034 Crossline 926 28° 09' 19.7"N   89° 29' 48.5"W (location A Block 801)
Line 5975 Crossline 911 28° 09' 07.6"N   89° 28' 50.6"W (location C)
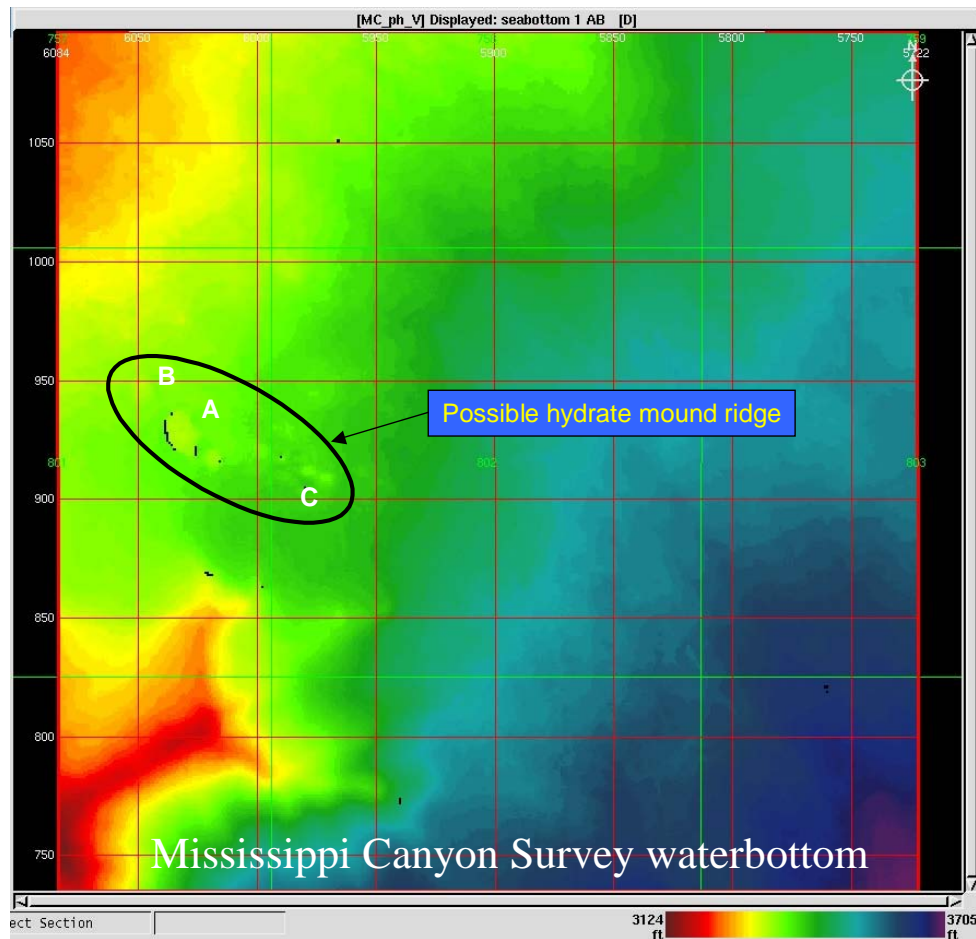
Figure B.7. Mississippi Canyon 802 water bottom map with possible hydrate mound ridge.

Interpretation:
Water bottom
Unconformity
Base slope fan
Top Luann salt

Possible area for investigation:
Location A (inline 6034/xline 926 Block 801) mound with apparent gas chimney and chaotic zone.

Crossline Migrated 926

Possible hydrate mound

Gas plume

Mississippi Canyon Survey Block 801 crossline 926
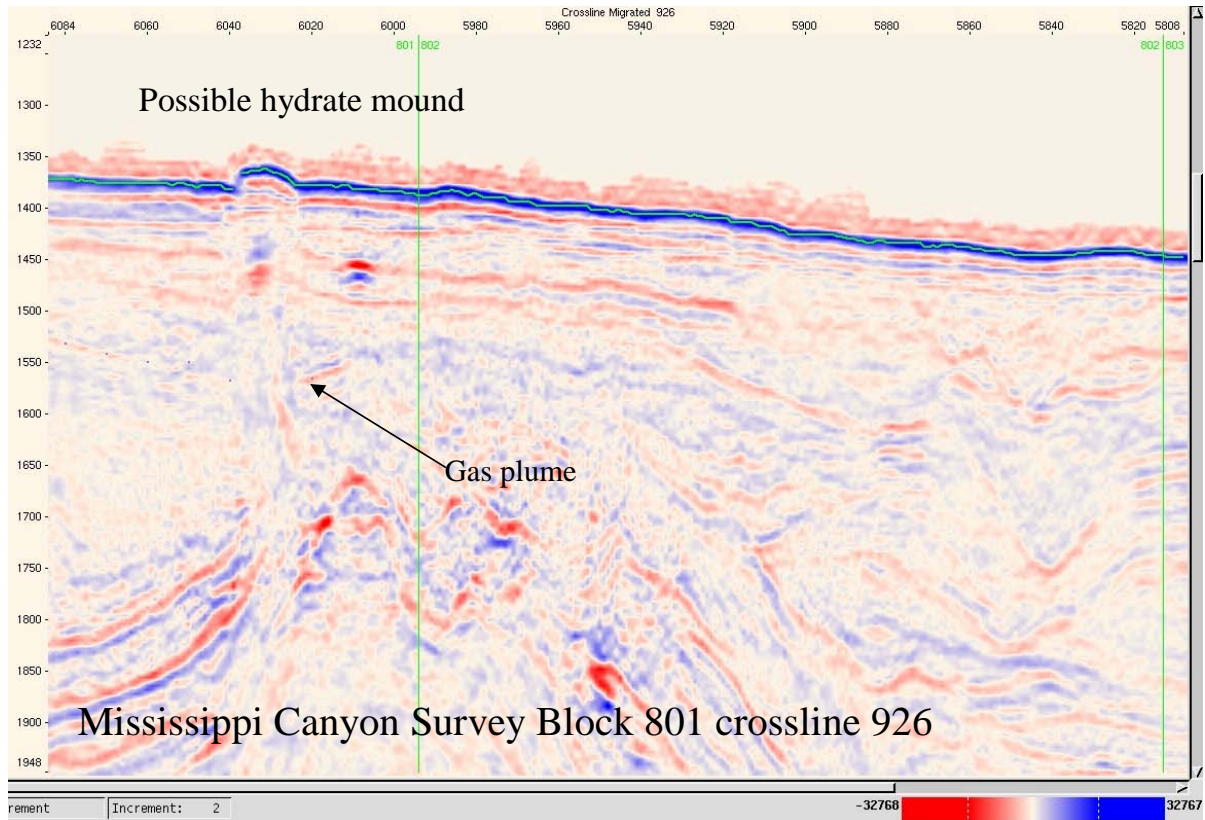
Figure B.8. Mississippi Canyon 802 seismic with possible hydrate mound and gas plume.

B.1.4 Alaminos Canyon 856

The Alaminos Canyon 856 block is ranked #4 as to the quality of the hydrate characteristics.

The data appear to be near zero-phase as evidenced by the water bottom reflector in which the increase in acoustic impedance shows as a peak or positive excursion without a strong leading side lobe. Counter regional water bottom dip is evidenced due to salt movement (Figure B.9). There is no strong evidence of hydrates in Block 856. The proposed BSR seen in Block 857 (Figure B.10) is highly suspect due to the offset by a regional fault (Figure B.11). This event is more likely a stratigraphic boundary parallel to the water bottom with a charge of gas, thereby giving it the bright anomaly. It is still very possible that hydrates exist above this reflector, but it is unlikely that this feature is a BSR. The hydrate stability zone of 90-96% methane is estimated to extend below the mudline approximately 1400-1700 m (~1.8 sec TWT).
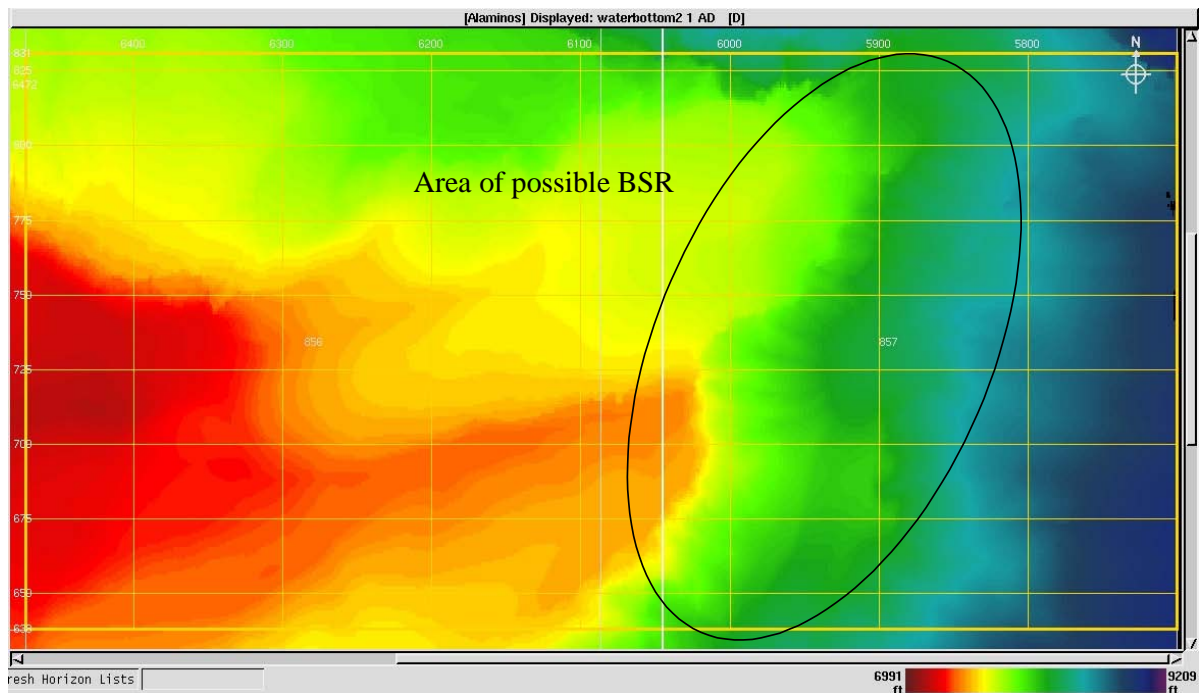
Alaminos Canyon Block 856 - 857

Figure B.9. Alaminos Canyon 856/857 with areal extent of possible BSR.

Interpretation:
Water bottom
Slope fan

Possible area for investigation:
Area of interest centered at inline 679/xline 6000 Block 857. No distinguishable hydrate mounds. No amplitude blanking zones or gas chimneys. BSR may not be valid due to fault offset seen on some lines (inline 649 Figure B11).

Figure B.10. Alaminos Canyon 856/857 Inline 679 with possible BSR.

Figure B.11. Alaminos Canyon 856/857 Inline 649. Possible BSR unlikely due to offset by faulting.

25

B.1.5 Green Canyon 184 & 185

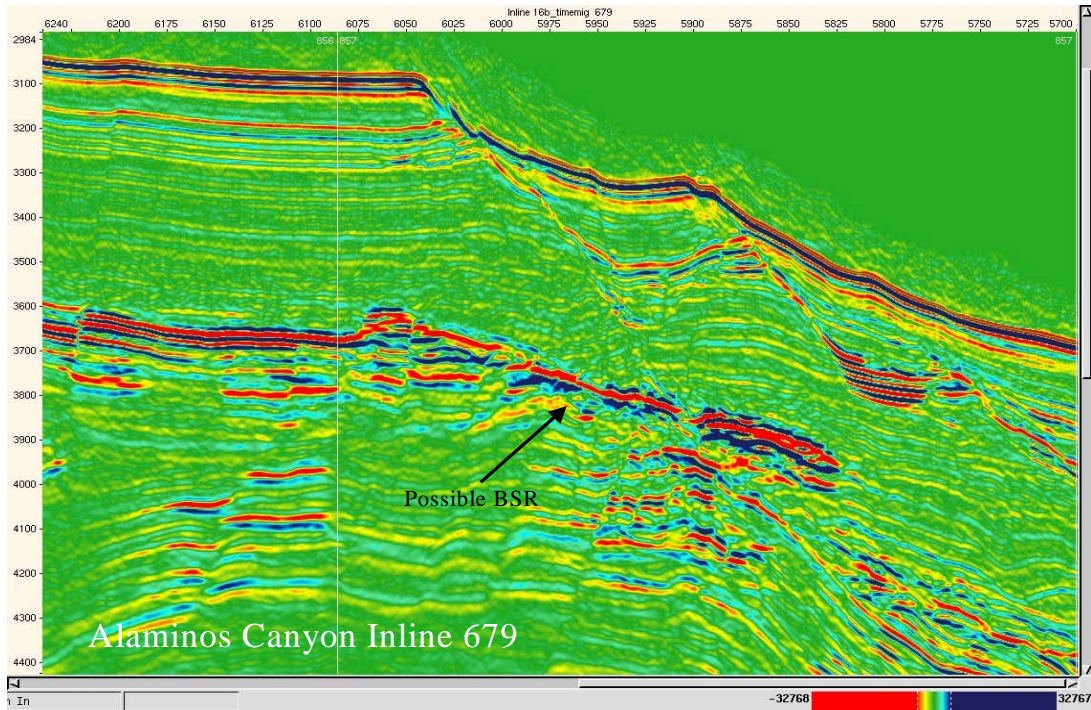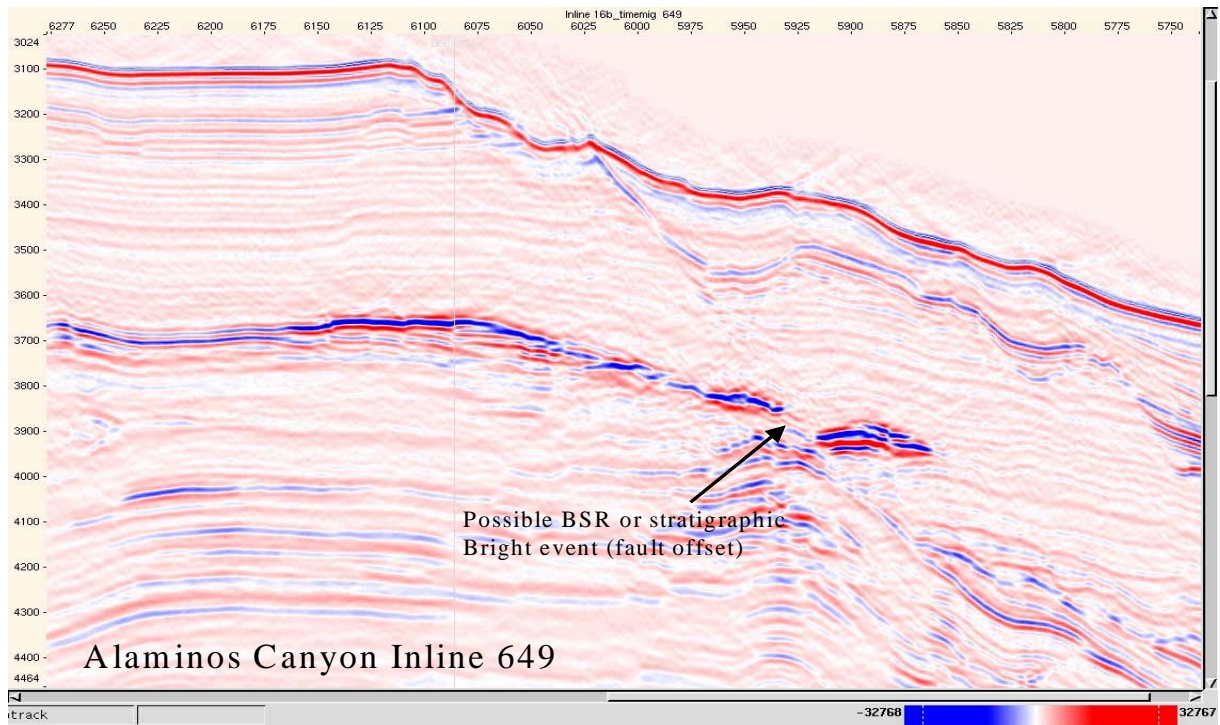**The Green Canyon 184 & 185 blocks are ranked #5, not due to the quality of the hydrate characteristics, but rather to the lease restrictions (which were later rescinded).**

The data are WesternGeco 2000 vintage and appear to be near zero-phase as evidenced by the water bottom reflector in which the increase in acoustic impedance shows as a peak or positive excursion. However, a slight leading negative side lobe is evident and probably indicates mixed phase.

We identified two areas of probable gas hydrate mounds (Figures B.12 – B.16). The presence of the main mound is validated from previous work (Bush Hill). Numerous other mounds coalesce into an elongated N-S ridge and exhibit strong amplitude polarity reversal at the water-mound interface compared to normal water bottom seismic expression. This is likely due to the shallow free gas / hydrate boundary (BSR). Hydrate extension is likely 1.8 km north of the mound ridge based upon attribute analysis. No regional BSR is evident in any of the areas, although Bush Hill exhibits polarity reversal near the seafloor, which may be a shallow BSR. The main mound ridge is approximately 2 km long by 0.7 km wide and is underlain by an area of amplitude blanking which extends more than 1.5 seconds BML. This is likely caused by the presence of a large amount of free gas below the mound. The hydrate stability zone of 90-96% methane is estimated to extend to 200-500 m BML (~300-500 ms TWT).

A swath of eight lines (lines 4041-4048) over Bush Hill were initially selected as a calibration test for prestack time migration reprocessing at 2 ms sampling. Additional work was done in this area and several initial inversion and modeling locations were selected on these lines.

Possible hydrate locations (centered at):
Line 4044 Crosslines 2850-3000 - Bush Hill
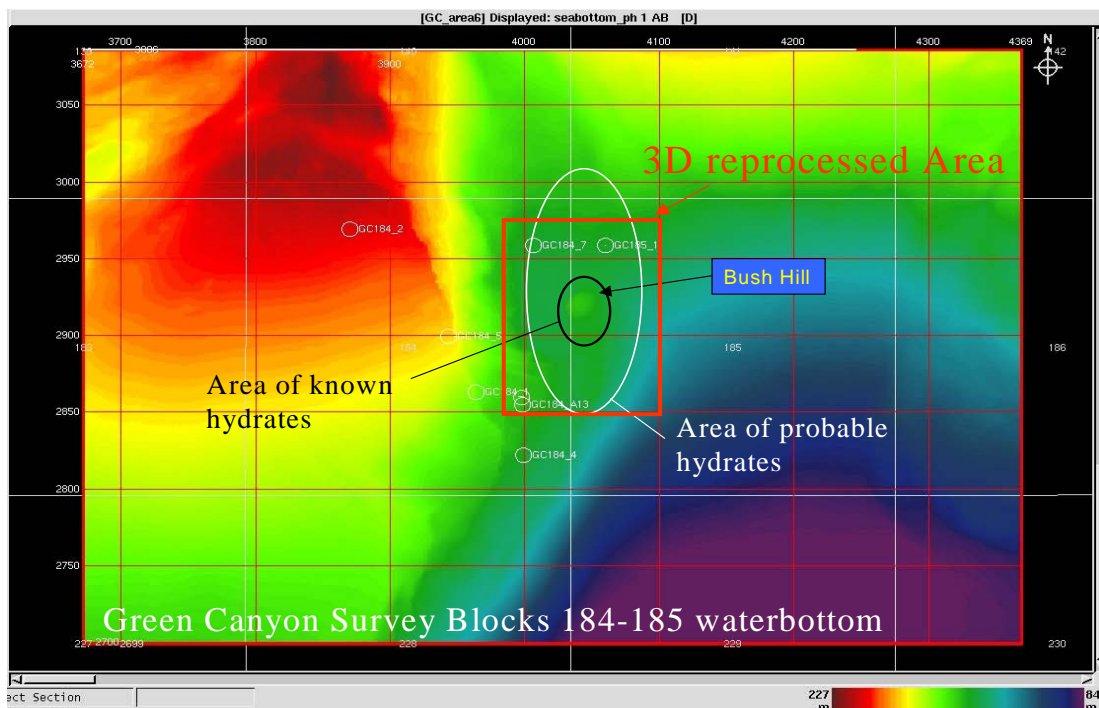
Figure B.12. Green Canyon 184-185 water bottom map with area of known hydrates and aerial extent of the 3-D seismic data reprocessing.

26

Interpretation:
Water bottom
Hydrate ridge area
High stand
Unconformity

Well markers:
Trim. A
Trim. B

Possible areas for investigation:
None - Presence of known hydrates but excluded due to existing concessions
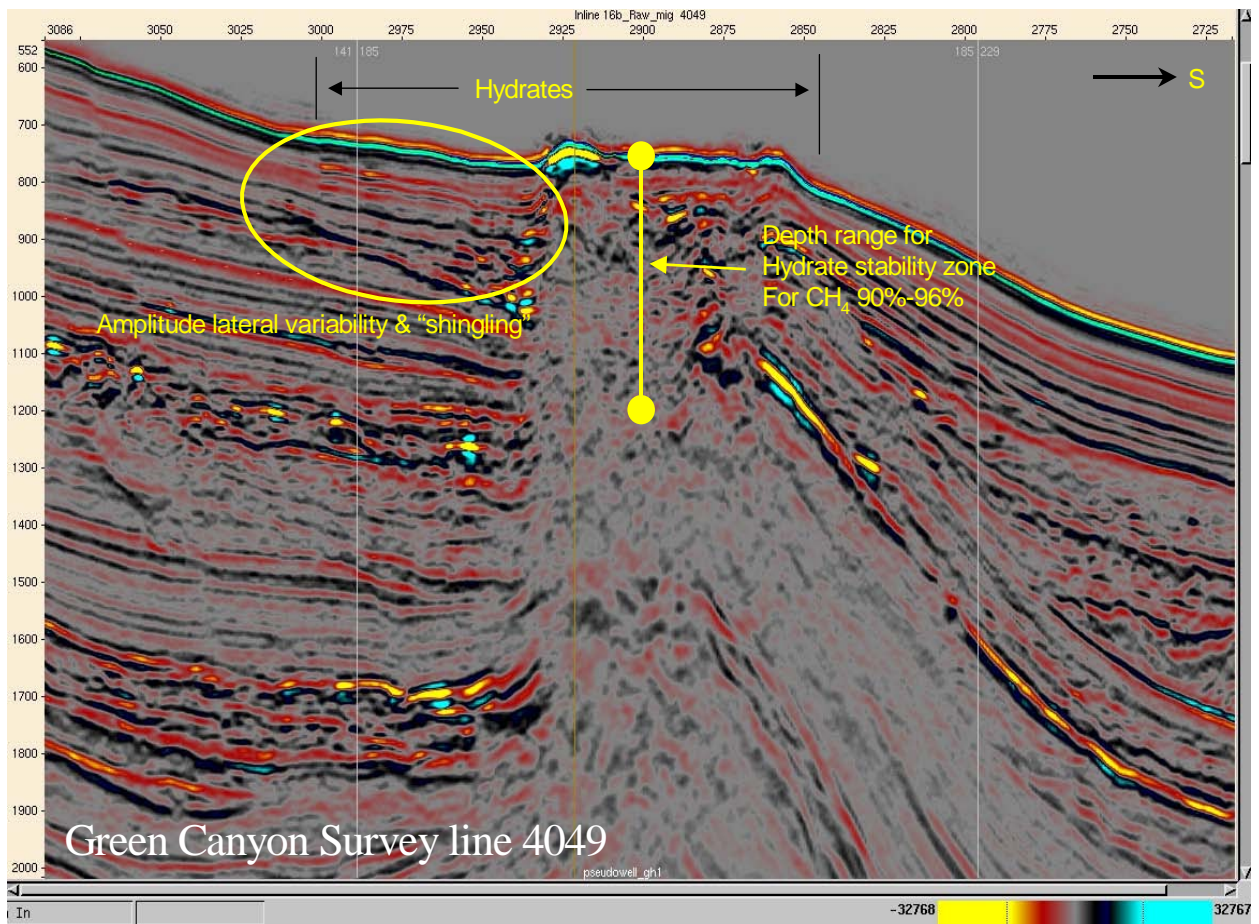
Figure B.13. Green Canyon 184/185 Inline 4049 showing Bush Hill hydrate mound with associated gas flux, depth of hydrate stability zone and hydrate seismic characteristics.
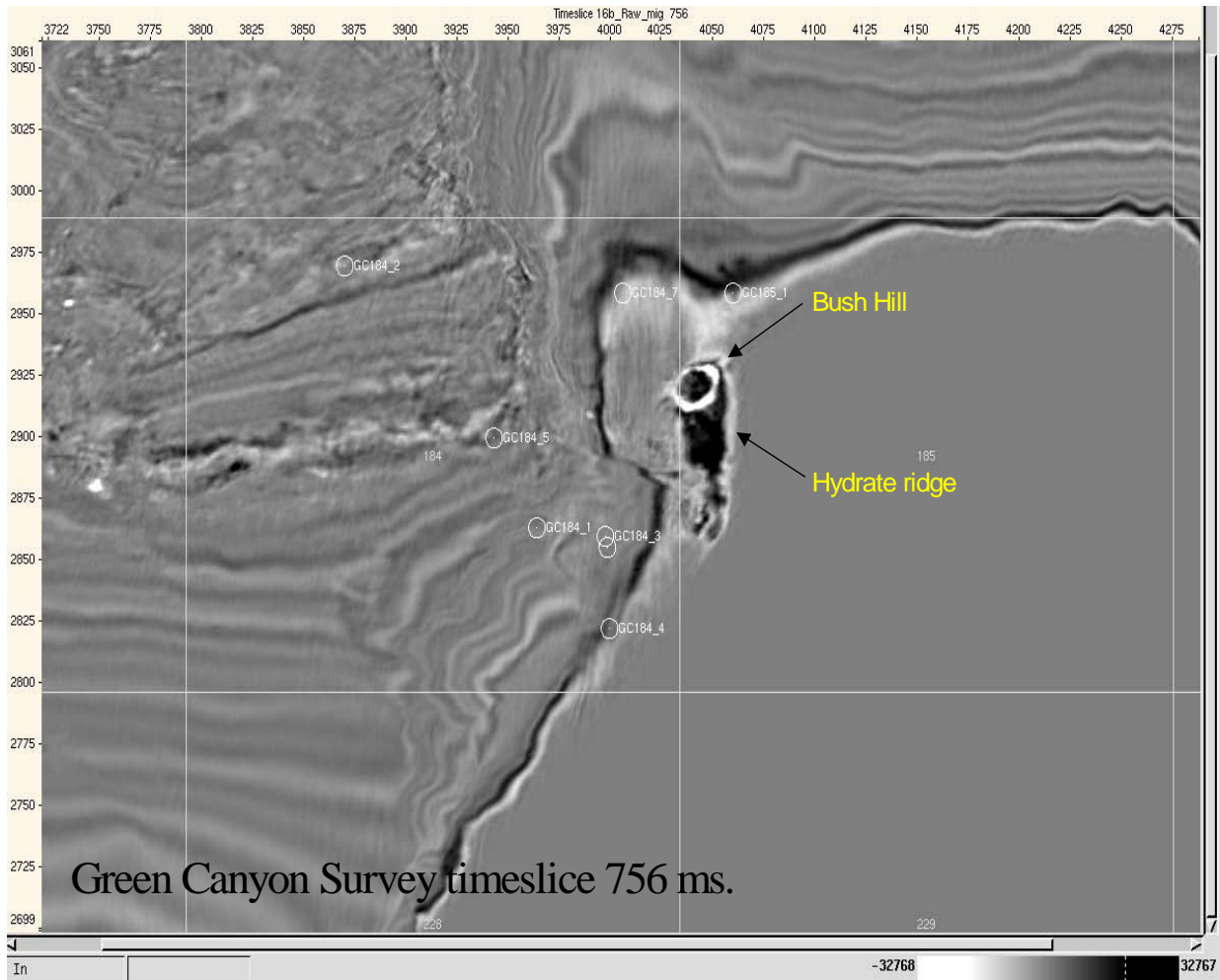
Figure B.14. **Green Canyon 184/185 time slice at 756 ms showing Bush Hill Mound and associated hydrate ridge.**

B.2 Detailed Seismic Interpretation of Green Canyon 184 & 185

From the five areas originally screened, the Atwater Valley and Keathley Canyon candidates were selected for reprocessing that involved prestack time migration (PSTM), inversion and modeling work. Drilling and coring sites will also be chosen from these two areas for JIP Phase 2 work. Green Canyon was also chosen for the initial detailed seismic interpretation, modeling and analysis work, using re-processed PSTM data, due to the existence of known hydrates. Results were also used to test and calibrate rock modeling and seismic hydrate detection methods.

The Green Canyon data were limited to an area surrounding Bush Hill in OCS Blocks 184 and 185. This area included several deep well bores, as well as known and sampled hydrate

mounds. As part of understanding where hydrates could be located outside of the mound area itself, it was necessary to describe in detail, from the seismic data, the near-surface lithology and depositional history adjacent to Bush Hill. Below (Figure B.15) is shown part of a N-S line over Bush Hill where several inversion locations were placed. The high amplitude polarity reversal near the seafloor is indicative of the vertical limit of free gas (BSR), above which hydrate is likely to be present. The high amplitude "flat spots" on the left side suggest free gas accumulation, or the base for the hydrate stability zone adjacent to the mound. An E-W crossline 29585 through the section also describes near-surface lithology (Figure B.16).

An amplitude map of the flat-spot features was also made (inset, Figure B.17). This active hydrate area is bounded by faults and fractures, which are the mechanisms for upward migration of gas. Note the polarity reversals periodically visible below the ridge. These spots are also likely zones of hydrate concentration. The vertical resolution is approximately 6-7 m.
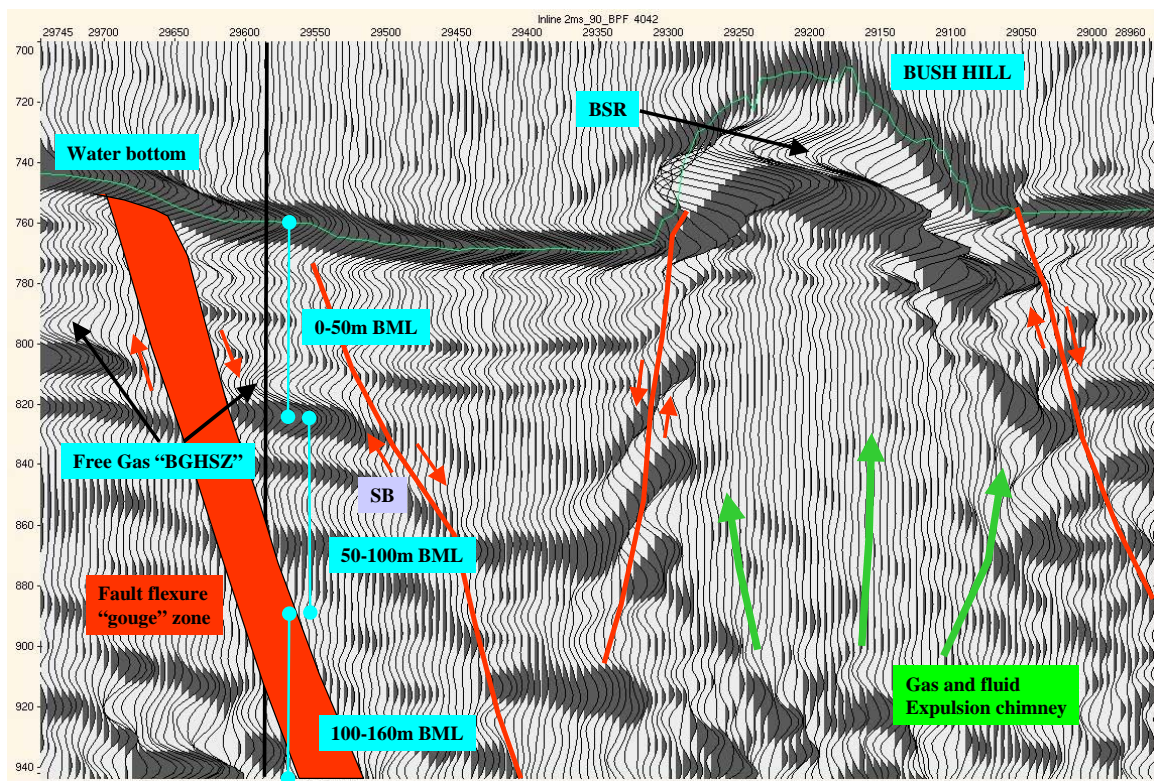

Figure B.15. Green Canyon 184/185 Bush Hill N-S line 4042 showing detailed depth packages, flat spots and gas chimney.
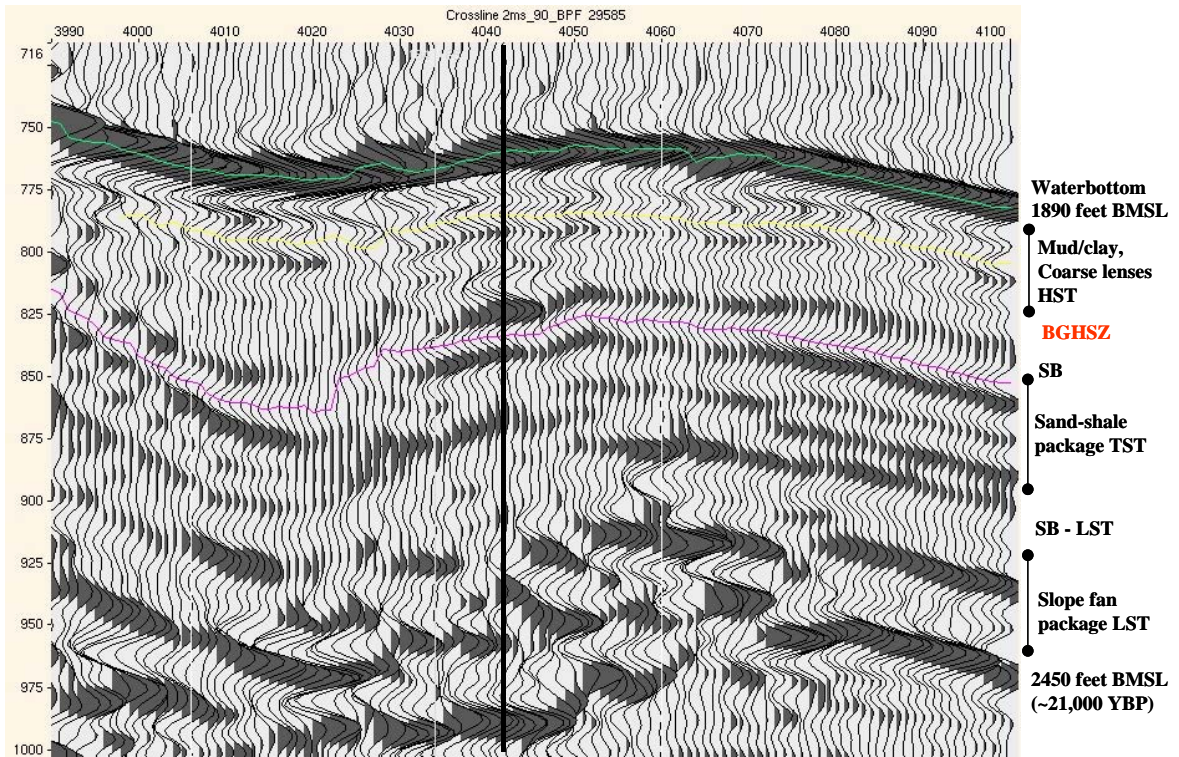
Figure B.16. Green Canyon 184/185 Bush Hill N-S line 4042 showing detailed depth packages, flat spots and gas chimney.
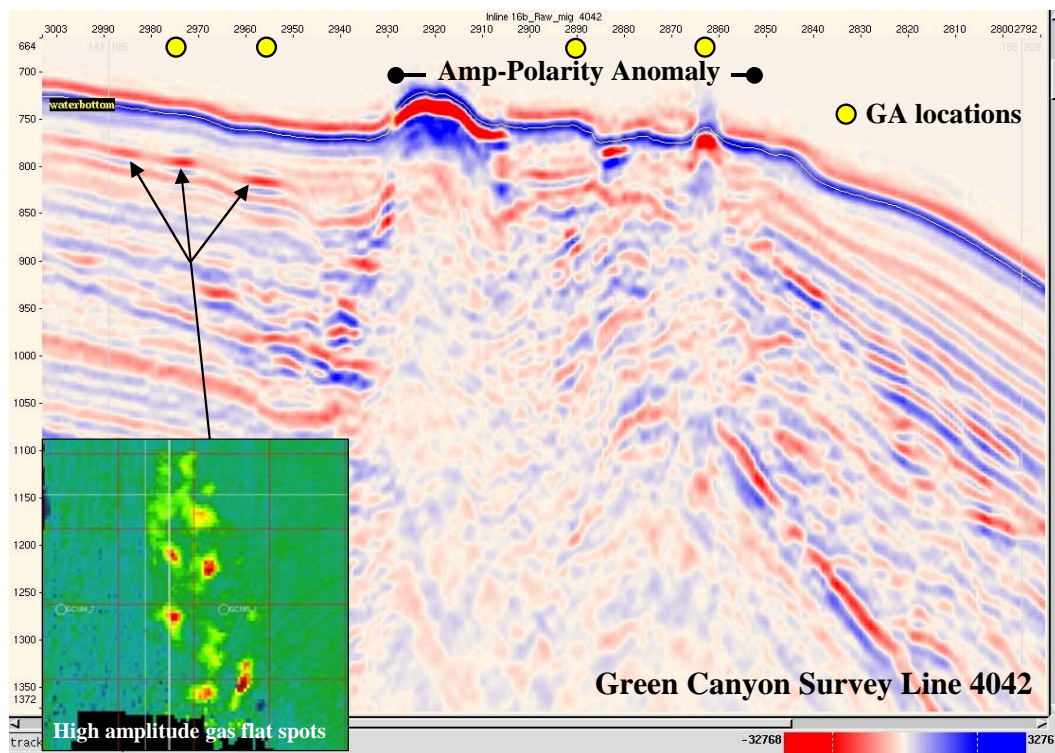

Figure B.17. Green Canyon 184/185 Bush Hill N-S line 4042 showing inversion locations and amplitude map of the free gas occurrences.

30

Several horizons were mapped to decide on proper locations for full-waveform inversion. For initial work in the Green Canyon area, these included the water bottom, a shallow high-stand boundary and a low-stand sequence boundary, which just followed the end of the last Pleistocene glaciation (Figure B.17b). However, the presence of the gas cloud around and below Bush Hill made interpretation difficult.

Also of interest was an amplitude and frequency anomaly seen down-slope from Bush Hill (Figures B.18, B19). Because of the polarity reversal relative to the water bottom, this shallow anomaly was mapped as possibly a gas-charged sand channel feature with hydrate accumulation above. An east-west crossline is shown below in Figure B.18 followed by a map view of an instantaneous frequency extraction with a 4 ms window around the anomaly.

In order to match seismic to anticipated lithology and potential hydrate occurrences, seismic inversion was generated. The inversion locations were chosen with two objectives in mind; Obtain characteristics of zones with no gas hydrates evident, and then compare with results from zones that contained gas hydrates. However, the amplitude wipeout zone under Bush Hill excluded placement directly at the mound (Figures B.15, B17). From the seismic signature, Bush Hill appears to have hydrates limited entirely to the very near surface, and these sediments have already been cored. In all, there were 12 inversion locations chosen of which six were thought to be hydrate bearing and six thought to be non-hydrate bearing. Inversion is discussed in more detail later in this report. Results can be found in the appendices.
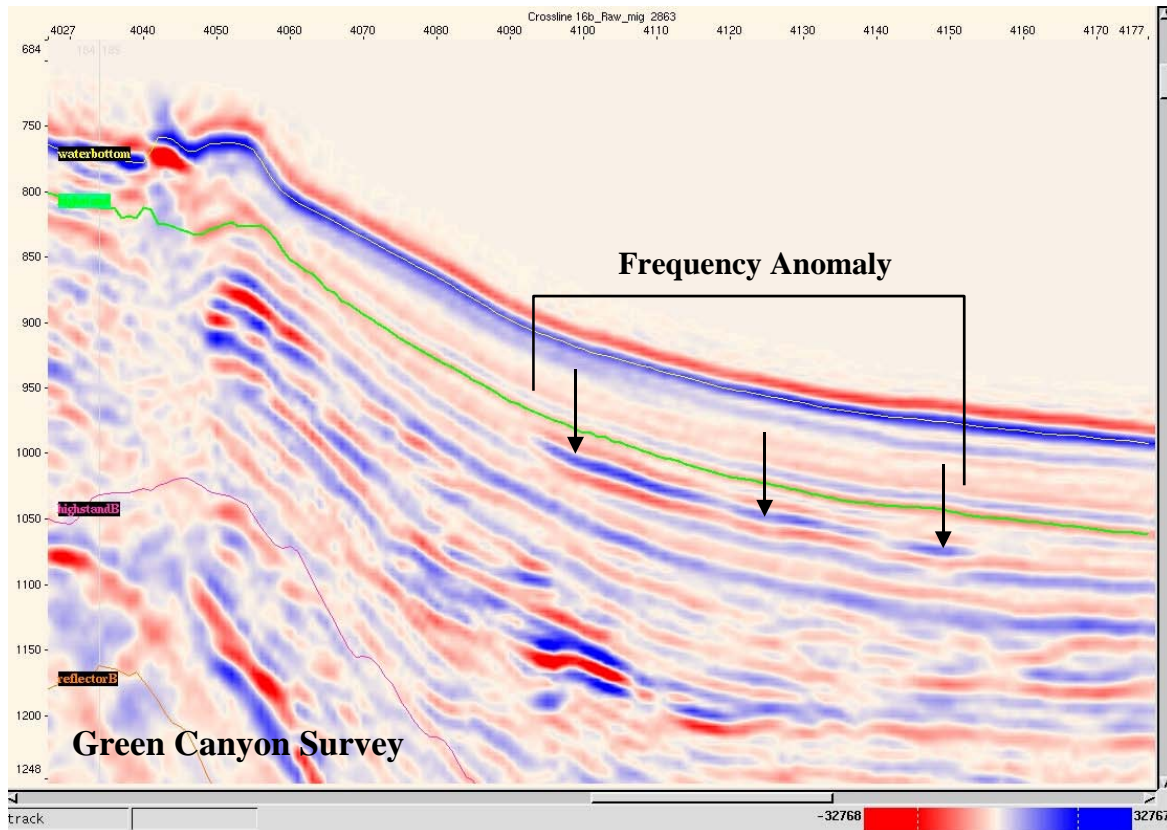
Figure B.18. Green Canyon 184/185 Crossline downslope from Bush Hill showing anomaly location.
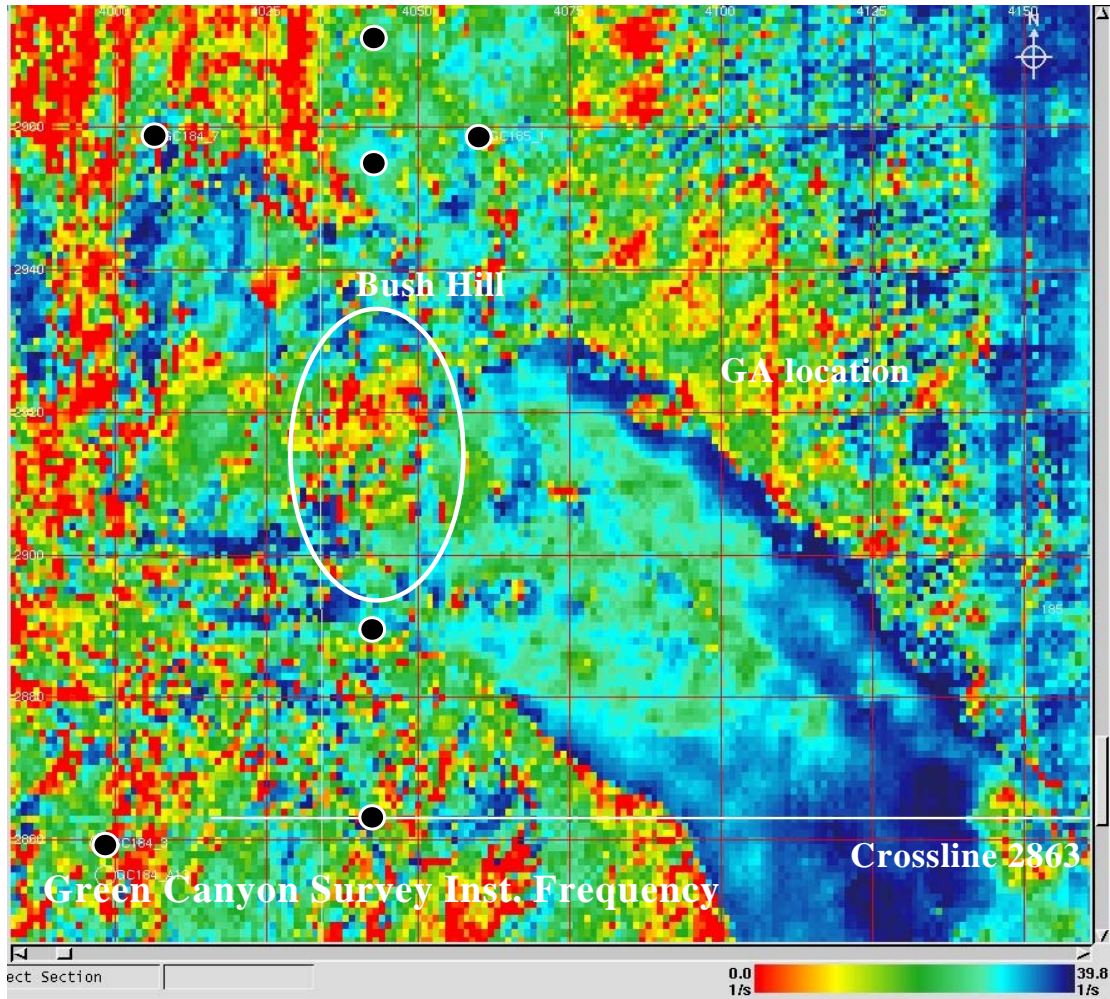
Figure B.19. Green Canyon 184/185 instantaneous frequency extraction over a 4 ms window at the horizon shown in Figure B.18.

B.3 Detailed Stratigraphic Evaluation – Part 2

The objectives of Part 2 were to apply the process as developed at Green Canyon in Part 1, where a small subset of selected locations were analyzed, to the full 3-D prestack time migrated re-processed volumes. For this phase, Atwater Valley 14 and Keathley Canyon 195 datasets were chosen as agreed upon by the JIP members.

B.3.1 Atwater Valley 14

The Atwater Valley project included a one-block area centered about the intersection of Atwater Valley Blocks 13 and 14 (Figure B.20). All data were re-processed through PSTM following which a detailed interpretation was performed. The area of interest included at least five possible gas hydrate mounds of which three (designated for this study as mounds "B", "D", and "F") are extremely likely possibilities for gas hydrates. Mound "F" in particular was studied in detail using an inline along which inversion locations were placed (Figures B.28, B29). Inversion at the other

mound locations was not possible due to the amplitude blanking zones beneath them (Figure B.23).

<u>Geologic Setting</u>

The Atwater project area is centrally located within the Mississippi Valley channel complex and therefore has a thick clastic blanket responsible for salt movement (Figures B.20, B.21). Sediments deposited during this active Pleistocene period are complex and chaotic with evidence of many channel levee and slope fan systems. Mobilization of the salt is responsible for creating the NW-SE trending fault pattern, which also allowed the migration of gas and the formation of the hydrate deposits. Water depth ranges from approximately 4100 ft in the western part of the survey to 4350 ft in the eastern part (1250-1325 m).
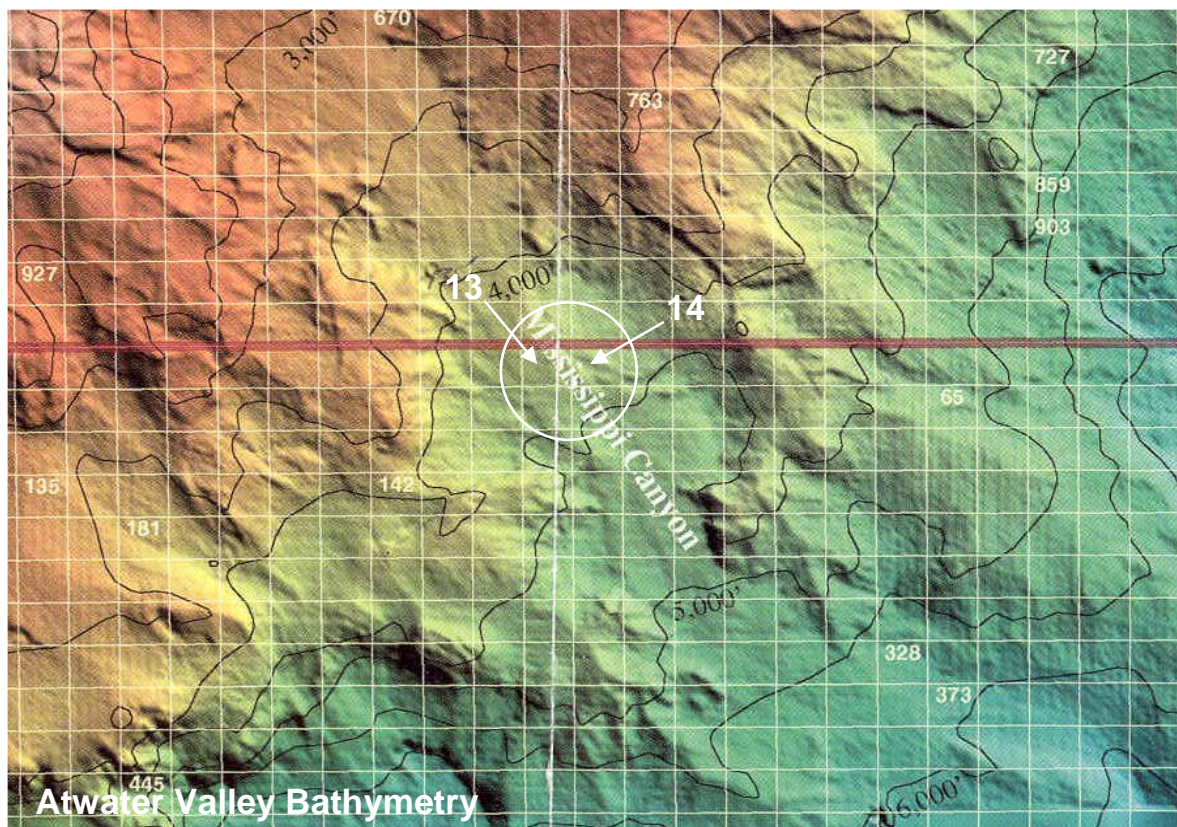
Figure B.20. Atwater Valley 14 location map showing project centrally located in the Mississippi Canyon channel.
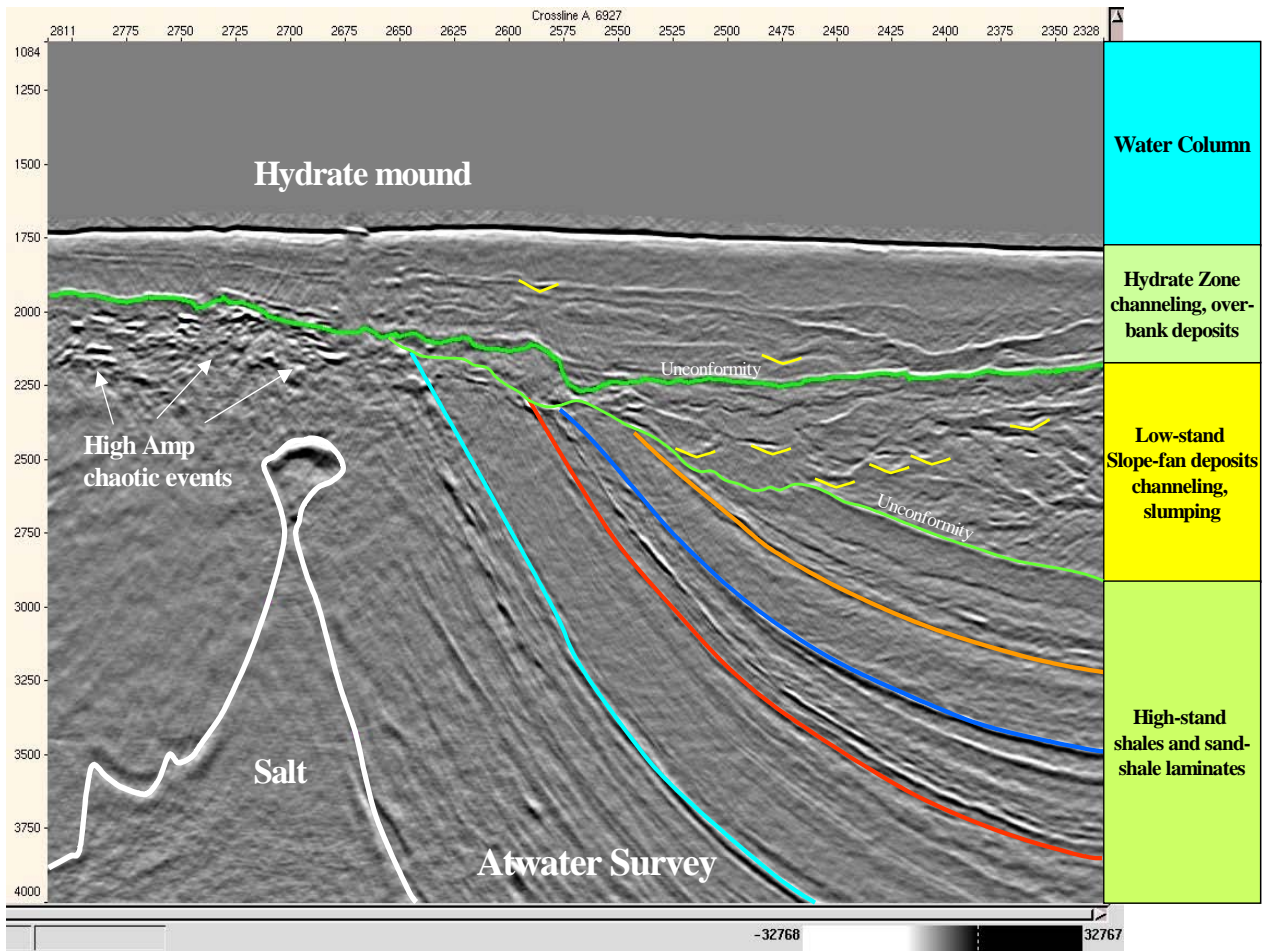
Figure B.21. Atwater Valley 14 Crossline showing hydrate mound, lithology and thick clastic wedge below the unconformity.

Gas Hydrates

Of particular interest are two mounds; mound "D" in Block 13 and mound "F" in Block 14 (Figures B.22, B.23). These mounds offer two different possible hydrate scenarios. From seismic interpretation and seismic analysis, mound "D" appears to have hydrates confined to the very near surface, possibly within a few meters below the mudline. This can be seen by the close proximity to the seafloor of the reversed polarity seismic reflector, which defines the upper limit of free gas. Mound "F" is associated with a deeper reversed polarity event, and therefore deeper GHSZ. The depth at which hydrates are likely to extend at this location is approximately 50 m BML. Mound "F" also exhibits a "draped" BSR, which appears to extend downward and terminate in the deeper lithology (Figure B.23). This is likely the result of a high gas-fluid flux destabilizing the near surface thermobaric zone. On the same figure, a velocity "pull-down" can be seen in the reflectors below the mounds. This results from the slow velocity gas cloud below the mound affecting the two-way travel time.
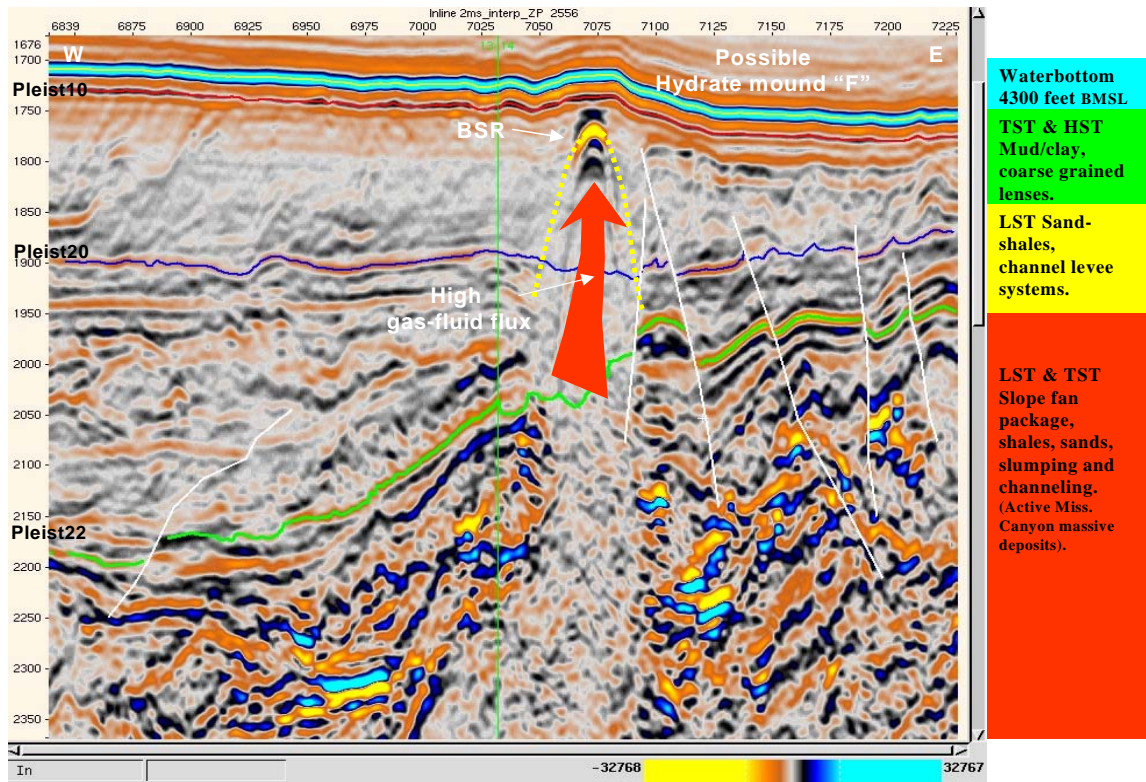
Figure B.22. Atwater Valley 14 Line 2556 across mound "F". Typical lithology of the area and potential as a hazard appears as color-coded annotation on the right. The high-amplitude chaotic zone below the Pleist22 horizon is a possible hazardous drilling region.
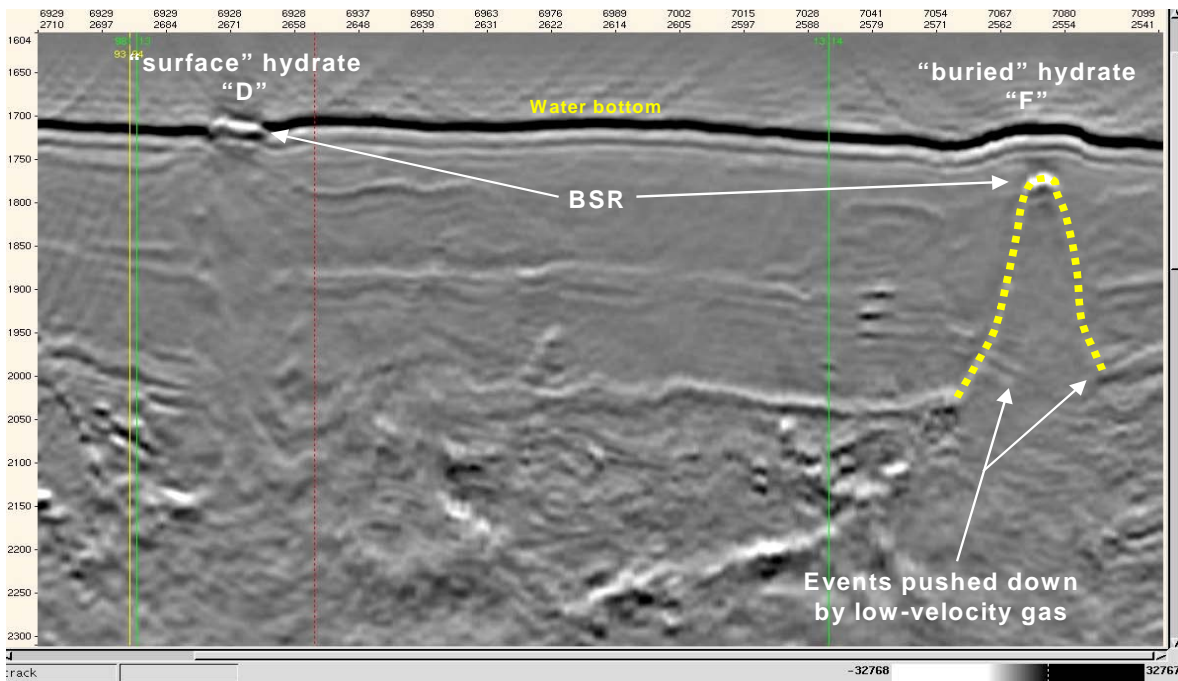
Figure B.23. Atwater Valley NW-SE traverse through mounds showing "perturbed" or de-stabilized BSR below mound "F".

<u>Maps</u>

To define the framework of the area, several subsurface structural and stratigraphic maps were made from interpretation of the two-way time seismic data. All horizons except the Top of salt are shown in Figure B.22. These surfaces included:

 a) Water bottom (Figure B.22 – yellow, Figure 24).

 b) A shallow high-stand sequence boundary of approximately 1000 years before present (Figure B.22 – Pleist10 red, Figure 25).

 c) An intermediate Low-stand / Transgressive system track Pleistocene surface approximately 40,000 years before present (Figure B.22 – Pleist22 green, Figure 26).

 d) Top of salt (Figure B.27).

All maps (Figures B.24 – B.27) have been converted to depth using seismic-derived velocity information. Age estimates were made from available published sedimentation rates.
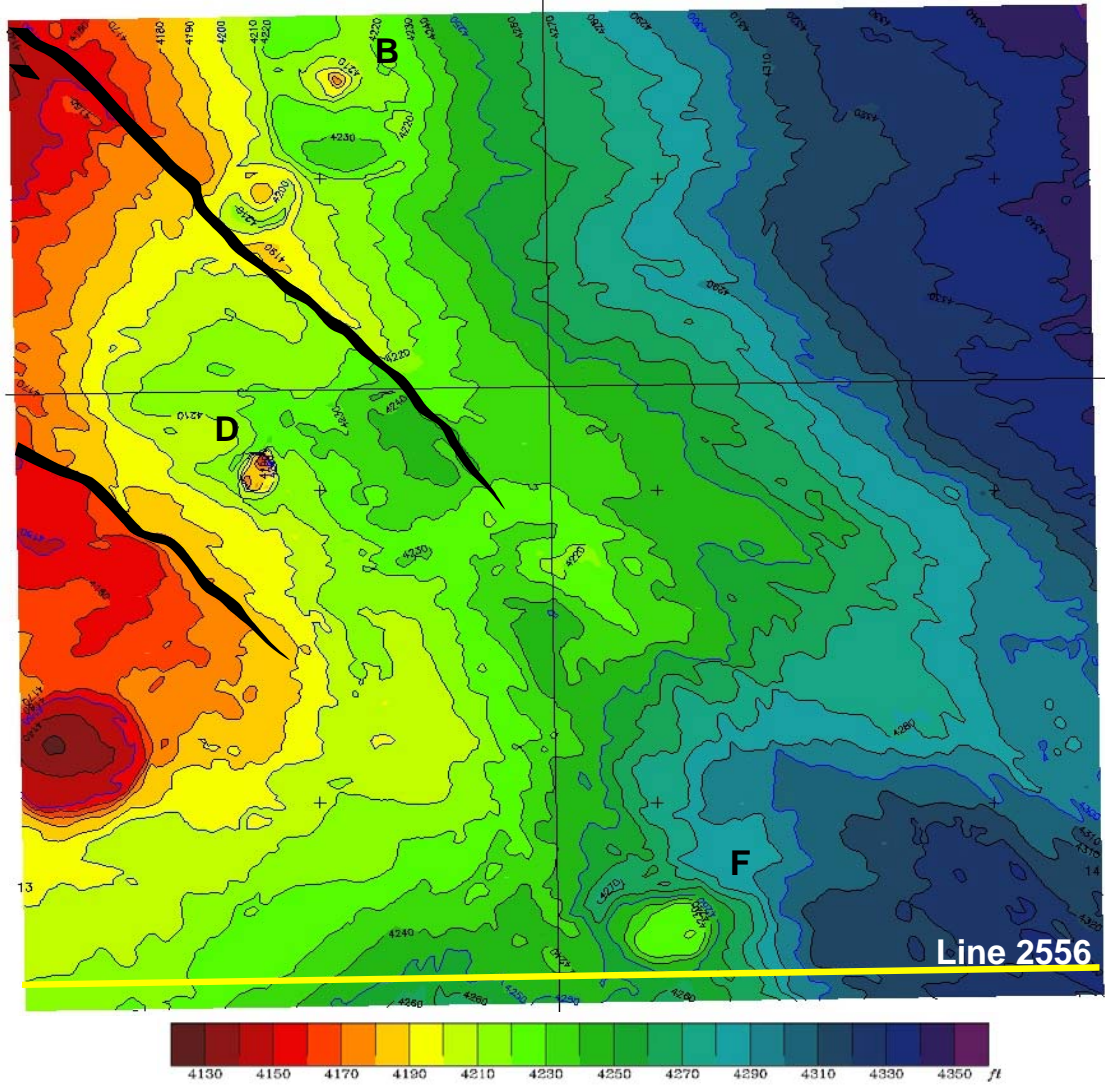
Figure B.24. Atwater Valley Water bottom horizon depth structure map. CI = 10 ft.

Figure B.25. Atwater Valley Pleist10 horizon depth structure map. CI = 10 ft.

4575 4625 4675 4725 4775 4825 4875 4925 4975 5025 5075 5125 5175 5225 5275 5325 5375 5425 5475 5525 5575 *ft*
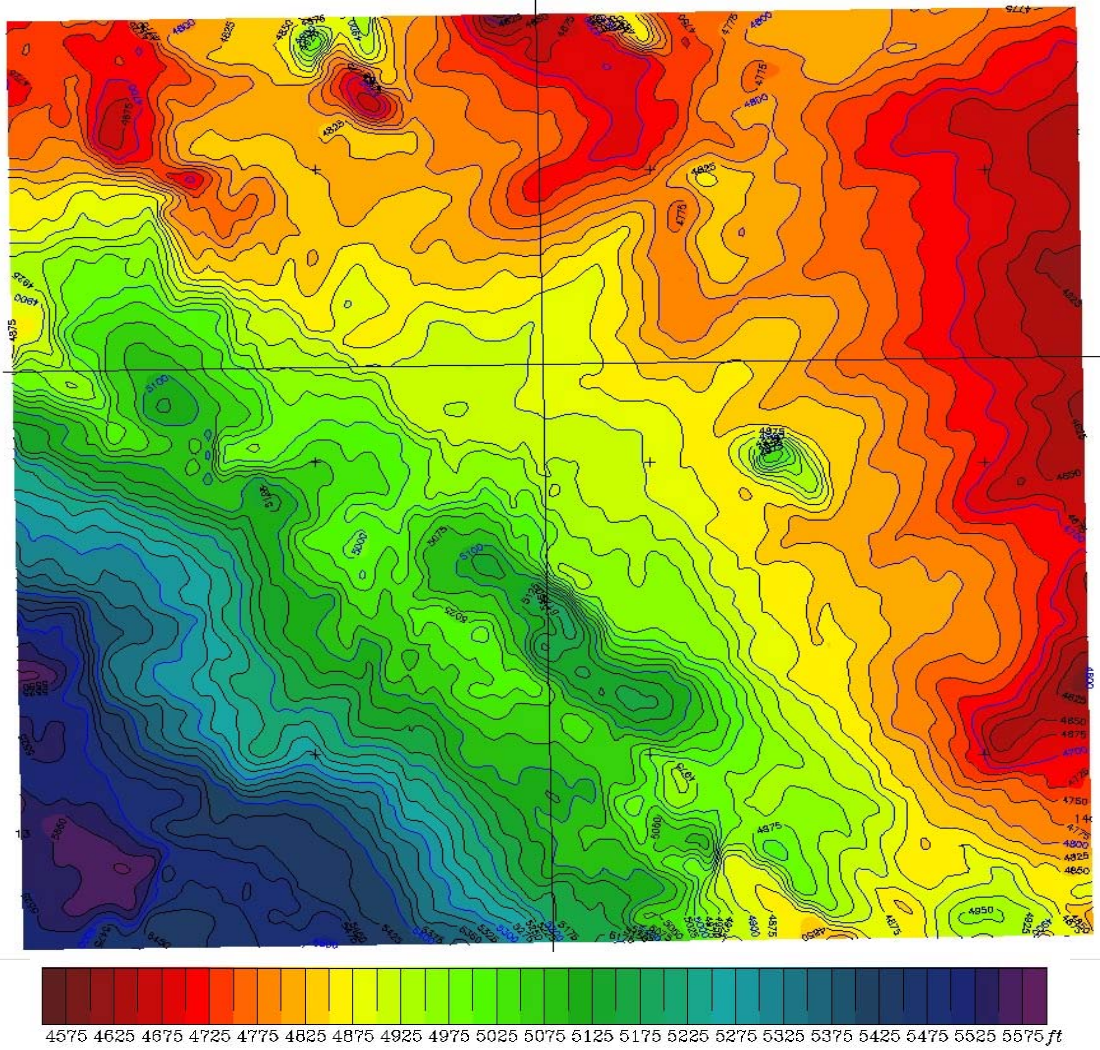
Figure B.26. Atwater Valley Pleist22 horizon depth structure map. CI = 25 ft.
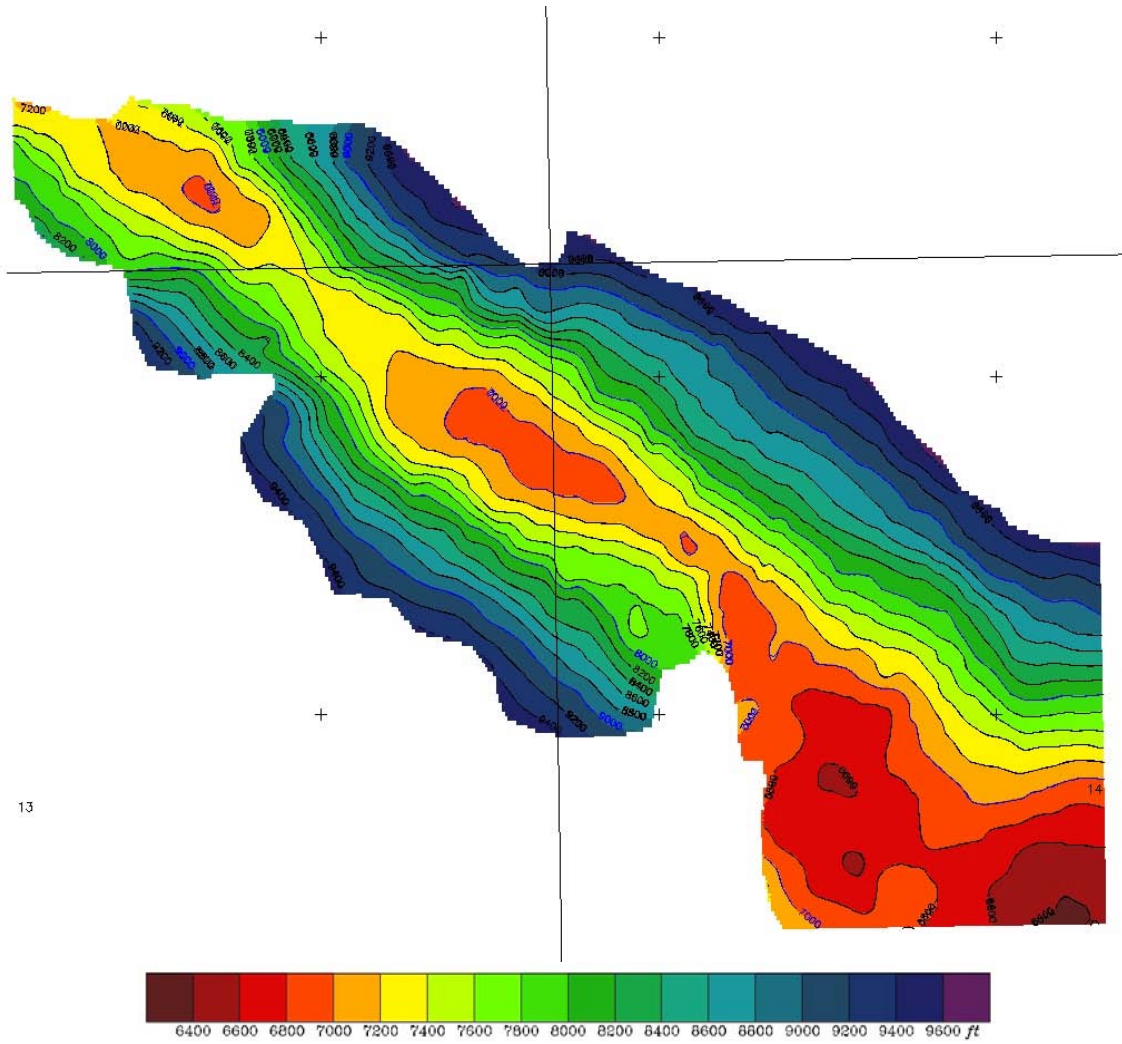
Figure B.27. Atwater Valley Top of Salt depth structure map. CI = 200 ft.
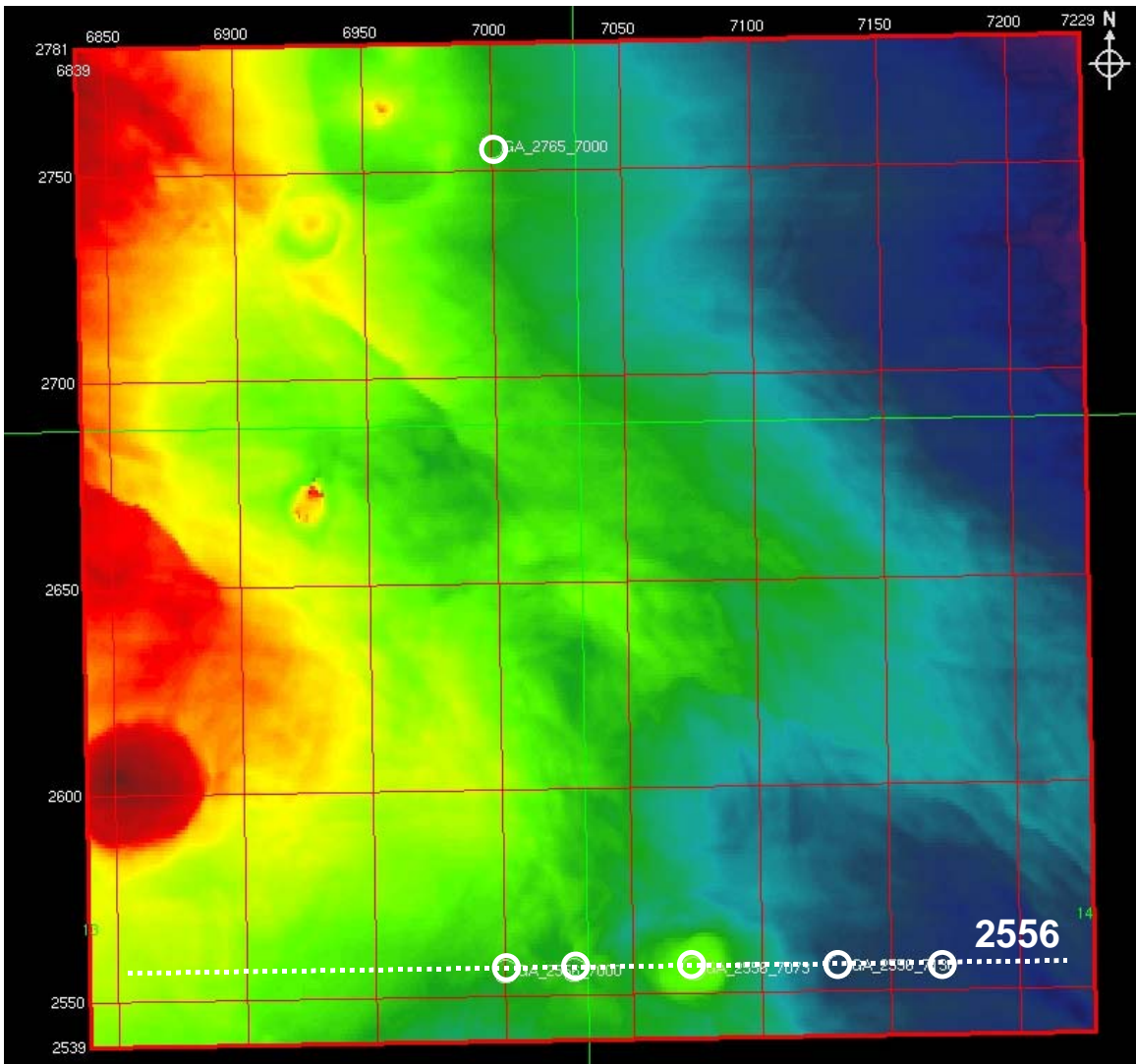
Figure B.28. Atwater Valley pseudo-well inversion locations.

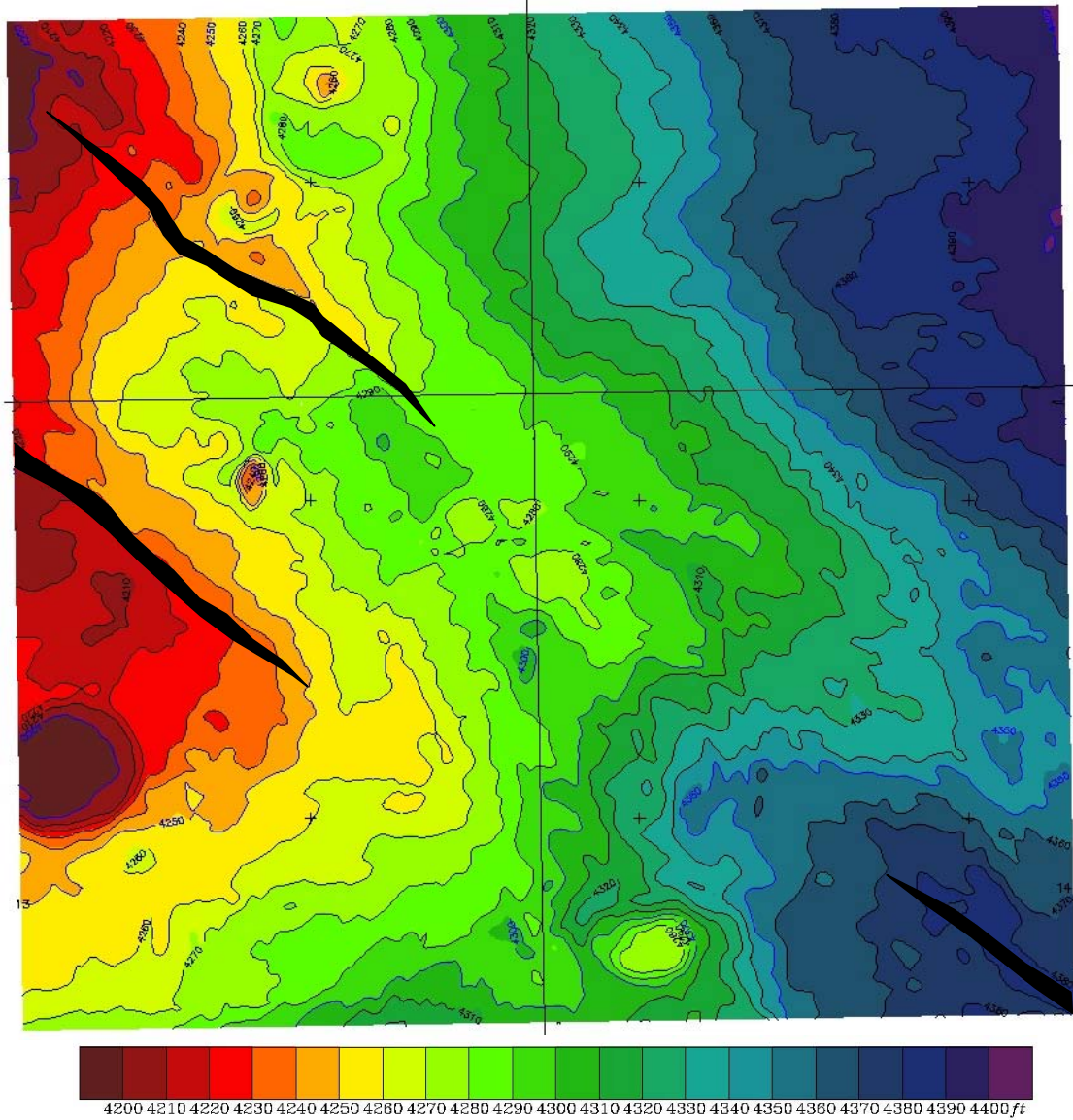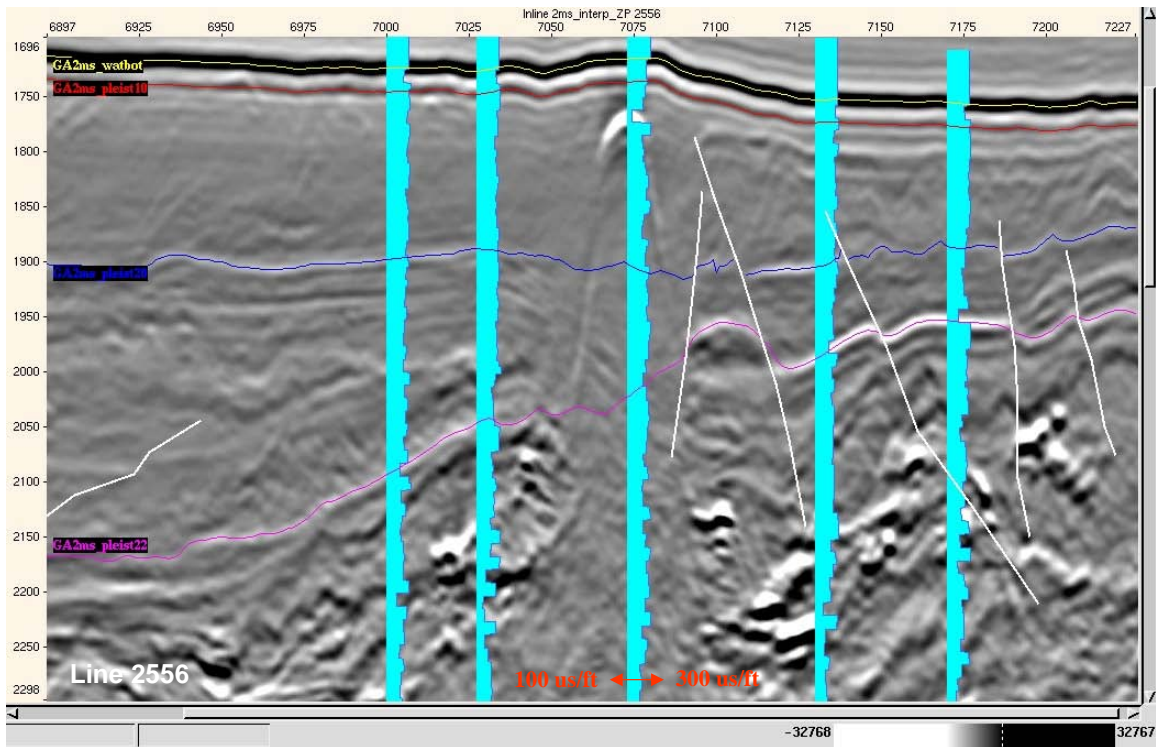**Figure B.29. Atwater Valley matching Vp waveform inversion pseudo-wells to seismic data response. Note good tie at water bottom, Pleist22 horizon and free gas zones. Blue pseudo-wells are plotted in slowness (us/ft).**

Preliminary Drill Site Recommendations

1. Mound "F" **Inline 2556 Crossline 7073 27° 56' 11.8"N   89° 16' 46.0"W.** This will enable sampling and testing of the BSR event about 50 m below the mudline. It will also allow for geochemical analysis of the gas-fluid plume and thermal gradient measurements. In addition to the mound itself, the east and west flanks should also be cored to determine the base of the GHSZ. This location also coincides very closely with the location where the Texas A&M group undertook an earlier coring project.

2. Mound "D". **Inline 2670 Crossline 6926 27° 57' 24.6"N   89° 17' 54.6"W.** This will enable sampling and testing of the BSR identified at the surface and determine the depth to which the hydrate zone might extend. As with mound "F", geochemical and thermal measurements should also be made.

Comprehensive drill site recommendations for both Atwater 14 and Keathley Canyon 195 are available as a separate document in conjunction with the USGS interpretation group and Naval Research Laboratory.

B.3.2 Keathley Canyon 195

The Keathley Canyon 195 project included a one-block area centered roughly about the intersection of Blocks 151, 152, 195 and 196. All data were re-processed through PSTM following which a detailed interpretation was performed. The area of interest included a prominent BSR event in the western half of the survey and at least one possible gas hydrate mound in the southeastern part.

Geologic Setting

The Keathley Canyon 195 project area is located along a NW-SE trending salt induced fault ridge, which also bisects two East-West mini-basins (Figure B.30). Deep Louann salt movement created this ridge, which as in the Atwater Valley area, was responsible for the fault-fracture fabric necessary for the upward gas migration and hydrate formation. This ridge culminates in a locally high peak within the study area (OCS Block 196). Water depth varies from approximately 4000 toward the top of the ridge in the south-central part of the survey to 4700 ft on either side (1200-1400 m).
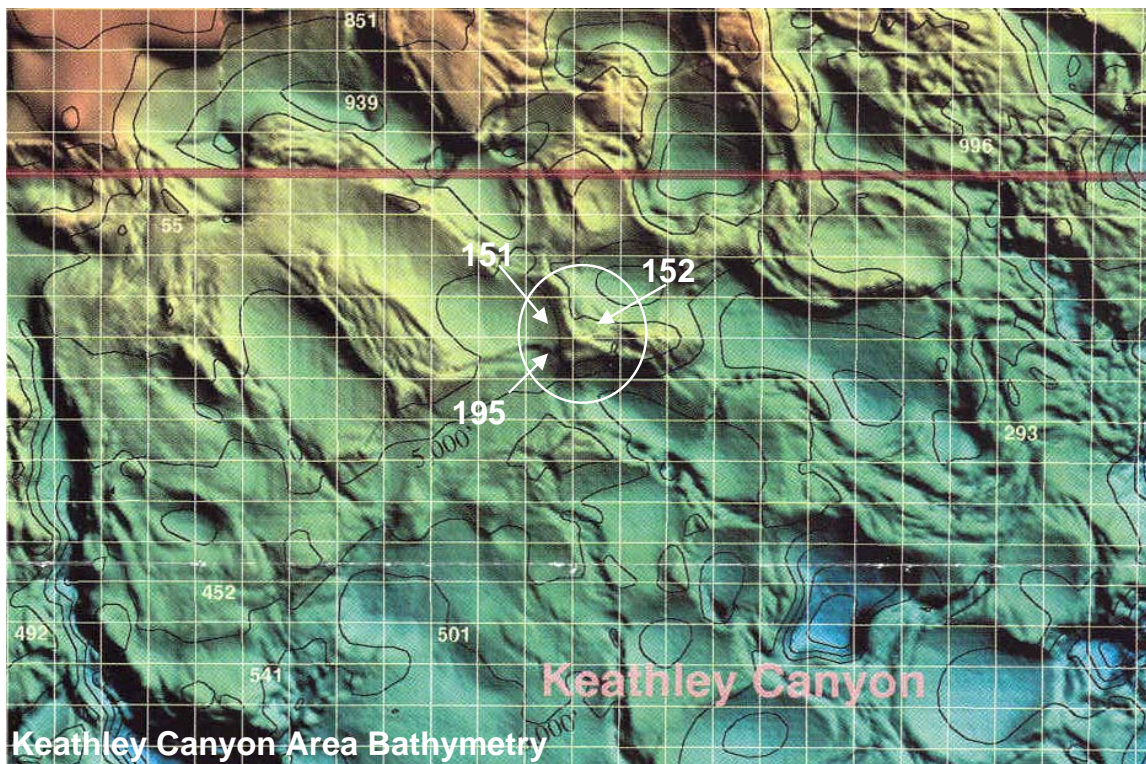
Figure B.30. Keathley Canyon area bathymetry showing fault induced ridge separating east and west mini-basins.

Gas Hydrates

The main target of interest in Keathley Canyon is the prominent BSR, which is mostly evident to the west of the fault ridge (Figure B.31). Visible mainly as a clear boundary cross-cutting the lithology and semi-parallel to the water bottom, it is sometimes definable only by termination of high-amplitude bright events. These anomalous events, which define the base of the GHSZ, are due to free-gas sands having a lower acoustic impedance than the surrounding sediments. The crosscutting lithology can be seen on the color-coded amplitude line (Figure B.32) where the red and brown colors are the more permeable gas sands. It is likely that the major faults, which bound the BSR to the east, are not only a source of gas migration, but high fluid flux as well. These fluids have the effect of disturbing the equilibrium of the BSR so that it appears much shallower than in the no-fault western area. It is also likely that the hydrate concentration is greatest in the sands closest to the faults due to the large availability of migrating free gas.

In addition to the BSR, the Keathley Canyon survey area also shows evidence of a hydrate mound (inline 5591) on the east side of the major fault ridge (Figure B.33). Below this mound is evidence of free gas accumulation and a possible destabilized BSR near the surface. This mound is directly adjacent to one of the major faults.

Numerous inversion locations were run in the Keathley Canyon area. Inline 5700 (Figure B.39) shows a good match between the pseudo-well and seismic response. This is particularly evident at the BSR and the free gas sands below. The same can be seen in Figure B.40, which describes a traverse through two additional inversion locations.
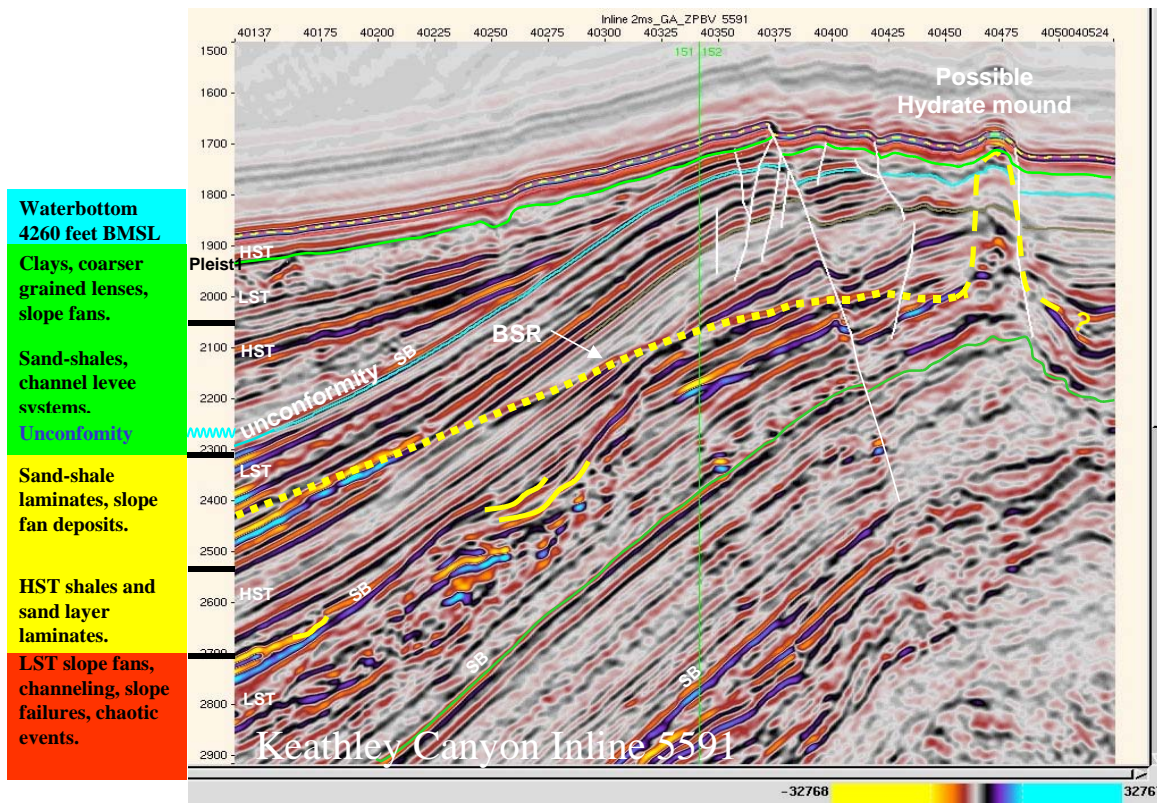
Figure B.31. Keathley Canyon Valley line 5591 showing typical lithology and interpreted horizons. Note the chaotic slumping and slope failure features in the lower section (red).
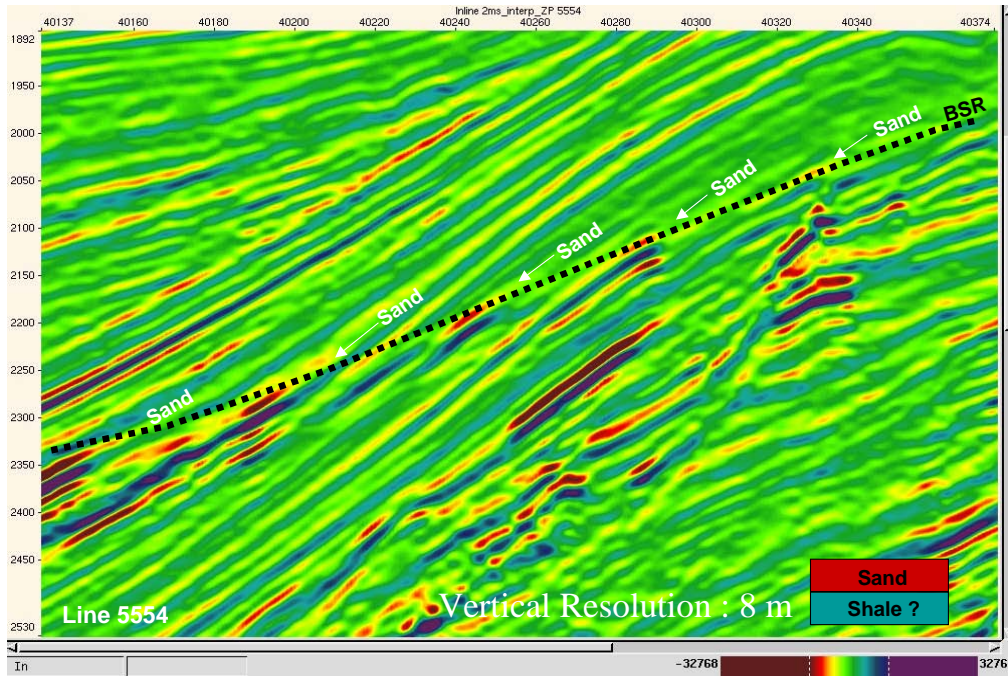
Figure B.32. Keathley Canyon line 5554 showing bright sand terminations defining the BSR.
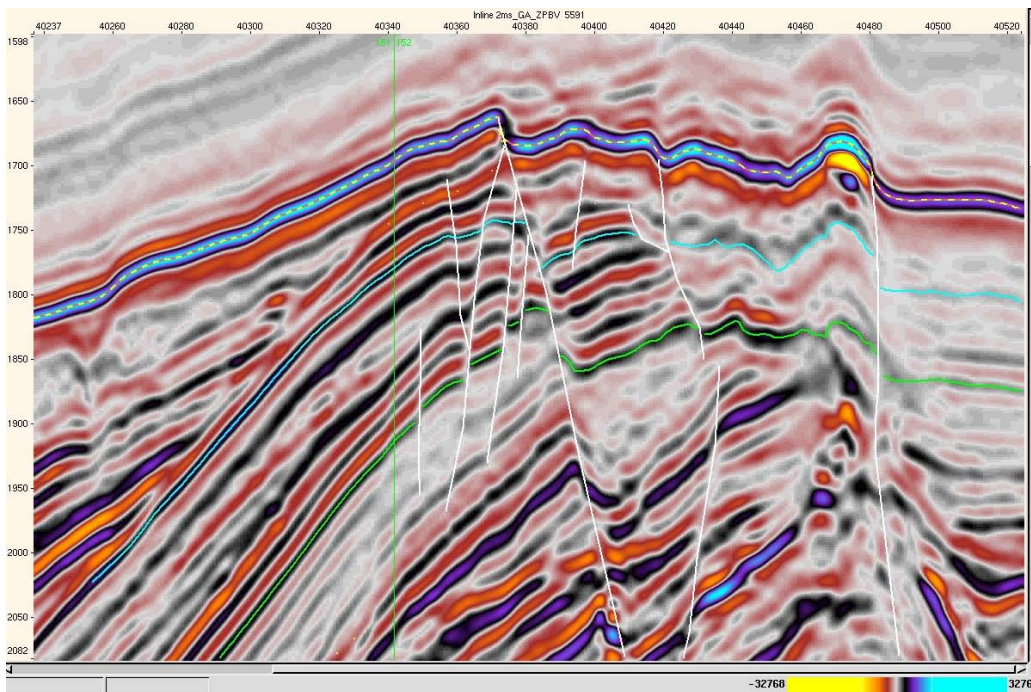
Figure B.33. Keathley Canyon line 5591 showing possible hydrate mound (right side) and proximity to faults.

45

<u>Maps</u>

To define the near-surface framework, several subsurface structural and stratigraphic maps were made. Figure B.31 shows one seismic line with all horizons. These surfaces included:

a) Water bottom (Figure B.31 – dashed, Figure 34).

b) A shallow high-stand sequence boundary (Figure B.31 – light green, Figure 35).

c) An unconformity surface above the BSR (Figure B.31 – blue, Figure 36).

d) The BSR depth structure map and a GHSZ isopach map (Figure B.31 – dashed yellow, Figure 37). The isopach map is very useful in showing the relative thickness of the GHSZ, which varies between 900 and 1400 ft. This is well within the maximum depth computed by modeling the thermo baric conditions for 94% methane.

e) A high stand sequence boundary below the chaotic LST and BSR (Figure B.31 – dark green, Figure 38).

All maps have been converted to depth using the seismic derived velocity information.
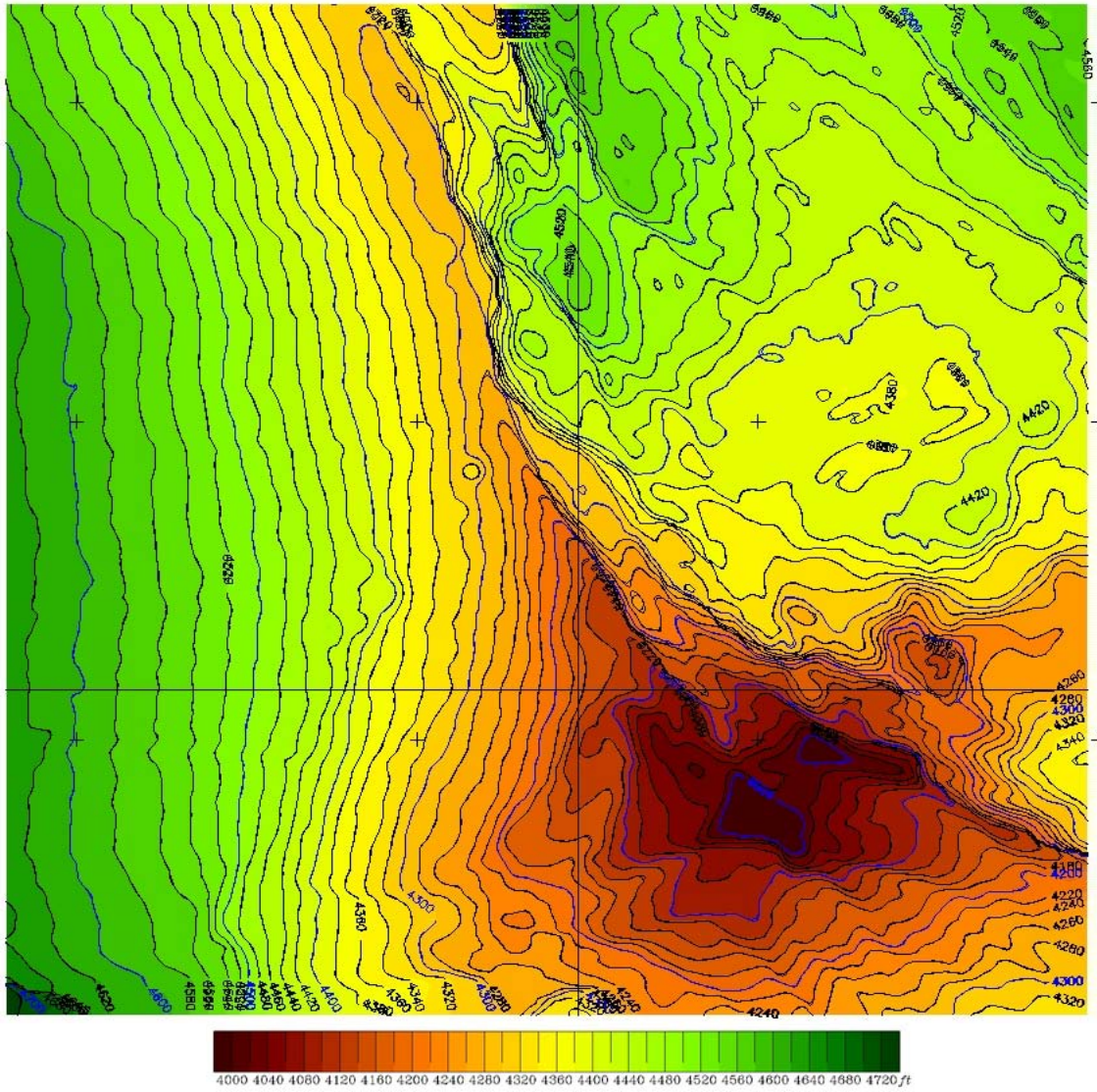
Figure B.34. Keathley Canyon Water bottom depth structure map. CI = 20 ft.
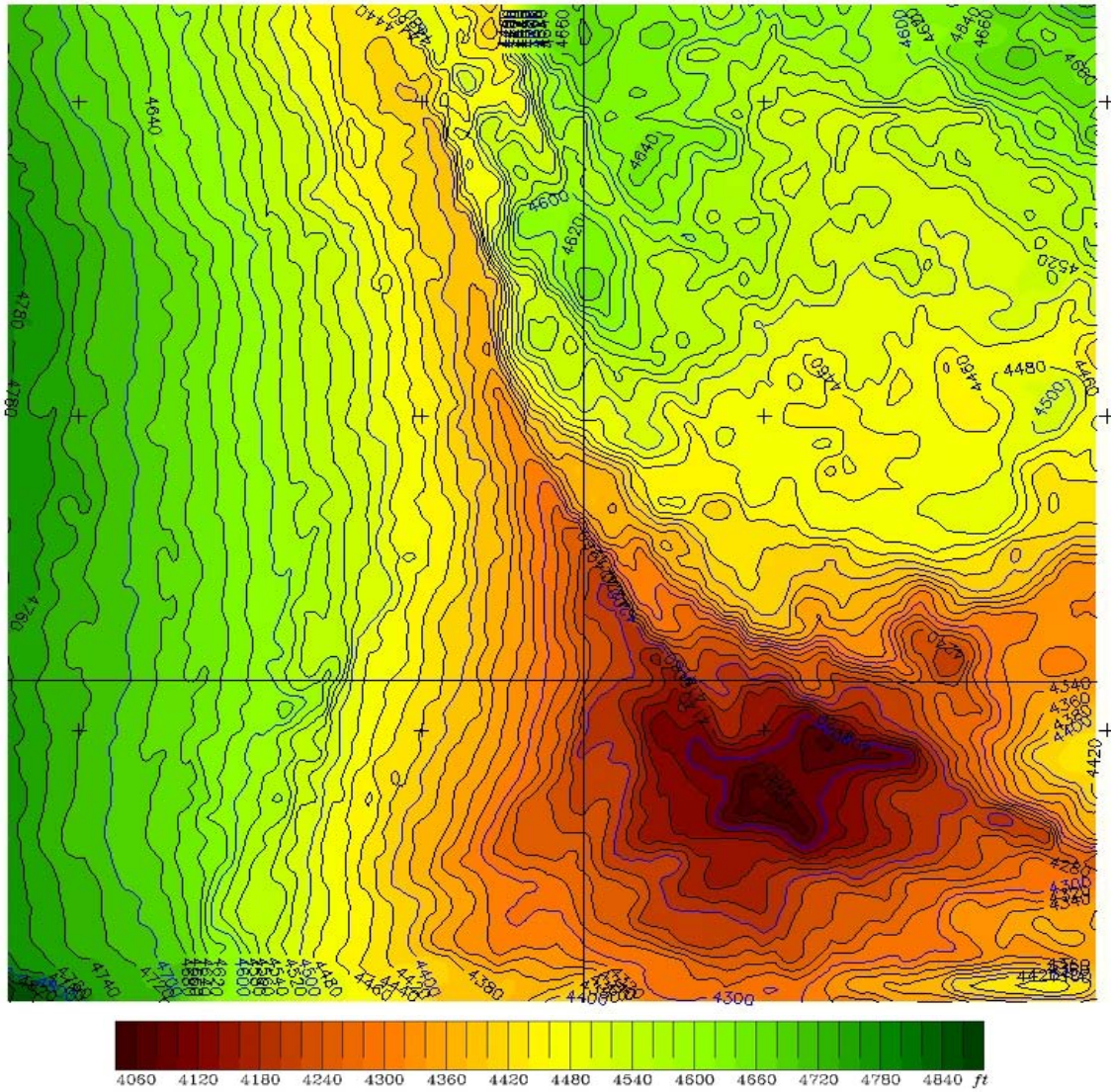
Figure B.35. Keathley Canyon Pleist1 horizon (~50 ms below water bottom) depth structure map. CI = 20 ft.
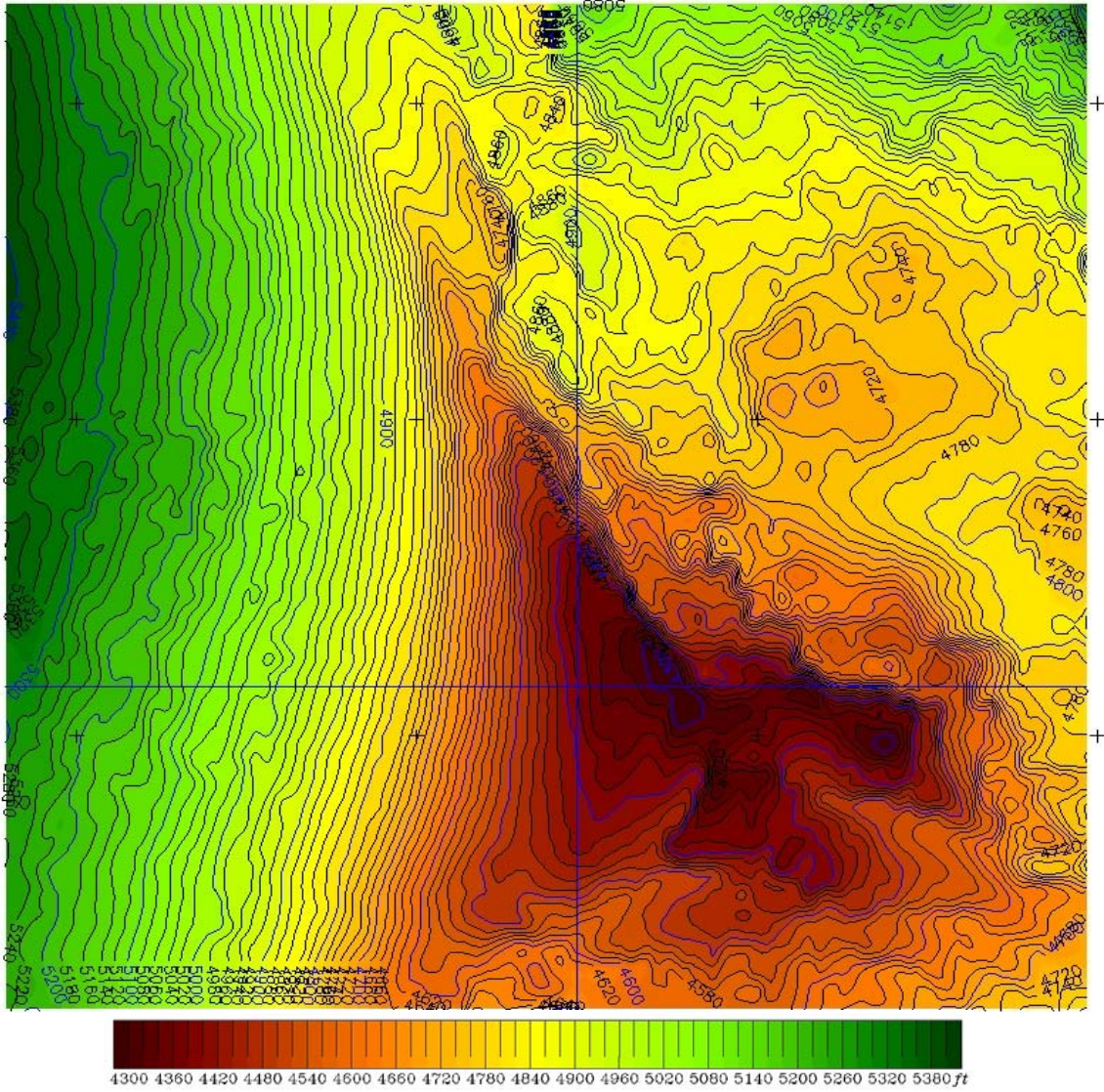
Figure B.36. Keathley Canyon upper unconformity horizon depth structure map. CI = 20 ft.
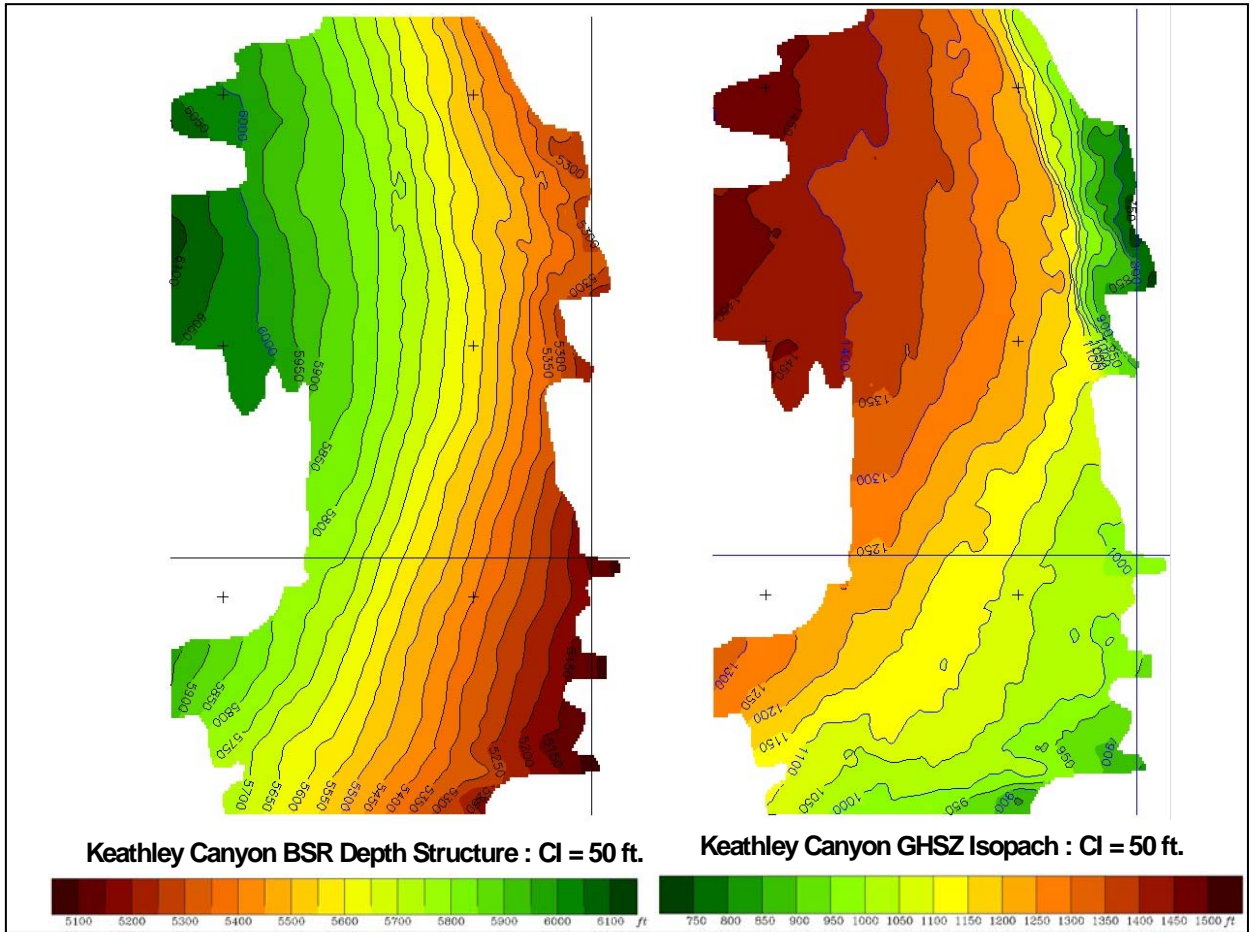
Figure B.37. Keathley Canyon BSR depth structure and water bottom-to-BSR isopach maps.

50
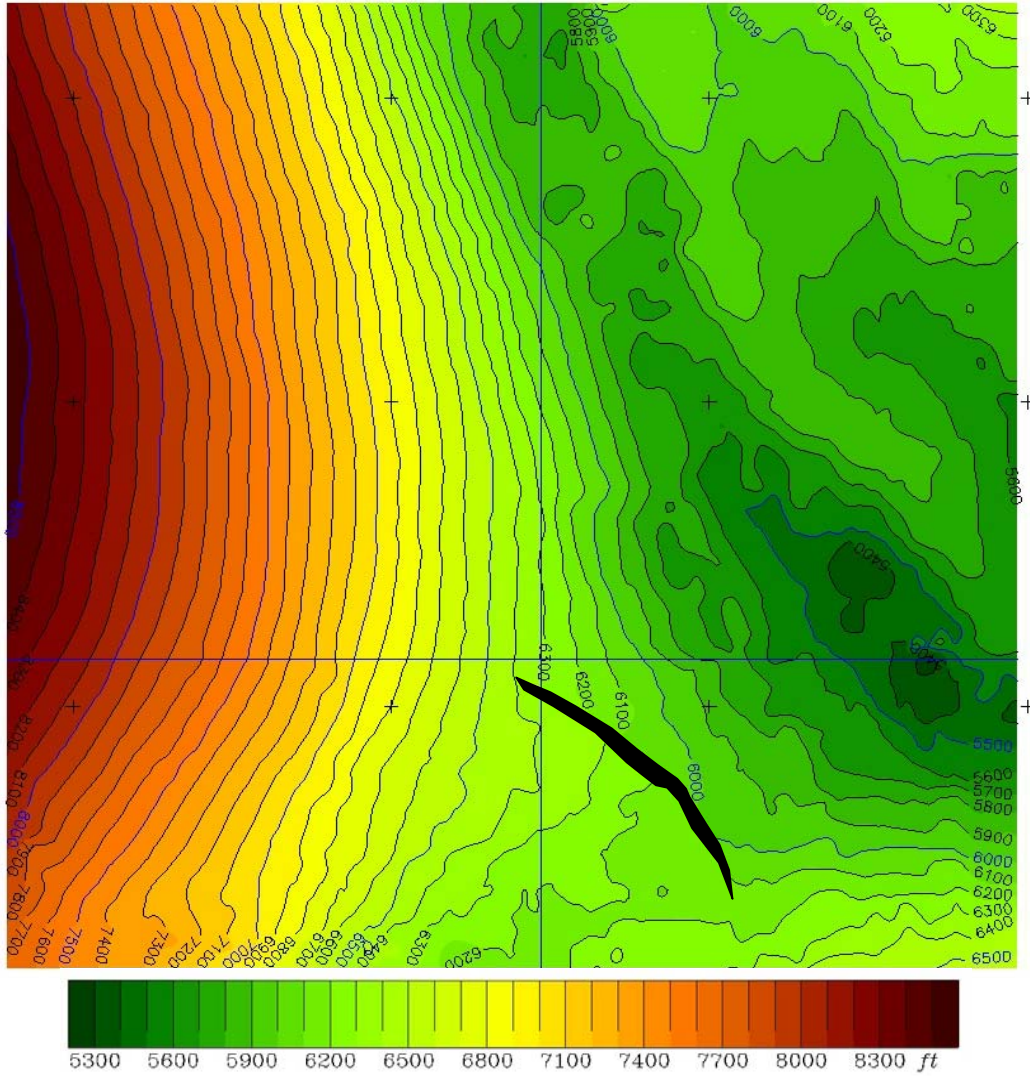
Keathley Canyon Deep High Stand Depth Structure : CI = 100 ft.
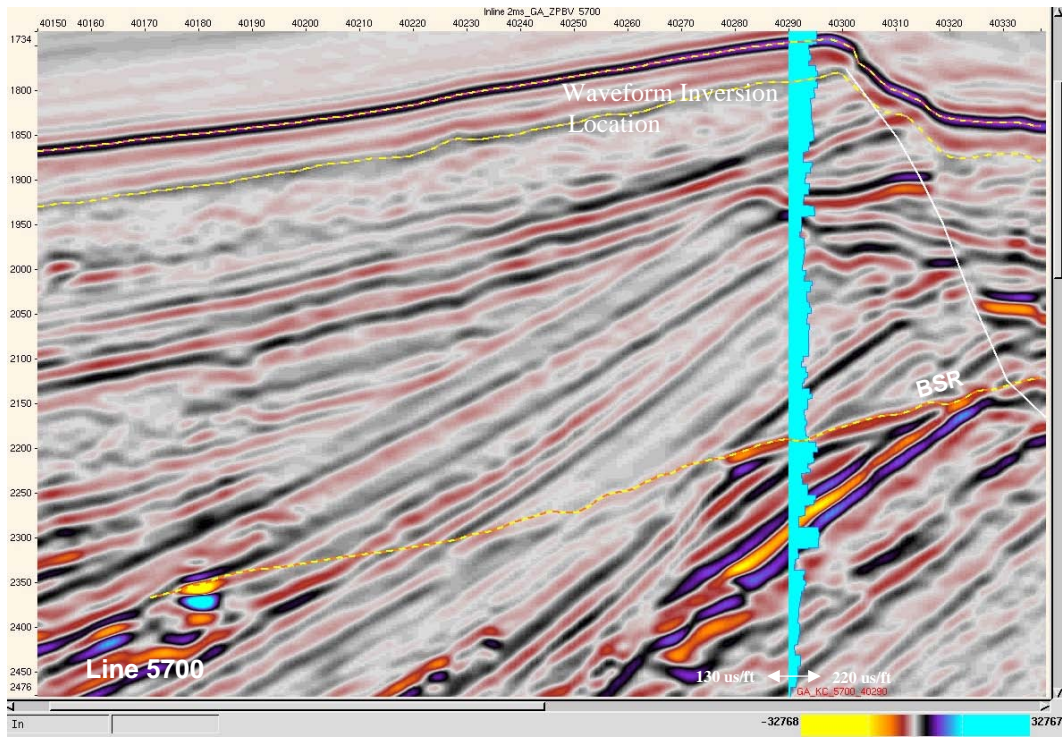
Figure B.39. Keathley Canyon matching seismic to full-waveform inversion pseudo-well. Log curve is in 'slowness' (us/ft). Note good match at BSR and deeper gas sands.
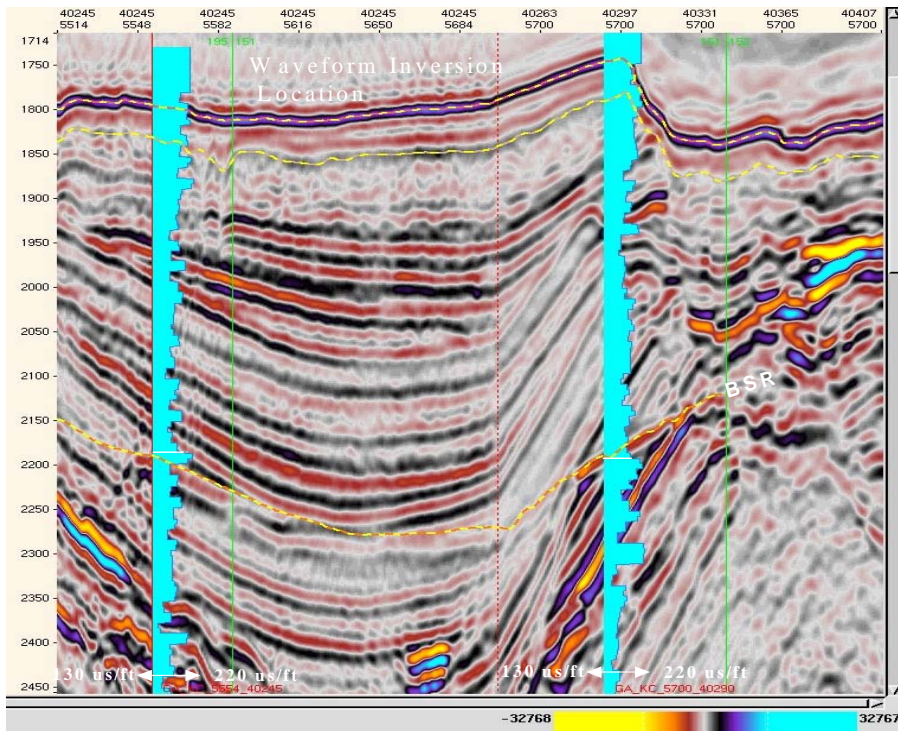
Figure B.40. Keathley Canyon traverse matching seismic to full-waveform inversion pseudo-wells.

Preliminary Drill Site Recommendations

Inline 5700 crossline 40320 26° 49' 22.6"N   92° 58' 53.2"W. BSR very evident and pinching out at a terminating bright gas sand anomaly.   The sand can be mapped and extends approximately 2 km north and south from the location. Location is also west of the fault to avoid possible unfavorable flux flow.

Inline 5601 crossline 40392 26° 48' 18.2"N   92° 58' 20.6"W. BSR is very evident extending up to a bright anomaly at the fault intersection. Similar to 5700/40320 location but closer to the fault and with a brighter event.

Inline 5591 crossline 40473 26° 48' 11.7"N   92° 57' 43.9"W. Possible hydrate mound with both near surface and deeper hydrate concentrations likely.

Comprehensive drill site recommendations for both Atwater 14 and Keathley Canyon 195 are available as a separate document in conjunction with the USGS interpretation group and Naval Research Laboratory.

B.4   Stratigraphic Evaluation Summary and Conclusions

The seismic analysis indicated that all surface hydrate mound features seem to form in close proximity to a fault/fracture network. This is apparent with the deep-seated BSR in Keathley Canyon as well. This relationship is reasonable as the near seafloor deepwater sediments typical of the Gulf of Mexico are predominantly muds and clays of high porosity, but of low permeability. Charging these sediments with gas requires a mechanism, such as deformation and faulting, to facilitate gas-fluid migration. More substantial concentrations of gas hydrate would likely be found in the coarser-grained sediments near these fault zones.

Because of the high fluid/gas flux moving up within the fault zone area and below the possible gas hydrate mound, the BSR could likely be destabilized upward from its normal deeper equilibrium state under the mound. This produces a seismically detectable BSR reflector with a "draped" effect extending down to the deeper hydrate stability zone. Wood (2002) modeled this effect as a boundary perturbation. This effect was also very evident in the Atwater Valley survey over mound "F" (Figure B.23).

If the BSR seen directly below some of the mounds is in fact a true BSR, its depth below the mudline can suggest something about the thickness and qualities of the hydrate above it and of the fluid flux environment. For example, mound "D" in Atwater Valley 14 (Figure B.23) shows indications from the shallow possible BSR of a very shallow and thin hydrate "cap" at or near the seafloor.   Mound ("F") show evidence of a possible deeper BSR, and is likely to have concentration of hydrates down to about 50 m.

The BSR in Keathley Canyon is definable not only by a linear boundary parallel to the water bottom, but also by bright sand terminations. This is expected in the GOM sediments in which the gas sands commonly are laminated with shales and clays. The result is that the free gas within the sands have a higher than normal amplitude anomaly just below the base of the gas hydrate stability zone. This enables not only accurate mapping of the BSR, but also detailed mapping of individual sand packages. This effect was also illustrated by McConnell and Kendall (2003).

The hydrates found within 100 m of the mudline in the GOM are neither likely to be thick nor massive as seen in some other parts of the world (Mallik well, Canada). This is due to the low permeability of the unconsolidated high-stand clays found in the shallow lithology typical of deep-water GOM sediments. Thicker and more continuous zones of hydrate would not be expected until reaching the deeper coarser transgressive and low stand system tract sands, many of which are below the hydrate stability zone

While the 3D data were crucial in identifying possible hydrate features and providing the basis for inversion and modeling, the broader bandwidth of the high-resolution data from the USGS survey (not shown in this report) was very useful in detailing some of the shallow lithology. Typically, the conventional 3D seismic data were of a quality that was unable to image through the "amplitude wipeout zones" below some of the mounds. Additional 3-D data collection in the search for gas hydrates would likely benefit from multi-component acquisition (4-C), which would better resolve the gas cloud with a shear-wave component, and "Q" acquisition, which would make available a much broader bandwidth with an improved signal to noise ratio.

C.   Seismic Attribute Analysis

To add further value to the interpretation and stratigraphic evaluation process just described, numerous seismic attributes were also generated and evaluated for each of the three areas. Although there are a large number of possible attributes that can be created, it is not feasible, nor productive, to analyze them all.   Furthermore, the objective was to aid in the detection of anomalous gas hydrates zones and hydrate characteristics.   Because hydrates often possess certain physical characteristics and exhibit known acoustic and elastic properties, only a few attributes were considered applicable.   The attributes selected were frequency-based, amplitude-based, phase-based and coherency-based.

C.1   Green Canyon

As discussed earlier, Green Canyon was studied first because the area contained known concentrations of gas hydrate.   Although we knew hydrates existed at Bush Hill, we didn't know the spatial and temporal limits.   Figure C.1 below shows four different attributes of the same N-S line across the Bush Hill hydrate mound.   While instantaneous frequency is useful in defining stratigraphic details and reflection strength is useful in illuminating anomalous amplitude packages, the dip-azimuth attribute, which measures the rate of change trace-by-trace, helped
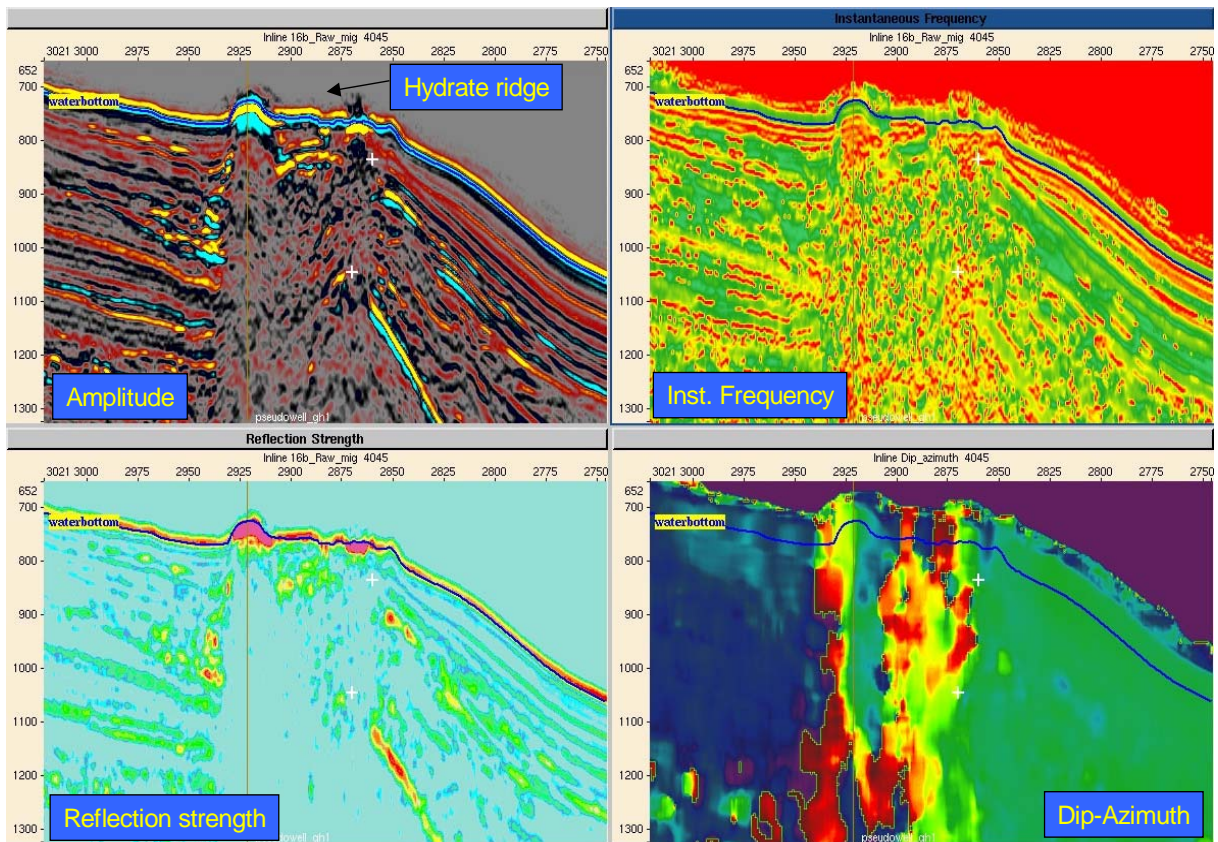
Figure C.1.   Green Canyon 195 area seismic attributes of inline 4045 through Bush Hill hydrate mound.   Clockwise from top left: Amplitude, Instantaneous frequency, Dip-azimuth change and Reflection strength.

delineate the gas chimney that appears below the mound complex. Figure C.2 shows another closer look at this line with the dip-azimuth attribute overlaying seismic traces displayed in cosine of phase. Bush Hill is the seafloor mound on the left. Note that the vertical and spatial extent of the gas chimney and hydrate occurrences appear to cover a much broader area than only that of the main mound. The chimney can also be seen to closely follow the faulting pattern.
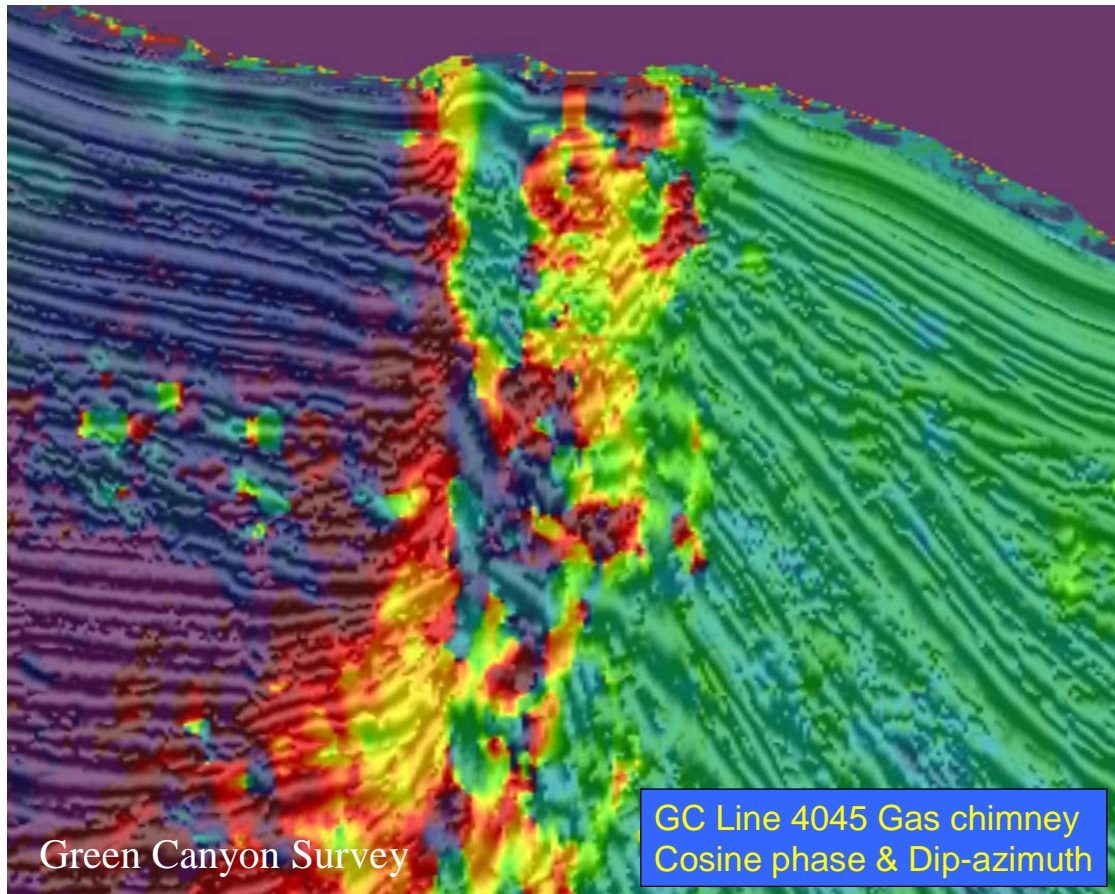
Figure C.2. Green Canyon184/185 Inline 4045 showing attribute display of Bush Hill Mound with gas flux overlaying cosine of phase seismic trace attribute.

C.2   Atwater Valley 14

The predominant interest in the Atwater Valley 14 area are in the numerous seafloor mounds, most of which are probable indicators of shallow gas hydrates. Because shallow faulting is thought to be associated with hydrate mounds, surface pattern recognition can be a useful hydrate exploration tool. Figure C.3 shows an image of the water bottom displayed in artificial illumination, which is useful in highlighting these surface features. All five mounds are evident, as is the NW-SE trending fault and fold fabric. Mound "D" (left center) is situated midway in a large faulted graben, whereas mound "F" (bottom center) is located on the edge of the fault area. Perhaps this positional difference with respect to the faults is one reason the two mounds exhibit different seismic characteristics.
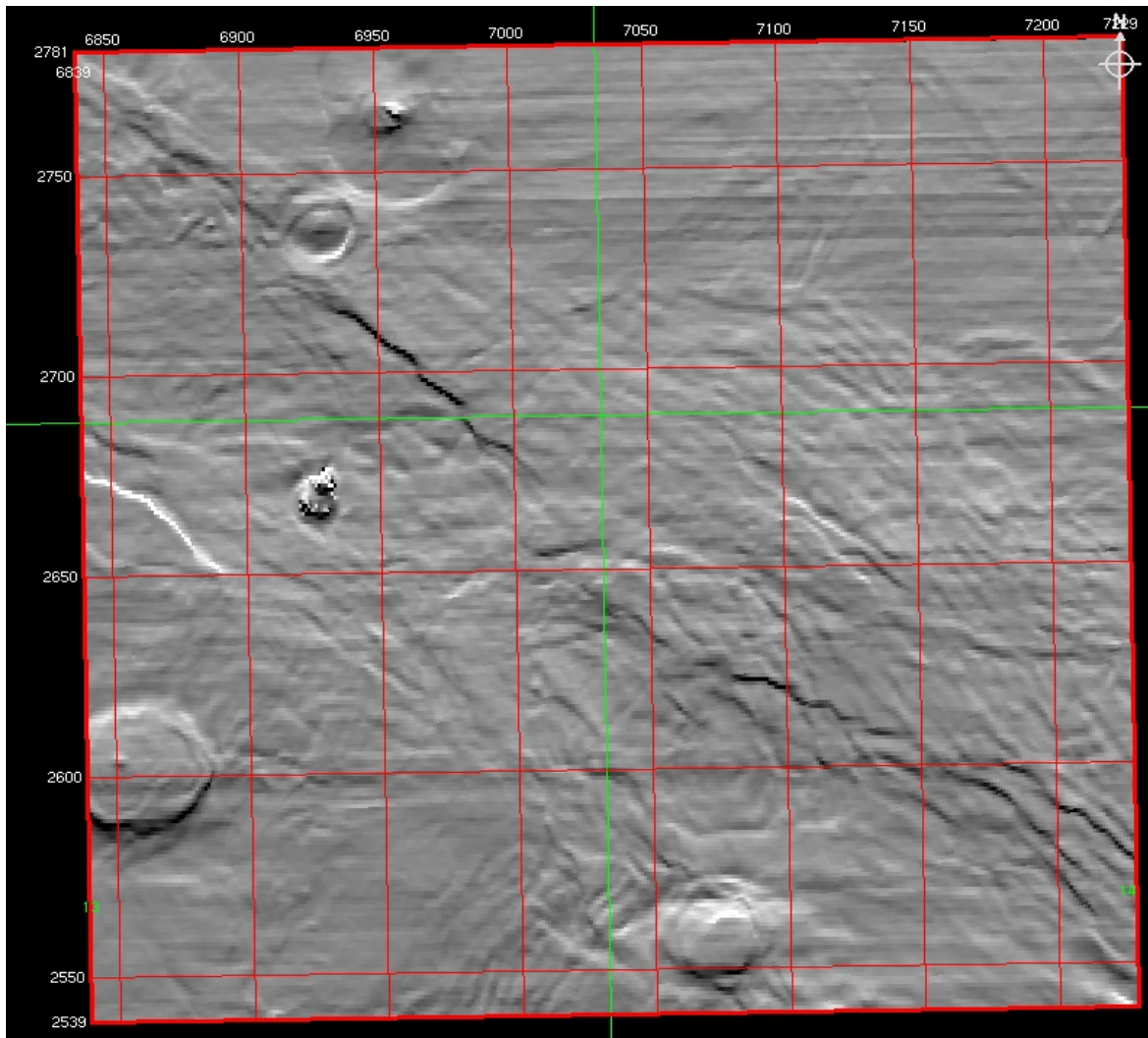
Figure C.3.   Atwater Valley 14 area water bottom displayed in artificial illumination attribute. The mounds and faults are optically enhanced.

Once the mounds were discovered on the seismic, they were examined in more detail individually. Figure C.4 below shows a single east-west line across the southern flank of mound "F" displayed with several different attributes. Clockwise from top left are amplitude, cosine of phase, instantaneous frequency and dip-azimuth. Amplitude and phase are useful in seeing the structure and stratigraphy, whereas dip-azimuth and frequency are helpful for delineating the mound and associated gas chimney. In this example, instantaneous frequency was very useful in determining the temporal limits of the gas chimney.
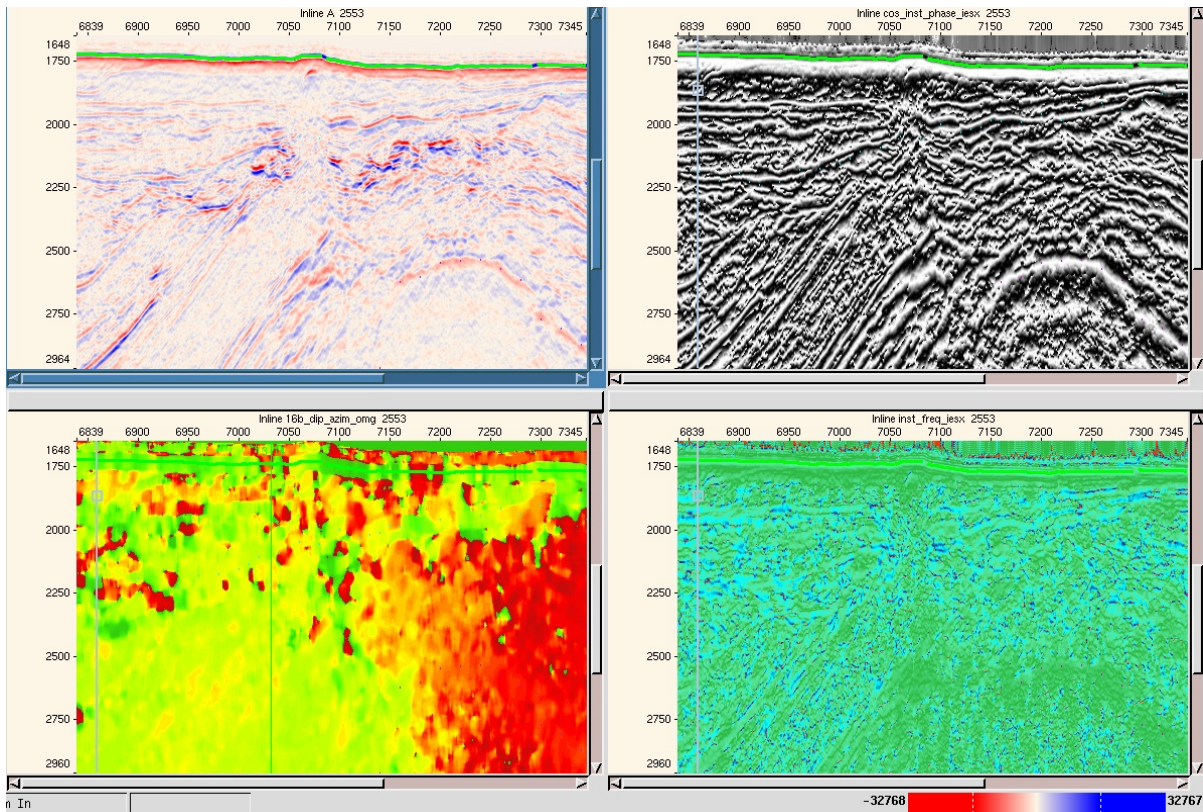
Figure C.4. Atwater Valley 14 area W-E line 2553 through mound "F". Clockwise from top left; amplitude, cosine of phase, instantaneous frequency and dip-azimuth attributes.

Attribute extraction of other sites and areas are available upon request.

C.3   Keathley Canyon 195

The focus in the Keathley Canyon area is on the BSR, which lies approximately 5300 to 6000 ft below the mudline, and bounded by the controlling fault fabric. Figure C.5 shows an image of the water bottom displayed in artificial illumination, which is useful in highlighting the surface and near surface features.   The NW-SE trending fault and fold fabric is clearly evident, as are several circular collapse pockmark features to the west of the main fault.   These collapse features are possibly gas release vents or failed hydrate mounds and are telltale signs of active gas generation and migration within the area.
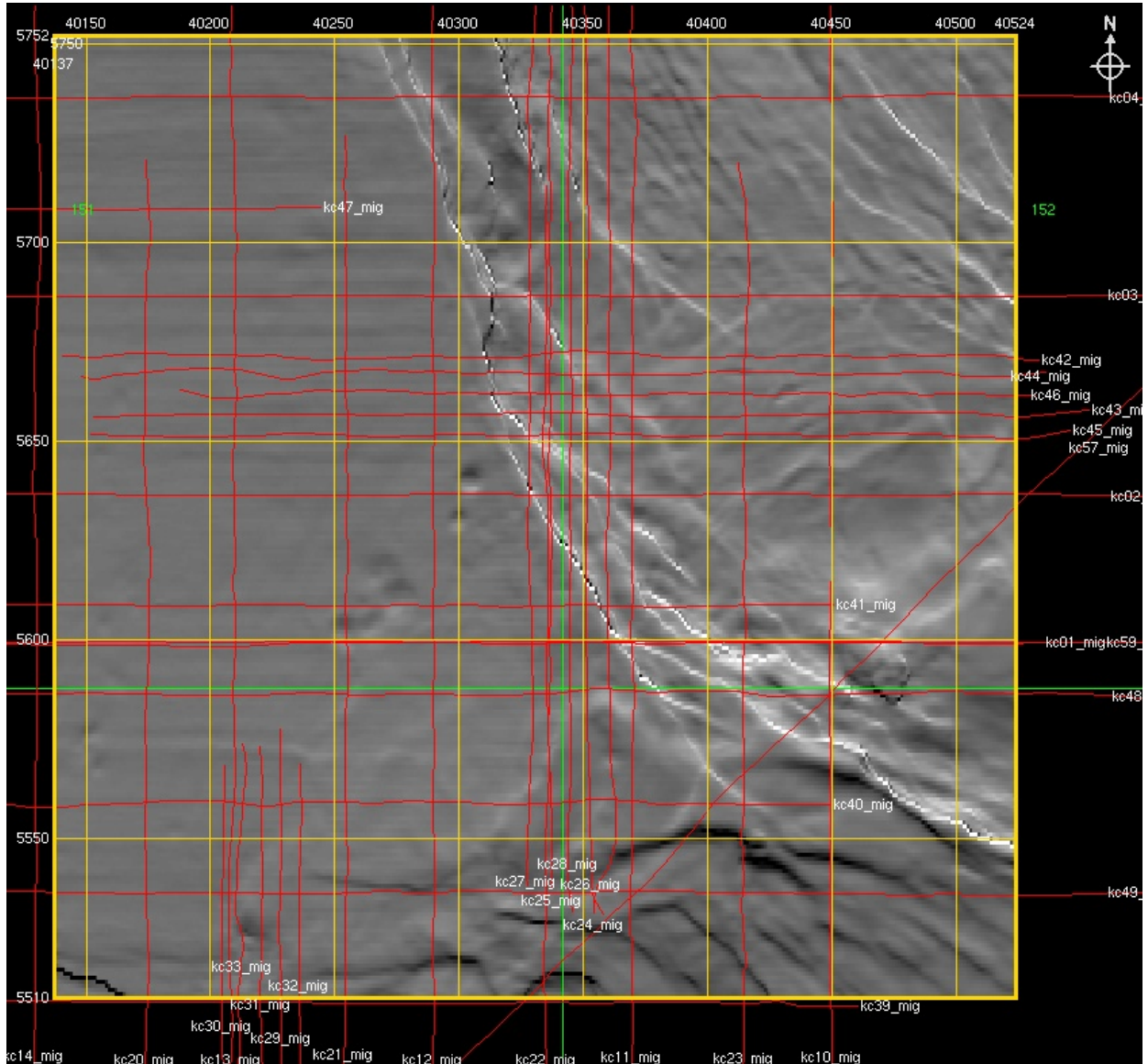
Figure C.5.   Keathley Canyon 195 area water bottom displayed in artificial illumination attribute. Note the numerous circular gas collapse "pock-mark" features west of the main fault.

Figure C.6 below shows the water bottom displayed in the instantaneous frequency attribute. This attribute is useful for seeing reflectivity character changes along a windowed horizon. Here, the faults are clearly outlined and the possible hydrate mound in the lower center of the figure is visible as a frequency anomaly.
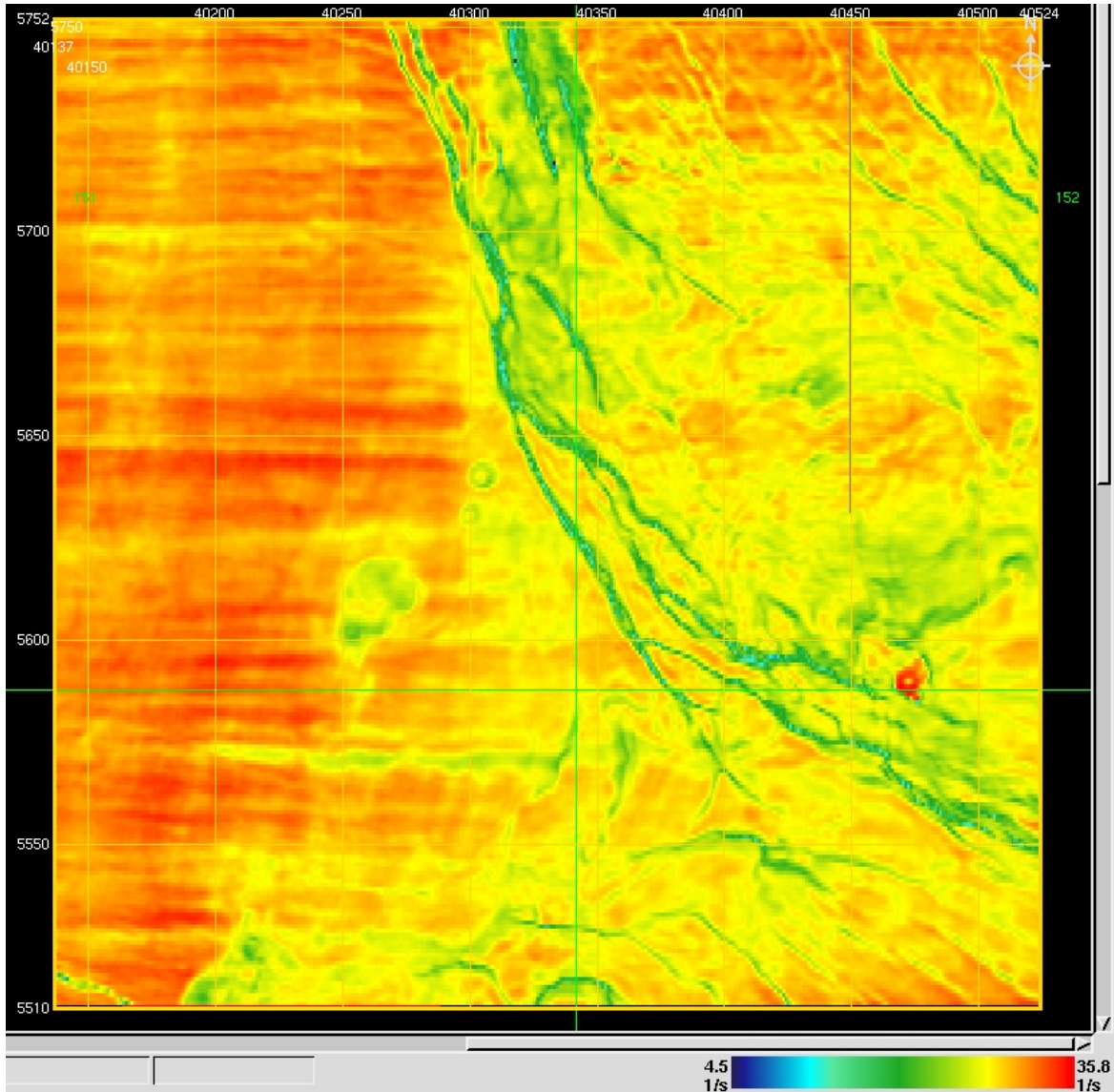
Figure C.6. Keathley Canyon 195 area water bottom displayed in instantaneous frequency attribute. Note the possible hydrate mound delineated by high frequency (circular red feature) on the lower right side.

In stratigraphy not parallel to the water bottom, the BSR will typically crosscut the lithology in order to maintain a stable thermo-baric boundary. Cutting across sand and shale or other heterogeneous lithology will result in a laminated appearance. Figure C.7 shows this effect by the banded appearance of the instantaneous amplitude extraction. The anomalously high amplitudes from the free gas sands are seen as the brown and orange colors.
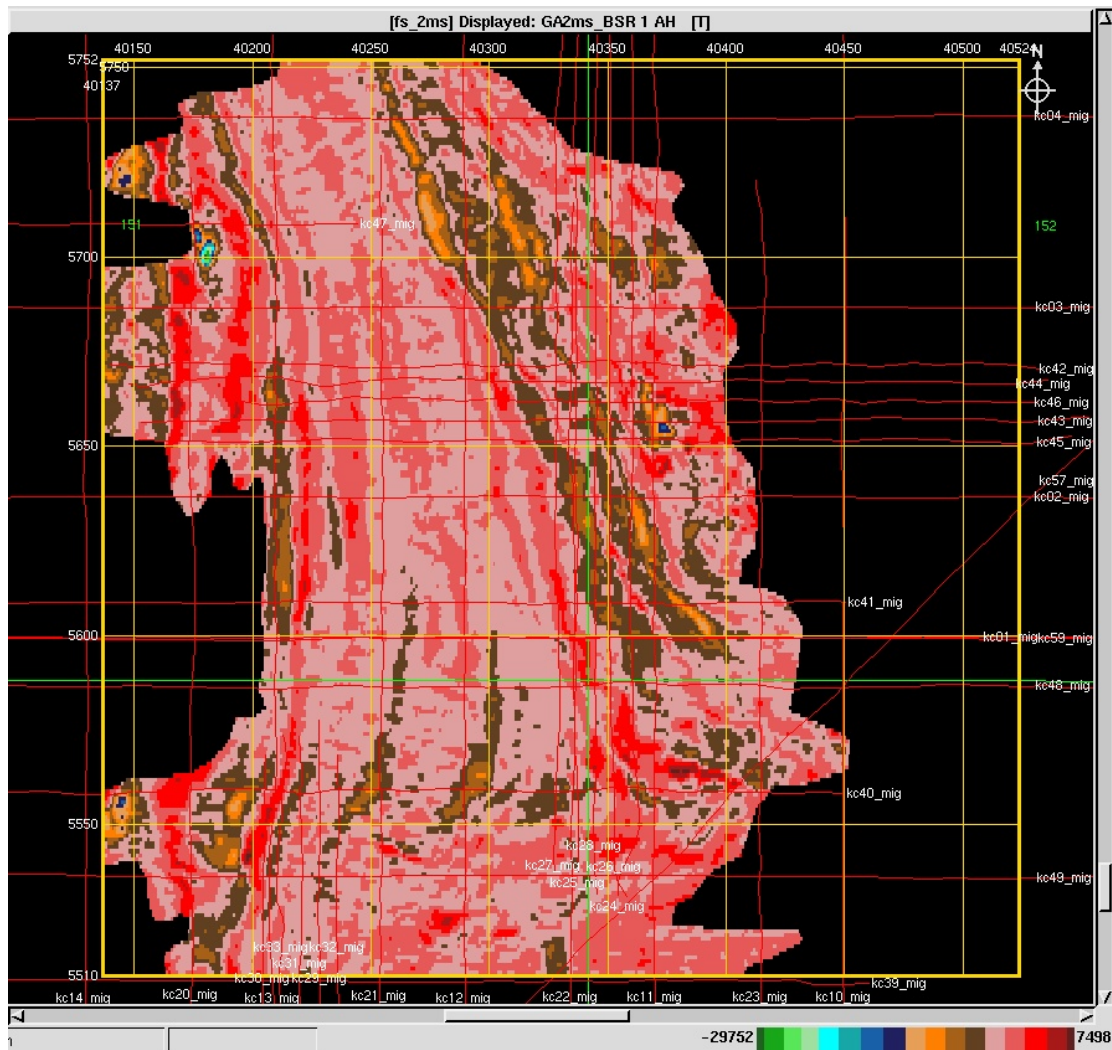
Figure C.7. Keathley Canyon 195 BSR displayed in instantaneous amplitude. Note the BSR crosscutting the lithology seen as the banded colors. The darker N-S trends in the center are the high amplitude free gas sands as they pinch out against the BSR and near the fault.

A similar effect can also be seen using the instantaneous frequency attribute (Figure C.8). The laminar beds are even more pronounced, although the amplitude anomalies of the free gas sands are not as obvious as in Figure C.7.

Figure C.9 shows a reflection strength attribute extracted along east-west line 5601. This line shows the BSR terminating against the fault in the center of the line denoted by the bright amplitude free gas at that point. Below this level is thought to be free gas, with hydrate existing above.

The final Figure C.10 is an east-west line intersecting the possible hydrate mound to the east of the main fault system. The 4-panel attribute display shows the mound (right side of each picture) and associated structures. Especially of note is the dip-azimuth attribute in the lower left panel. This attribute possibly outlines the gas chimney traveling up along the fault and fracture pathways.

61

Figure C.8. Keathley Canyon 195 BSR displayed in instantaneous frequency. The BSR cross-cutting the lithology can be seen as the banded colors.
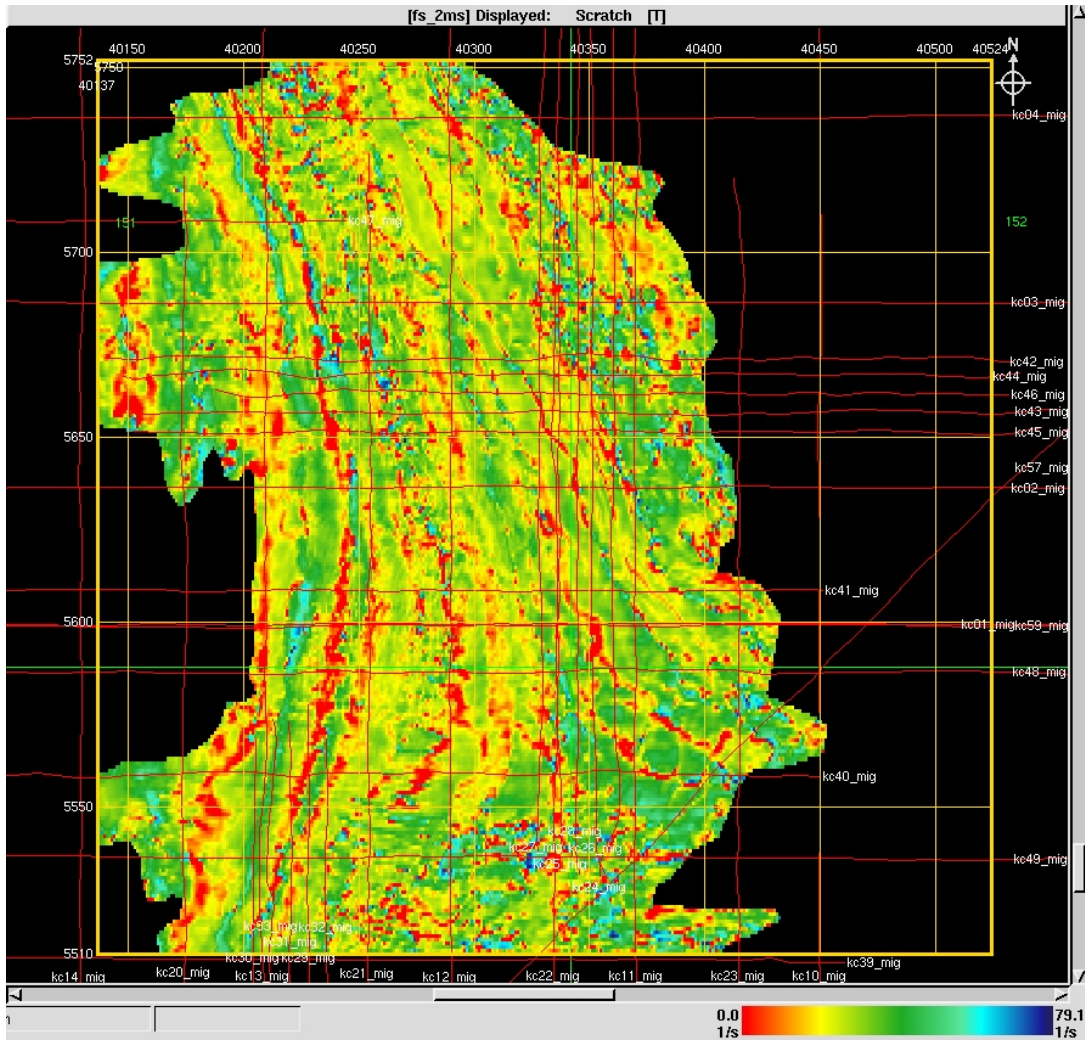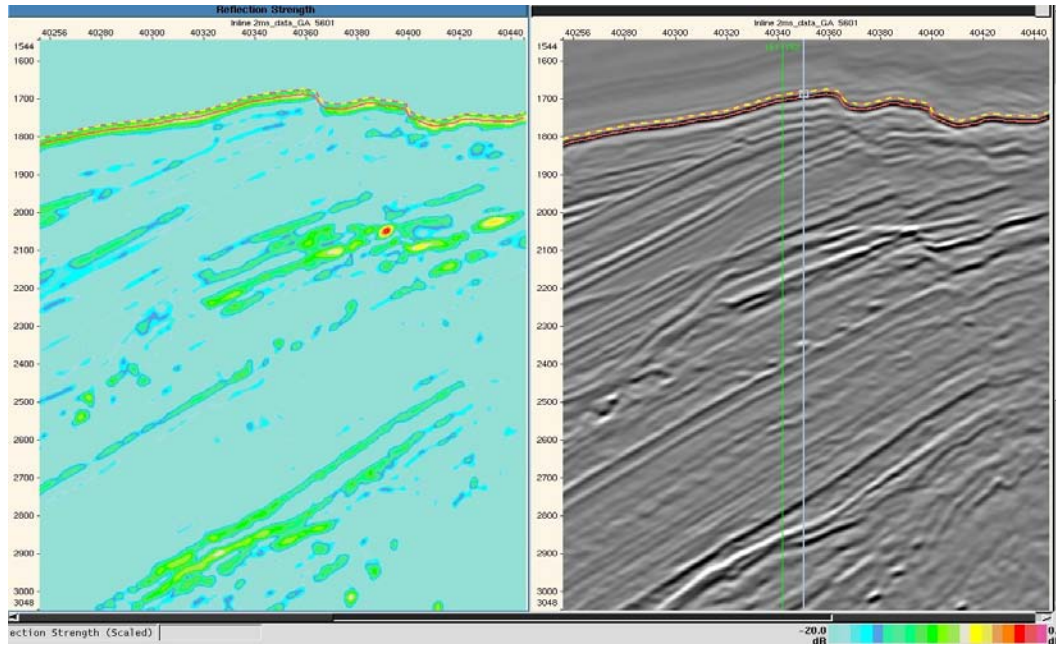
Keathley Canyon BSR – Reflection Strength and Amplitude

Figure C.9. Keathley Canyon 195 BSR displayed in instantaneous frequency. The BSR cross-cutting the lithology can be seen as the banded colors.
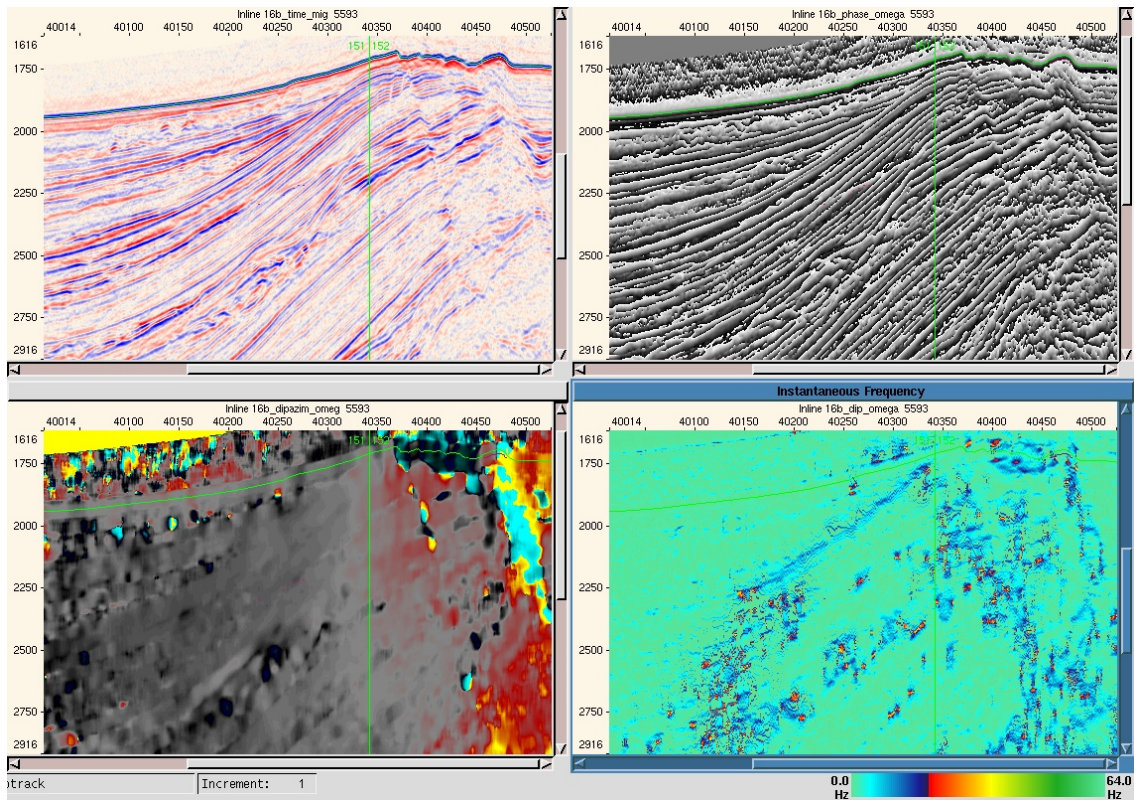

Figure C.10. Keathley Canyon 195 line 5593 clockwise from top left; amplitude, cosine of phase, instantaneous frequency and dip-azimuth.

D. Rock Property Modeling and Inversion

D.1 Rock Physical Properties of Gas Hydrates and Hydrate-bearing Sediments

The purpose of studying the rock physical properties of gas hydrates is to learn how the introduction of gas hydrate into shallow sediments affect the elastic properties of P-wave velocity, S-wave velocity and bulk density. Understanding the rock properties of hydrate bearing sediments can enable us to predict the elastic properties, and thereby quantitatively estimate the amount of gas hydrate present in the rock from well or seismic measurements.

D.1.1 Definition and Classification

Gas hydrates are naturally occurring crystalline inclusion-compounds of water molecules forming a rigid lattice with cages each occupied by a molecule of natural gas. The structure of gas hydrates is strictly determined by the molecular size of the inclusion gas. There exist three types of structures in naturally occurring gas hydrates.
- Structure I (sI) forms with small natural gas molecules, mostly methane.
- Structure II (sII) forms with larger molecules, such as ethane, but smaller than pentane.
- Structure H, the most recent discovery, contains the largest molecules, up to the size of common components of gasoline (Sloan, 1998).

Gas hydrates are also categorized as either biogenic or thermogenic according to their genesis. Biogenic gas hydrates are formed from the breakdown of previously living organisms, while thermogenic hydrates are formed through the influx of deep thermal gas along faults, bedding and other conduits. Numerous studies have dealt with the physical/chemical properties of these two types of hydrates. Readers are referred to Sloan (1990, 1998) for more details.

D1.2 Elastic Properties of Pure Gas Hydrates

Typical elastic properties of gas hydrates include: 1) bulk modulus ranging from 5.6 to 8.3 GPa, 2) shear modulus from 2.4 to 3.3 GPa, and 3) density from 0.9 to 0.92 g/cc (Figure D.1). These values are comparable to those of ice, which have a bulk modulus of 8.8 GPa, shear modulus of 3.9 GPa, density of 0.92 g/cc.

| Property		Bulk Modulus (GPa)	Shear Modulus (GPa)	Bulk Density (g/cc)	P-wave Velocity (km/s)	S-wave Velocity (km/s)
Gas hydrate	sI	5.6* 8.1**	2.4* 3.3**	0.90* 0.91**	3.1~3.7	1.6~1.9
	sII	8.3*		0.92*		
Ice		8.8*	3.9*	0.92*		
Water		2.3	0	1.04	1.5	0
Quartz		36	45	2.65	6.05	4.09
Clay***		21	7	2.60	3.41	1.64

Figure D.1. Elastic properties of gas hydrate bearing sediments. Values denoted by * are from Sloan (1998), ** from Helgerud et al. (2002). Clay values (***) are from Tosaya (1982). The others are typical values from Mavko et al. (1998) .

D.1.3 Elastic Properties of Gas Hydrate-bearing Sediments

The elastic parameters for gas hydrates, compared to those of pore fluids, are much higher. The effect of this is that the introduction of hydrates into the shallow sediments tends to increase the overall P-wave and S-wave velocities of the host rocks. Results of recent drillings for gas hydrates worldwide have demonstrated consistent increases in the elastic properties of the shallow gas hydrate bearing sediments. The Mallik 2L-38 well of Mackenzie River Delta in northern Canada, where high saturation gas hydrate occurred throughout the interval between 897.25 and 1109.5 m (Collett, 2000) below the ground level, revealed high P-wave and S-wave velocities, with P-wave velocity over 3 km/s and S-wave velocity over 1.5 km/s (Figure D.2). The gas hydrate interval at the well is also indicated by high resistivity readings. Figure D.3 shows the crossplots P-wave versus S-wave velocities, and Poisson's ratio versus P-wave velocity, both color-coded with resistivity values. High P-wave and S-wave velocities are indicated from the crossplot (left panel, Figure D.3), and slightly lower Poisson's ratio for the gas hydrate intervals (right panel, Figure D.3). Leg 164-995B of Ocean Drilling Program (ODP) at Blake Ridge, Atlantic Ocean also demonstrates higher P-wave velocity at the gas hydrate-bearing interval between 200 and 400 m below the mudline (Figure D.4). Similar trends were also observed in the drillings of Nankai Trough region of Japan, North Slope of Alaska, Middle-America Trench off the Pacific coast of Guatemala, and the Cascadia continental margin off the Pacific coast of Canada.

It is well accepted that the elevated elastic properties of the gas hydrate bearing sediments is a key diagnostic feature for detection both from geophysical logs and seismic data. A fairly large number of gas hydrate characterization studies and quantitative estimation were done based on abnormally high P-wave velocity/impedance estimation from both geophysical logging and/or seismic inversion results (Lu, 2001, Ecker et al. 2000, Helgerud et al., 1999) through either empirical relations or rock physical models of gas hydrates.
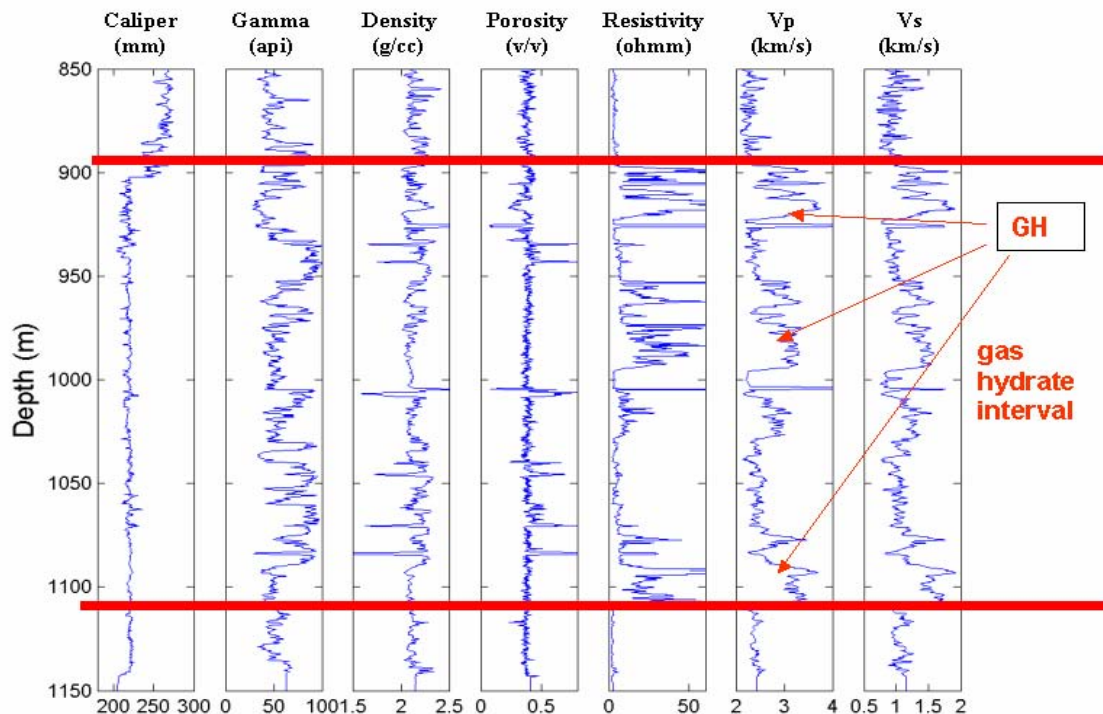
Figure D.2. Log curves of Mallik 2L-38 of Mackenzie River Delta, northern Canada. The hydrates zone is between the red lines. Columns 6 and 7 are the P-wave and S-wave velocities (km/s) measured from the well, both of which show dramatic increases at the gas hydrate interval.
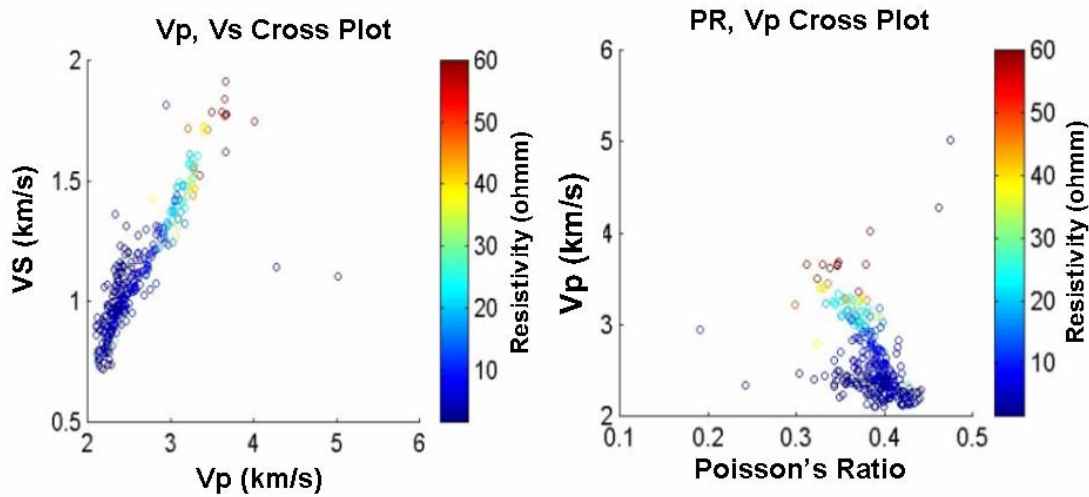
Figure D.3. Crossplots of S-wave and P-wave velocities (left panel), and P-wave velocity with Poisson's ratio (right panel). The color-coding are the resistivity values. Gas hydrate samples are shown by the high resistivity readings as indicated by the bright (yellow and red) color, revealing both high P-wave and S-wave velocities at the left panel and slightly lower Poisson's ratio at the right panel for the gas hydrate interval.
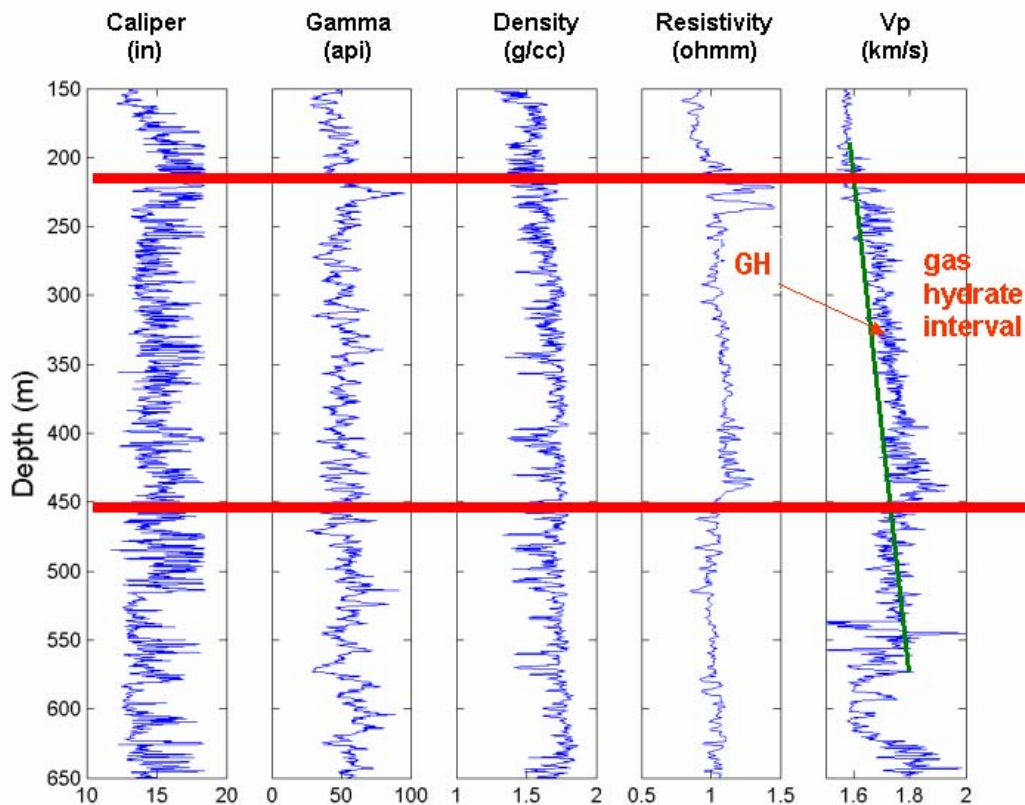

Figure D.4. Log curves of ODP 164-995B at Blake Ridge, Atlantic Ocean, USA. Gas hydrate zone is between the thick red lines. Note the P-wave velocity increase at the gas hydrate interval relative to the velocity trend (green line, panel 5). The resistivity curve as shown in panel 4 shows increases in the hydrate interval.

66

Although It is known that gas hydrates will increase the elastic properties of the gas hydrate bearing sediments, exactly how microscopically the gas hydrates are distributed with the host rocks, and how that will affect the elastic properties of the host rocks, have been subjects of intensive investigation. At this time, results remain inconclusive, although there exists a variety of gas hydrates rock physics models and empirical relationships. However, there are still large variations among these model predictions. It is clear then that a practical model must be carefully chosen or derived to quantitatively estimate the volume of gas hydrates present in the sediments.

D.1.4 Existing gas hydrates rock physical models

Results of recent gas hydrate drillings worldwide, such as the Mallik 2L-38 well in Northern Canada and Ocean Drilling Program's (ODP) Leg 164 wells at Blake Ridge on the Atlantic coast as previously mentioned, have demonstrated a consistent relationship between the rock elastic properties and gas hydrate saturations in the sediments. As a basic relationship, higher concentrations of gas hydrate yield increases in the rock's elastic properties.

There are a number of rock physics-based models in the literature that attempt to quantify this effect (Figure D.5). The cementation models of Dvorkin and Nur (1996, 1993) treat the grains as randomly packed spheres where the gas hydrates occur at the contact point (Model 1) or grow around the grains (Model 2). However, these models predict large increases in the elastic properties with only a small amount of gas hydrate, but stay relatively flat as the concentration of gas hydrate increases further. Models 3 and 4 are variations of the cementation models, but consider the gas hydrate as either a component of the load-bearing matrix or filling the pores (Dvorkin et al., 2003, Dvorkin et al., 1999, Helgerud et al., 1999, Ecker et al., 1998). Models 3 and 4 use the Hertz-Mindlin contact theory (Mindlin, 1949) to calculate dry rock moduli at critical porosity (35 to 40%). A modified lower Hashin-Shtrikman (HS) bound is used for porosity smaller than critical porosity, and a modified upper HS bound is used for porosities larger than critical porosity. The Gassmann equation is then used to derive the composite rock velocities. Model 5 is an inclusion-type model (based on Kuster and Toksoz, 1974) that treats gas hydrate and grains as the matrix and inclusions respectively, solving for elastic moduli of the system by iteratively solving either the inclusion-type or self-consistent type equations iteration (e.g., Zimmerman, 1991). Models 1 through 5 all consider gas hydrate as homogeneously distributed in the sediments. However, evidence of gas hydrate coring reveals that hydrates often exists as nodules and fracture fillings in the shallow shaly sediments. This geometry is illustrated in Model 6, although no quantitative treatment of this geometric model exists in the literature. Not illustrated in Figure D.5 are a series of empirical relations to describe the acoustic properties of gas hydrates (e.g., the weighted average equation by Lee et al, 1996, 1993). The advantage of an empirical relation is that it is based upon real observations and very simple to implement. However, empirical relationships are not necessarily valid in all geological settings or for rock properties different from where they were formulated.
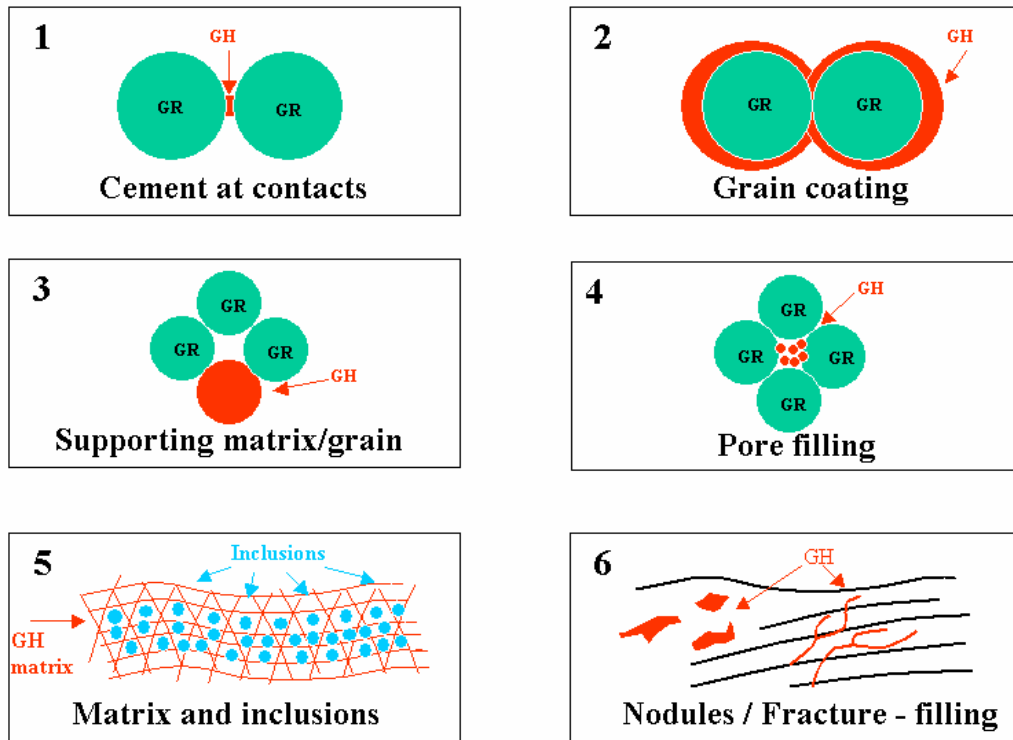
Figure D.5. Existing micro-structural models of gas hydrate bearing sediments (GR-grain; GH-gas hydrate).

Figures D.6 and D.7 display the P-wave and S-wave velocity estimations of all the models versus gas hydrate saturation that changes from 0 to 1 as a function of the volumetric fraction of porous space. These are calculated using identical input parameters that represent the average background properties of gas hydrate host rocks at the Mallik 2L-38 well. The background rock is assumed to a be quartz-grained sandstone with a porosity of 35%, a co-ordination number of 8.5, and a critical porosity of 38%. As indicated in these figures, the red dash and solid lines are the responses of Model 1 and 2 respectively (cementation models). Green dash and solid lines are the responses of Models 4 and 3 respectively (effective theory models). The pink solid line is the response of Model 5 (inclusion model). The blue triangles are the actual gas hydrate saturation-velocity pairs from Mallick 2L-38 well. The pink asterisks are the second-order least-square regression result of the gas hydrate saturation-velocity pairs of the Mallik 2L-38 well (blue triangles). The models (colored lines) are compared to the actual well data (blue triangles). Note that the prediction of model 3 closely follows the blue triangles for both the P-wave and S-wave data.
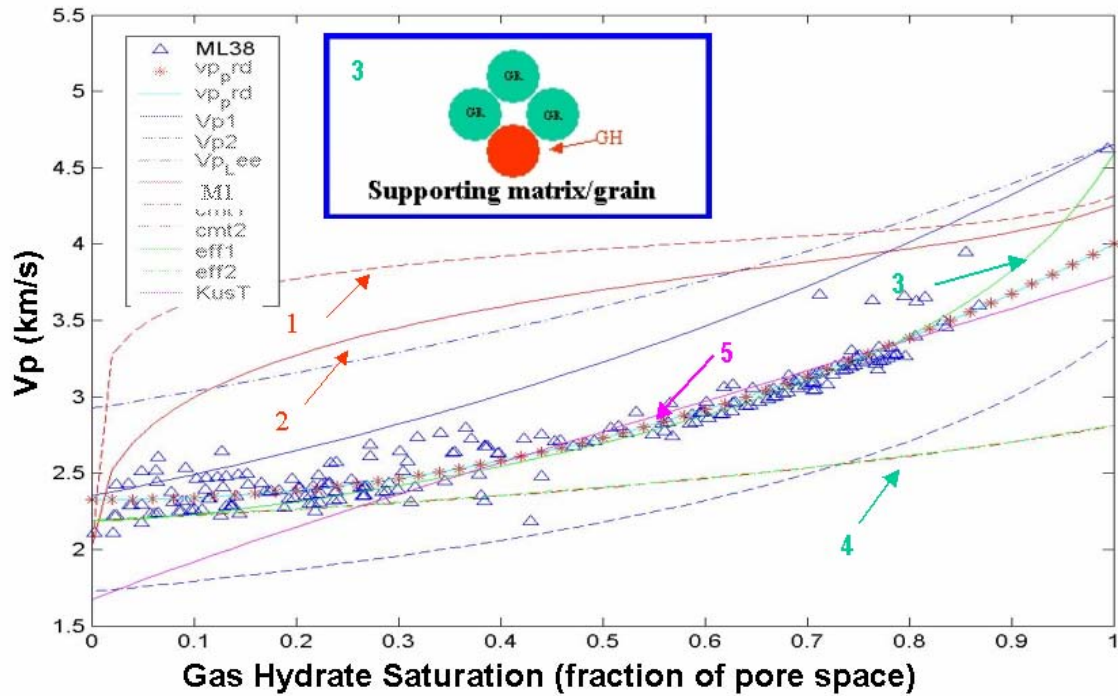
Figure D.6. P-wave velocities versus gas hydrate saturation for the rock physics models shown in Figure D.5. Model 3 (inset) is the best model that matches the gas hydrate saturation at the Mallik 2L-38 well.

Figure D.7. S-wave velocity versus gas hydrate saturation for the rock physics models shown in Figure D.5. Model 3 (inset) is the best model that matches the gas hydrate saturation at the Mallik 2L-38 well.
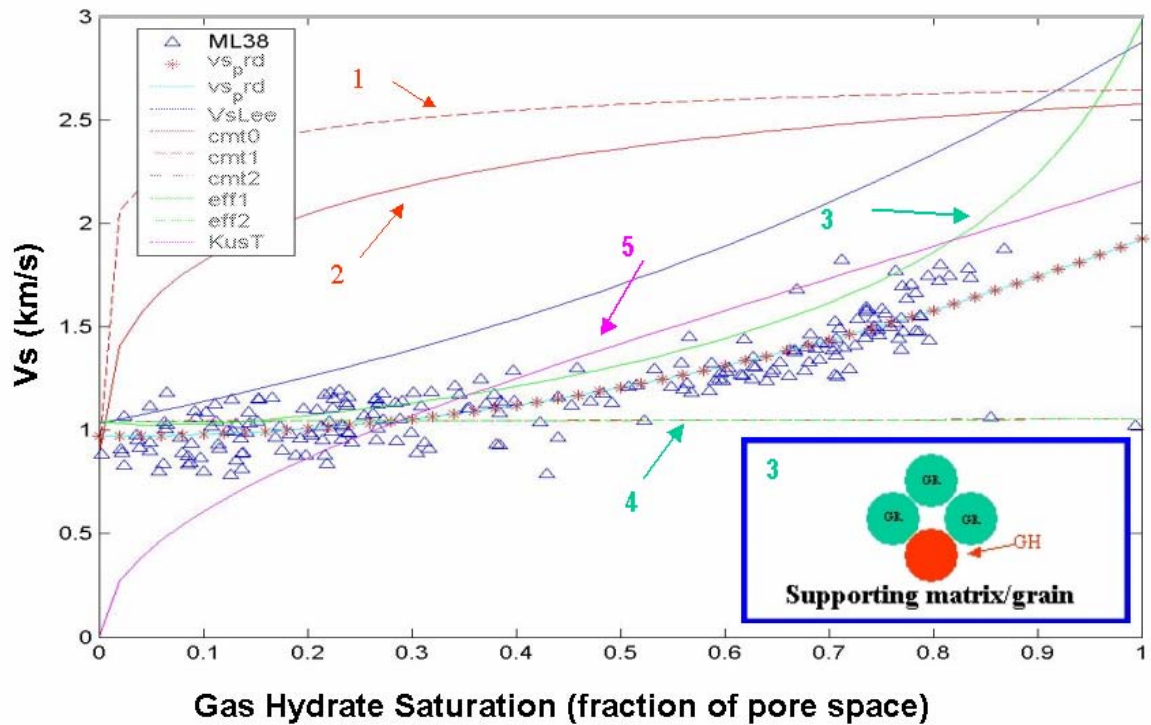
From Figures D.6 and D.7 we observe that there exist large variations in the relationship between velocity and gas hydrate saturation among the existing gas hydrate rock physical models. However, model 3 tends to best match the gas hydrate saturation data from Mallik 2L-38 well. As will be discussed in the next section, this model also accurately predicts the P-wave velocity at Leg 164-995B borehole of Blake Ridge. Therefore, we adopted this model for our modeling work and gas hydrate estimation using seismic data. It must be noted, however, that this model tends to overestimate S-wave velocity at high gas hydrate saturation (Figure D.7). It is also sensitive to the choice of co-ordination number, critical porosity, and component elastic properties.

Shaliness is a predominant characteristic of sediments in Gulf of Mexico, and is especially true for those at shallow burial depths. The effect of shaliness on rock properties, such as porosity and bulk density, are well noted. Shale content also has an effect upon the elastic properties, such as velocity. Model 3 treats shale and shale-related porosities indiscriminately, grouping them together with sand grains. This may cause errors in predicting elastic properties of shaly sand rocks. Xu and White (1995) developed a shaly sand model that predict P-wave and S-wave velocities given the shale and sand properties, volumetric fraction and aspect ratio of the related pores. The model has demonstrated some successful applications and can be a good alternative for modeling gas hydrates in shaly sand environments.

D.1.5 Gas hydrate stability zone and its prediction

Gas hydrates are formed at high pore pressures and low temperatures. The gas hydrate stability zone (GHSZ) refers to the interval in which gas hydrates can be generated and are stable. The GHSZ range is therefore determined by water depth at the location, seafloor temperature, thermal gradient, and gas composition. There also exist some compounds in the fluid, such as salinity, that inhibit or aid the formation of gas hydrates. Figure D.8 shows the phase curves of pure methane (dark blue color) and two gas vent samples from Green Canyon (GC, green color) and Mississippi Canyon (MC, red color). It can be observed from the figure that as the water depth (vertical axis) increases, the temperature threshold for gas hydrate also increases. At similar water depths, the temperature thresholds for gas samples at GC and MC, which contain other gases in addition to methane, are higher than that of pure methane as they possess larger size gas molecules. Knowing water depth and thermal gradient at a location, the GHSZ can be estimated by finding the seafloor temperature (black curve, Figure D.8) and drawing a straight line with the appropriate thermal gradient. The depth at which the straight thermal gradient line intersects the gas hydrate phase curve represents the deepest depth at which gas hydrate can be formed with a given composition of gas. The two parallel cyan and purple colored straight lines with a thermal gradient of 25°C/km, represent the GHSZ at Green Canyon, Atwater Valley and Keathley Canyon regions. It can be seen that the predicted GHSZs are within 500 m below the seafloor for Green Canyon, and over 500 m, but no more than 1000 m below the seafloor, for Atwater Valley and Keathley Canyon regions. The cross plot of GHSZ intervals with water depth (Figure D.9) is based on the three phase curves as shown in Figure D.8, assuming a thermal gradient of 25°C/km. GHSZ intervals (vertical axis) can be conveniently estimated through Figure D.9, knowing water depth (horizontal axis) of the location.
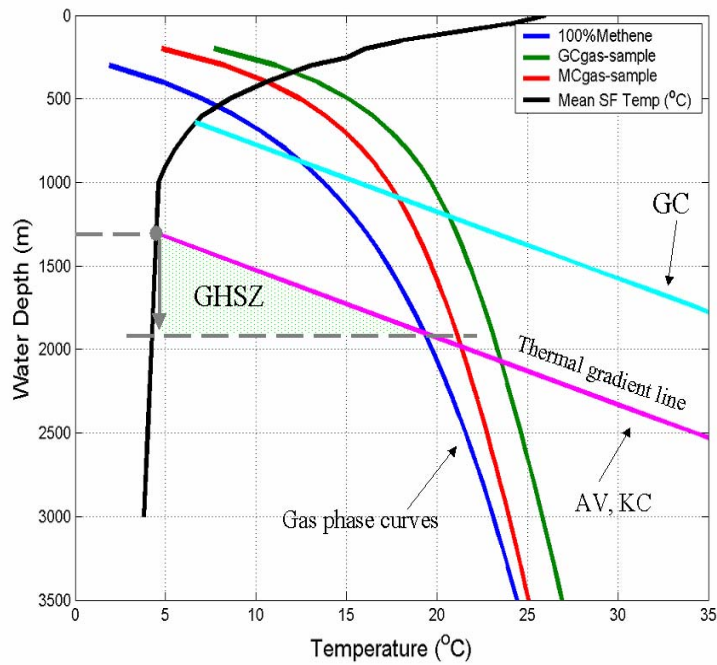
Figure D.8. Prediction of gas hydrate stability zone in the deepwater Gulf of Mexico. The colored curves (blue, red, and green) are the phase curves of the three gas samples using methods of Sloan (1998) and the black curve is the seafloor temperature from NOAA (2002). The parallel straight lines represent the thermal gradient of 25°C/km (GC-Green Canyon, AV-Atwater Valley, KC-Keathley Canyon).
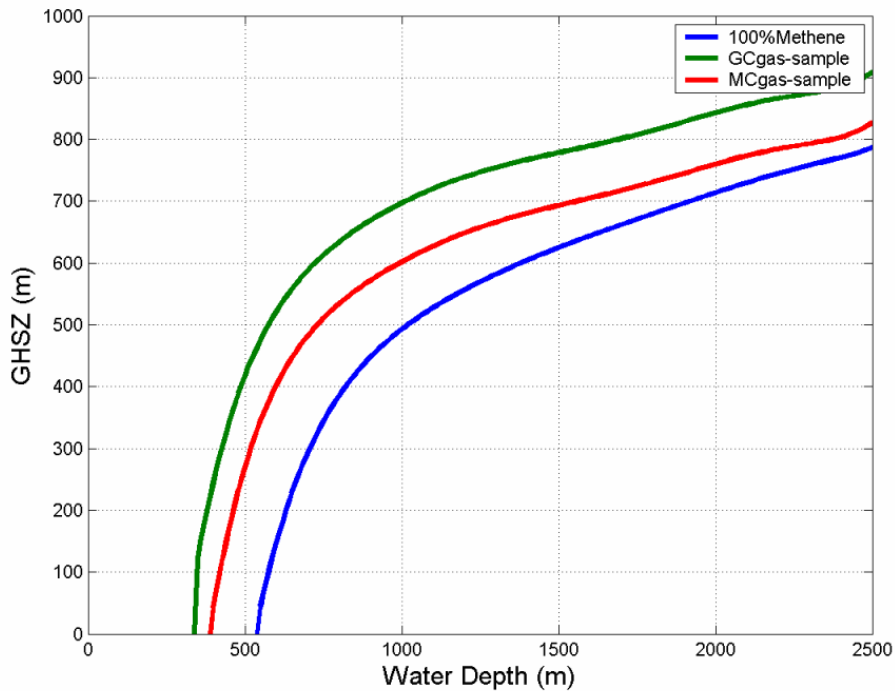

Figure D.9. Gas hydrate stability zone charts. The horizontal axis is water depth and the vertical axis is the GHSZ interval, assuming an average thermal gradient of 2.5^{o}C/100 m.

71

In comparison with the few known (possible) BSRs, such as the one in Keathley Canyon, Alaminos Canyon, and East Breaks region in GOM, the GHSZ estimations shown here all suggest deeper values than what have actually been seen by these BSRs. As the water depth and seafloor temperature are fairly well defined, and the thermal gradient (2.5°C/100) used is at the high end of conventional values in the GOM, the over estimation of GHSZ is thought to be caused by the non-linear shallow sediment thermal gradient. In other words, the shallow thermal gradient is probably much larger than the average value, resulting in a smaller GHSZ thickness than conventionally estimated. If the thermal gradient used in the estimation is correct, then the remaining possible reason is the existence of gas hydrate inhibitors in the porous fluid. However, this is less likely. Further studies of shallow thermal gradient profile need be done to better constrain the GHSZ prediction.

D.1.6 Sediment properties at shallow depth

It can be observed form GHSZ charts (Figures D.10 and D.11) that the gas hydrates are only stable at a very shallow interval below the seafloor, normally less than 500 m. The BSR seen at Keathley Cannon is approximately 500 ms below mudline (BML), or about 400 m BML. For gas hydrate studies, the zone of interest is usually within 1000 m BML, and even more likely within 500 m BML.

Rock properties, such as porosity, density, P-wave and S-wave velocities are extremely variant at shallow depths. Porosity for shales at shallow burial depths can range from 80% at the seafloor to less than 40% at 500 BML where compaction becomes greater. Figures D.10-D.11 below show the range of rock properties within the first 1000 m of the sediments BML. Because gas hydrates in the GOM are found in the near sea-floor sediments where shales make up a large percentage of those sediments, burial depth and porosity relationships serve to further illustrate that understanding the shallow rock properties is essential for gas hydrates delineation and volume estimation.
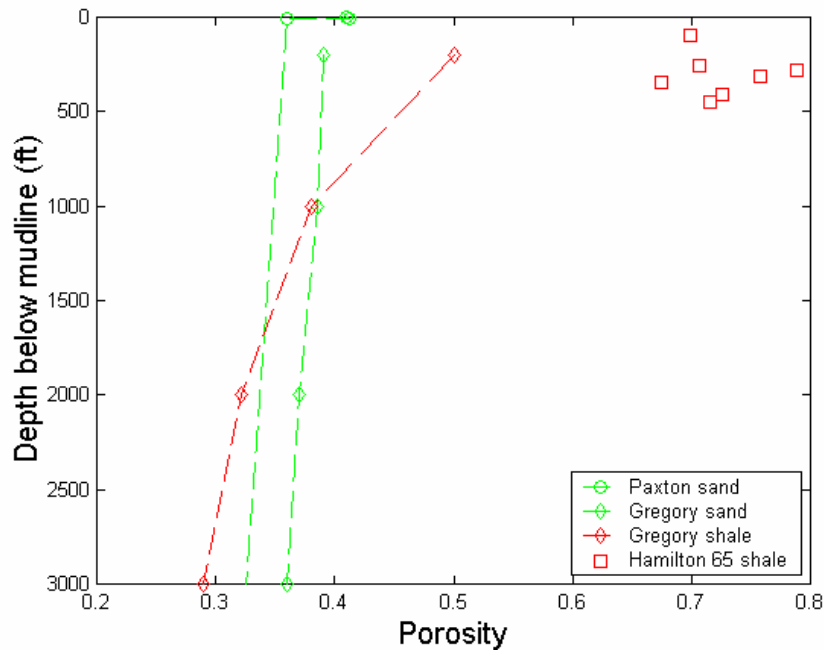

Figure D.10. GOM shales and sands (Gregory, 1977), rigid sand global (Paxton et al., 2002), and Hamilton's data (1965) showing porosity at the first few thousand feet BML.
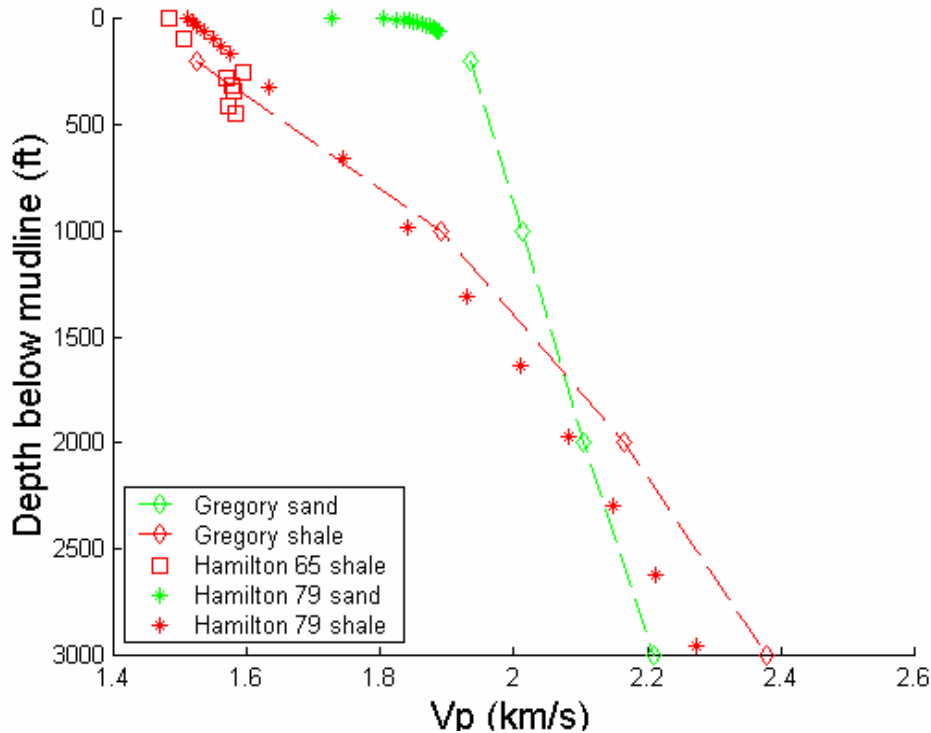
Figure D.11. GOM shales(Gregory, 1977), Rigid sand global(right panel, Paxton et al., 2002), and Hamilton's data (1965, 1971) showing Vp at the first few thousand feet BML.

D.2 Prediction and verification of gas hydrate model: ODP Leg 164-995B

By understanding the porosity-depth trend at shallow depths due to compaction, and by using appropriate velocity-porosity models at shallow depths, a background rock physics trend can be constructed. Further, using the gas hydrate rock physics model (Model 3) discussed earlier, velocities for different gas hydrate saturations can be predicted. This was done for the Blake Ridge well 995B, matching the P-wave velocities measured at the well very closely. Results are shown in Figure D.12. The blocky colored lines in the Vp column are the replacement curves for different gas hydrate saturations through gas hydrate rock physical model (Model 3). The P-wave measurement lies mostly within the 10% gas hydrate saturation line and occasionally between 10-20% at the base of gas hydrate zone, which is in good agreement with the estimations from several other means published in the literature. Panel 3 shows the S-wave estimation based on the P-wave measurement and estimation of Vp/Vs ratio predicted by Model 3. Panel 4 shows the bulk density variation with different gas hydrates saturations. The bulk density decreases as the gas hydrate saturation increases due to the lighter density of the gas hydrate compared to the fluid. However, the effect is negligible.
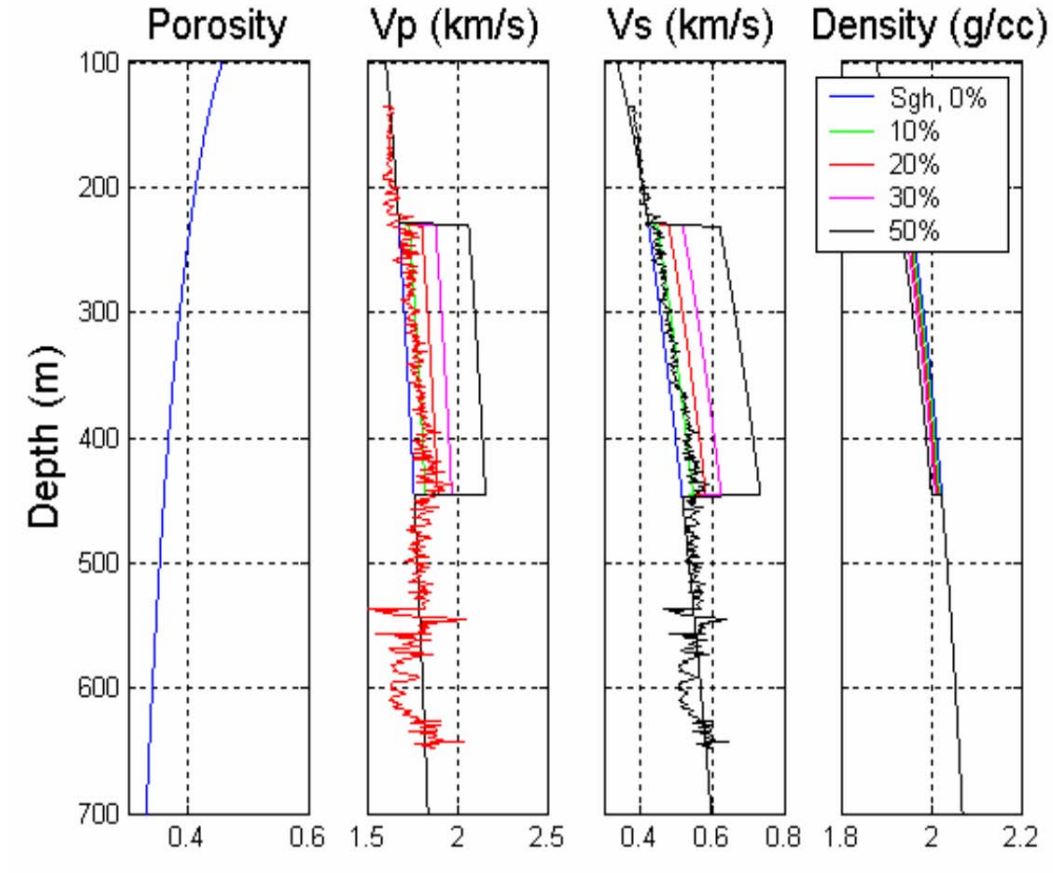
Figure D.12.   Gas hydrate modeling at ODP Leg164-995B, Blake Ridge.

D.3 Geophysical modeling of gas hydrate

The objective of geophysical modeling is to produce a full-waveform seismic response of a geological model that contains gas hydrate bearing sediments so as to understand the seismic signature for recognition and prediction. This process is composed of model construction and actual modeling.

D.3.1 Construction of multilayer gas hydrate models and AVO modeling

Based on the understanding of petrophysical properties of gas hydrate bearing sediments and shallow rock properties as discussed above, four simplified multi-layered models were constructed for one-dimensional full-waveform prestack modeling.   Models 1 and 2 are constructed with 4 layers, starting with a 0.5 km water layer, below which is a 0.2 km shallow sediment layer, a 0.3 km gas hydrate bearing sediment layer (10% hydrate saturation for Model 1, and 30% hydrate saturation for model 2), followed by a 0.3 km shallow sediment layer of same property as layer 2. These same models were also used in AVO model testing. Figure D.13 lists the properties of both models.

74

	P-wave (km/s)	S-wave (km/s)	Density (g/cc)	Thickness (km)
Water	1.485	0	1.036	0.5
Background	1.787	0.543	2.036	0.2
GH (10%), Model 1	1.854	0.583	2.031	0.3
(30%), Model 2	2.015	0.670	2.021	0.3
Background	1.787	0.543	2.036	0.3

Figure D.13. Properties of 4-layer gas hydrate models 1 and 2.

Figure D.14 shows the images of models 1 and 2 (upper panel) and their corresponding AVO response at the interface on top of the gas hydrate layer (lower panel). These two models do not contain basal gas at the base of the gas hydrates zone (no-BSR). The AVO plots (lower panel) displays the P-wave reflectivity (Rpp) versus the angle of incidence that changes from 0 to 40 degrees. Both AVO plots show small positive values at zero offset and a fairly flat AVO response for all the angles.
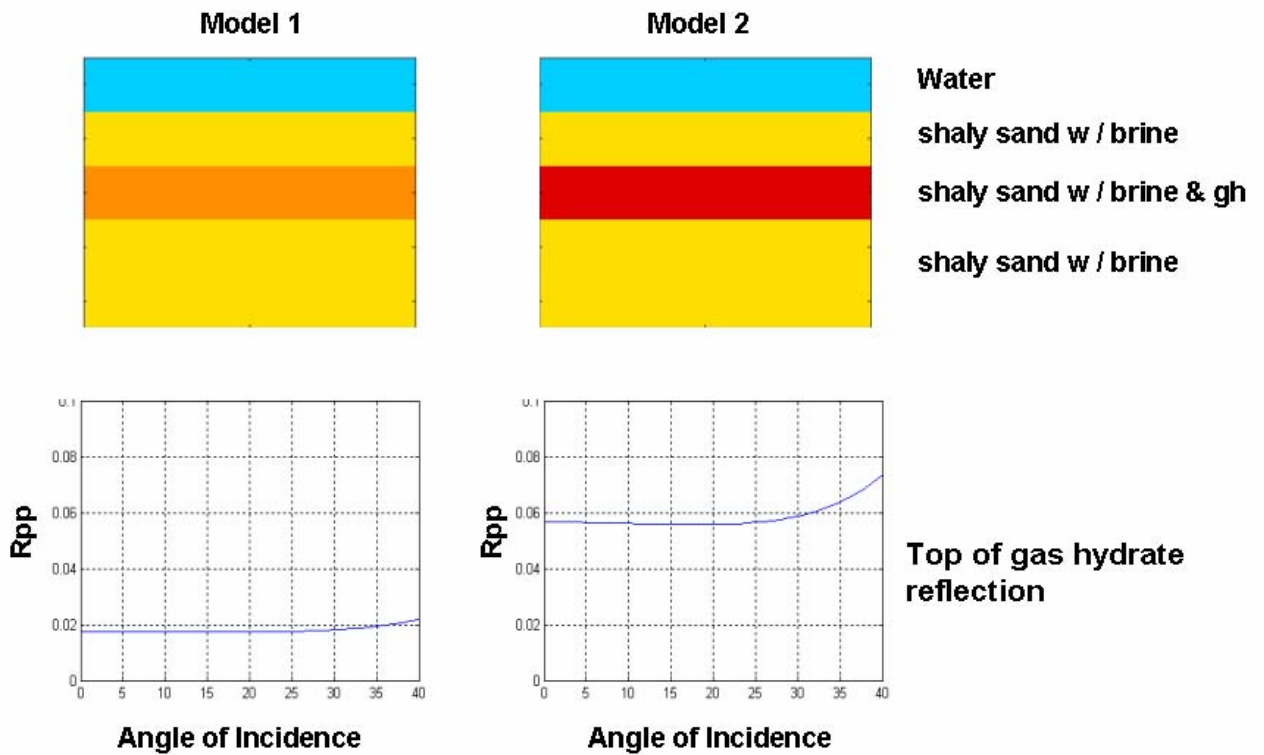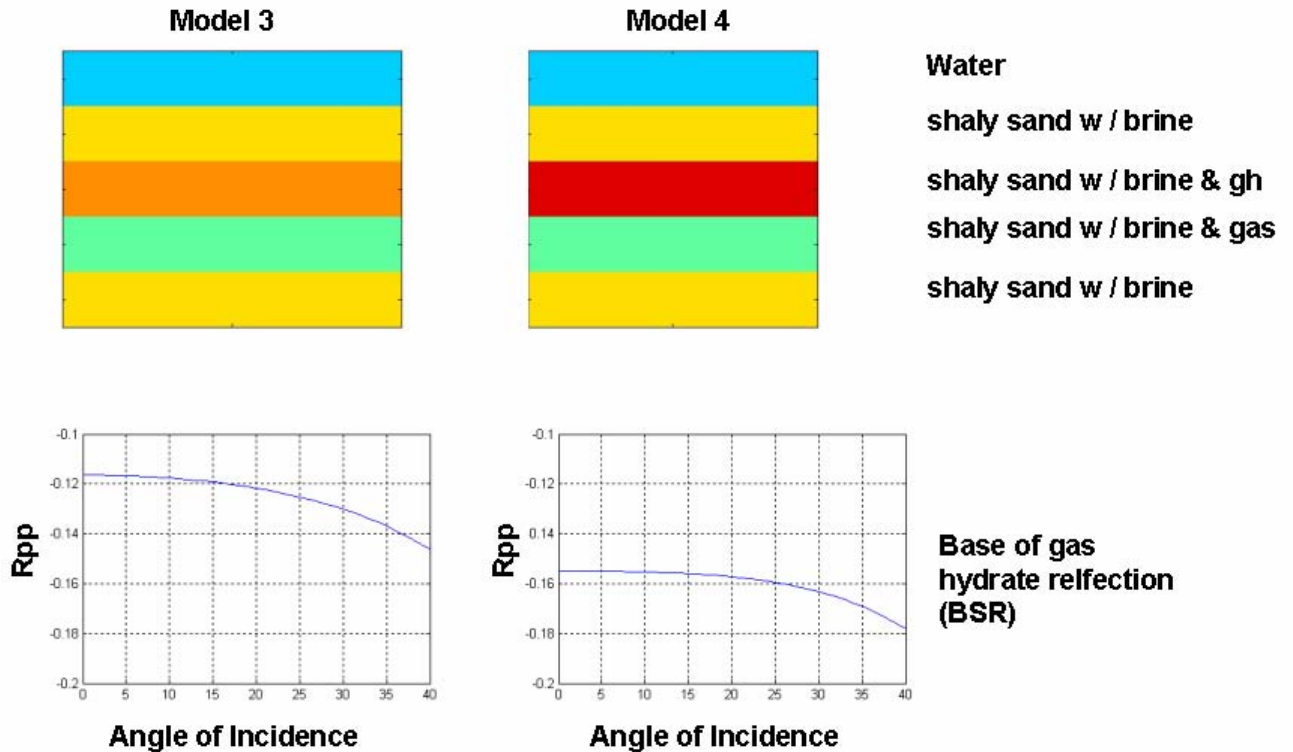

Figure D.14. Geological model and AVO response of two no-free-gas 4-layer gas hydrate models. Model 1 contains 10% gas hydrate, model 2 contains 30% gas hydrate.

	P-wave (km/s)	S-wave (km/s)	Density (km/s)	Thickness (km)
Water	1.485	0	1.036	0.5
Background	1.787	0.543	2.036	0.2
GH (10%), Model 3	1.854	0.583	2.031	0.3
(30%), Model 4	2.015	0.670	2.021	0.3
Basal Gas	1.616	0.576	1.85	0.3
Background	1.787	0.543	2.036	0.3

Figure D.15. Properties of 5-layer gas hydrate models 3 and 4.

Figure D.16 shows the images of models 3 and 4 (corresponding to data in Figure D.15), in which a layer of gas hydrate with 10%, and 30% saturation is intercalated in the background below the seafloor, and a 300-meter thick basal gas zone is inserted at the base of the gas hydrate zone (BSR). The addition of the gas results in the 5-layer model. The lower panel displays the AVO response at the base of the gas hydrates zone (BSR), which shows a large negative reflection coefficient at zero offset with high AVO gradients. This is a typical class III reflection.

Figure D.16. Geological model and AVO response of two free-gas 5-layer gas hydrate models. Model 3 contains 10% gas hydrate, model 4 contains 30% gas hydrate.

Figure D.17 shows a comparison of the gas hydrate AVO responses (red and green lines) with other typical types. The three AVO class responses are represented by the blue lines.

It must be noted that the four models discussed so far simulate gas hydrate behavior at the Blake Ridge area. Here, gas hydrates show an elastic anomaly from the background trend with a small elastic property contrast (usually less than 10% difference). These models display a small

positive reflectivity at the near offset and a flat AVO response. In the case of the layered gas hydrate occurrence as penetrated by the Mallik 2L 38 well, as well as in the wells in the Nankai Trough, larger property contrasts exist at the gas hydrate interface. In this case, large positive near offset reflectivity and gradient is expected, which is typical of a type 1 AVO response. Shallow sediments of the GOM are considered shalier, and may not manifest a significant contrast between sands and shales (personal communication with Dutta, 2003).
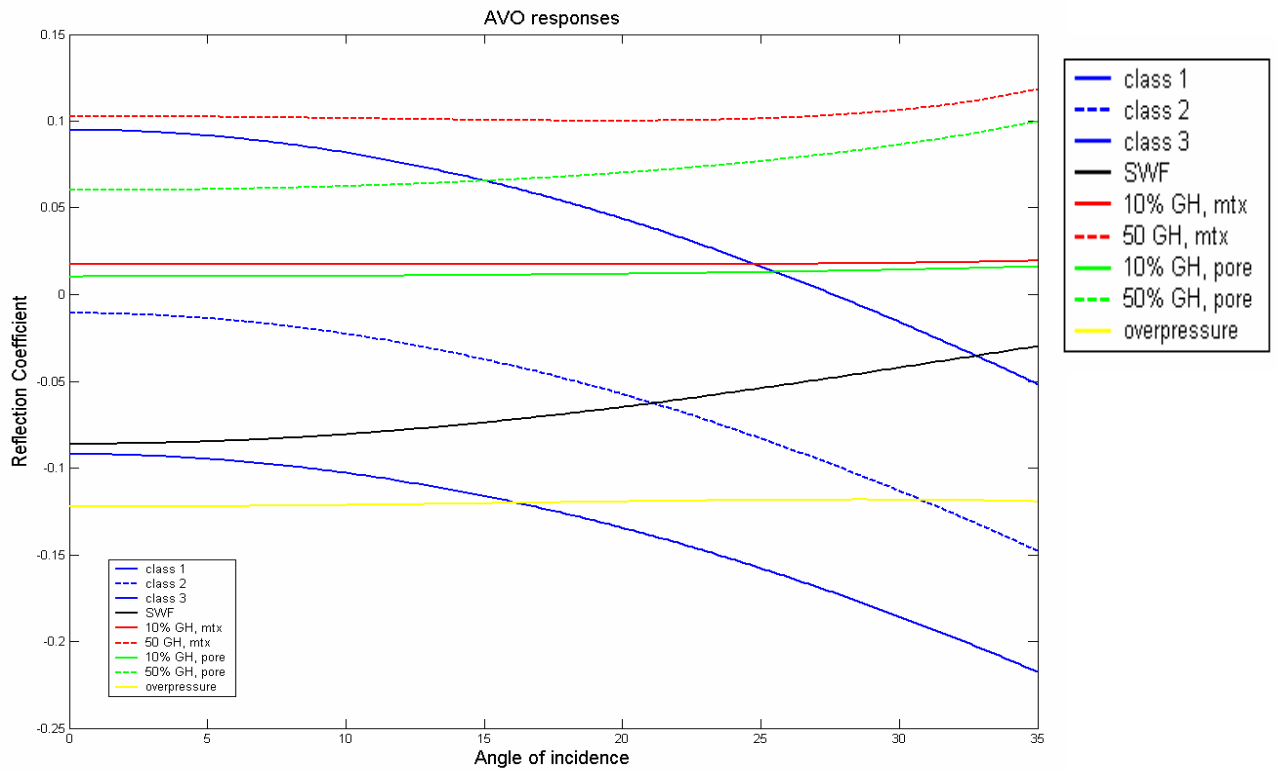
Figure D.17. Typical AVO responses to gas hydrate sediments

D.3.2 One-dimensional full-waveform prestack modeling

Full-waveform prestack seismic responses of these four models were generated using ANIVEC, a reflectivity method based on an elastic forward modeling algorithm. The shot and receivers were placed beneath water level, hence simulating a streamer situation. Each gather contains 47 traces, with the nearest trace offset at 0.4 km, the farthest trace offset at 6.15 km and a trace interval of 0.125 km. The angle coverage (angle of incidence) reaches approximately 60 degrees for the gas hydrate intervals of the models.

Figure D.18 shows full-waveform prestack responses to model 1 and model 2 of Figure D.14. Both show a strong reflection at the seafloor. Model 2 displays stronger reflection at both the top and the base of gas hydrates due to high gas hydrate saturation, while the indications of gas hydrate of model 1 are not as obvious. This relationship provided the basis for quantitative estimation using seismic amplitude information.

Figure D.19 shows full-waveform prestack responses to model 3 and model 4 of Figure D.16. Except for a strong reflection event at the seafloor, both possess strong amplitude events at the base of the gas hydrates zone due to the presence of free gas below. These are the BSR, which show opposite amplitude polarity relative to the seafloor reflection, and with magnitude comparable to that of the seafloor.
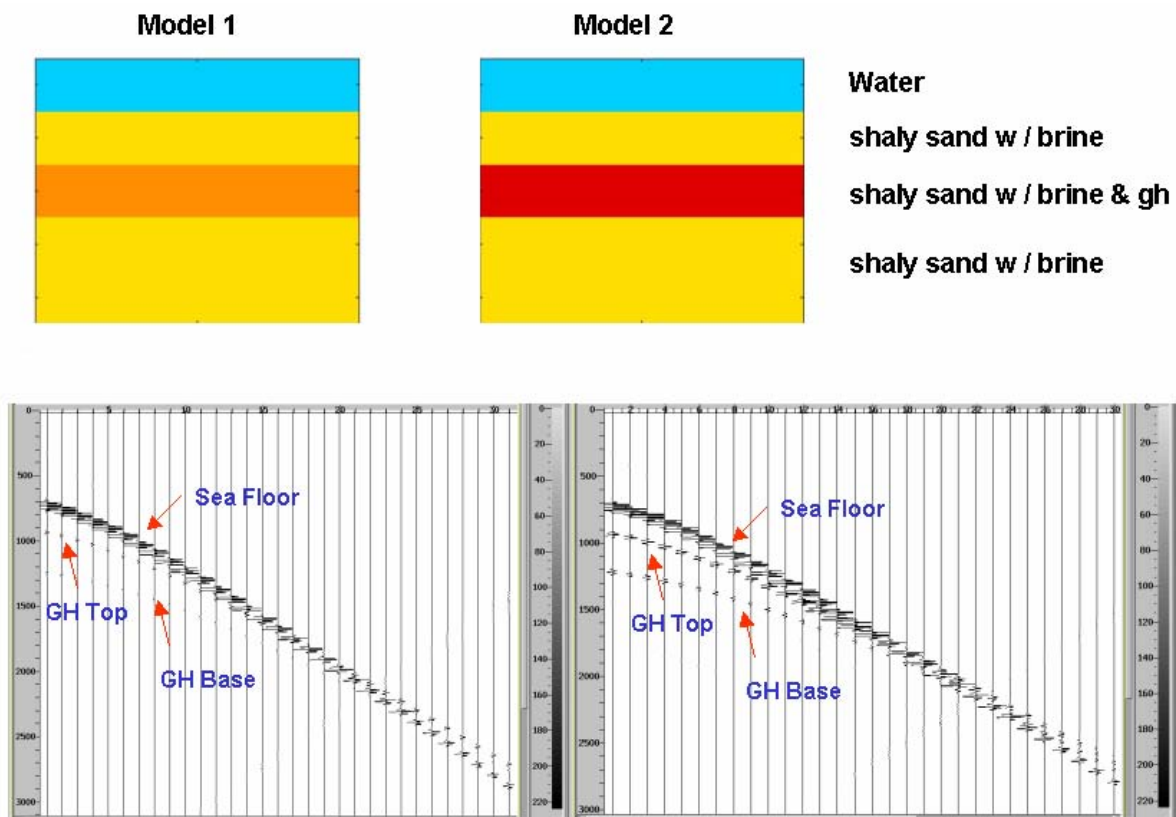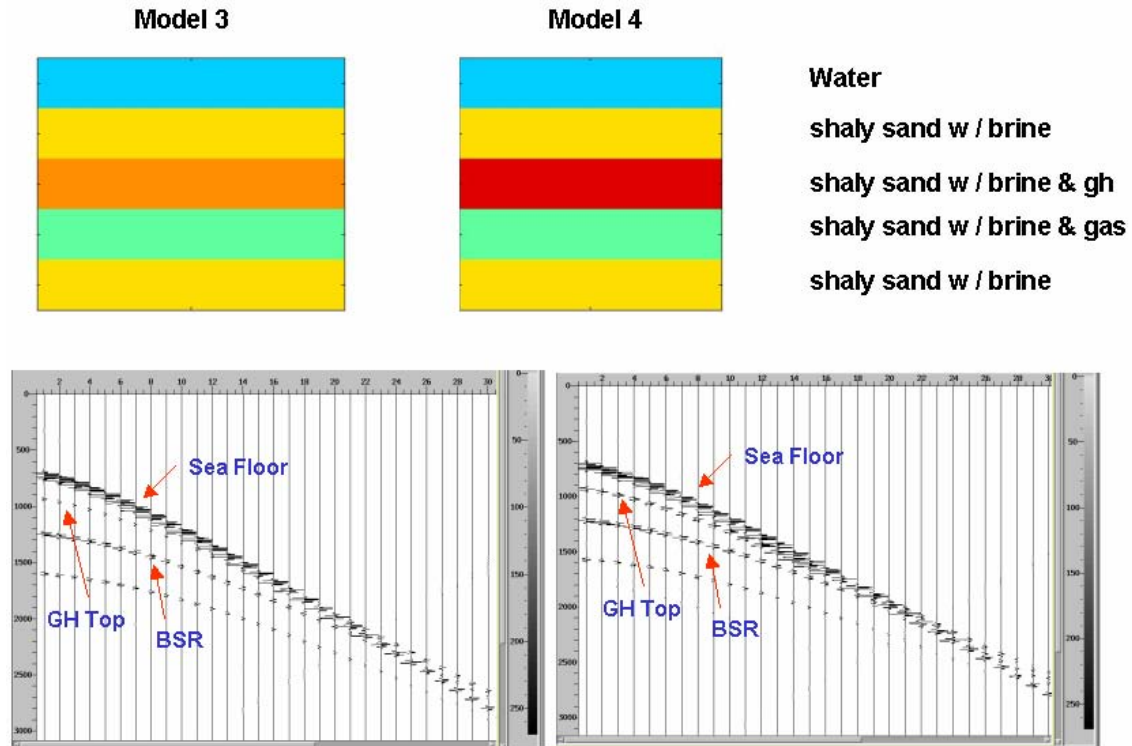

Figure D.18. Full-waveform prestack response of two no-free-gas 4-layer models. Model 1 contains 10% gas hydrate, model 2 contains 30% gas hydrate.

Figure D.19. Full-waveform prestack response of two free-gas 5-layer models. Model 3 contains 10% gas hydrate, model 4 contains 30% gas hydrate.

D.4 Rock elastic property inversion

Gas hydrate rock physical properties, rock physics-based models, and model responses were discussed in the previous sections. This section covers the derivation of rock elastic properties from seismic information. It also contains discussion about the spatially continuous velocity analysis (SCVA), full-waveform prestack inversion (FWPI) and hybrid inversion of the seismic volumes under study.

D.4.1 Spatially Continuous Velocity Analysis (SCVA)/ Automated Velocity Model Building (AVMB)

SCVA/AVMB is a process developed by WesternGeco to automatically update high-resolution 2D and 3D interval velocity models from seismic data. A proprietary automated velocity picker, SCVA (Spatially Continuous Velocity Analysis), generates a spatially continuous stacking velocity field based on semblance-style stacking correlations and picked horizons generated from the seismic data. AVMB uses a constrained least squares regression method to generate interval velocities that best match the computed stacking velocities. Laterally cascaded median smoothing is used to preserve any lateral velocity discontinuities within the data according to user specified resolution criteria. The SCVA / AVMB methodology is quality controlled by human intervention at key steps. This is done by comparing results with those from the semblance analysis procedure (IVP), which was carried out during the data processing procedures.

Figure D.20 shows east-west line 5700 extracted from the Keathley Canyon 195 area. The lower panel shows the P-impedance response from the full-wave inversion, and the top panel shows the corresponding SCVA result. While the BSR is not readily evident in the velocity field (top panel), several anomalous zones (middle and left-center) can be seen in the area of the GHSZ. SCVA 3-D volumes are available for both the Keathley Canyon and Atwater Valley study areas.
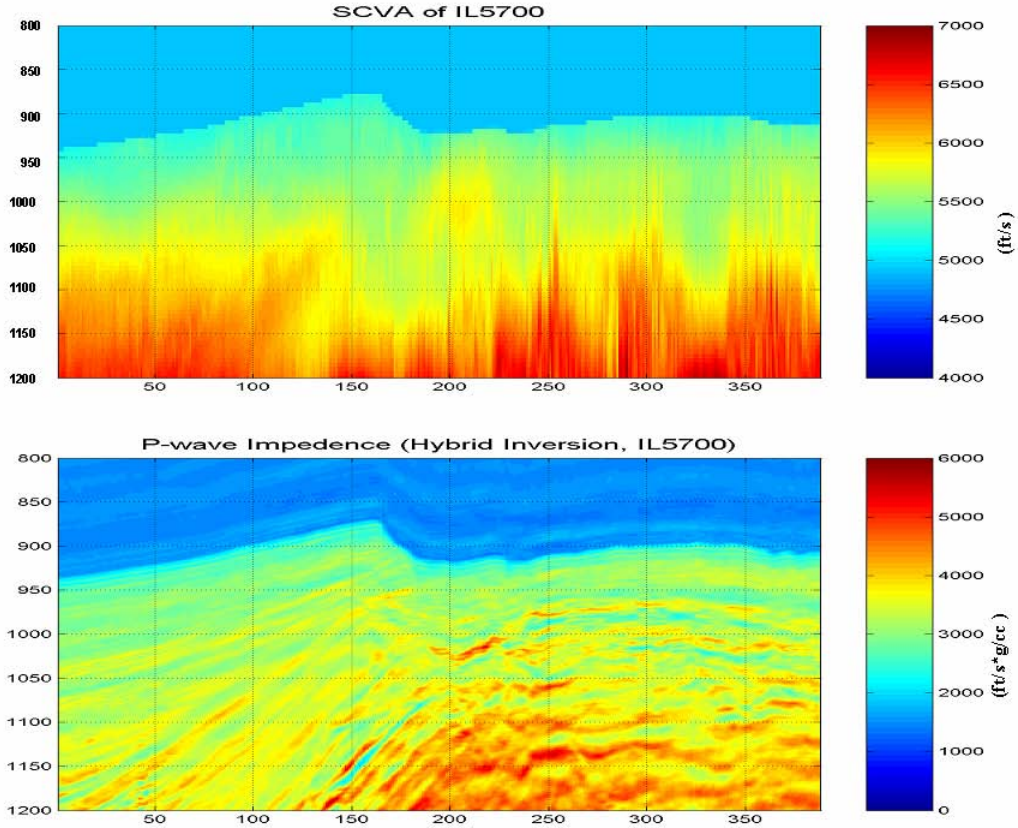

Figure D.20 SCVA result and P-impedance derived from hybrid inversion for line 5700 in the Keathley Canyon 195 area. Vertical axis is one-way travel time.

D.4.2 Full-waveform Prestack Inversion

D.4.2.1 Introduction

Full-waveform prestack inversion (FWPI) using a genetic algorithm based on methodology by Mallick (1995, 1999), was used to estimate 1-D elastic models (Vp, Vs, Poisson's ratio and density) at selected locations over Green Canyon Block 184/185, Keathley Canyon Block 195 and Atwater Valley Block 14. These estimated elastic models were then used as pseudo-well logs to interpret the potential presence of hydrates and for background low frequency (0-8 Hz) impedance trends for hybrid inversion (Mallick et al., 2000).

D.4.2.2 Inversion

The primary advantage of using full-waveform prestack inversion is the ability to use the full-wave equation-based forward modeling [reflectivity method: Frasier (1970), Fuch and Muller (1971), Kind (1976), and Kennett (1983)] on a discrete (thin), layer-based model. This allows the inversion process to account for tuning effects, the interference of multiples and converted waves, and the reflection and transmission effects due to the velocity gradients.

The full-waveform prestack inversion process begins with the generation of a random population of elastic earth models (Vp, Poisson's ratio or Vs and density) within specified search intervals from the initial model. The next step is an iterative process that matches the computed synthetic CMP gather to the actual CMP gather. Finally, a subsequent modification of the model is made until the best match between the synthetic and the data is achieved. The algorithm finds the minimum misfit between the synthetic and the actual gather by following a biological evolution process, in which the elastic models (chromosomes) are coded in binary form, undergo genetic processes of selection, reproduction, crossover and mutation. A more detailed description of the processes is given in Stoffa and Sen (1991), Sen and Stoffa (1992), Mallick (1992a,b, 1993a) and Mallick (1999).

In this project, the initial models for the Vp were constructed based on stacking velocities, which are subsequently used to derive the initial models for Poisson's ratio and density using the background rock model trend that relates Vp, Vs and density. For additional information regarding the physical rock model used, please refer to the previous Section D.1.4. The zone of interest ranges from the water bottom to approximately 500 ms TWT BML (below mudline). The time window for the inversion process is set to 1024 ms, beginning from 50 ms above the water bottom reflector.

The prestack inversion was divided into two phases. The first phase used a thick (~9-11 m) discrete layer and wide search intervals (10% for Vp, 10% for Poisson's ratio and 2% for density). The second phase, which was a refinement of the first phase, used the results from the first phase inversion for the initial models with thin discrete layers (~4-6 m) and narrow search intervals (2% for Vp, 2% for Poisson's ratio and 1% for density). The final output is an elastic model (pseudo-logs) of Vp, Vs, Poisson's ratio and density. More details of the individual inversion results for Green Canyon, Atwater Valley and Keathley Canyon are given in appendices A - C.

D.4.2.3 Sensitivity of Prestack Inversion Process for Hydrates – Synthetic Models

How reliable are the results from the FWPI process? To answer this question, we designed tests using synthetic models. The models represent two possible hydrate configurations: A hydrate layer underlain by a gas sand layer (models 3 and 4 in Section D.3) and a hydrate layer underlain by a wet sand layer for both 30% and 10% hydrate saturations (models 1 and 2 in Section D.3).

As discussed in section D.3.2, the synthetic seismic responses for these models were generated using ANIVEC, a reflectivity method based on an elastic forward modeling algorithm. The inversion results of these models are shown in Figures D.21 through D.24. The results indicate that the prestack inversion on the hydrate models is more sensitive to Vp and consequently, can more reasonably estimate accurate Vp as opposed to Poisson's ratio and density. The error bars, shown as yellow bars in each figure, measure the level of uncertainty, or standard deviations (posterior model covariance matrix), in the estimation of the elastic model parameters in the statistical (Monte Carlo type) optimization process of the FWPI. The large standard deviations in estimating Poisson's ratio and density relative to the variation of the parameters itself imply Poisson's ratio and density are less resolvable in the inversion process.

81

Figure D.21 Inversion result for 30% gas hydrate saturation (Model 4-wet sand, hydrate, gas sand).

Figure D.22 Inversion result for 30% gas hydrate saturation (Model 2-wet sand, hydrate, wet sand).

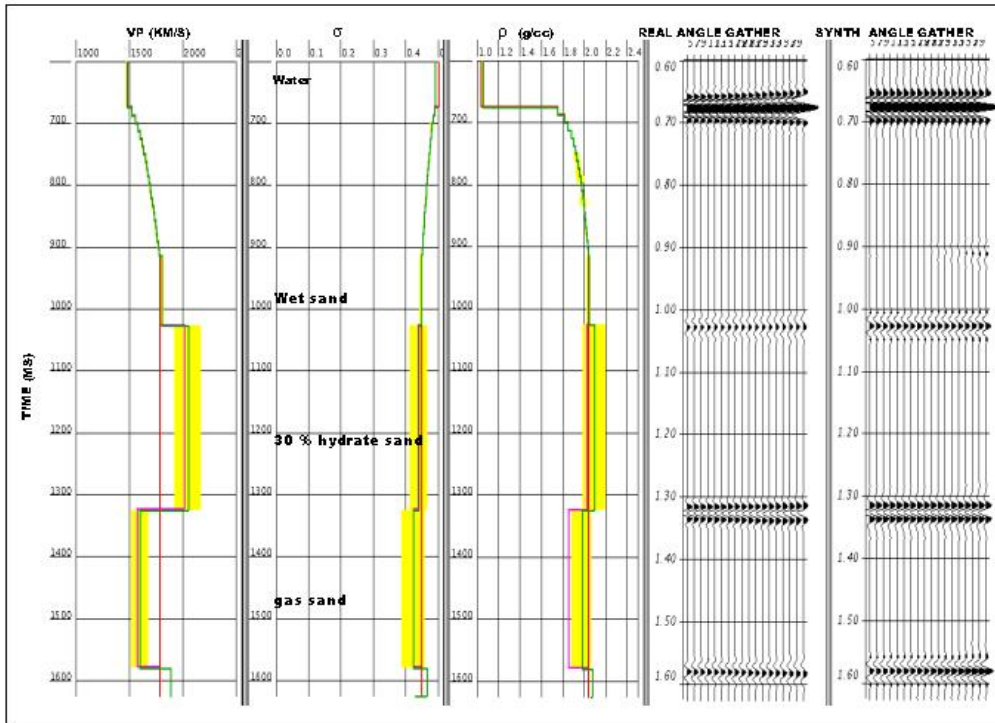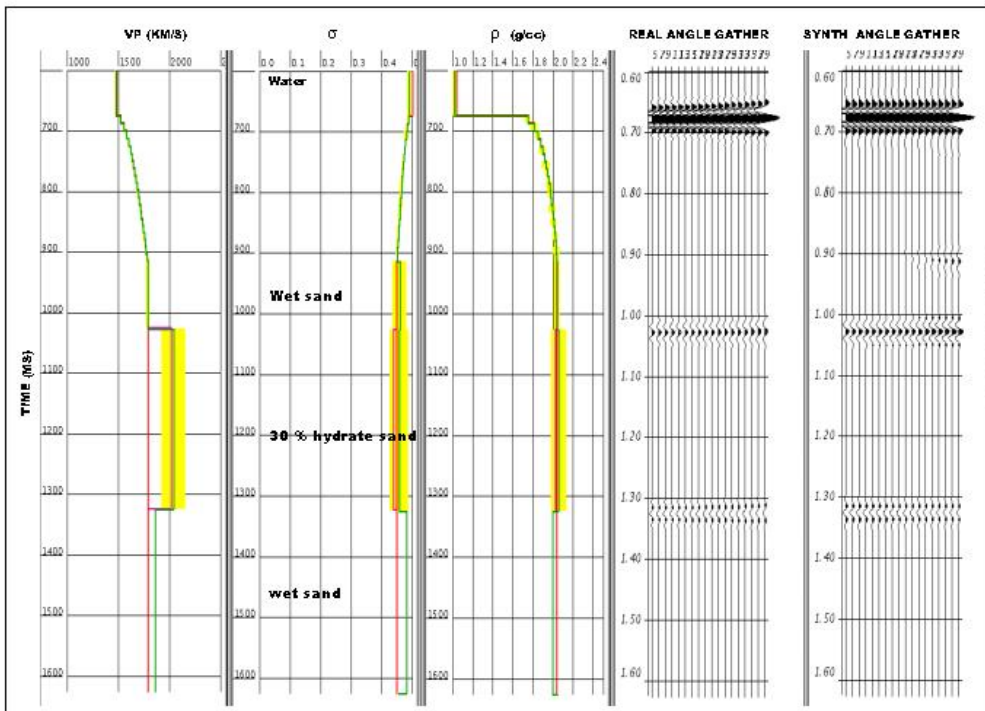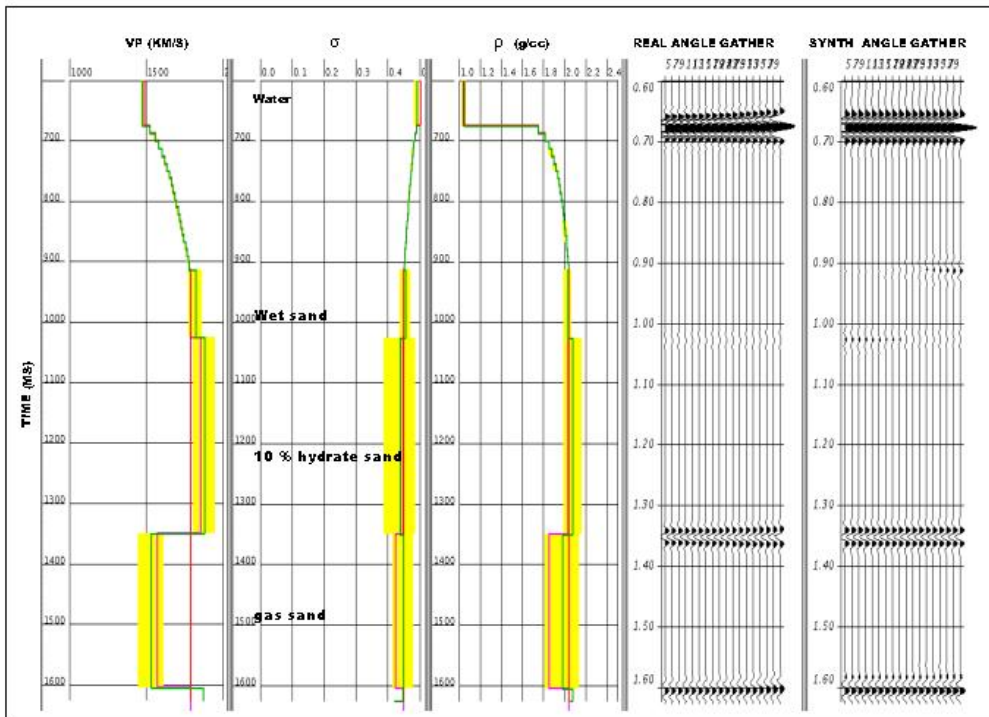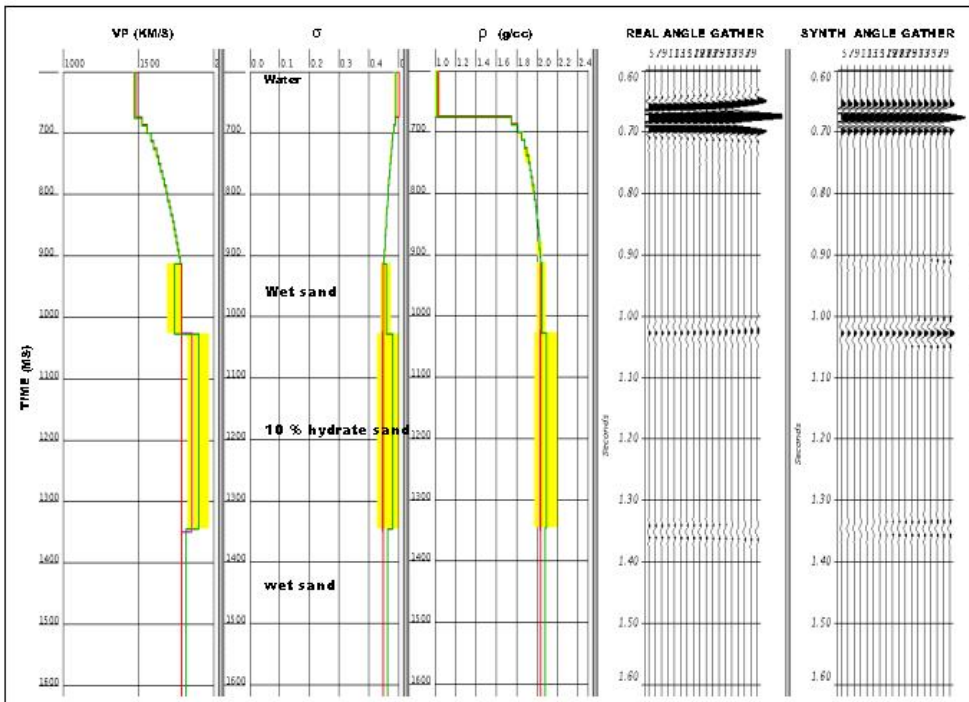**10 % Gas hydrate and gas, Maximum correlation = 0.9070**

Figure D.23 Inversion result for 10% gas hydrate saturation (Model 3-wet sand, hydrate, gas sand).

10 % Gas hydrate, Maximum correlation = 0.8928

Figure D.24 Inversion result for 10% gas hydrate saturation (Model 1-wet sand, hydrate, wet sand).

Figures D.21 through D.24 show prestack inversion results on the four hydrate synthetic models; (D.21) is for 30% hydrate saturation underlain by gas sand, (D.22) is for 30% hydrate saturation underlain by wet sand, (D.23) is for 10% hydrate saturation underlain by gas sand, and (D.24) is for 10% hydrate saturation underlain by wet sand. The green curves on each figure are the estimated elastic (Vp, Poisson's ratio and density) parameters. The pink and the red curves are the true and the initial elastic parameters. As mentioned previously, the yellow band is an error bar representing standard deviation in parameter estimation. Note that the "real angle gather" is the correct response from the actual hydrate model, whereas the "synthetic angle gather" is the inversion result. All four model gather responses closely matched the corresponding inversion result. This provided an important measure of confidence in our process for the subsequent FWPI using actual seismic data in the three study areas.

D.4.2.4 Results from Seismic Data

Green Canyon 184/185 was used as an initial prestack inversion test bed and calibration area. Prestack inversion was only performed on gathers that provided approximately 10° minimum incidence angle relative to the shallow zone of interest (700 – 2700 ms). Figure D.25 shows the area (red box) for FWPI locations in Green Canyon 184 and 185. Although the corresponding inversion results are shown in Appendix A, the overall results demonstrated a very close correlation between the FWPI result and actual seismic data. This further confirmed our observations from the synthetic models that the inversion process was performing well.
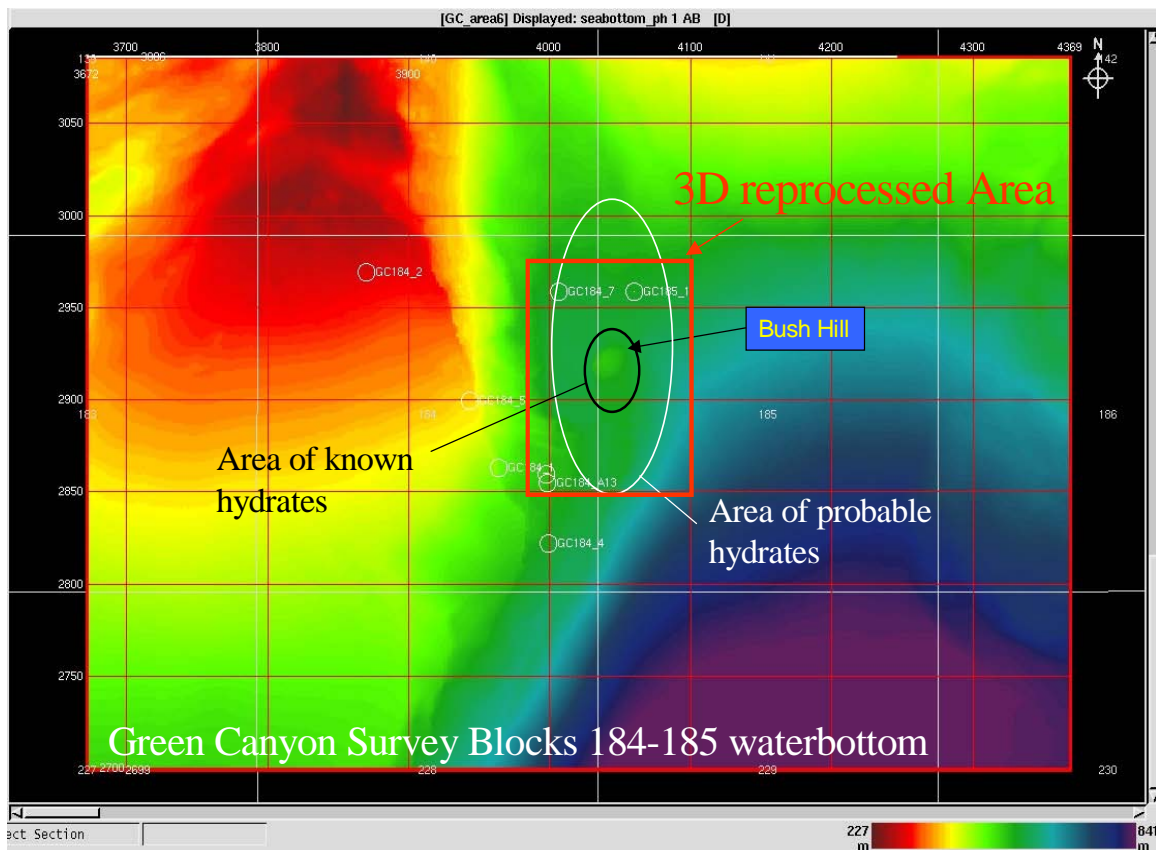
Figure D.25. Green Canyon area showing work area and possible extent of hydrates.

84

Evidence of a BSR was not found over the Green Canyon area. However, a surface hydrate mound was identified along an area delineated by a strong polarity reversal at the water bottom interface (Bush Hill area on Figure D.25). This is presumably caused by a thin high-velocity zone (hydrate) overlaying low-velocity free gas below the mound. Prestack inversion is unusable overlying this feature due to the dominant chaotic amplitude-blanking zones below the surface.

The available well sonic log (Well 184-3) in Block 184 only recorded the deeper section below the suspected gas hydrate zone. However, aside from this comparison limitation, Vp curves from the FWPI and from the sonic log both proportionally fit the velocity trends from check shot and spatially continuous velocity analysis (SCVA) as shown in Figure D.26. Estimated density from FWPI can be compared to density log at the lower portion of the zone of interest where they have a good match (except at the level where the caliper shows a washout).
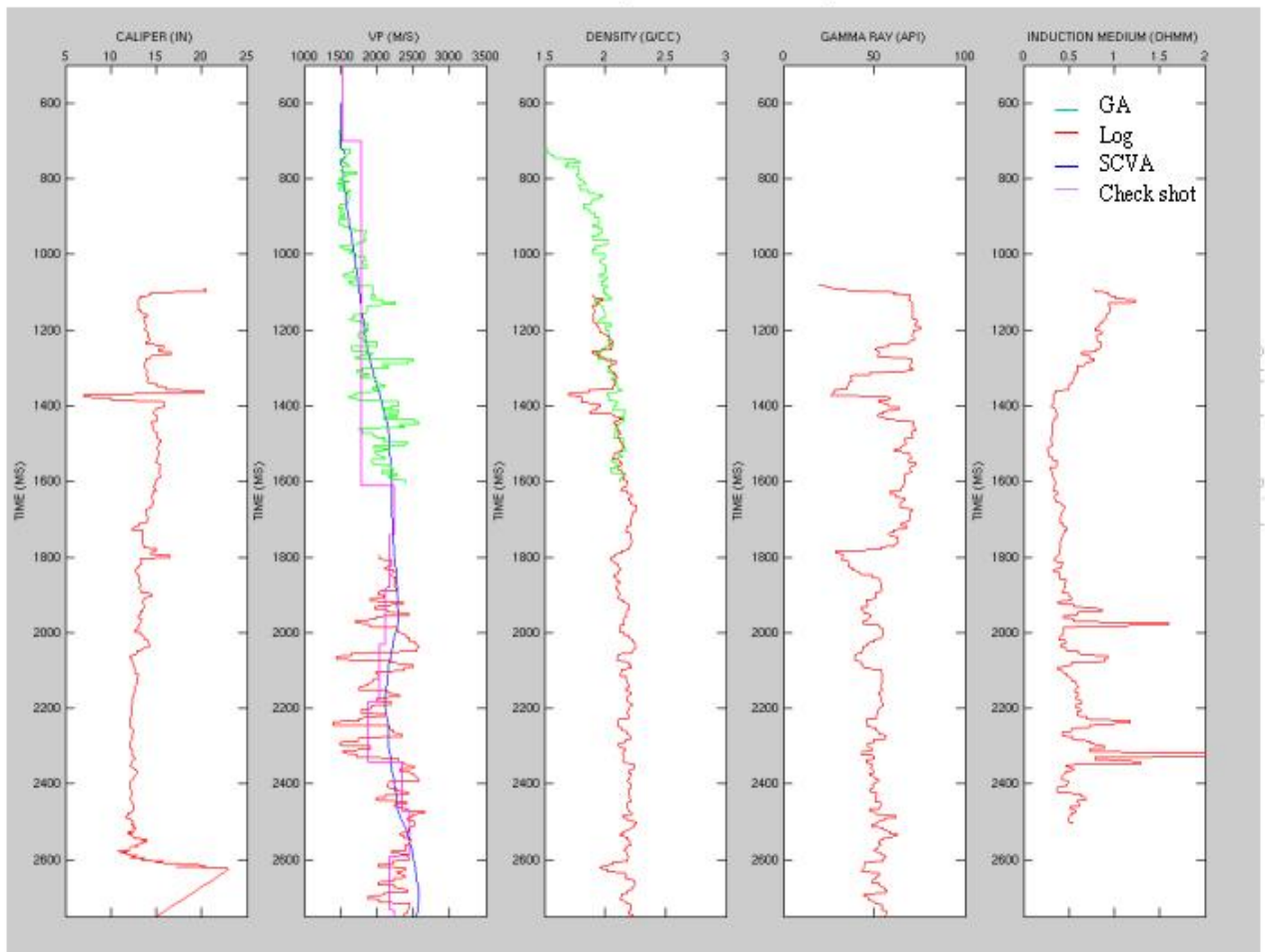
Figure D.26. Comparison of P-wave velocities from well logs, inversion, check shot and SCVA.

The inversion results on Keathley Canyon (Appendix B) were expected to give more reliable Poisson ratio estimation than for the Green Canyon area. This was due to the deeper zone of interest (1700-2700 ms) in Keathley Canyon Block 195. This enabled the prestack inversion to be applied on a wider incidence angle coverage (5° to 40$^{o)}$). Figure D.27 shows selected locations for prestack inversion in Keathley Canyon Block 195.

The occurrence of a BSR in Keathley Canyon area is clearly identifiable from seismic interpretation as crosscutting dipping reflectors. The inversion results at locations IL5554 - XL40245 (Figure B.1 in Appendix B) and IL5650 - XL40195 (Figure B.3 in Appendix B) exhibit distinct interface characteristics of a high-velocity layer overlying low-velocity gas interpreted as a BSR. In other locations (IL5635 - XL40260, IL5700 - XL40290 and IL5730 - XL40275) inversion results do not clearly show these characteristics. Ambiguity in the inversion results could potentially come from the dipping layers since the assumption for the prestack inversion is a 1D layer model. Evidence of a hydrate mound is also shown at inversion location IL5591 - XL40474 (Figure B.7 in Appendix B).
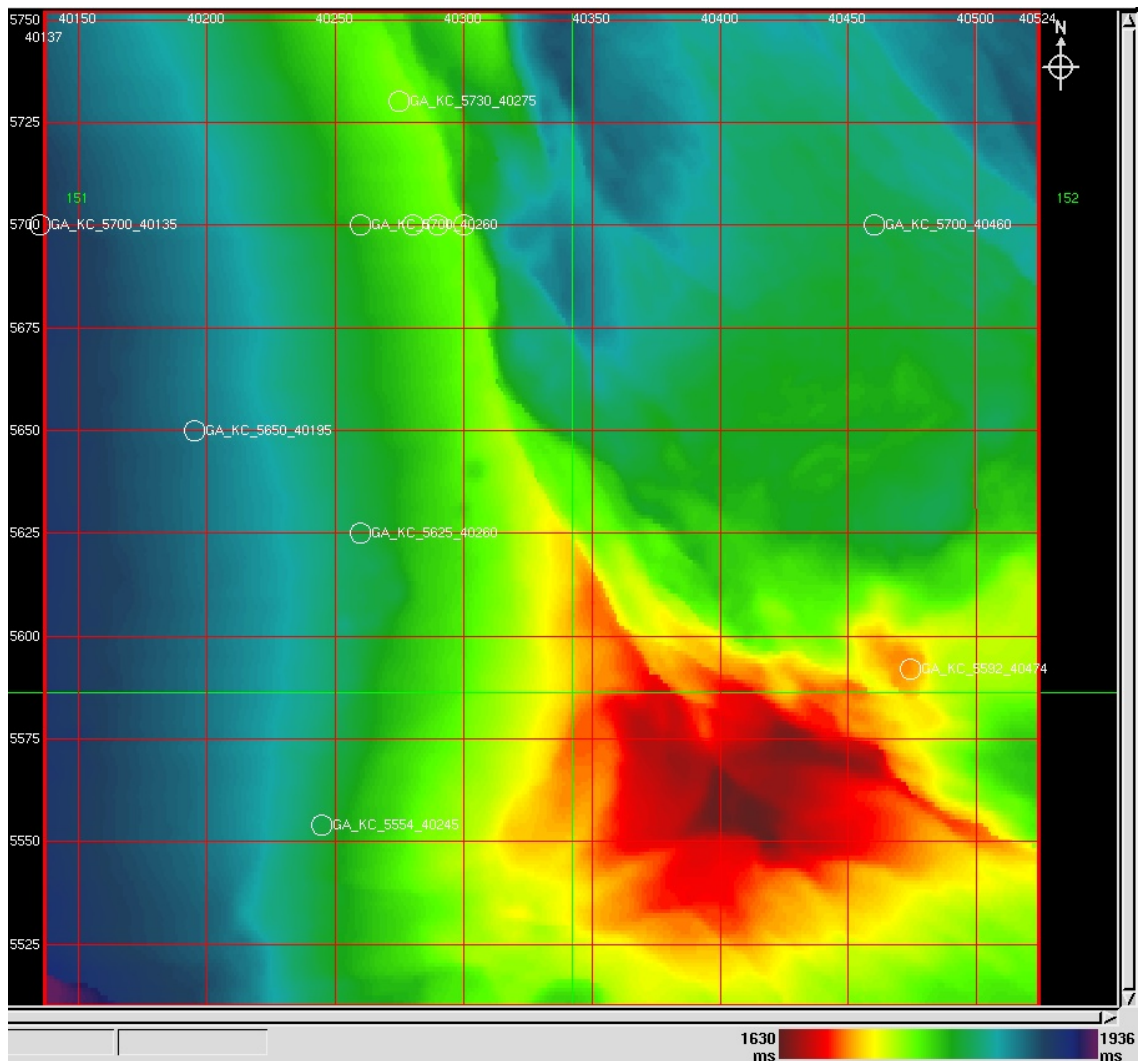
Figure D.27. Prestack Inversion locations in Keathley Canyon Block 195 area.

The Atwater Valley area is similar to Keathley Canyon in that a deep zone of interest (~1750-2750 ms TWT) provides wide incidence angle coverage from 5° to 40°. Figure D.28 shows selected locations for prestack Inversion locations in the Atwater Valley Block 14 area. The inversion results are shown in Appendix C. Evidence of a BSR is not found in this area, although several surface hydrate mounds show amplitude polarity reversal (Figure C.4 in Appendix C), which possibly could be a shallow BSR. Others do not show this characteristic, possibly because the thin layers are beyond the seismic resolution (Figure C.2 in Appendix C).
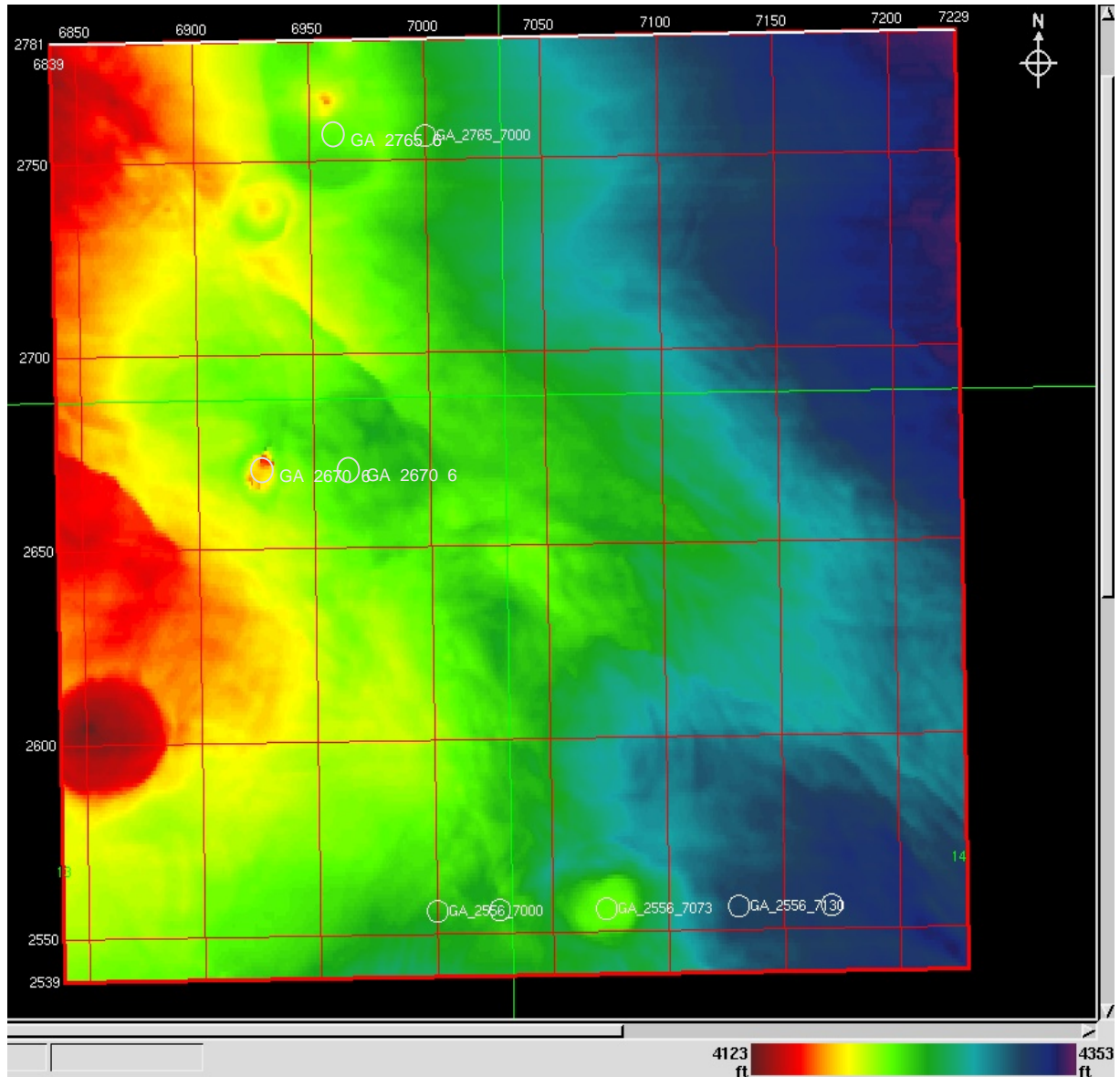
Figure D.28. Prestack inversion locations in Atwater Valley Block 14 area.

D.4.2.5 Summary

Tests on the synthetic models indicate that the FWPI for the hydrates is most sensitive to the seismic Vp, and can be reliably used to estimate the P-wave velocity. This shows the value of the FWPI when applied to the actual seismic data.

The BSR and the hydrate mounds are identifiable from the prestack inversion in conjunction with the seismic interpretation.

Calibration to reliable well information is needed for quantitative interpretation results. In addition, 3-D seismic data with a broader frequency bandwidth and improved signal-to-noise ratio would improve inversion results.

Understanding the lithology is very important to analyzing the inversion results. Confidence in the inversion process requires an appreciation in the regional geology.

D.4.3 Hybrid Inversion

Hybrid seismic inversion is a combination of prestack full-waveform inversion (FWPI) and poststack inversion that allows efficient inversion of large data volumes in the absence of well information (Mallick et al., 2000).

The first step in hybrid inversion is FWPI. As has been discussed in Section D.4.2, FWPI compared to other prestack inversions, such as AVO inversion or elastic impedance inversion, is more rigorous. FWPI accounts for thin-bed tuning and velocity gradients by incorporating all wave modes and multiple reflections in the inversion calculations. Consequently, FWPI gives a detailed estimate of the following elastic earth parameters: P-wave velocity, Poisson's ratio, and density.

In this project, FWPI was followed by an AVO analysis of each prestack data volume to generate AVO intercept and gradient volumes, which were then transformed into P-wave and S-wave impedance contrasts volumes.

Following the AVO analysis, the AVO attributes, P-wave and S-wave impedance volumes were inverted using a recursive inversion (Pseudo-Acoustic Impedance Transform) algorithm. This generated the P- and the S-wave impedances. The P- and the S-wave impedances from FWPI at control locations were used to constrain the low-frequency impedance trends in these inversions.

For a comprehensive account of hybrid seismic inversion, readers are referred to Mallick et al. (2000) for detail.

Hybrid inversions were performed on Green Canyon 184-185, Keathley Canyon 195, and Atwater Valley 14 blocks to generate P-wave impedance volumes of each studied region. Figures D.29 and D.30 display the results on two typical seismic lines, one from Keathley Canyon 195 block (Inline 5700) and the other from Atwater Valley 14 block (Inline 2556).

It can be observed from Figures D.29 and D.30 that the magnitude of the P-wave impedance ranges from about 1500 to 6000 (m/s*g/cc) for the shallow 500 ms (two-way travel time) sediments, which are the appropriate values of the shallow sediments. The BSR in Keathley Canyon 195, as indicated by the red arrow at about 1100 ms one way time on Figure D.29, is discernable in the impedance section. Also, several high-impedance anomalies were indicated in both figures. These anomalies may indicate possible occurrence of shallow gas hydrates and, with an appropriate gas hydrate rock physics model, these anomalies can be quantified for gas hydrate saturation.

Figure D.29. P-Impedance of Inline 5700, Keathley Canyon 195 .

Figure D.30. P-Impedance of Inline 2556, Atwater Valley 14.
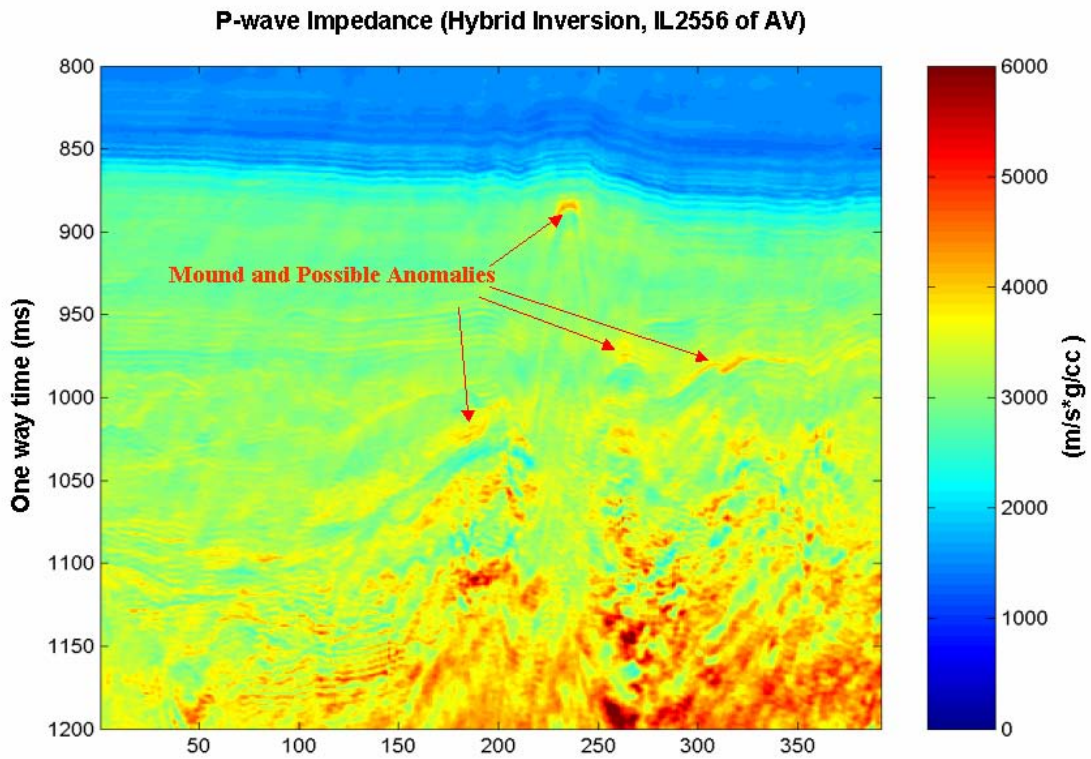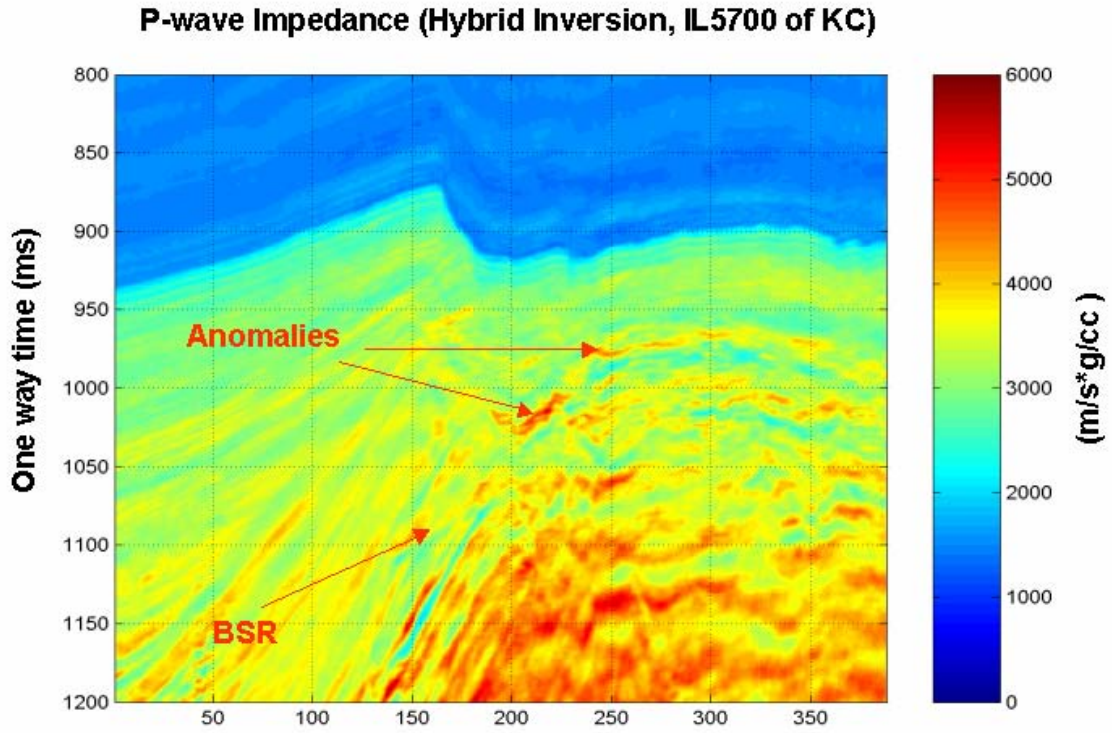
D.5 Summary

Elevated P-wave and S-wave velocities are diagnostic features of the occurrence of gas hydrates in the shallow sediments, which provide the basis for gas hydrate detection both from acoustic logs and seismic data (through inversion). Investigation of a number of existing gas hydrate rock physical models revealed large variations in predicted P-wave and S-wave velocities. Among these models, the effective medium model (Dvorkin and Nur, 1993, Helgerud et al, 1999, Ecker et al., 2000), taking gas hydrates as part of load-bearing matrix, better predicts the gas hydrate effect in both P-wave and S-wave velocities. However, this model tends to overestimate S-wave velocity especially at high gas hydrate saturation values. In addition to the velocity-gas hydrate saturation model, we also developed a compaction model of porosity and velocity at shallow depth where gas hydrate occurs. Combining the two models, we constructed shallow gas hydrate pseudo logs with properties typical of the GOM.

Prestack full-waveform modeling of gas hydrate bearing sediments displays both velocity anomalies and distinct offset responses, providing the physical basis for seismic detection of gas hydrates. Full-waveform prestack inversion correctly ties to the seismic data without the benefit of actual well data. Gas hydrate anomalies and a BSR are clearly indicated in the inversion results.

Combining full-waveform prestack inversion results, elastic property (P-wave impedance) volumes were generated through Hybrid inversion, which provide database for gas hydrate interpretation and quantification.

It must be noted, however, that gas hydrate logging and coring data are scarce. More gas hydrate drilling and lab work are needed to develop and fine-tune gas hydrate rock physical models.

E. Quantitative Estimation of Gas Hydrates

With no actual hydrate drilling information available, we designed a quantitative estimation procedure that included elastic property inversion, rock physical modeling, and quantitative gas hydrate saturation calculation based on seismic data.

E.1 Methodology

The process of quantitative gas hydrate estimation, as we have applied it, includes three steps shown in Figure E.1; Elastic property inversion, rock physical model construction, and gas hydrate saturation calculation. The following discussion contains results from these processes.
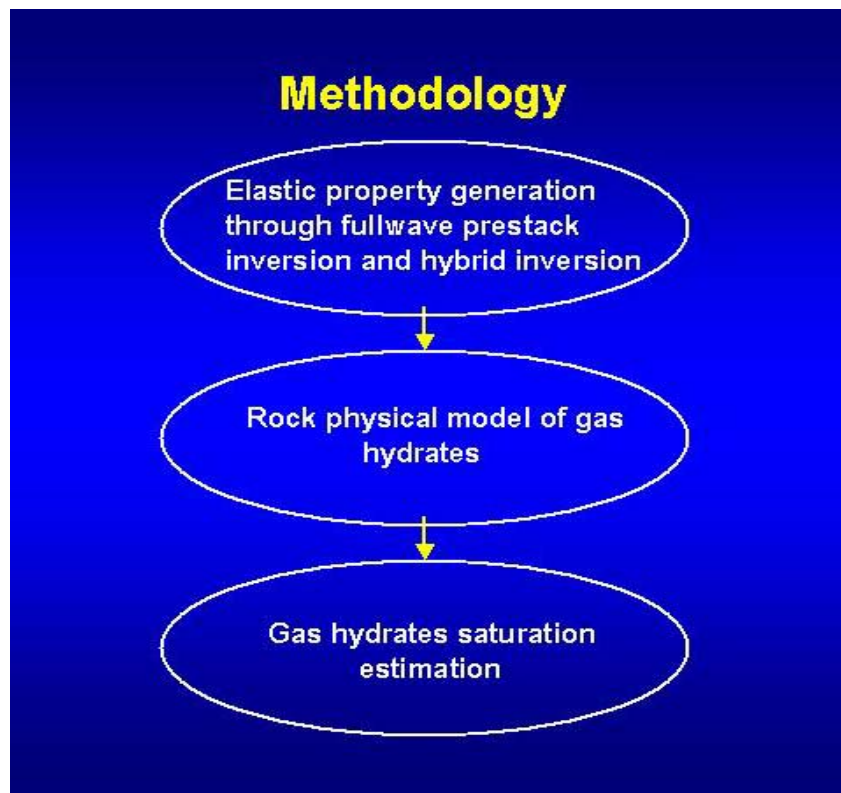
Figure E.1. Work flow for quantitative gas hydrate saturation estimation

Realistic gas hydrate quantitative estimation based on seismic data relies on accurate elastic property estimation through seismic inversion and practical gas hydrate rock physical modeling. As discussed previously, full-wave prestack inversion applied at Green Canyon 184/185, Atwater Valley 14 and Keathley Canyon 195, provided high-resolution and robust one-dimensional estimation of P-wave and S-wave velocities. Shallow sand-shale sequences, BSR, and possible gas hydrate anomalies were readily recognized through the full-wave inversion results (Figures E.2 and E.3). The elastic volume used was created from Hybrid inversion, which combines the full-wave inversion together with conventional linear prestack inversion for robustness and efficiency.

E.2 Gas Hydrate Quantification Based on 1D Full-waveform Prestack Inversion (FWPI) Result

Figure E.2 shows two examples of P-wave velocity (blue curves) derived from full-waveform prestack inversion of seismic data at two locations in Keathley Canyon 195. The BSR is clearly identified by the extreme low P-wave velocity values (blue curves) at approximately 2200 ms TWT on the plots as indicated by the red dotted lines.

Based on these high-resolution data, gas hydrate saturation has been quantitatively estimated (Figure E.3). As indicated from the estimation work flow (Figure E.1), we initially fit a shallow rock physics model to the impedance curves, then overlay with gas hydrate saturation charts (group of colored curves in Figure E.3). Finally, gas hydrate saturation values shown at the left sides of both panel are interpolated through the group of gas hydrate saturation charts.
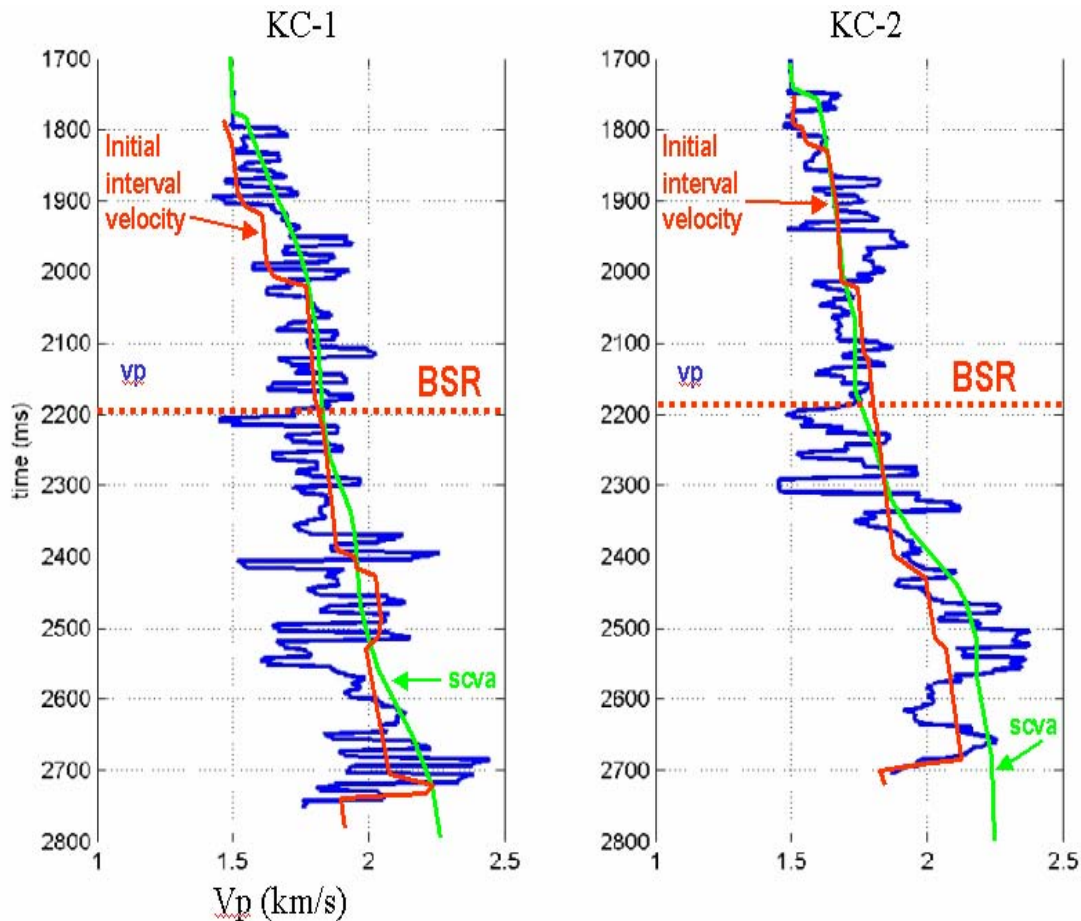
Figure E.2 P-wave velocity estimation from seismic data at two Keathley Canyon locations through full-waveform prestack inversion (blue curve). Red curves are the starting interval velocity (derived from stacking velocity) model input to the inversion. Green curves are velocities from spatially continuous velocity analysis (SCVA).
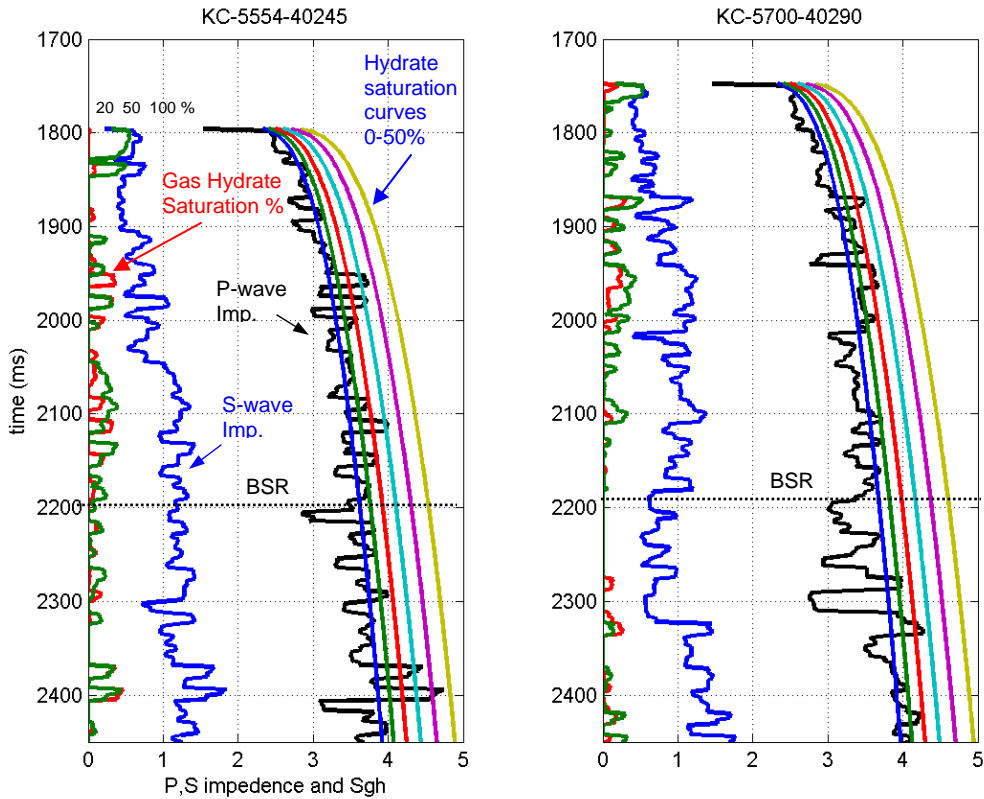
Figure E.3. Gas hydrate saturation estimation at two Keathley Canyon locations. Black and blue curves are P- and S-wave impedance values estimated from full-waveform prestack inversion. The group of smooth colored curves are gas hydrate saturation charts ranging from 0 to 50% in steps of 10%. Red and green curves on the left side of each panel are gas hydrate saturation estimated from P- and S-wave impedance in terms of volumetric fraction of pore space.

E.3 Gas Hydrate Quantification Based on Hybrid Inversion Volumes

3D gas hydrate saturation volumes at KC 195 and AW14 were derived based on P-wave impedance volumes from hybrid inversion through a similar approach as described in Section E.2. Figures E.4 and E.5 display estimation results at two typical inlines from the two volumes.

Gas hydrate saturation as shown at these two locations and for the two sections, generally ranges from 0% to a maximum of 30-40% of pore space. It should be noted, however, that the concept of this estimation method attributes a high elastic anomaly solely to the effect of gas hydrates, much like gas hydrate replacement from a background hosting sediment. It should be understood that factors such as lithology variation might also cause impedance increases. In addition, the anomaly may be caused by the combination of gas hydrate and lithology variations. Hence, the saturation values derived represent the upper bound, meaning the largest possible gas hydrate saturation estimate. In frontier areas where no well data are available and lithology is poorly defined, this type of estimation of upper bounds provides valuable information for selecting potential drill sites to further quantify gas hydrate saturations and properties. Also, in geological environments similar to Blake Ridge where the host rock does not have distinctive layer structure, this type of estimation of upper bound may be close to the actual gas hydrate saturation.

94

P-wave Impedance (Hybrid Inversion at KC)
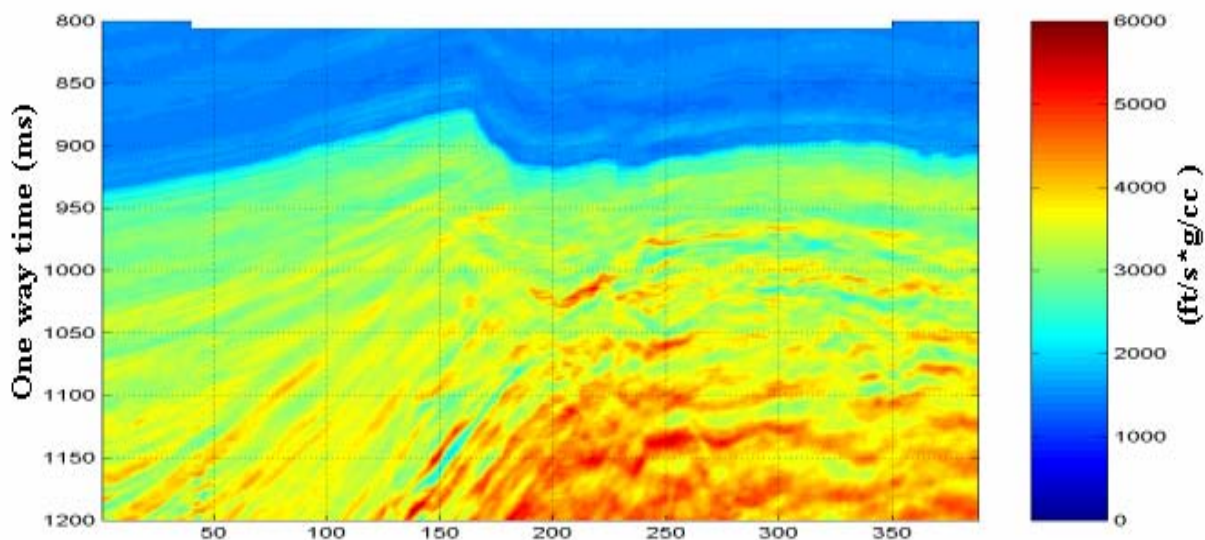
Gas Hydrate Saturation Estimation (KC)
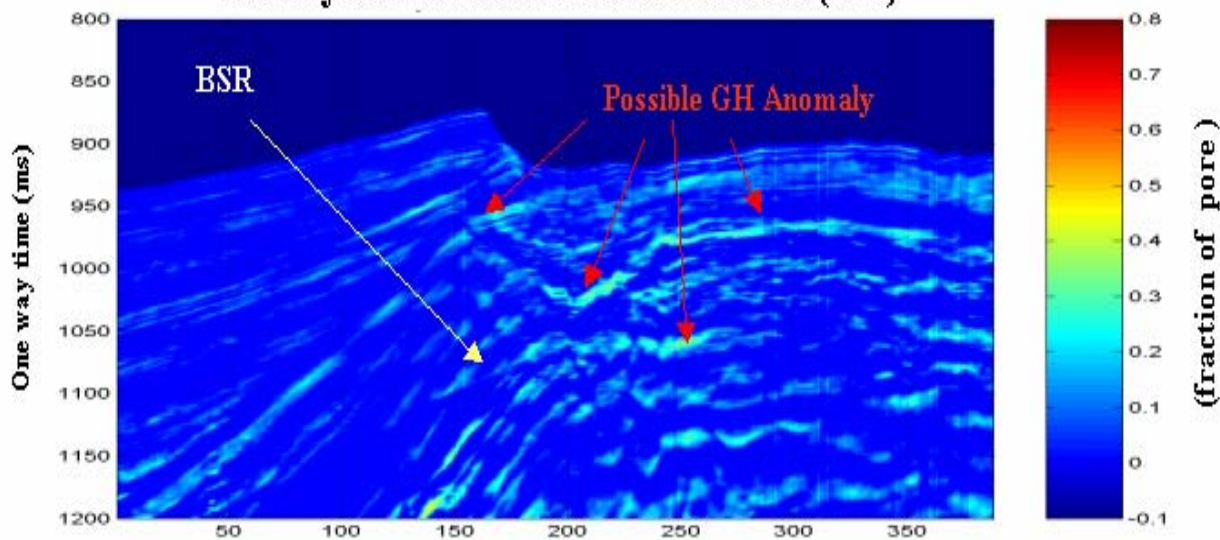
Figure E.4 Gas hydrate saturation at inline 5700 of Keathley Canyon 195. Upper panel displays the P-impedance derived from hybrid inversion and the lower panel shows the estimated gas hydrate saturation.
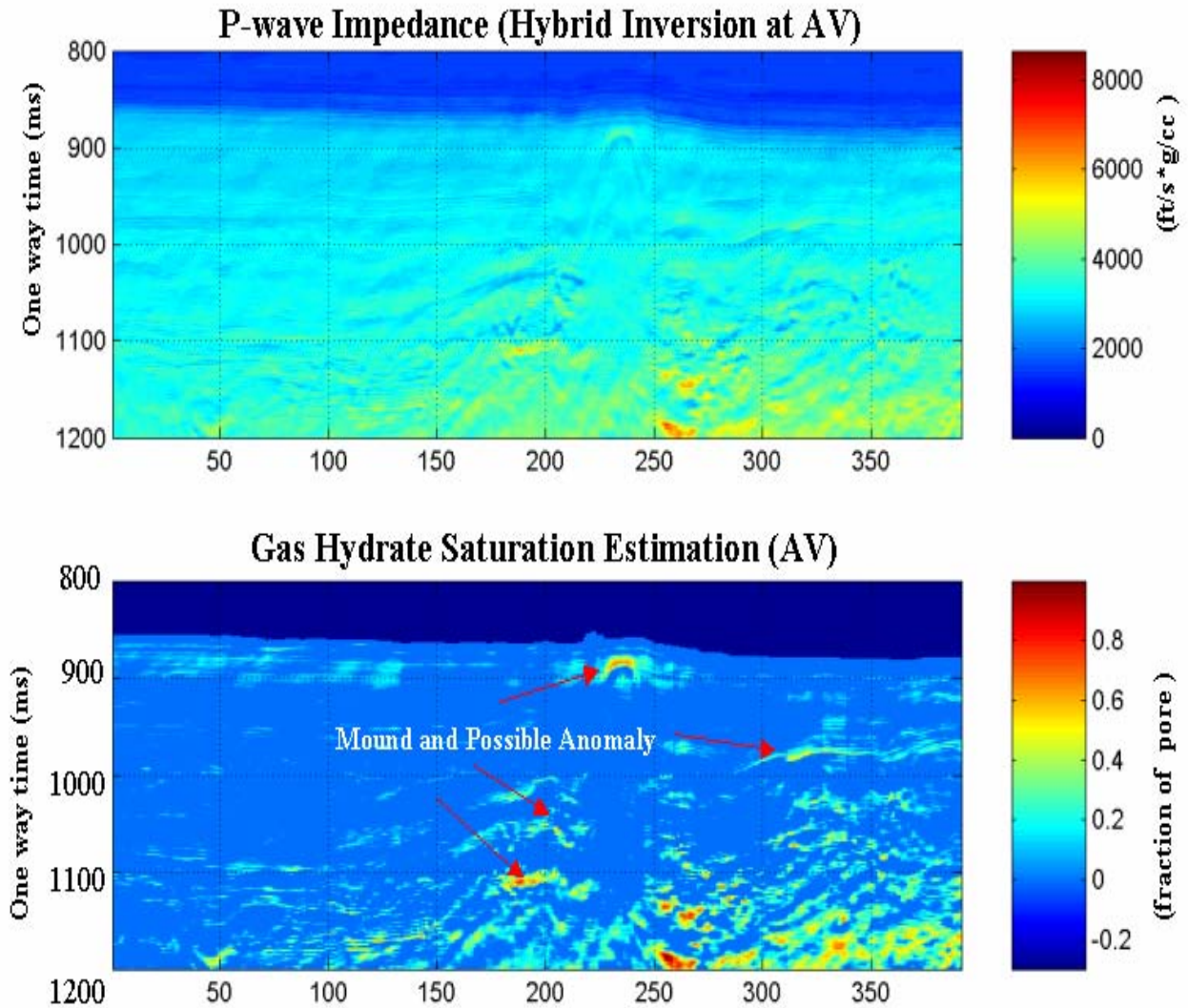
Figure E.5. Gas hydrate saturation at inline 2556 of Atwater Valley 14. Upper panel displays the P-impedance derived from hybrid inversion and the lower panel shows the estimated gas hydrate saturation.

How reliable are our predictions? There are numerous sources of ambiguities as discussed earlier. Gas hydrate saturation cubes such as those shown in Figures E.4 and E.5 must be calibrated. It should be noted that, despite the large number of drilled hydrate wells worldwide, quality hydrate logging and coring data are scarce, especially in the Gulf of Mexico. Such data are urgently needed. This must also be supplemented by controlled laboratory measurements on the properties of gas hydrates where parameters can be controlled.

In conclusion, seismic detection and quantification of gas hydrates rely on qualitative processing, robust elastic inversion, and practical gas hydrate rock physical model construction. The five-step integrated multidisciplinary approach proves to be an effective tool for gas hydrate characterization using seismic data. Full-waveform prestack inversion and hybrid inversion generate robust elastic property volumes from seismic data. From this, and with our gas hydrate rock physics-based tool, gas hydrate saturation volumes can be generated, thereby providing guidance for the detection of gas hydrates and a potential quantitative resource estimation tool.

F. References

Bangs, N. L. B., D. S. Sawyer, and X. Golovchenko, 1993, Free gas at the base of the gas hydrate zone in the vicinity of the Chile triple junction, Geology, 21, p. 905-908.

Chen, Q., and S. Sidney, 1997, Seismic attribute technology for reservoir forecasting and monitoring, The Leading Edge, May, p. 445-456.

Collett T., 2000, Quantitative well-log analysis of in-site natural gas hydrates, PhD. Dissertation, Colorado school of Mines, p. 45-55.

Cook, D., and P. D'Onfro, 1991, Jolliet Field thrust fault structure and stratigraphy Green Canyon Block 184, offshore Louisiana, Transactions – Gulf Coast Association of Geological Societies, v. XLI, p. 100-121.

Cooper, A., and P. Hart, 2002, Seismic studies of the gas-hydrate stability zone, northern Gulf of Mexico, Proceedings of the Fourth International Conference on Gas Hydrates, Yokohama, May 19-23, p. 115-123.

Dvorkin, J., A. Nur, R. Uden, and T. Taner, 2003, Rock physics of a gas hydrate reservoir, The Leading Edge, September, p. 842-847.

Dvorkin, J., and A. Nur, 1996, Elasticity of high-porosity sandstones: Theory for two North Sea datasets, Geophysics, 61, p. 1363-1370.

Dvorkin, J., and Nur, A., 1993, Rock physics for characterization of gas hydrates, in "The future of energy gases", USGS publications.

Ecker, C., J. Dvorkin, and A. Nur, 1998, Estimating the amount of gas hydrate and free gas from marine seismic data: Geophysics, Vol. 65, No. 2, p. 565-573.

Frasier, C.W., 1970, Discrete time solution of plane P-SV waves in a plane layered medium: Geophysics, Vol. 35, p197-219.

Fuchs, K., and Muller, G., 1971, Computation of synthetic seismograms with reflectivity method and comparison with observation: Geophysics. J. Roy. Astr. Soc., Vol. 76, p.461-481.

Gregory, A.R., 1977, Aspects of rock physics from laboratory and log data that are important to seismic interpretation, in Seismic Stratigraphy - Applications to Hydrocarbon Exploration: AAPG Memoir 26, 15-45.

Hamilton, E.L.,1965., Sound speed and related physical properties of sediments from experimental Mohole (Guadalupe site), Geophysics, no. 2., pp 257-261.

Hamilton, E.L., 1971, Elastic properties of marine sediments, *J. Geophys. Res., 76*, 579-601.

Helgerud, M. B., J. Dvorkin, A. Nur, A. Sakai, and T. Collett, 1999, Elastic-wave velocity in marine sediments with gas hydrates: Effective medium modeling, Geophysical Research Letters, 26, p.2021-2024.

Kennett, B.L.N., 1983, Seismic wave propagation in stratified media: Cambridge Univ. Press.

Kind, R., 1976, Computation of reflection coefficients for layered media: J. Geophysics, Vol. 42, p.191-200.

Kuster, G. T., and M. N., Toksoz, 1974, Velocity and attenuation of seismic waves in two-phase media. Geophysics, 39, p.587-618.

Lee, M. W., 2001, Biot-Gassmann theory for velocities of gas hydrate-bearing sediments, Geophysics, Vol. 67, No. 6, p.1711-1719.

Lee, M. W., D. R., Hutchinson, T. S., Collett, and W. P., Dillon, 1996, Seismic velocities for hydrate-bearing sediments using weighted equations: Journal of Geophysical Research, Vol. 101, p. 20347-20358.

Lee, M. W., D. R., Hutchinson, D. R., Dillon, J. J., Miller, W. F., Agena, and A. B., Swift, 1993, Method of estimating the amount of in-situ gas hydrates in deep marine sediments: Marine Petroleum Geology 10, p. 493-506.

Lu S. and G. A. McMechan, 2002, Estimation of gas hydrate and free gas saturation, concentration, and distribution from seismic data, Geophysics, Vol. 67, No. 2, p. 582-593.

Mallick, S., 1992a, Genetic algorithm and inversion of amplitude-versus-offset data: presented at the 1992 joint SEG/EAEG summer research workshop on how useful is amplitude-versus-offset (AVO) analysis ?, Aug.9-14, Big Sky, Montana, U.S.A.,

Mallick, S., 1992b, Inversion of amplitude-versus-offset data using genetic algorithm: 62nd Ann. Internat. Mtg., Soc. Expl. Geophs., Expanded Abstrtact, p.844-847.

Mallick, S., 1993a, Waveform inversion of amplitude-versus-offset data using genetic algorithm: 63rd Ann. Internat. Mtg., Soc. Expl. Geophys., Expanded Abstracts, p.750-753.

Mallick, S., 1995, Model-based inversion of amplitude-variations-with-offset data using a genetic algorithm: Geophysics, Vol. 60, p.939-954.

Mallick, S., 1999, Some practical aspects of prestack waveform inversion using a genetic algorithm: An example from East Texas Woodbine gas sand: Geophysics, Vol. 64, p.326-336.

Mallick, S., Huang, X., Lauve, J., and Ahmad, R., 2000, Hybrid seismic inversion: A reconnaissance tool for deepwater exploration: The Leading Edge, p.1230-1237.

Mavko, G., T. Mukerji, and J. Dvorkin 1998, The Rock Physics Handbook: Tools for Seismic Analysis in Porous Media, Cambridge University Press, New York, p. 307.

McConnell, D., and B. Kendall, 2003, Images of the base of gas hydrate stability in the deepwater Gulf of Mexico: Examples of gas hydrate traps in northwest Walker Ridge and implications for successful well planning, The Leading Edge, April.

Mindlin, R.D., 1949, Compliance of elastic bodies in contact: J. Appl. Mech., 16, 259-268.

Milkov, A., 2000, Worldwide distribution of submarine mud volcanoes and associated gas hydrates, Marine Geology, v.167, p. 29-42.

Milkov, A., R. Sassen, 2002, Resources and economic potential of individual gas hydrate accumulations in the Gulf of Mexico continental slope, Marine and Petroleum Geology, November review, 45 pp.

Paxton, S.T., Szabo, J.O., Ajdukiewicz, J.M., and Klimentidis, R.E., 2002, Construction of an intergranular volume compaction curve for evaluating and predicting compaction and porosity loss in rigid-grain sandstone reservoirs, AAPG bulletin, v.86, no.12, p.2047-2067.

Sen, M.K., and Stoffa, P.L., 1992, Rapid sampling of model space using genetic algorithms: Example form seismic waveform inversion: Geophs. J. Internat., Vol. 108, p.281-292.

Sloan, E.D. Jr. 1998. Clathrate Hydrates of Natural Gas (2nd Edition). Marcel Dekker, New York p. 705.

Stoffa, P.L., and Sen, M.K., 1991, Nonlinear multiparameter optimization using genetic algorithms: Inversion of planewave seismograms: Geophysics, Vol.56, p.1794-1810.

Tosaya, C. and Nur, A., 1982, Effects of diagenesis and clays on compressional velocities in rocks: Geophys. Res. Lett., 84, 3532-3536.

Weimer, P., and B. Dixon, 1994, Regional sequence stratigraphic setting of the Mississippi fan complex, northern deep Gulf of Mexico: Implications for evolution of the northern gulf basin margin, GCSSEPM Foundation 15th Annual Research Conference Submarine Fans and Turbidite Systems, December, p. 373-381.

Weimer, P., P. Varnai, Z. Acosta, F. Budhijanto, R. Martinez, A. Navarro, M. Rowan, B. McBride, and T. Villamil, 1994, Sequence stratigraphy of Neogene turbidite systems, northern Green Canyon and Ewing Bank, northern Gulf of Mexico, GCSSEPM Foundation 15th Annual Research Conference Submarine Fans and Turbidite Systems, December, p. 383-399.

Wood, W., J. Gettrust, N. Chapman, G. Spence, and R. Hyndman, 2002, Nature, Decreased stability of methane hydrates in marine sediments owing to phase-boundary roughness, v. 420, p. 656-660.

Wood, W. T., P. L., Stoffa, and T. H. Shipley, 1994, Quantitative detection of methane hydrate through high-resolution seismic velocity analysis, Journal of Geophysical Research, 99, p. 9681-9695.

Xu, S., and R. E., White, 1995. A new velocity model for clay-sand mixtures. Geophysical Prospecting, 43, p.91-118.

Zimmerman, R.W., 1991, Compressibility of sandstones, Elsevier Science, Amsterdam, 173 pp.

Appendix A

Prestack Inversion results on Green Canyon Block 184/185

Results of the prestack full-waveform inversion for Green Canyon 184/185 are given in Figures A.1 through A.9. The three log plots for all figures in Appendices A-C are of Vp (km/sec), Poisson's ratio and density (g/cc). The seismic gather on the left panel shows the actual seismic data extracted at the line/cross line location. The gather on the right panel shows the modeled inversion result. The pink curves, representing the rock model elastic trends, are good low frequency guides for the high-frequency inversion results (green curves).
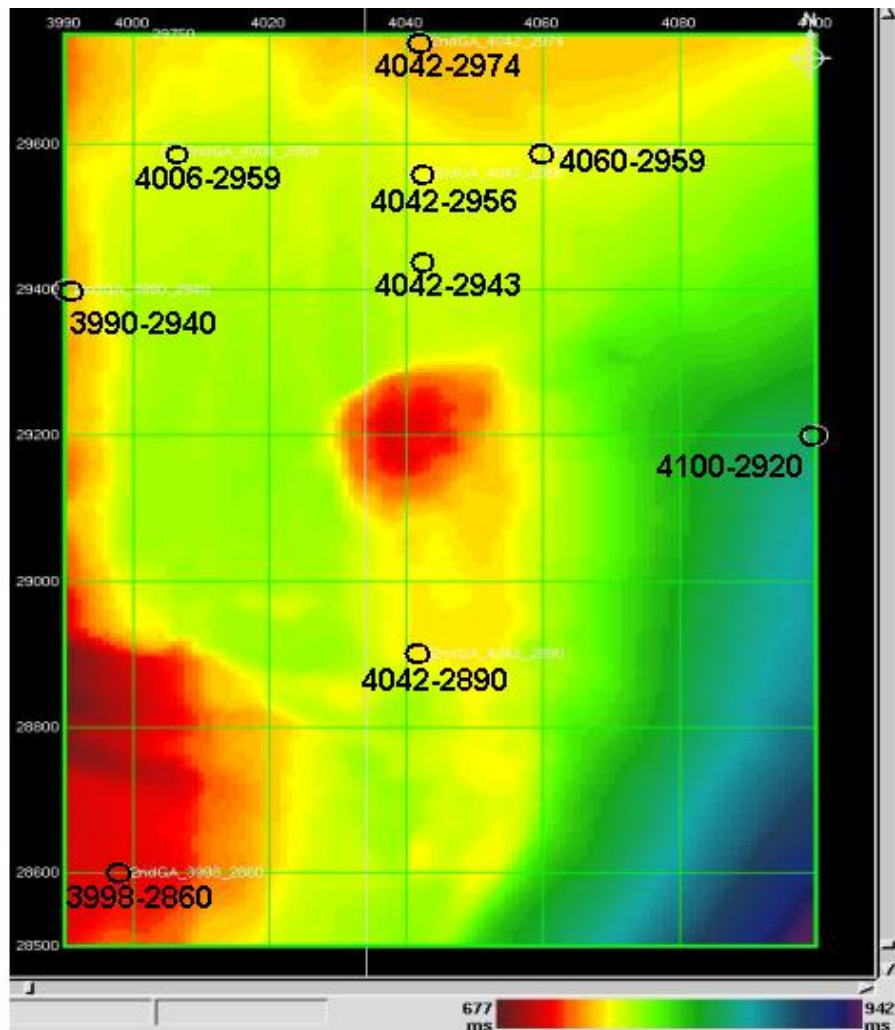
Green Canyon Block 184-185 showing inversion locations. Center is Bush Hill.
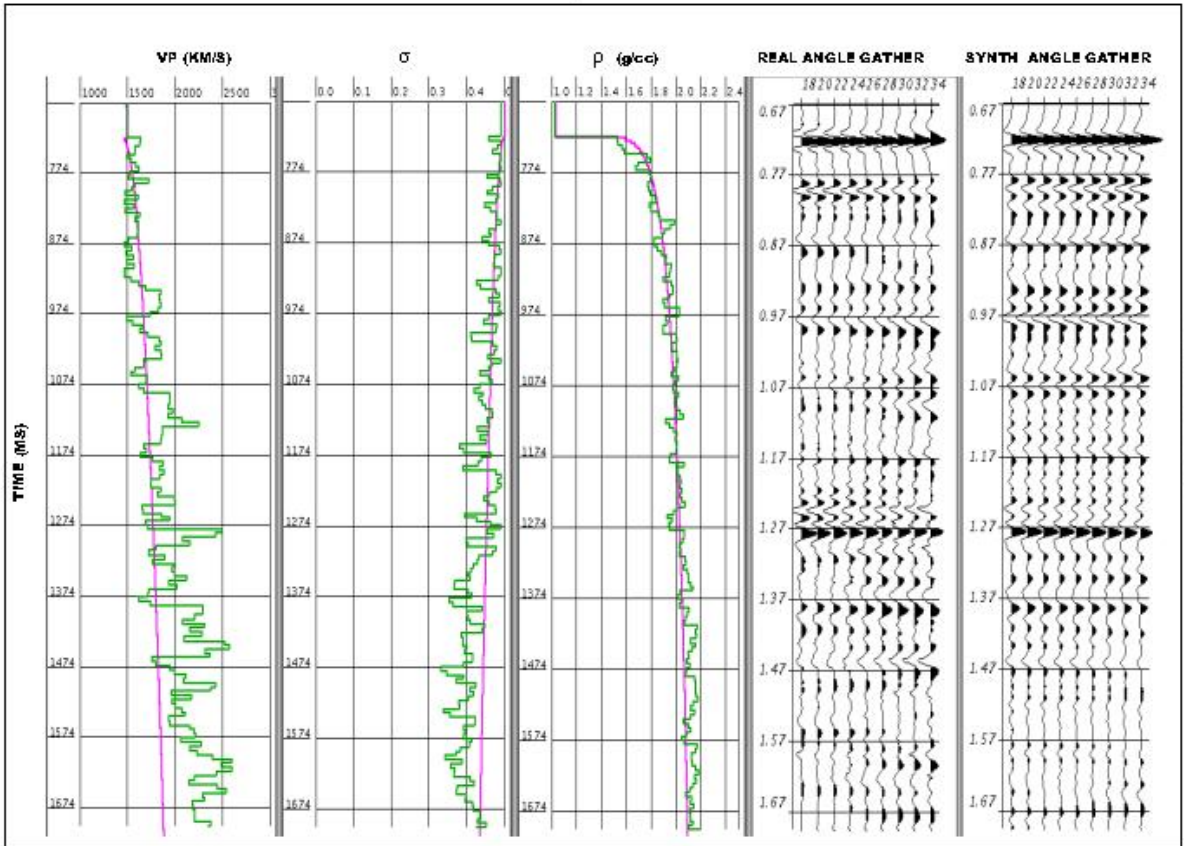
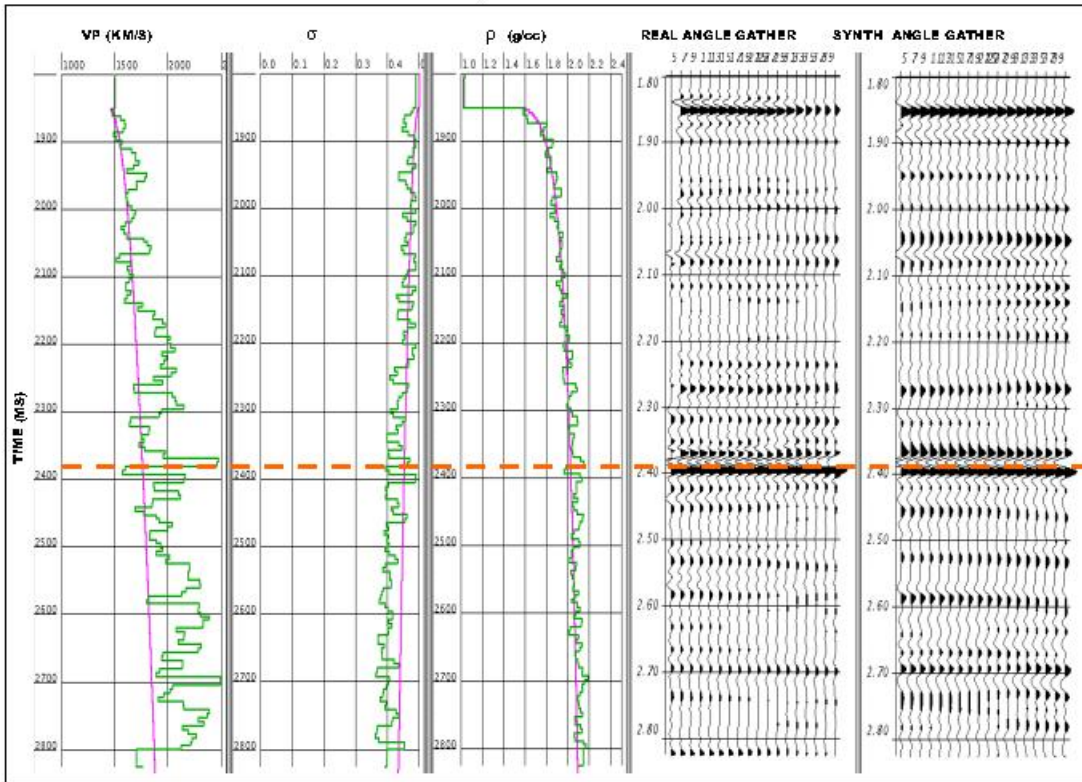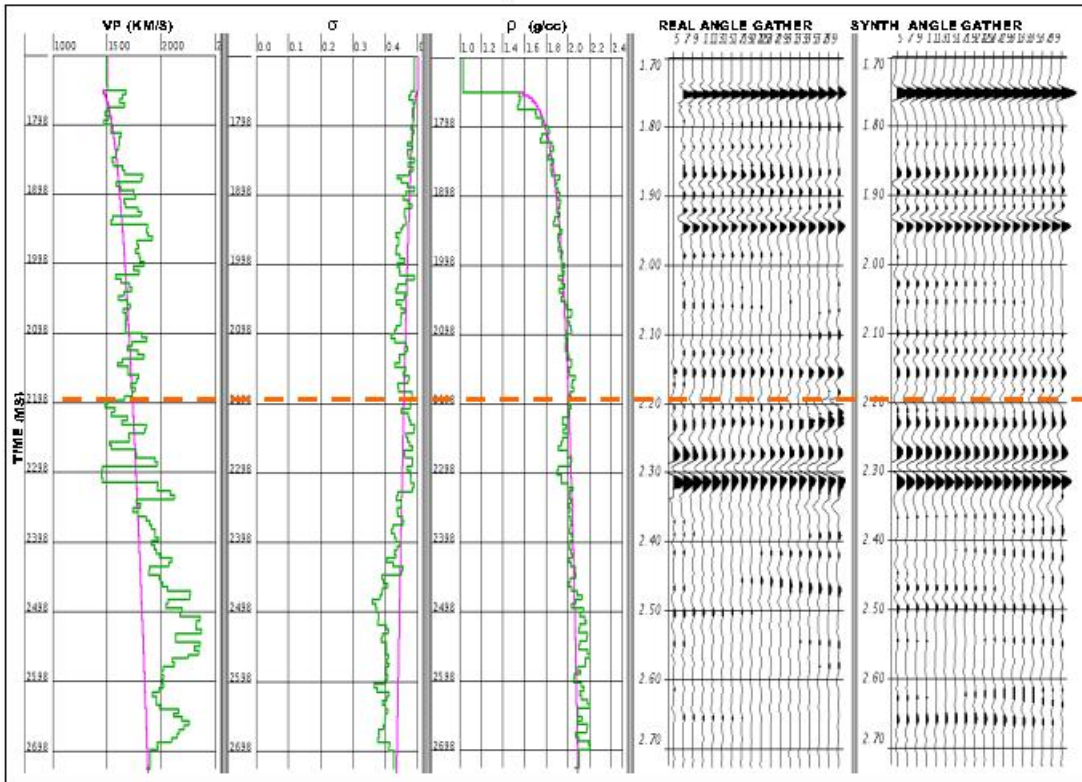Figure A.1. FWPI results at location IL3998, XL2860. The pink curves are the elastic parameter trends of the background rock model.
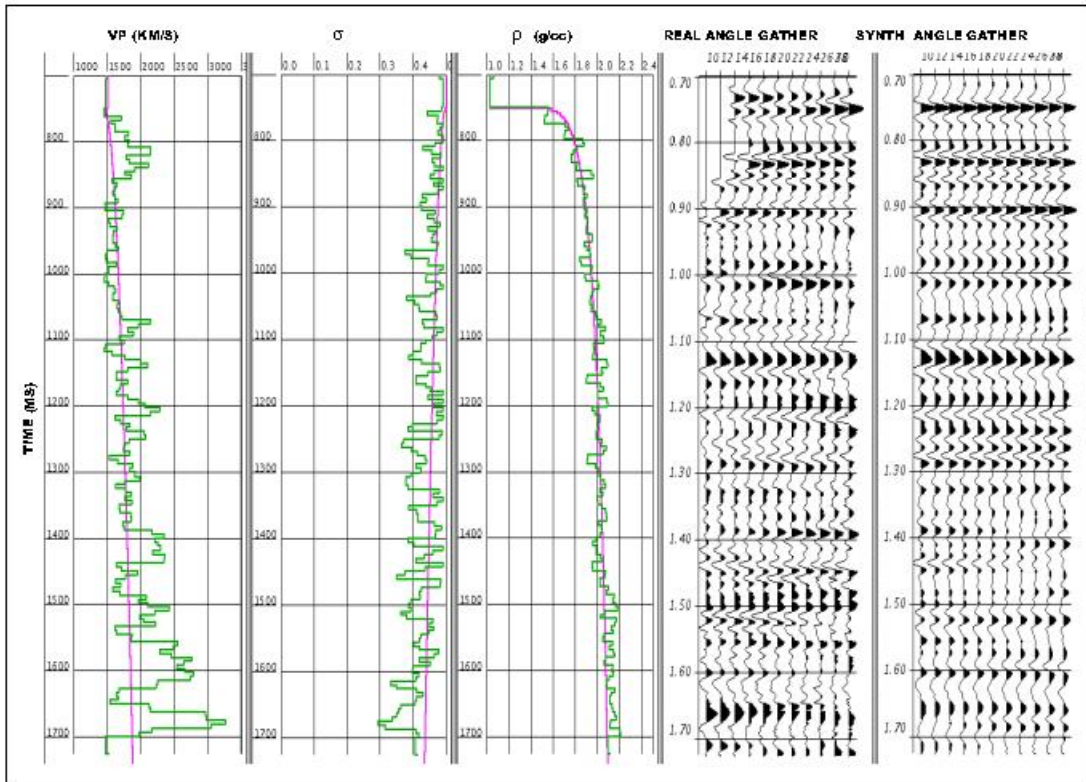
Figure A.2. FWPI results at location IL3990, XL2940. The pink curves are the elastic parameter trends of the background rock model.
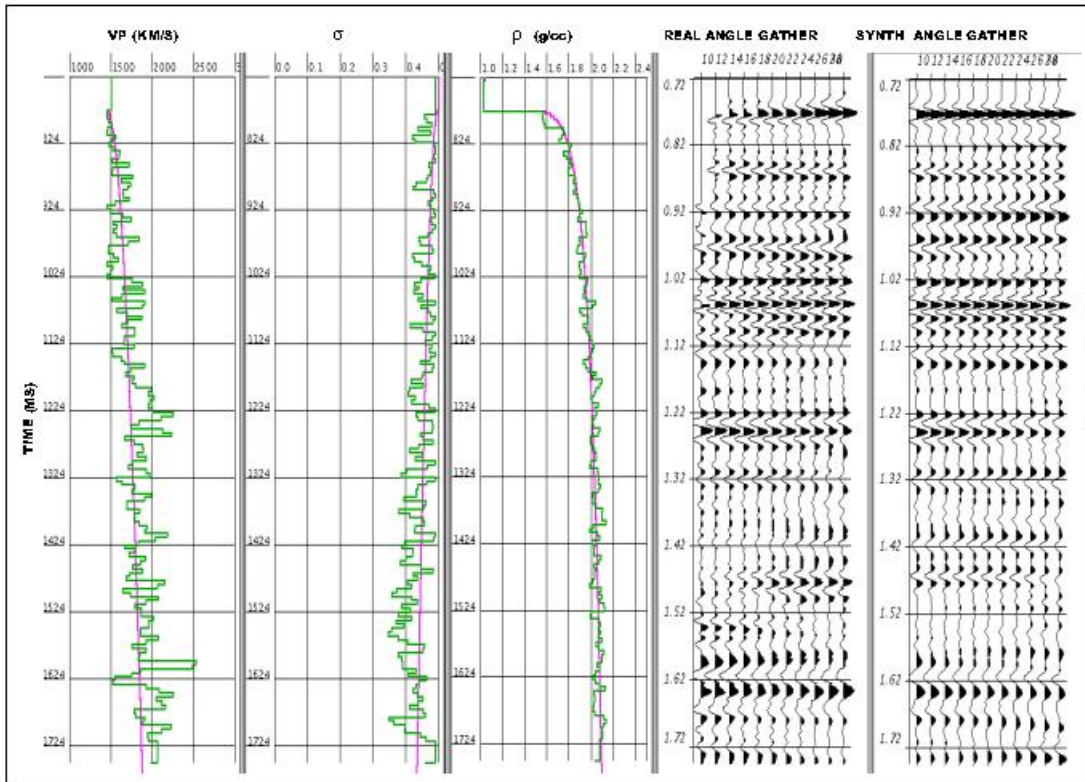
Figure A.3. FWPI results at location IL4006, XL2959. The pink curves are the elastic parameter trends of the background rock model.
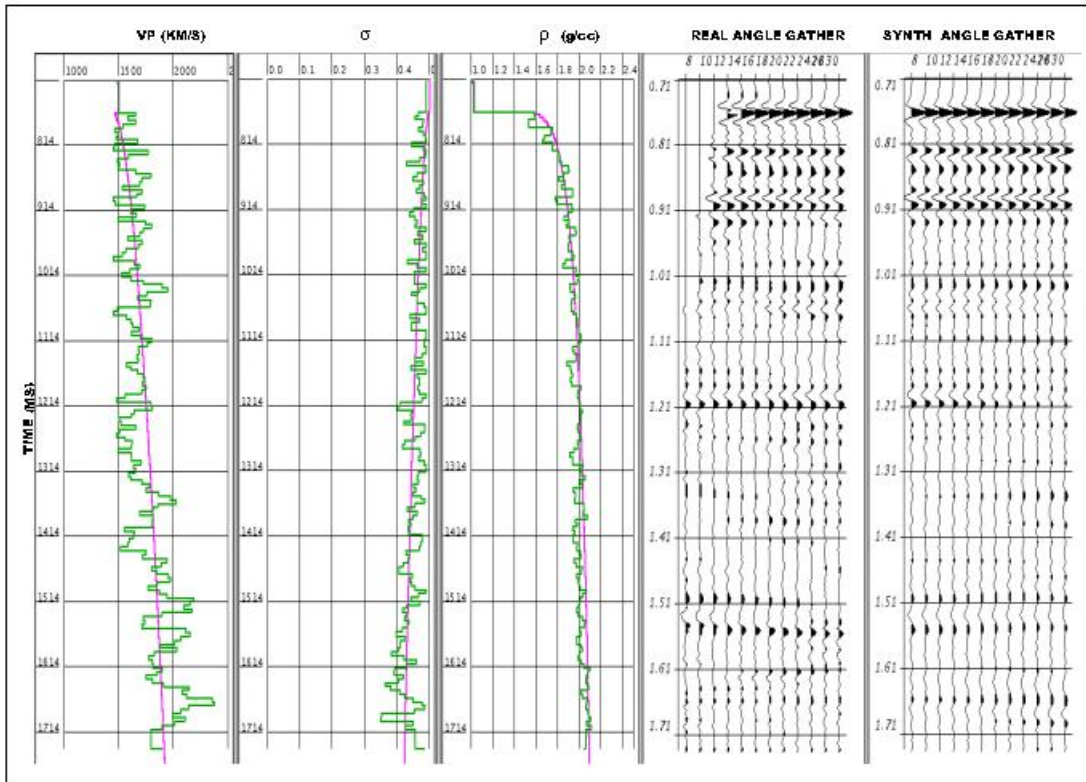
Figure A.4. FWPI results at location IL4042, XL2890. The pink curves are the elastic parameter trends of the background rock model.

GA 4042-2943, Maximum correlation = 0.8885
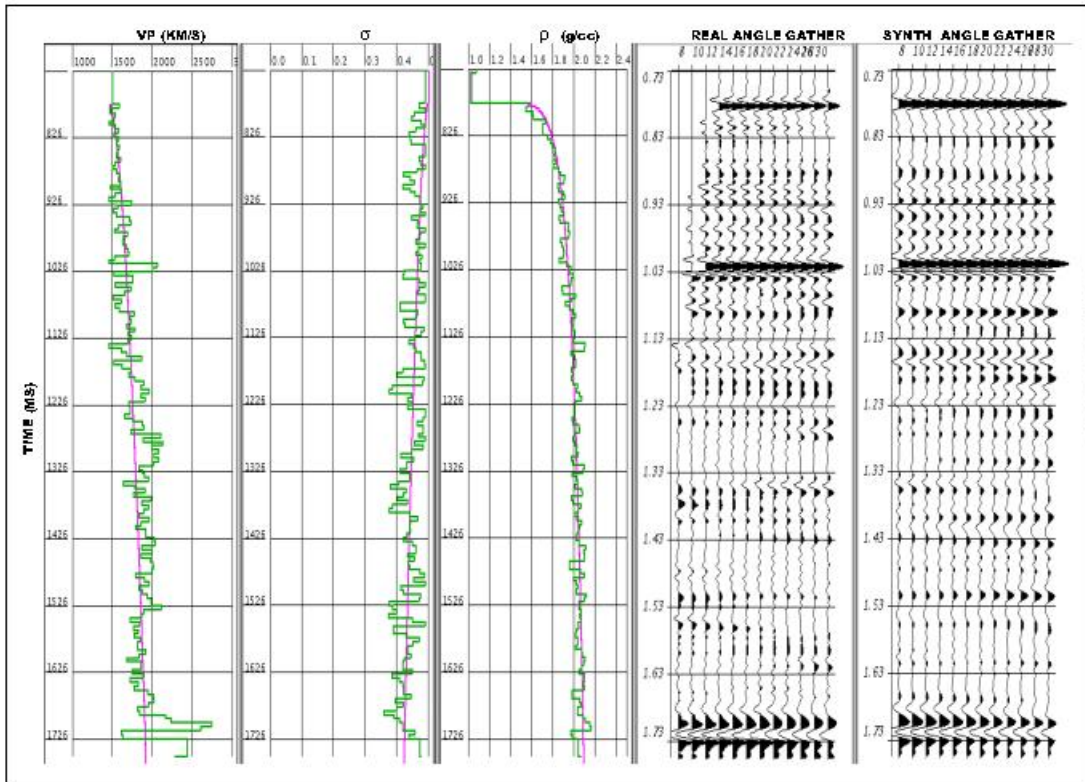
Figure A.5. FWPI results at location IL4042, XL2943. The pink curves are the elastic parameter trends of the background rock model.
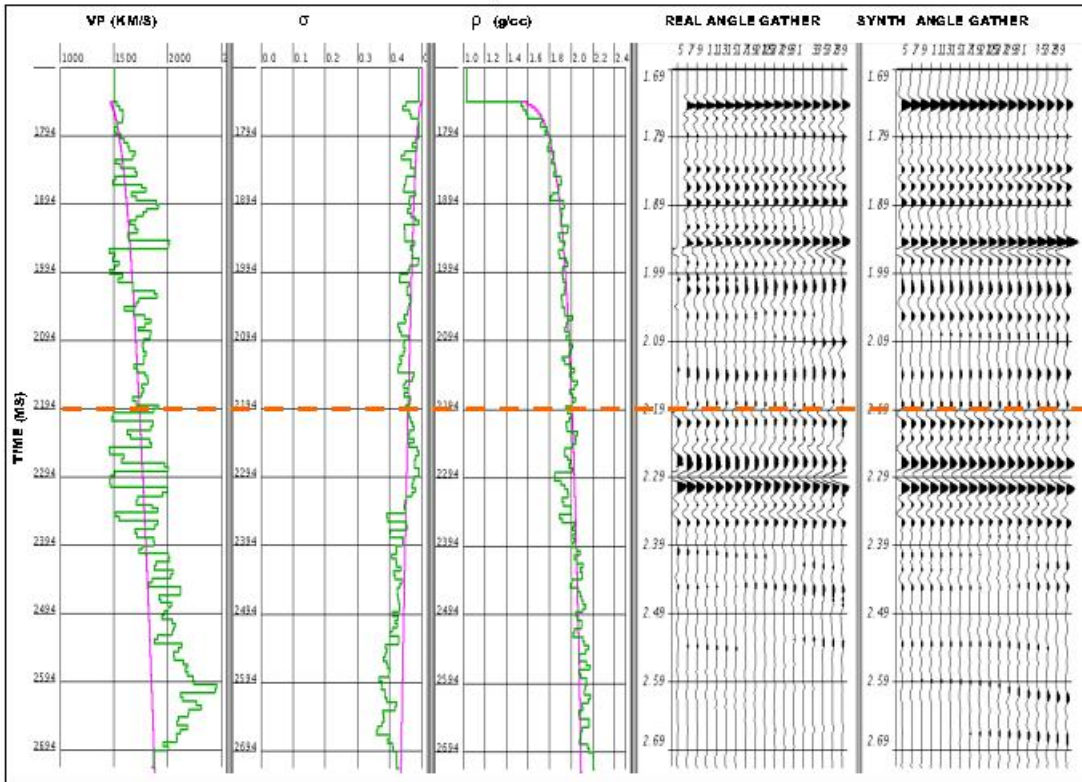
GA 4042-2956 , Maximum correlation = 0.8423
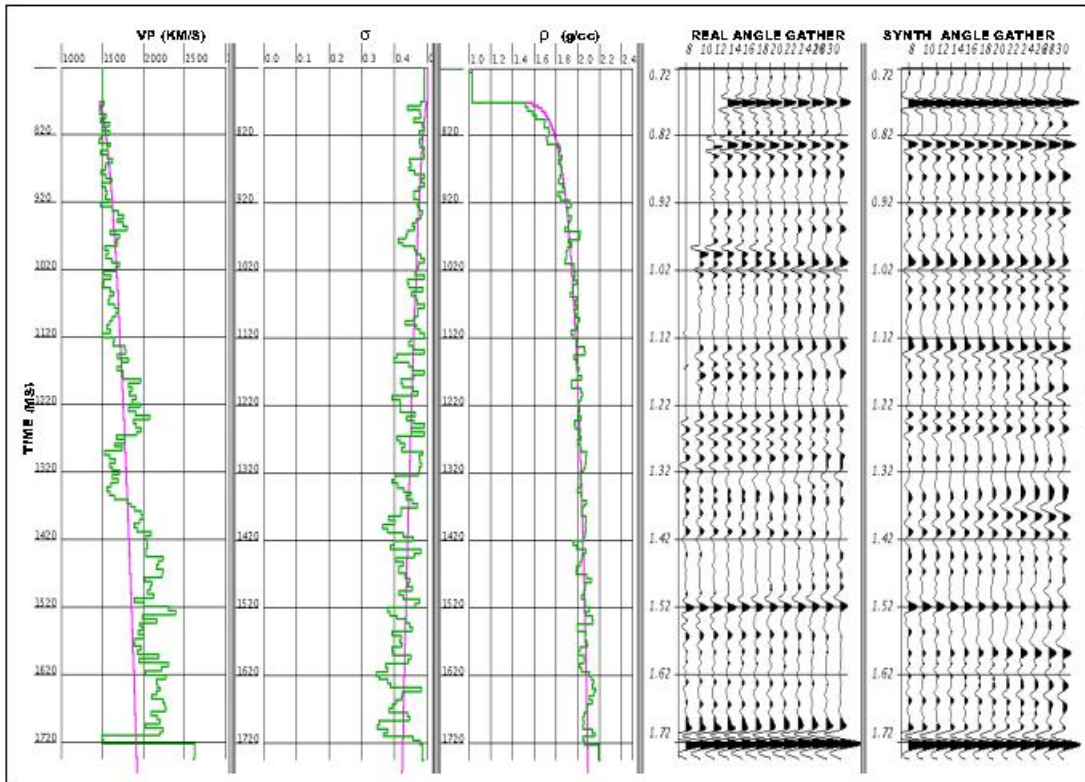
Figure A.6. FWPI results at location IL4042, XL2956. The pink curves are the elastic parameter trends of the background rock model.
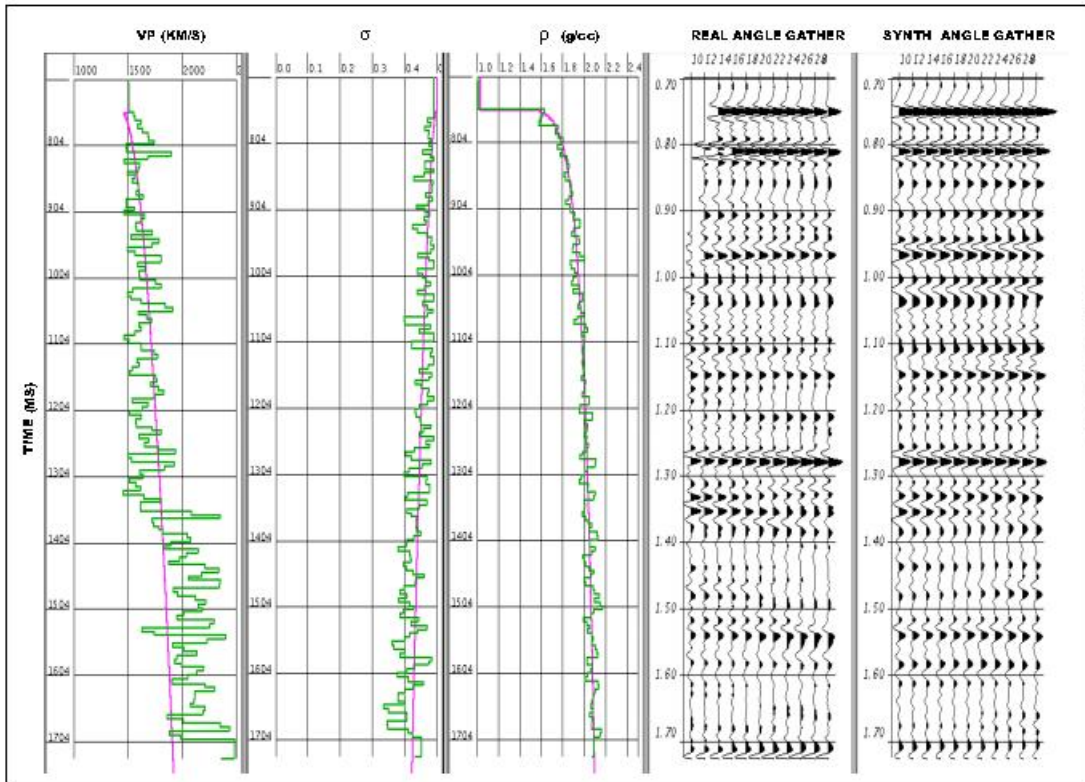
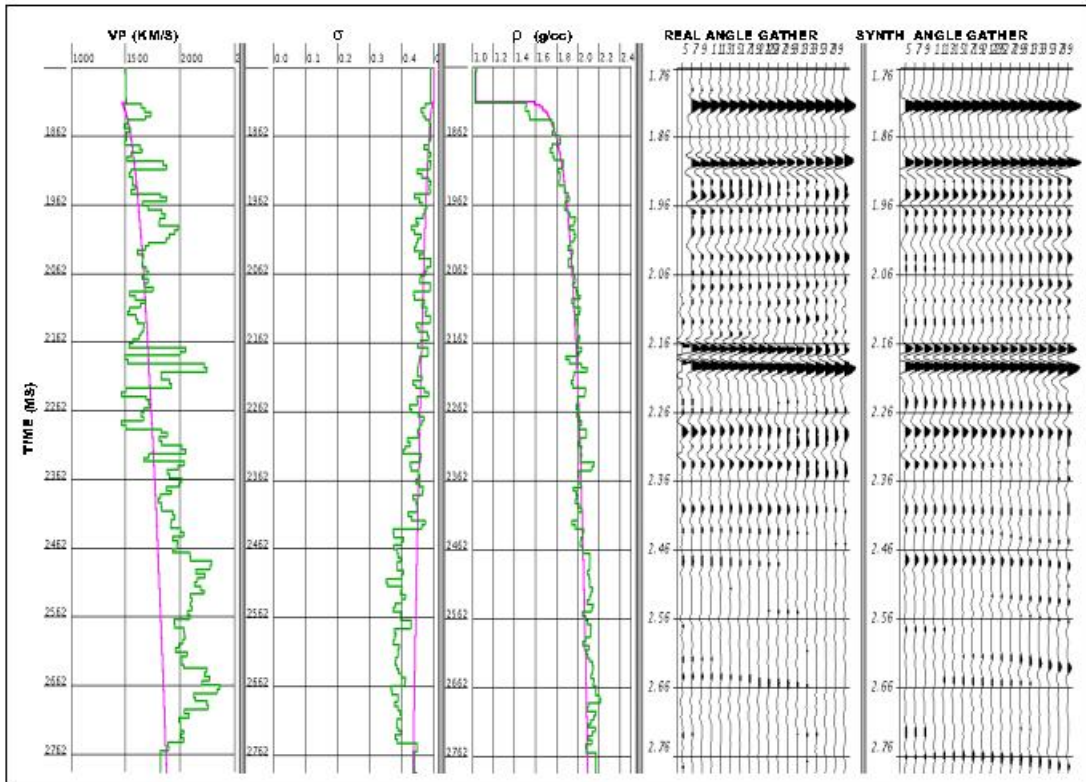Figure A.7. FWPI results at location IL4042, XL2974. The pink curves are the elastic parameter trends of the background rock model.
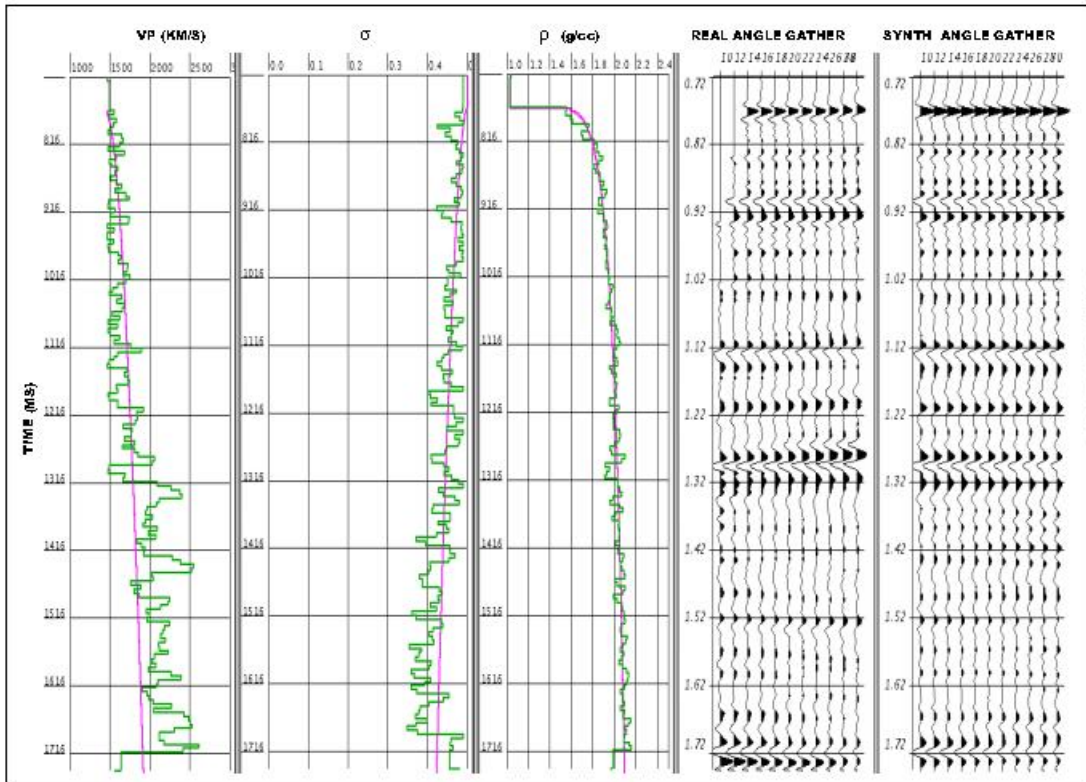
Figure A.8. FWPI results at location IL4060, XL2959. The pink curves are the elastic parameter trends of the background rock model.
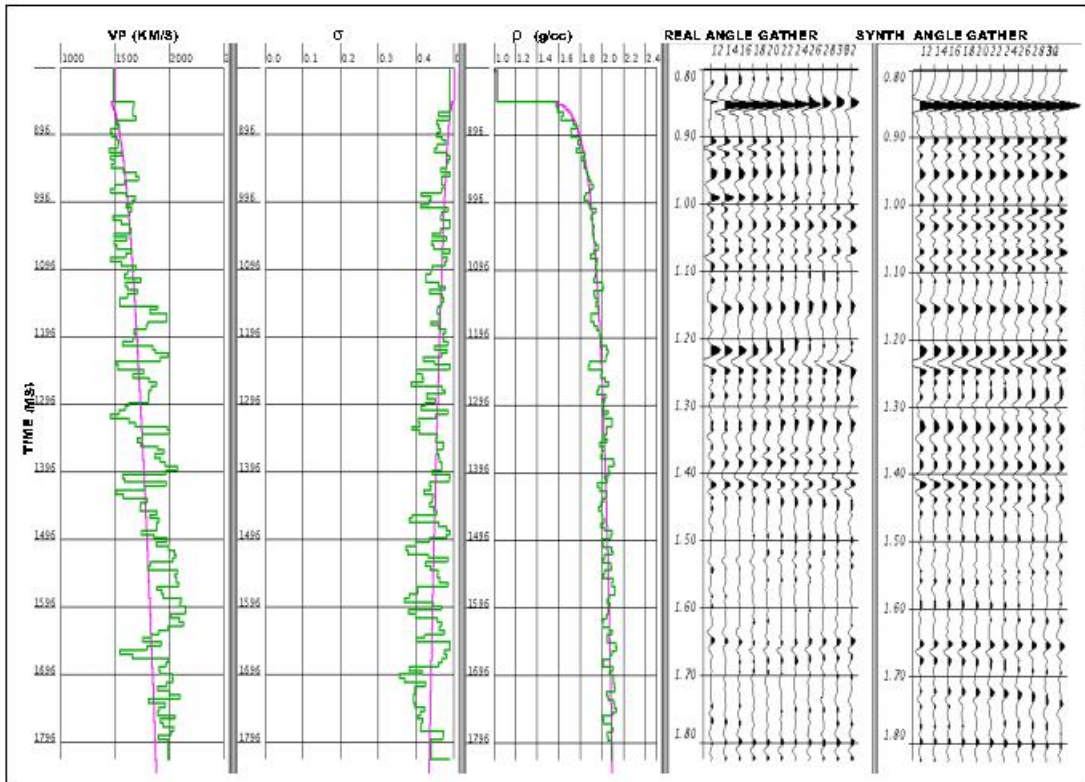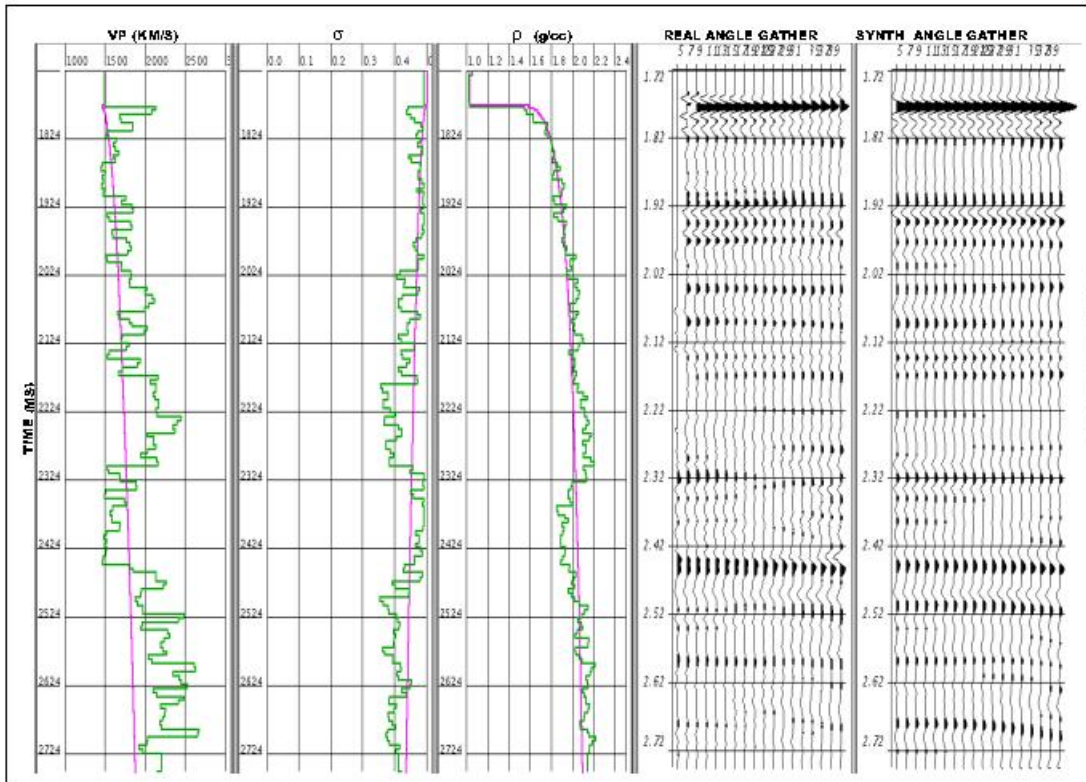
Figure A.9. FWPI results at location IL4100, XL2920. The pink curves are the elastic parameter trends of the background rock model.

Appendix B

Prestack Inversion results on Keathley Canyon Block 194-195.

The following figures are the results of prestack full-waveform Inversion on Keathley Canyon Blocks 194-195. The BSR is marked with a dashed orange line at those locations where it appears.
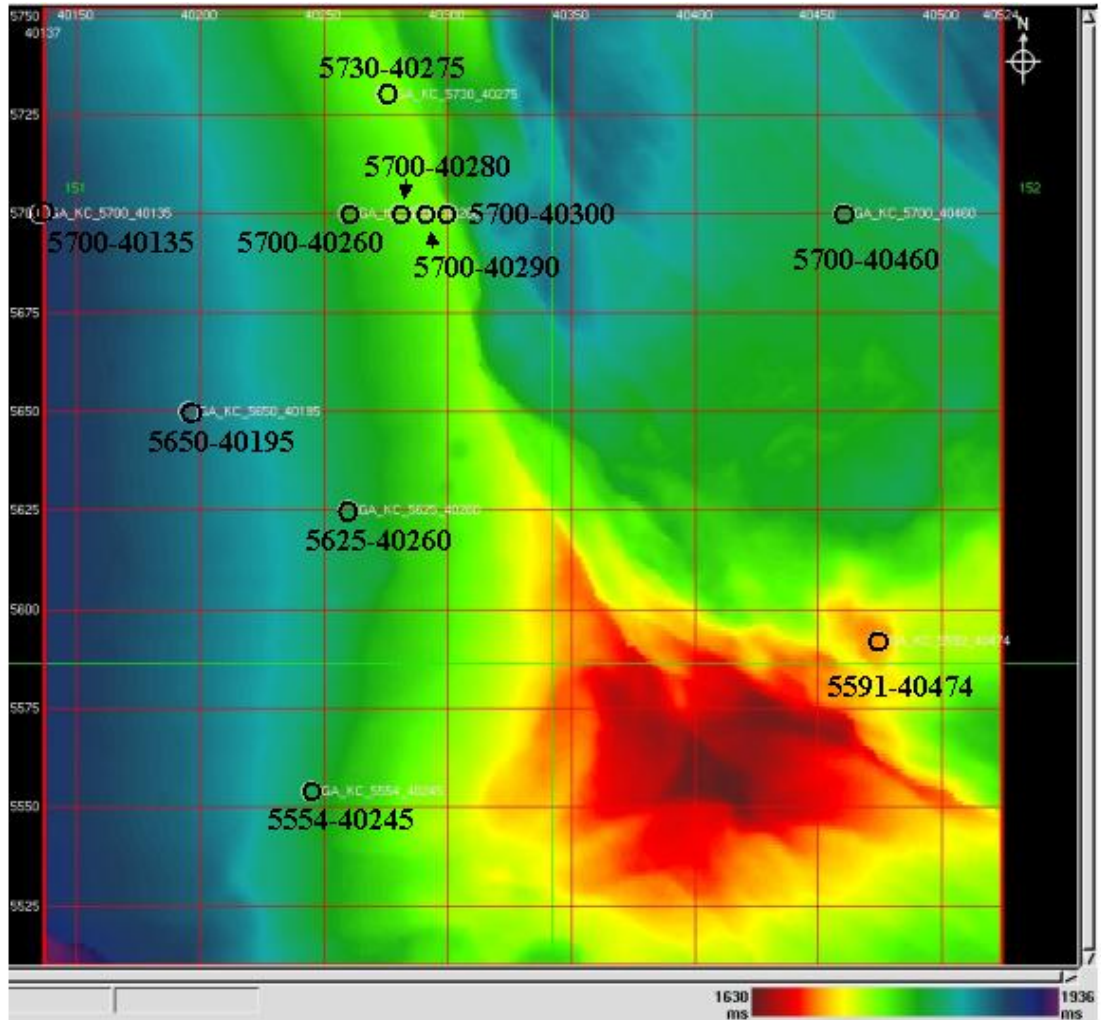
Keathley Canyon Block 195 showing inversion locations.

KC 5554-40245, Maximum correlation = 0.8923
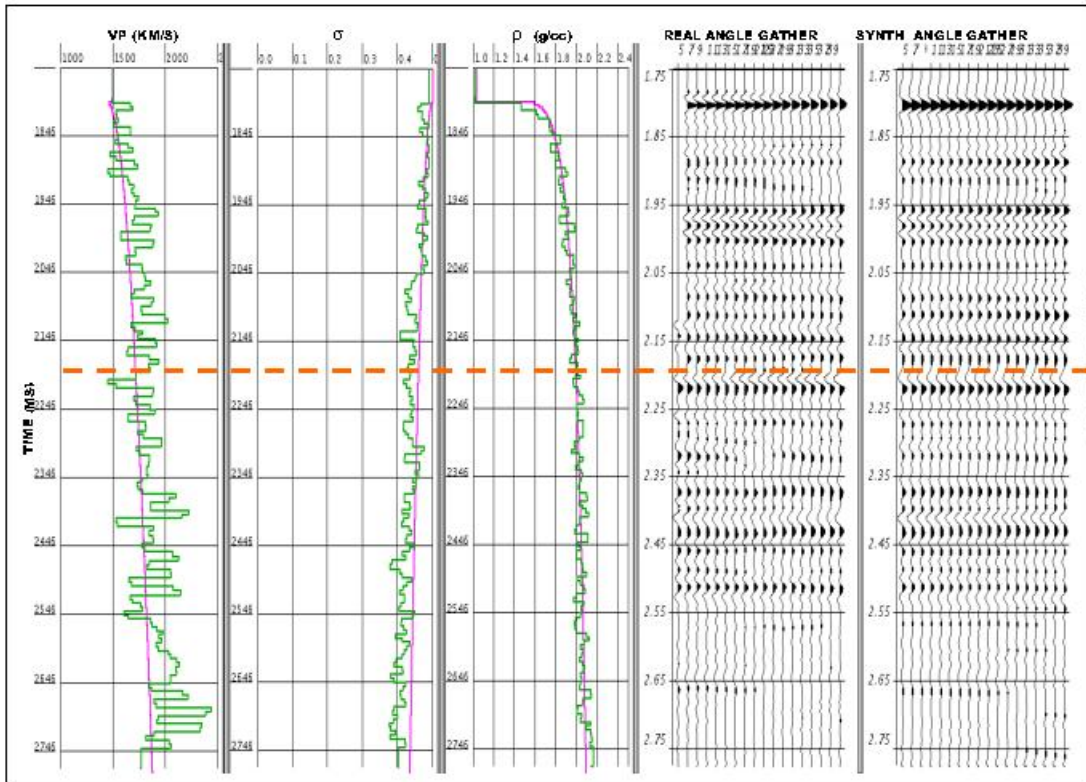
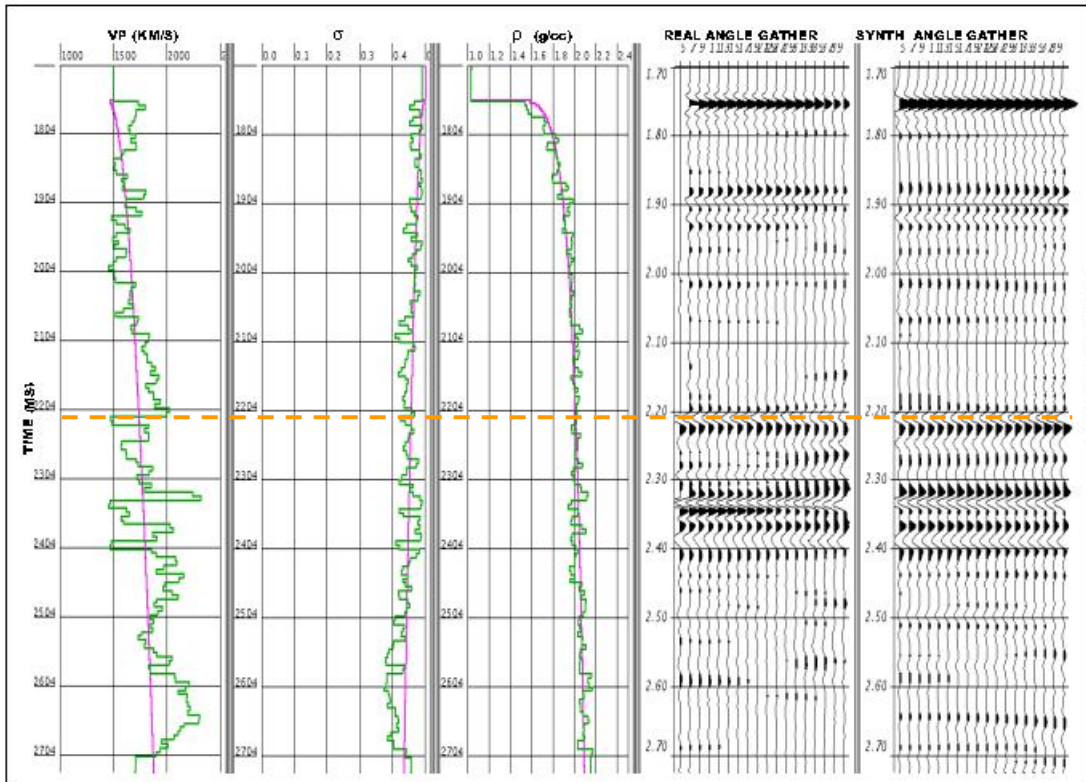
Figure B.1. FWPI results at location IL5554, XL40245. The pink curves are the elastic parameter trends of the background rock model. The orange dashed line is the interpreted BSR level.
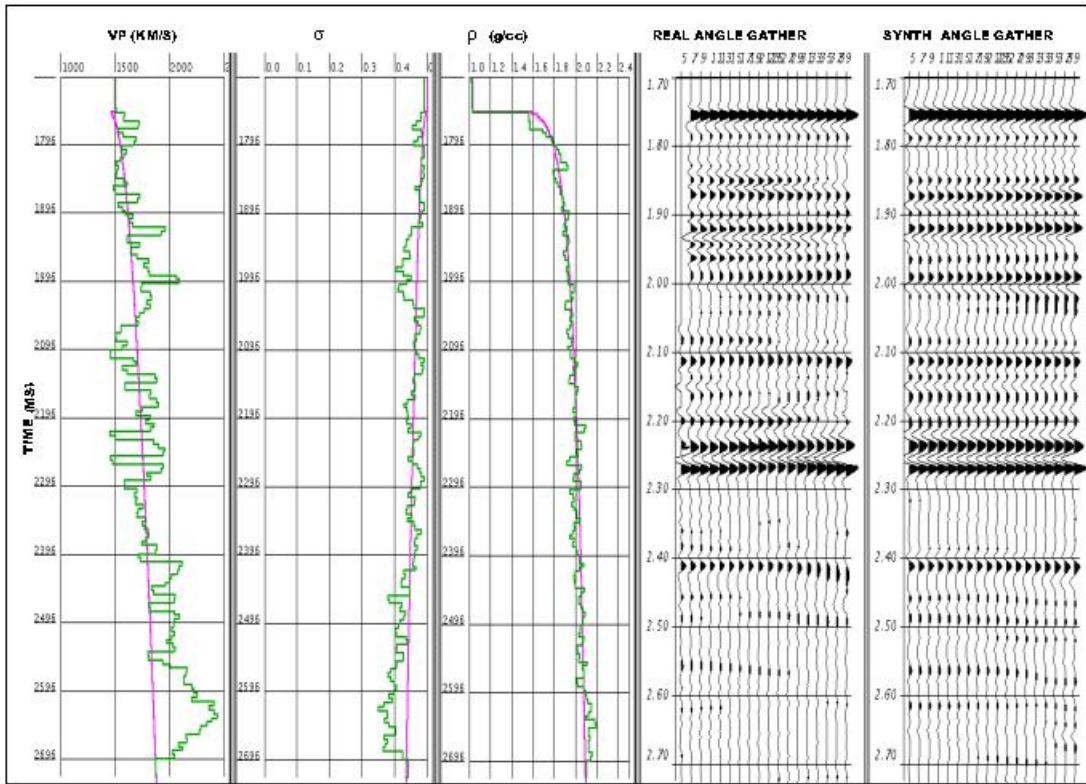
111
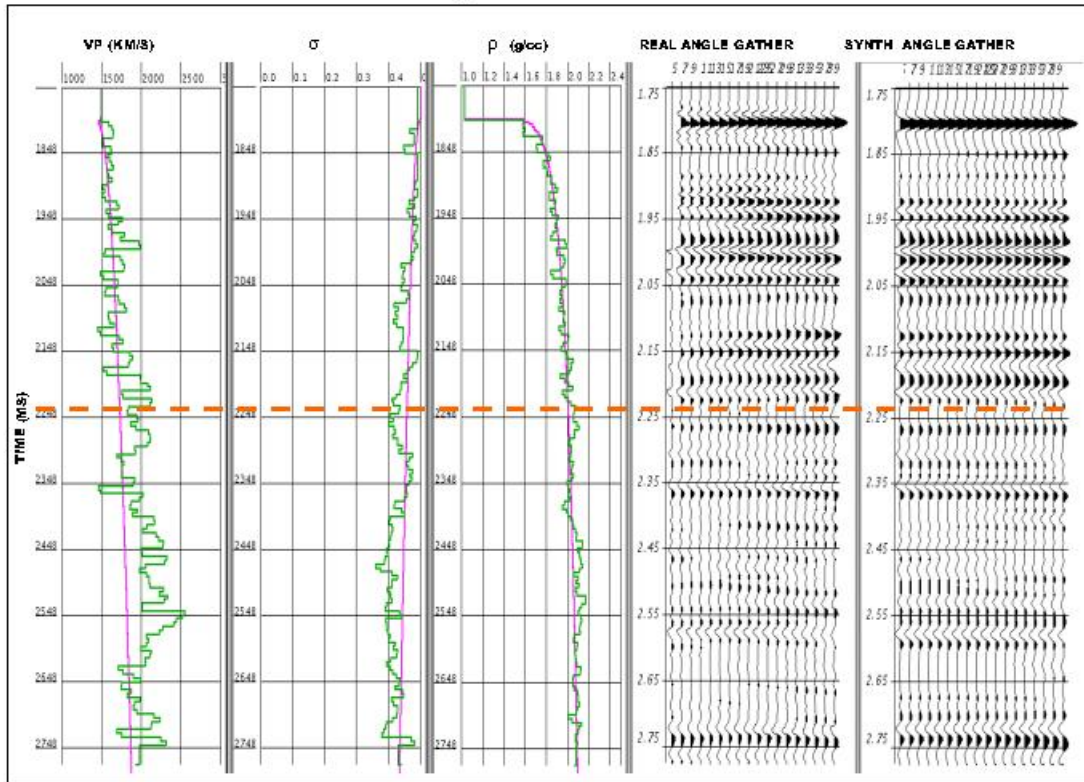
Figure B.2. FWPI results at location IL5625, XL40260. The pink curves are the elastic parameter trends of the background rock model. The orange dashed line is the interpreted BSR level.

Figure B.3. FWPI results at location IL5650, XL40195. The pink curves are the elastic parameter trends of the background rock model. The dashed orange line is the interpreted BSR level.
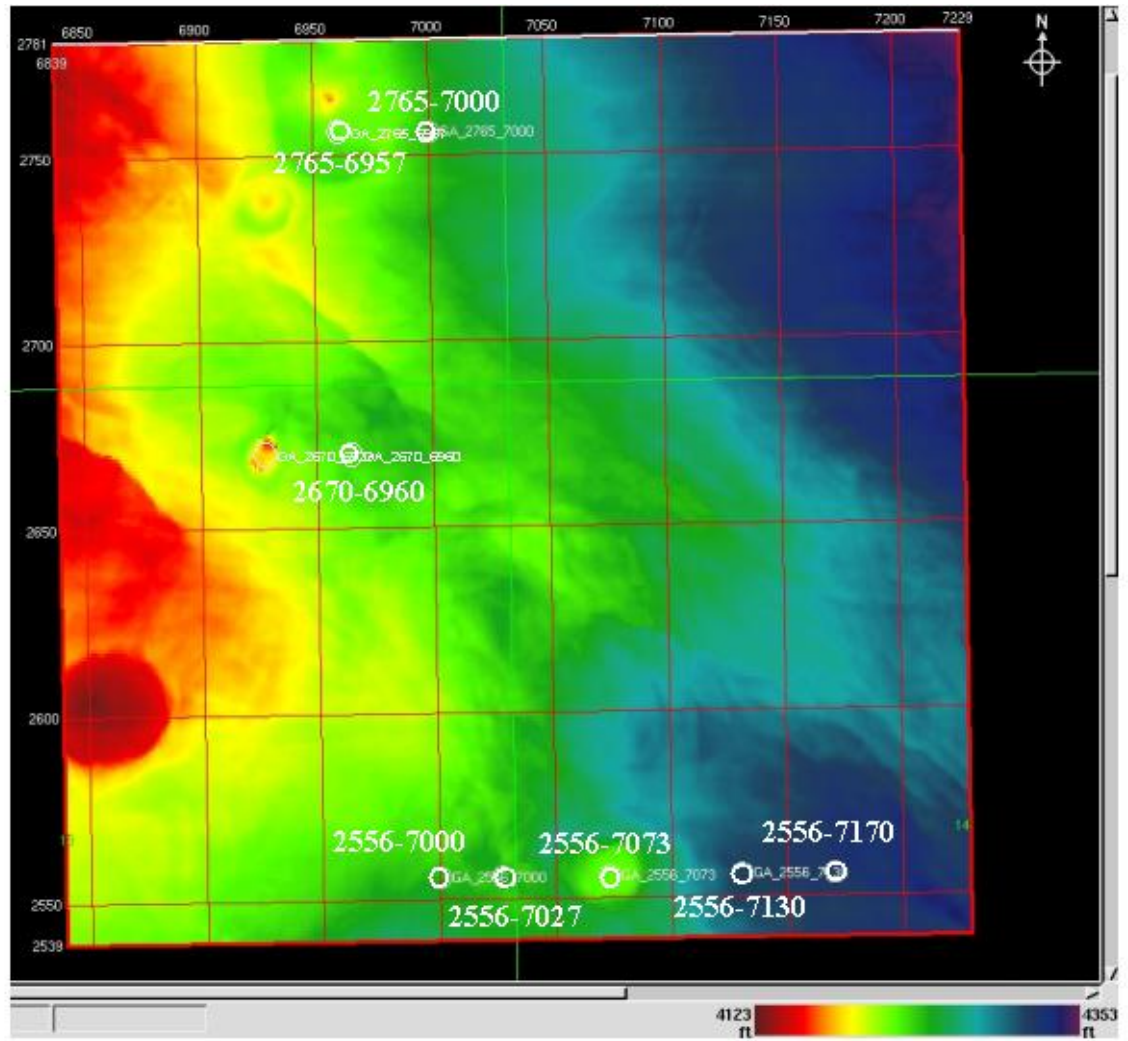
113

Figure B.4. FWPI results at location IL5700, XL40290. The pink curves are the elastic parameter trends of the background rock model. The dashed orange line is the interpreted BSR level.
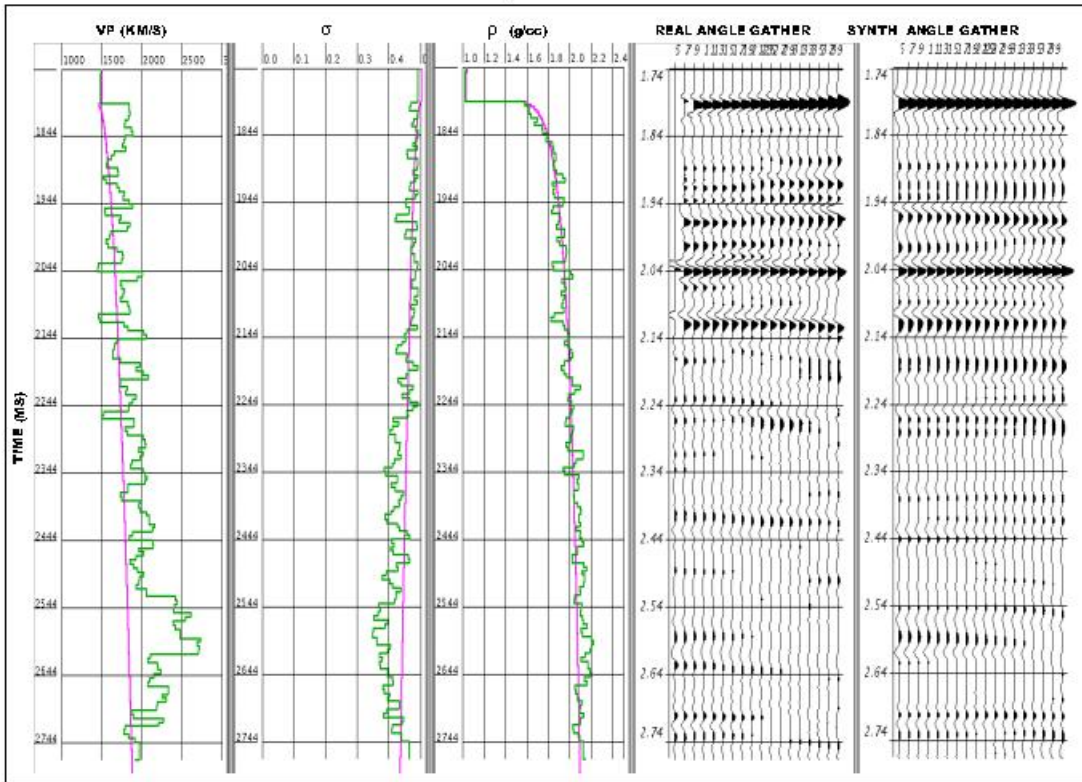
Figure B.5. FWPI results at location IL5700, XL40460. The pink curves are the elastic parameter trends of the background rock model.
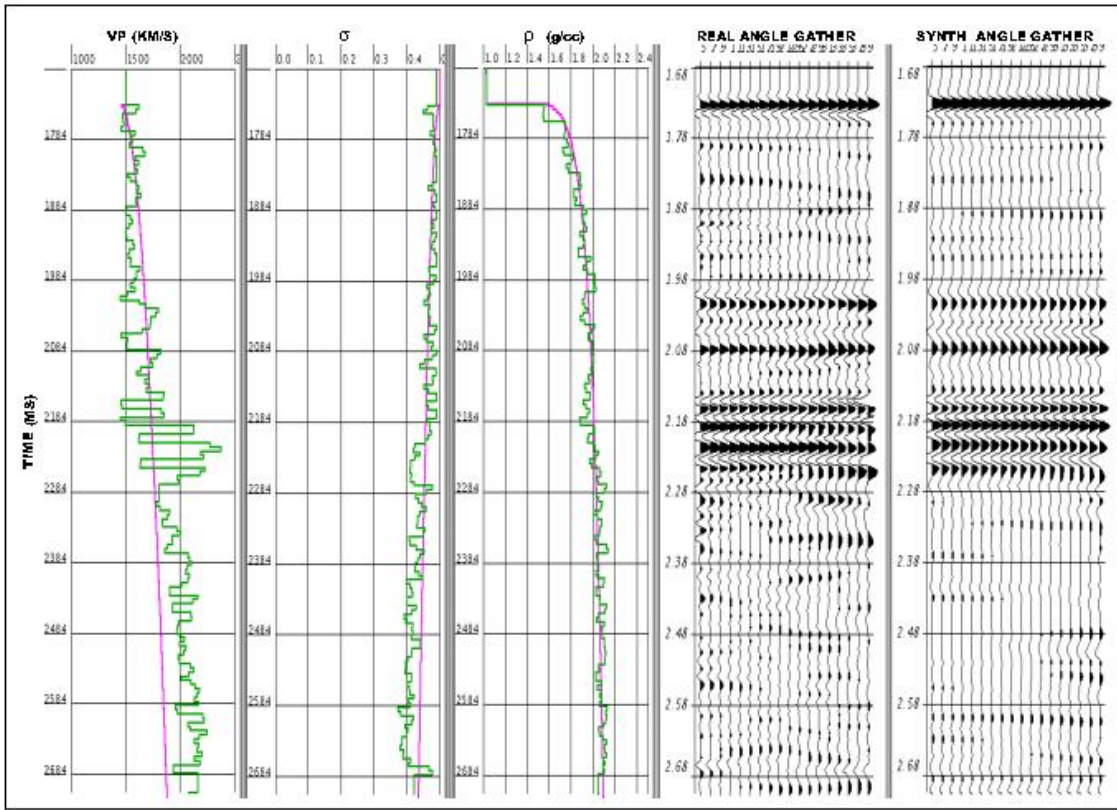
Figure B.6. FWPI results at location IL5730, XL40275. The pink curves are the elastic parameter trends of the background rock model. The dashed orange line is the interpreted BSR level.
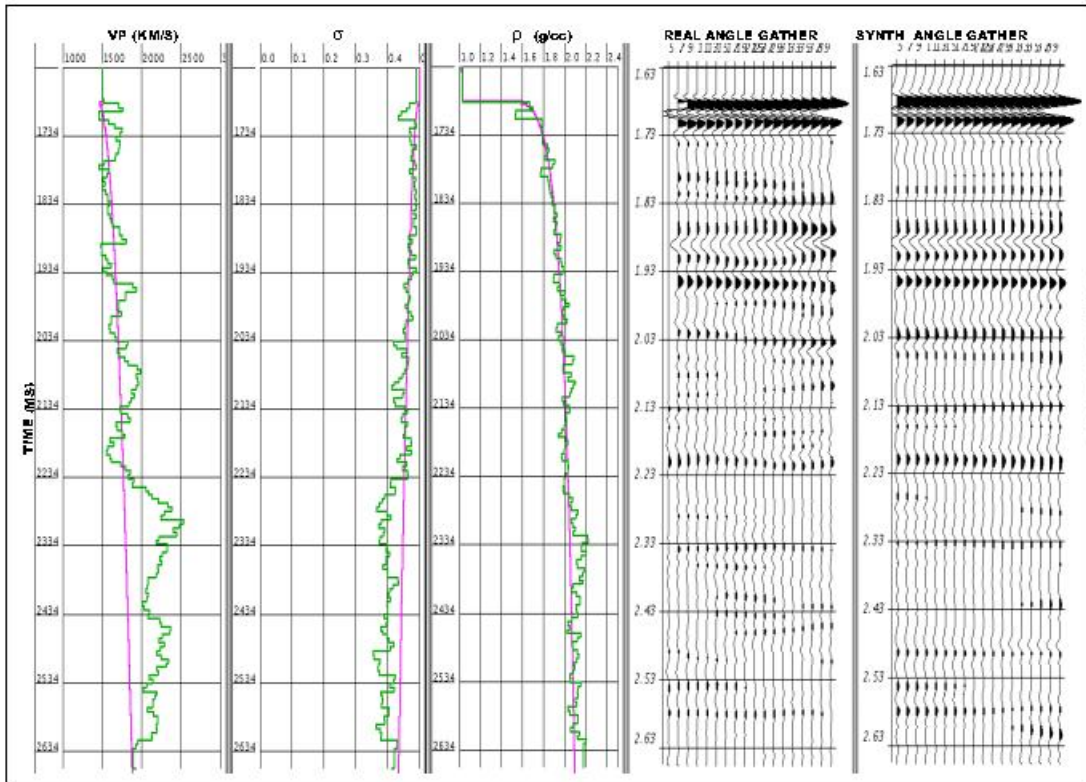
Figure B.7. FWPI results at location IL5591, XL40474 (possible hydrate mound). The pink curves are the elastic parameter trends of the background rock model.
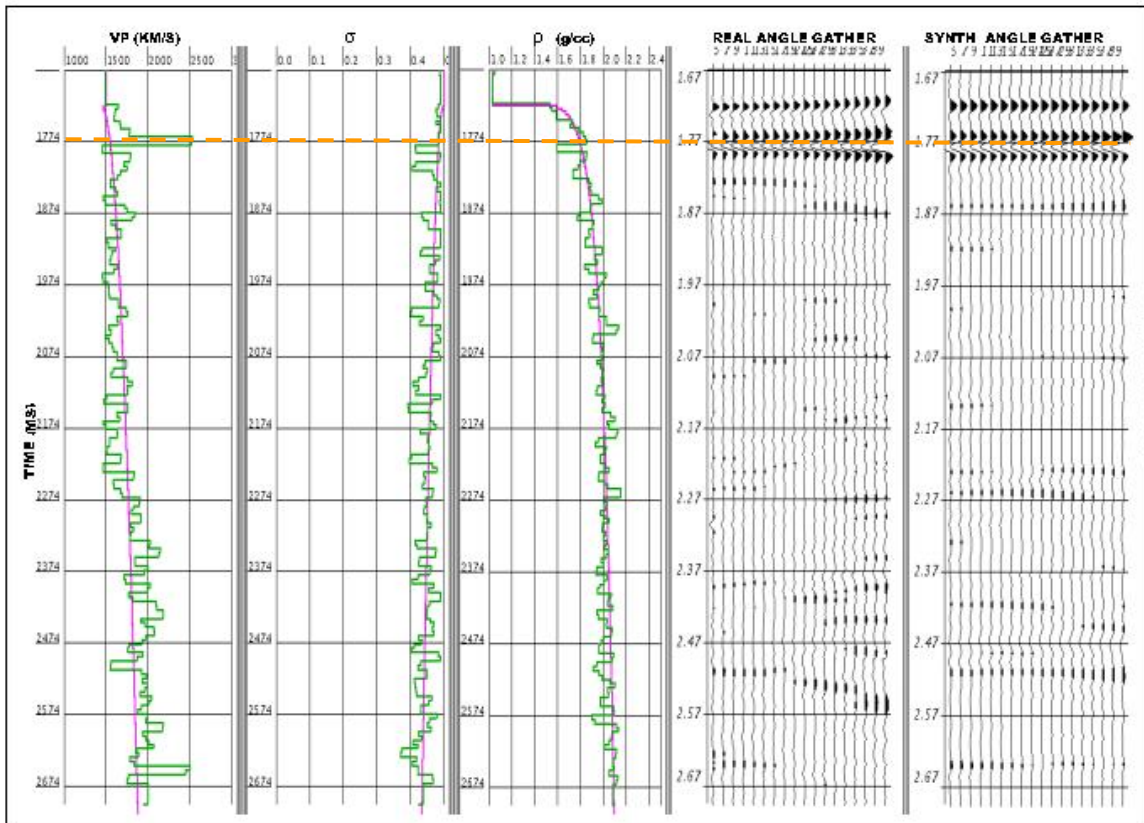
Figure B.8. FWPI results at location IL5700, XL40135. The pink curves are the elastic parameter trends of the background rock model.

Figure B.9. FWPI results at location IL5700, XL40260. The pink curves are the elastic parameter trends of the background rock model.

Figure B.10. FWPI results at location IL5700, XL40280. The pink curves are the elastic parameter trends of background rock model. . The dashed orange line is the interpreted BSR level.
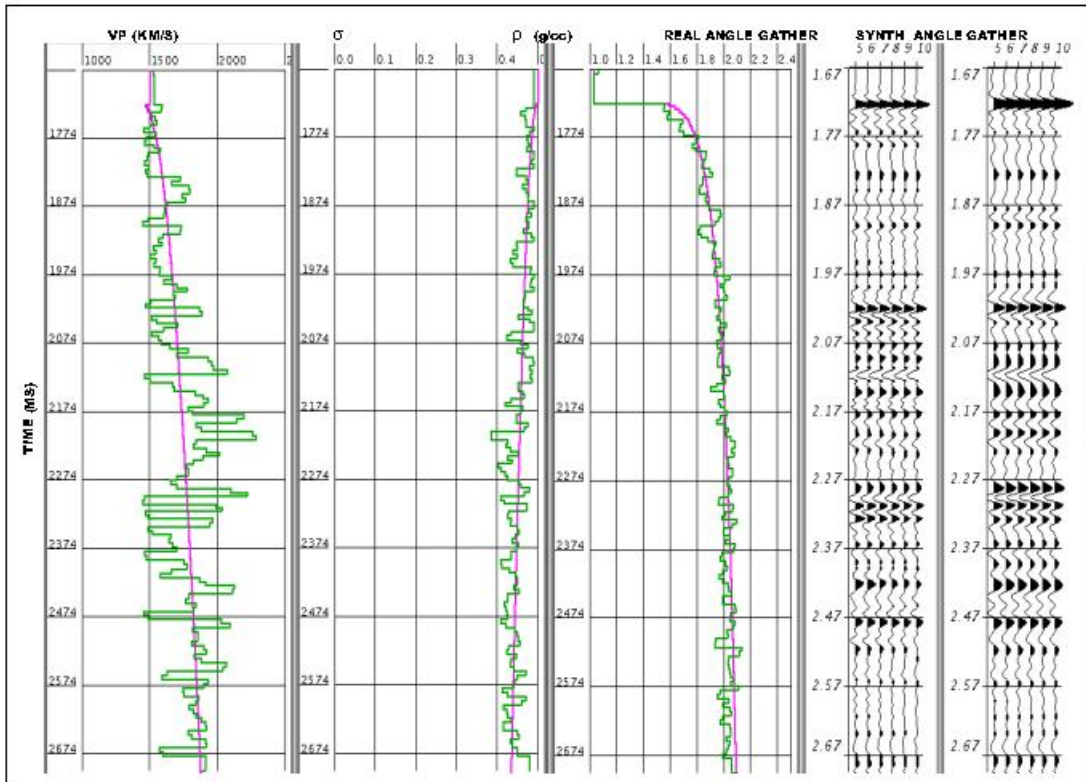
Figure B.11. FWPI results at location IL5700, XL40300. The pink curves are the elastic parameter trends of background rock model.

Appendix C

Prestack Inversion results on Atwater Block 14

The following figures are the results of GA prestack full-waveform inversion on Atwater Block 14.

Atwater Valley 14 showing inversion locations.
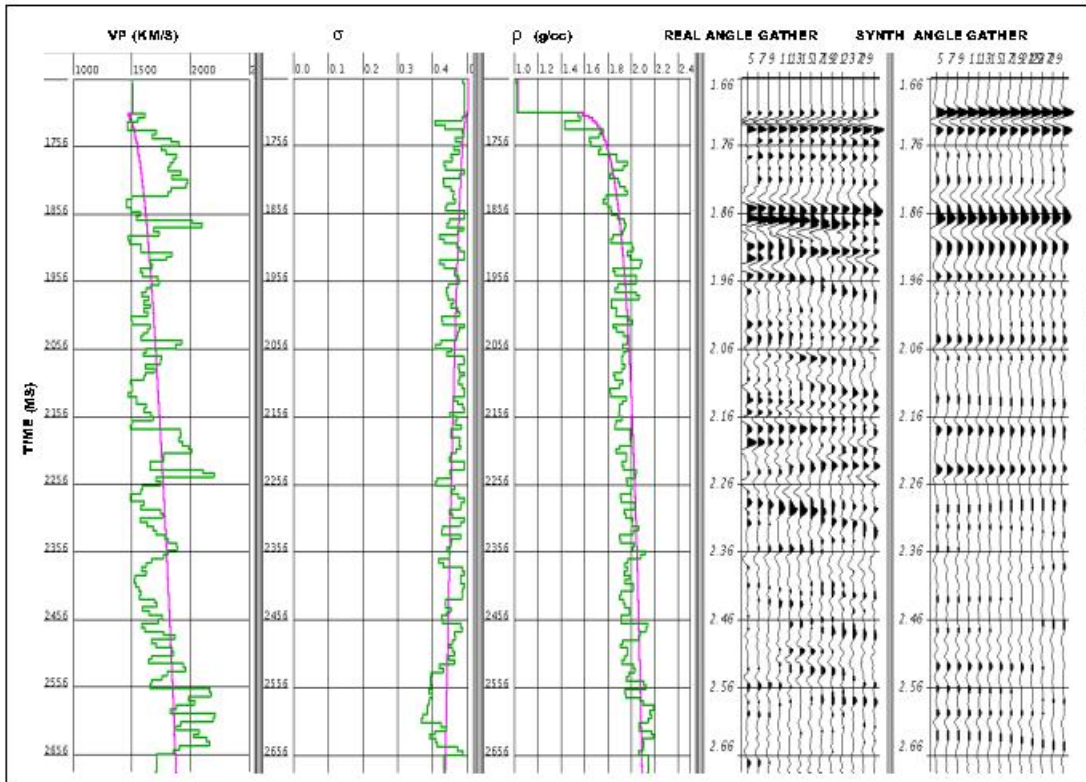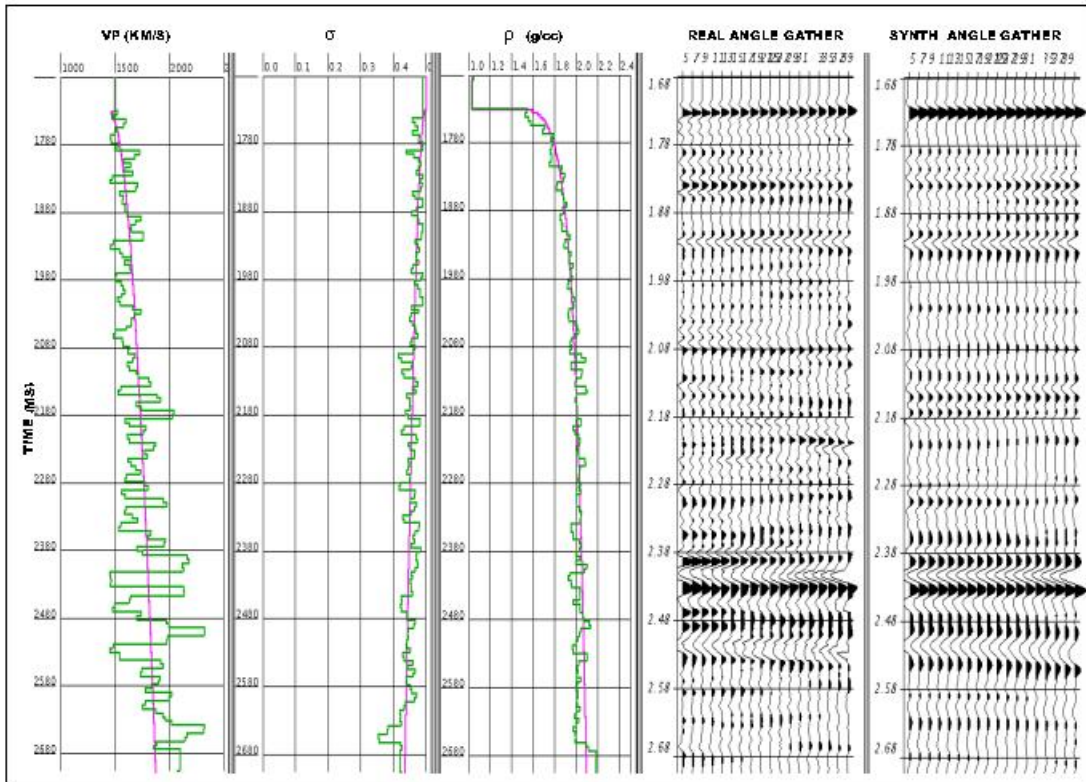
Figure C.1. FWPI results at location IL2556, XL7027. The pink curves are the elastic parameter trends of the background rock model.

Figure C.2. FWPI results at location IL2556, XL7073 (Mound "F"). The pink curves are the elastic parameter trends of the background rock model. The orange line is the possible shallow BSR below the mound.

Figure C.3. FWPI results at location IL2670, XL6960. The pink curves are the elastic parameter trends of the background rock model.

Figure C.4. FWPI results at location IL2765, XL6957. The pink curves are the elastic parameter trends of the background rock model.

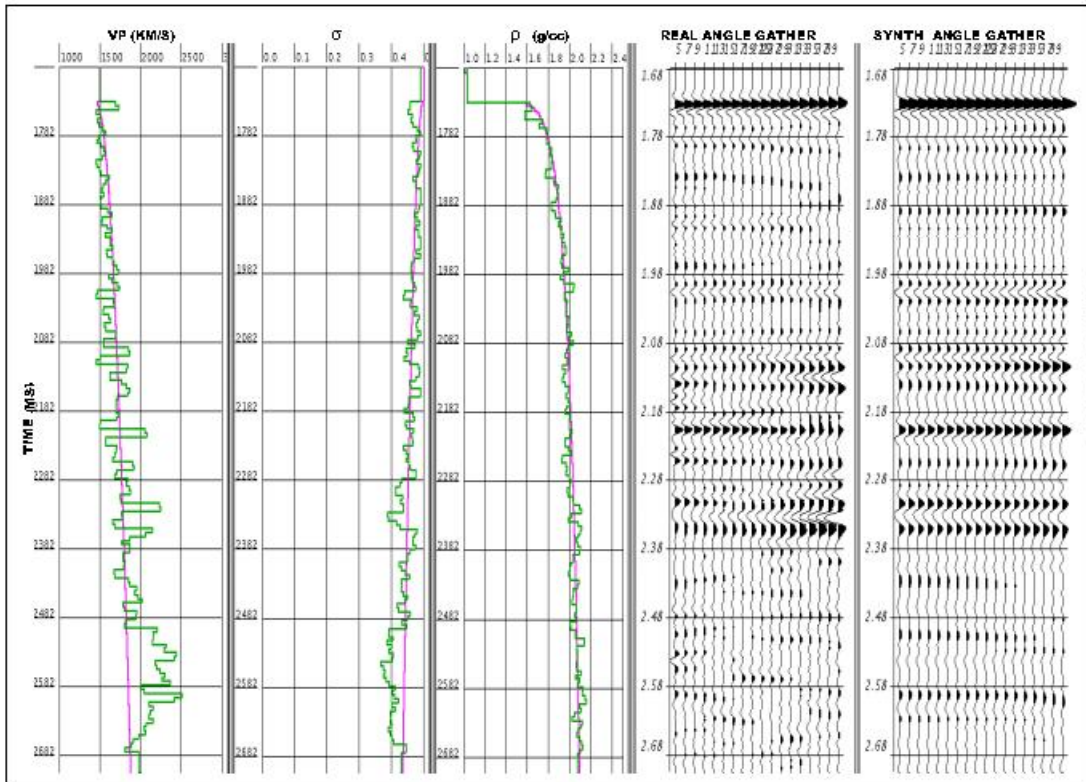Figure C.5. FWPI results at location IL2765, XL7000. The pink curves are the elastic parameter trends of the background rock model.

Figure C.6. FWPI results at location IL2556, XL7000. The pink curves are the elastic parameter trends of the background rock model.
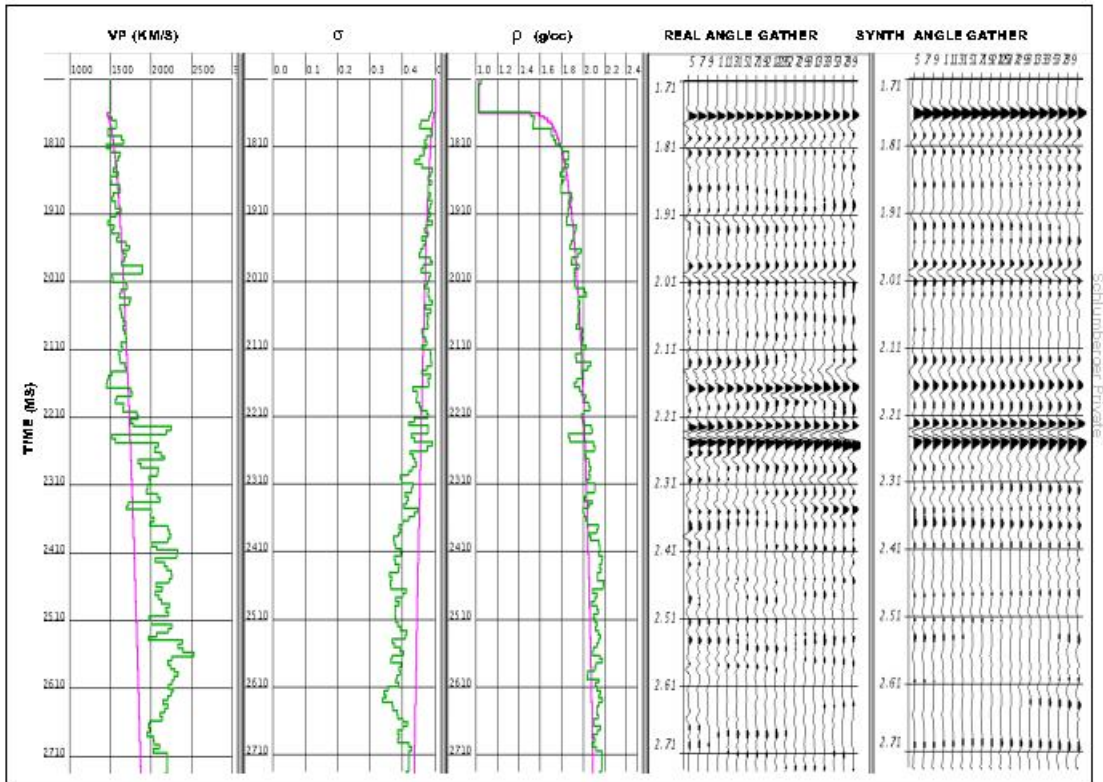
Figure C.7. FWPI results at location IL2556, XL7130. The pink curves are the elastic parameter trends of the background rock model.

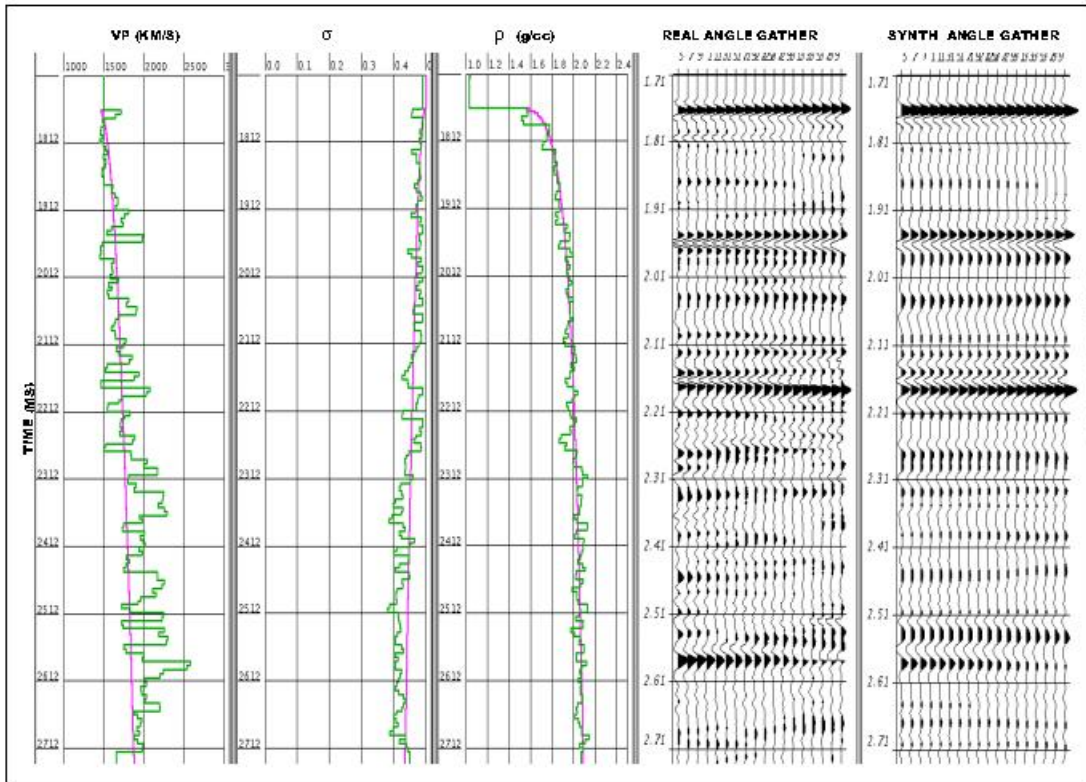**AV 2556-7170, Maximum correlation = 0.8054**

Figure C.8. FWPI results at location IL2556, XL7170. The pink curves are the elastic parameter trends of the background rock model.